Multi-threaded Congo River channel hydraulics: Field-based characterisation and representation in hydrodynamic models

Benedict Andrew Carr

Submitted in accordance with the requirements for the degree of

Doctor of Philosophy

The University of Leeds

School of Civil Engineering

School of Geography

September 2020

The candidate confirms that the work submitted is his own and that appropriate credit has been given where reference has been made to the work of others.

Acknowledgements

It was my partner Lauren who gave me the inspiration and support I needed to take on this research project, so first and foremost I want to thank her. Thank you for inspiring me with your own intrepid exploits and outlook, and for your unwavering love and encouragement.

Acknowledgement must go to the University of Leeds for funding my studentship, which provided me with the privileged opportunity to pursue this PhD. I am also grateful to the Royal Society and the UK Department for International Development, whose collaborative funding allowed me the opportunity to conduct fieldwork that has been absolutely central to my research.

I feel very lucky to have received excellent support and supervision over the course of my PhD. Special thanks to my lead supervisor Mark Trigg, who has been a good friend as well as a mentor. I had high expectations of this research project, and I cannot thank you enough for all you have done to ensure my expectations were not only met but surpassed. I am also very grateful to Mark Smith, who surely went beyond his role as secondary supervisor, not least in painstakingly honing every piece of my research writing over the last four years. Thanks to Duncan Borman for his insightful contributions during many hours of supervision meetings, and to Paul Bates who provided guidance in respect of the research presented in Chapter 5. I must also acknowledge Fiachra O'Loughlin, Alain Laraque, and Doug Alsdorf; their Congo River research efforts have been key sources of knowledge and data for me. Many others, too many to thank individually, have given me encouragement and feedback at conferences, workshops, and seminars, and have made me feel welcome in the academic community.

My fieldwork was a real collective effort, and I must thank those who helped make it a successful and epic experience. I am heavily indebted to Raphael Tshimanga, who worked tirelessly to facilitate the fieldwork. The perseverance and courage you showed to overcome so many challenges and setbacks I found remarkable. Much credit goes to Jean-Felly Ngandu for taking care of all things administrative in such a dependable way, which is no easy feat in DR Congo. Thanks to Catherine Awidi Mushi, Gode Bola, Pierre Kabuya, Jules Beya, Cedric Tschumbu and Fanzo Kibengele: you helped set up equipment, took measurements at unearthly hours, and shared many a Tembo with me. I must also thank the crews of Mpombie and Lomeka for their safe and skilful navigation of the river, the staff of CRREBaC for their organisational and logistical support, and Gabriel Mokango at Régie des Voies Fluviales for his influential support.

I wish to thank Preksedis Ndomba, Denis Hughes, Jeff Neal, and Felix Mtalo for welcoming me into the CRuHM consortium. Being part of CRuHM exposed me to a wealth of African research expertise, and has been of great benefit to my research. It also allowed me to conduct my research in a way that has helped build African research capacity, a feature that has been a great source of motivation and pride for me.

My decision to take on this research project was a gamble in some respects. It meant giving up a secure job, temporarily relocating, and embarking on high risk fieldwork. I must thank my parents for understanding my decision; your support made the gamble a lot less daunting. Finally, I have my sister Rachael to thank for tolerating two years of my couch-surfing, and for listening to me practise presentations late at night with sincere interest.

Abstract

Hydrodynamic processes that occur along the Congo Middle Reach are a key determinant of risks pertaining to biogeochemical cycling, ecology, public health, transportation, and flood risk. Knowledge of channel hydraulics is paramount to understanding and modelling these hydrodynamic processes, yet such knowledge is severely lacking here.

The aims of the research presented in this thesis were twofold. The first aim was to assess the water surface and in-channel hydraulic conditions along the Congo Middle Reach, and the capacity of satellite observations to determine these conditions. The second aim was to evaluate methods of channel geometric representation in hydrodynamic models of the multichannel Congo mainstem. Fieldwork was central to achieving these aims; the field data having been used to characterise hydraulics, assess satellite altimetry datasets, model bathymetry, and model fluvial hydraulics and hydrodynamics.

A key finding of the hydraulic characterisation was a complete absence of river flow constrictions that cause backwater effects, which partly explains the relatively subtle nature of inundation here. Assessment of existing satellite profiling altimetry datasets showed their spatial coverage adequately captures the water surface profile along more than 1,200 kilometres of the middle reach. However, coverage was insufficient through the Chenal entrance, where a downstream increase in bed-slope generates a significant drawdown effect. Satellite altimetry deviated from field measurements by two metres here, which is half the annual flood wave amplitude. The findings show that these satellite profiling altimeters cannot be relied on to capture significant water surface slope variability resulting from gradually varied flow conditions, even on the world's largest rivers.

Modelling work showed that the Congo's multi-threaded channel geometry can be simplified to an effective single channel in a hydrodynamic model, without introducing significant error. The resultant root mean square error in water surface elevation was estimated to be less than 0.25 metres, providing channel friction and shape parameters are calibrated to observations obtained across the entire flow range. This finding may apply to other large multi-threaded channel reaches, which are commonly found on the world's largest rivers.

Contents

List of Figures

List of Tables

List of Abbreviations

1D	One Dimensional
2D	Two Dimensional
ADCP	Acoustic Doppler current profiler
ALOS	Advanced Land Observing Satellite (Japanese Earth observing satellite program)
aSL	above Sea Level
ASTER GDEM	Advanced Spaceborne Thermal Emission and Reflection Radiometer Global Digital Elevation Model
AW3D30	ALOS World 3D - 30m
BM	bathymetry model
CICOS	Commission of the Congo-Oubangui-Sangha Basin
CMR	Congo Middle Reach
CNES	French government space agency
CRB	Congo River Basin
CRuHM	Congo River users Hydraulics and Morphology (research consortium)
Cryosat-2	An environmental research satellite under the European Space Agency
DEM	Digital Elevation Model
DRC	Democratic Republic of Congo
EB	estimated bathymetry
EGM2008	Earth Gravitational model 2008 (geoid)
EGM96	Earth Gravitational model 1996 (geoid)
ENVISAT	Environmental research Satellite under the European space agency.
ESC	effective single channel
GFM	global flood model
GIS	geographical information system
GNSS	global navigation satellite system
GPS	geographical positioning system
GRDC	Global Runoff Data Center
HEC-RAS	Hydrologic Engineering Center River Analysis System
Hydroweb	Online database providing time series of inland water surface elevation from satellite altimetry

ICESat	Ice, Cloud, and land Elevation Satellite
ICESat-2	Ice, Cloud, and land Elevation Satellite 2
IDW	inverse distance weighting
InSAR	Interferometric synthetic aperture radar
Jason	Joint Altimetry Satellite Oceanography Network
JERS-1	Japanese Earth Resources Satellite 1
LiDAR	Light Detection and Ranging
LISFLOOD-FP	a raster-based flood inundation model
MAE	mean absolute error
MBES	multibeam echosounder
MERIT	Multi Error Removed Improved Terrain DEM
MGB	Modelo de Grandes Bacias
MODIS	Moderate resolution Imaging Spectro-radiometer
MT	‘merging of individual channel threads’ hydraulic model experiment
PALSAR	Phased Array type L-band Synthetic Aperture Radar (Instrument of ALOS)
PANAV	Projet d'Appui à la Navigabilité des voies Fluviales et Lacustres
PPP	precise point positioning
R^2	coefficient of determination
RADARSAT-2	Canadian Space Agency Earth observation satellite
RMS	Root mean squared
RMSE	Root mean squared error
RVF	Régie des Voies Fluviales
SAGA	System for Automated Geoscientific Analyses
SAR	Synthetic Aperture Radar
Sentinel-3A	European Space Agency Earth observation satellite
SO-HYBAM	HYdro-geochemistry of the AMazonian Basin; a water resources observaton service
SRS	satellite remote sensing
SRTM	Shuttle Radar Topography Mission
Std Dev	standard deviation
SWE	shallow water equations
SWOT	Surface Water Ocean Topography satellite mission
TanDEM-X	TerraSAR-X add-on satellite mission for Digital Elevation Measurement

TerraSAR-X	a commercial German Synthetic Aperture Radar Earth observation satellite mission
UNOSAT	United Nations Operational Satellite Applications Programme
VS	Virtual Station
WC	Width constriction at high flow hydraulic model experiment
WSE	water surface elevation
WSP	water surface profile
WSS	water surface slope
XSV	‘omitting cross-sectional depth variability’ hydraulic model experiment

List of Units

%	percent
£	pound sterling
°C	degrees Celcius
cm/km	centimetres per kilometere
km	kilometres
km^2	square kilometres
m	metres
m/m	metres per metre
m/s	metres per second
m^2	square metres
m^2/m	square metres per metre
m^3	cubic metres
m^3/s	metres cubed per second
mm	millimetres
Mt/year	Mega tonnes per year
t/km^2 year	Tonnes per square kilometres per year
$s/m^{1/3}$	seconds per metre to the power of one third

CHAPTER 1
Introduction

Hydrodynamic processes that occur along the world's large rivers are a key determinant of a range of risks pertaining to biogeochemical cycling, ecology, food security, public health, transportation, and human exposure to flood risk. For instance, globally important biogeochemical processes such as the outgassing of carbon dioxide and methane occur as result of large scale fluvial inundation (Richey et al., 2002; Borges et al., 2015). Inundation and spatiotemporal diversity in river flow conditions maintains some of the world's most biologically diverse and productive ecosystems (Junk et al., 1989; Vander Vorste et al., 2017). Hydrodynamic processes are also linked to the infection dynamics of water related diseases such as malaria (Smith et al., 2013; Bertuzzo and Mari, 2017). Many agricultural practices in remote regions rely on a dependable supply of water and nutrients provided through seasonal inundation (Duvail and Hamerlynck, 2007), yet are vulnerable to extreme inundation (Pacetti et al., 2017). Similarly, inland water navigation, an important and sustainable form of transport across large remote regions often lacking land transport infrastructure (Bonnerjee et al., 2009), is reliant on a minimum depth of flow being maintained in river channels.

1.1 Study Area: The Middle Reach of the Congo River

Given the wide range and importance of risks and processes linked to large river hydrodynamics, studies of large river hydrodynamics are badly needed. This is especially true for the geographical study area of this research: the middle reach of the Congo River. The Congo Middle Reach flows for approximately 1,700 km from Kisangani to Kinshasa (Robert, 1946). It is a shallow sloped channel system that is highly multithreaded for over 1200 km of its length (Ashworth and Lewin, 2012), as shown in Figure 1-1. This channel system is one of the widest in the world, and is occupied by hundreds of vegetated islands that divide the channel into numerous individual channel threads, broadly classed as an anabranching channel pattern (Nanson, 2013). Very little is known about this channel system, there being a severe lack of in-situ hydraulic data (O'Loughlin et al., 2013). Water surface observations from satellite are available however, and have been used in the limited hydrodynamic research that exists (e.g. Lee et al., 2011; O'Loughlin et al., 2020).

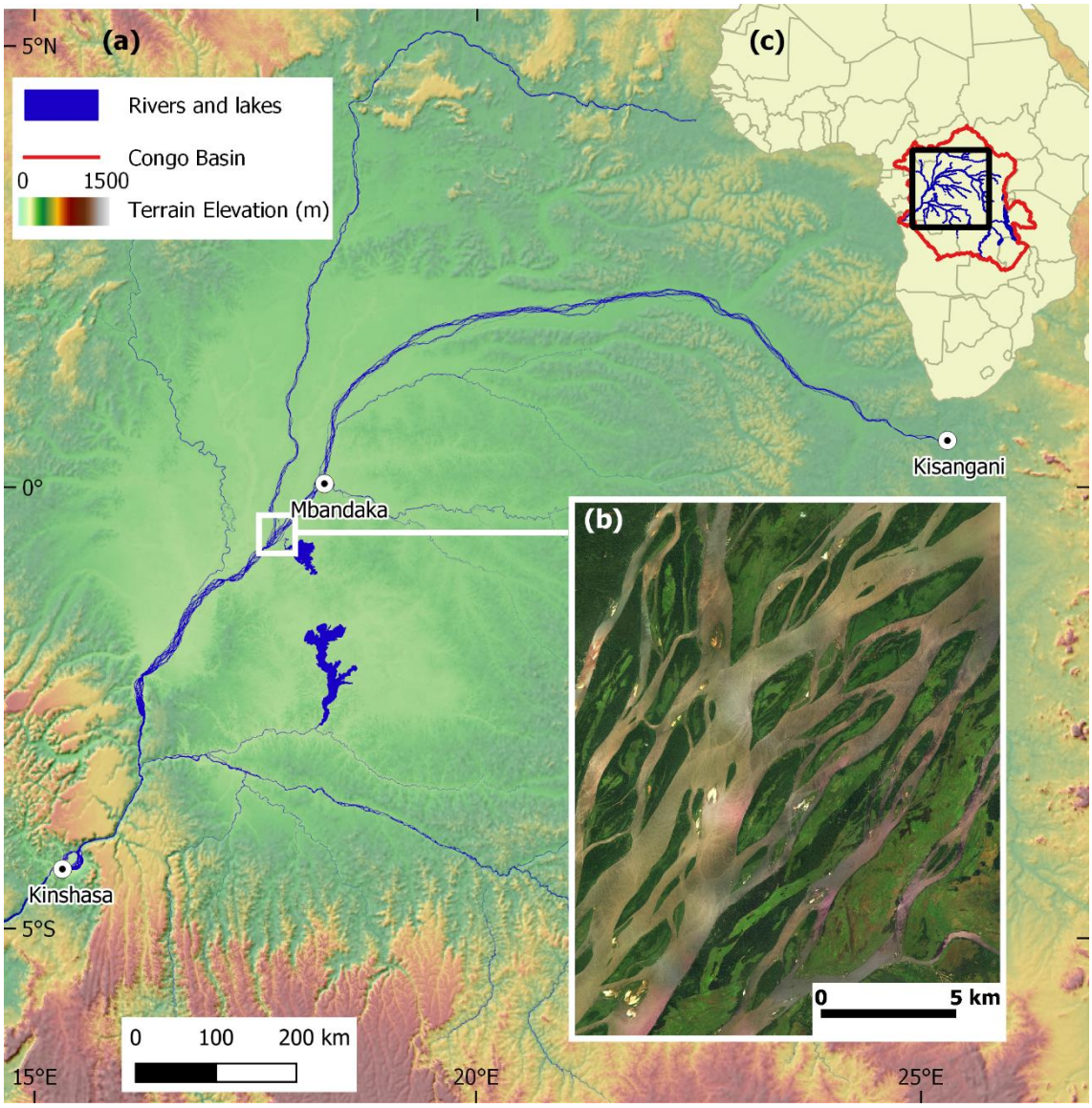

Figure 1-1. The Congo River: (a) The central Congo Basin, showing the mainstem middle reach that flows from Kisangani to Kinshasa, major tributaries, and terrain elevations; (b) Satellite image showing characteristic multichannel planform of the middle reach; (c) Location plan within the extent of the African continent, showing country boundaries. Rivers and lakes water mask from O'Loughlin et al. (2013), Terrain elevations from MERIT DEM (Yamazaki et al., 2017); satellite image from Bing (© 2020 Microsoft Corporation © 2020 DigitalGlobe © CNES (2020) Distribution Airbus DS).

Having received relatively little research attention, hydrodynamic research in the Congo River Basin also has the potential to contribute to resolving regionally and in some cases globally important earth science and development questions (Alsdorf et al., 2016). The middle reach of the Congo drains the world's second largest tropical wetland system: the Cuvette Centrale wetlands (Keddy et al., 2009). Inundation in these wetlands sustains peatlands that are estimated to store 20 years of current fossil fuel emissions

from the United States of America (Dargie et al., 2017), but inundation is also thought to emit globally significant amounts of carbon dioxide and methane (Borges et al., 2015). Inundation here also sustains some of the most biodiverse ecosystems in the world, and is linked to regional food security because of the dependence of agricultural and fishing practices on inundation (Comptour et al., 2016; Comptour et al., 2020). Research questions concerning this inundation, including quantification of inundated areas and its variability in time, and the extent to which fluvial flooding controls wetland inundation remain largely unanswered. Numerical hydrodynamic river models are likely to be a key tool in answering these questions (Trigg et al., 2009; Biancamaria et al., 2009; Paz et al., 2011; Schumann et al., 2013; Paiva et al., 2013).

A severe lack of transport infrastructure in the Congo River Basin means that inland water navigation on the mainstem middle reach and its major tributaries is the principal mode of transportation within the region, and is therefore of great regional importance (Bonnerjee et al., 2009; CICOS, 2015). Shallow water conditions combined with continuously evolving channel morphology results in frequent vessel groundings and periods of unnavigable conditions along the mainstem and key tributaries (Wood et al., 1986; Ndala, 2009). Accordingly, hydrodynamic modelling of in-channel flow conditions to predict water levels during low flow conditions and morphological changes has a potential role to play in managing these navigation risks. Predictions of flow conditions are also important to understand the hydrodynamic impacts of environmental changes that are anticipated in the Congo River Basin. Changes in land use, regional climate, and river abstractions and/or impoundments are all likely to change river flow rates considerably (e.g. Coe et al., 2011), and will therefore affect inundation and channel flow conditions.

1.2 Research Problem Statements

Flooding from large rivers and its related risks to biogeochemical cycling, wetland ecology and public health, are increasingly being evaluated using observations from space-borne satellites, and hydrodynamic river models that utilise these observations (Schumann, 2014; Bates et al., 2014; Bierkens, 2015; Schneider et al., 2018; Fleischmann et al., 2018). However, the usefulness of satellite observations is currently limited by their sparse and inconsistent observational coverage. Hydrodynamic modelling efforts are further limited by a paucity of river channel bathymetry data, which cannot yet be reliably obtained from satellite (Bates et al., 2014; Caballero et al., 2019). In-situ bathymetry measurements are often sparse or unavailable, especially for large rivers in remote regions. This is problematic, because the inclusion of river channel geometry information is crucial to the performance of a hydrodynamic model (Neal et al.,

2012; Sampson et al., 2015). To resolve this problem and facilitate the hydrodynamic analysis and modelling of rivers with limited or no bathymetry information, methods of estimating channel geometry have been developed and are increasingly being applied to large rivers in remote regions (Yoon et al., 2012; Neal et al., 2012; Schumann et al., 2013; Schneider et al., 2018; Fleischmann et al., 2018). However, treating river channel bathymetry as unknown increases the number of unknown parameters, and generally places greater importance on the hydraulic parameters for which observed data are available from satellite. Moreover, treatment of bathymetry as an unknown often involves simplification of channel geometry to a uniform cross-sectional shape, such that it can be represented by one or two parameter values in a hydrodynamic model. Yet a simple uniform channel shape may not be appropriate for representing the middle reach of the Congo River, which has a complex multichannel planform and remains poorly understood hydraulically. Thus, the research presented in this thesis is concerned with assessing the adequacy of Congo River hydraulic observations from satellite, and the applicability of simplified representations of Congo River channel geometry, in the context of hydrodynamic analysis and modelling. Specifically, the research addresses two research problems, which are each stated and elaborated on below.

Research Problem Statement 1: Satellite-derived observations of water surface conditions currently have limited spatial and temporal coverage, and the adequacy of this coverage for analysing the hydrodynamics of the Congo River is unknown.

Satellite observations of water surface elevation and water extents are used extensively in hydrodynamic analysis and modelling (Schumann et al., 2009; Yan et al., 2015). In recent decades, much progress has been made in observations of water surface information from satellite: the accuracy and utility of many datasets has been assessed (Frappart et al., 2006; Urban et al., 2008; Jarihani et al., 2013; Schumann and Moller, 2015; Normandin et al., 2018), and data coverage has increased in space and time. However, their spatial and temporal coverage remains relatively sparse and is inconsistent, varying between river systems and river reaches (Garambois et al., 2017). Research is therefore needed to understand how spatial and temporal deficiencies in satellite derived water surface observations limit their application in hydrodynamic analysis and modelling of different river systems.

Research Problem statement 2: Methods of representing the multichannel reaches of the Congo River in hydrodynamic models are not well established or verified.

Current approaches to large river hydrodynamic modelling often reduce channel geometric representation to a single mean cross sectional depth value, by representing channels as a simple shape such as a rectangle (e.g. Biancamaria et al., 2009). As well as allowing bathymetry to be treated as an unknown parameter to be calibrated, a simple shape also minimises model spatial resolution and therefore computational power requirements, which is important for large river simulations that span large spatial and temporal scales. Simplified channel representations are yet to be thoroughly tested, and may not be appropriate in some circumstances, such as applications where spatially distributed in-channel hydraulic information is required, or in multichannel river environments where a single rectangular channel is highly unrepresentative. Multichannel river environments are a common feature of large river systems: Latrubesse (2008) asserts that nine of the world's 10 largest rivers possess a channel pattern that is predominantly anabranching. Multichannel rivers are also particularly challenging in a channel representation context. This is partly due to observational challenges: the acquisition of a full bathymetry dataset requires navigation of multiple channel threads in order to sample the full channel cross-section (Altenau et al., 2017a), resulting in a collection route that is several times longer than for a single channel river, which may be prohibitive. Limitations on model spatial resolution are an additional challenge since the representation of narrower individual channel threads require a finer spatial resolution than a simplified effective single channel. Simplified channel representations are therefore highly appealing on multichannel rivers. However, approximating a complex multithreaded channel system as a single channel of uniform shape neglects many in-channel hydraulic processes such as the splitting and converging of sinuous channel threads around islands and the overtopping of mid-channel islands (Garambois et al., 2017). Channel geometry and hydraulics must be represented with sufficient accuracy in hydrodynamic models, in order to correctly simulate the onset and extents of fluvial inundation, and the speed with which flood waves move through the channel – floodplain system (Trigg et al., 2009; Dey et al., 2019). Research into the representation of multithreaded river channels in hydrodynamic models is therefore badly needed.

1.3 Thesis Aims and Structure

The aims of the research presented in this thesis are as follows:

1. ***To assess the water surface and in-channel hydraulic conditions along the middle reach of the Congo River, and the capacity of satellite-based observations to determine these conditions.***
2. ***To evaluate methods of channel geometric representation in hydrodynamic models of the Congo's multichannel middle reach.***

The objectives that have been identified in order to achieve these aims are set out in section 3.5, following the literature review. Chapter 2 and Chapter 3 constitute the Literature Review: Chapter 2 is a review of large river hydrodynamic research, and Chapter 3 is a review of hydrodynamic research in the Congo River Basin. Chapters 4, 5 and 6 document the research carried out, and Chapter 7 presents the research findings and conclusions together with future research directions. The structure of the entire thesis is depicted in Figure 1-2.

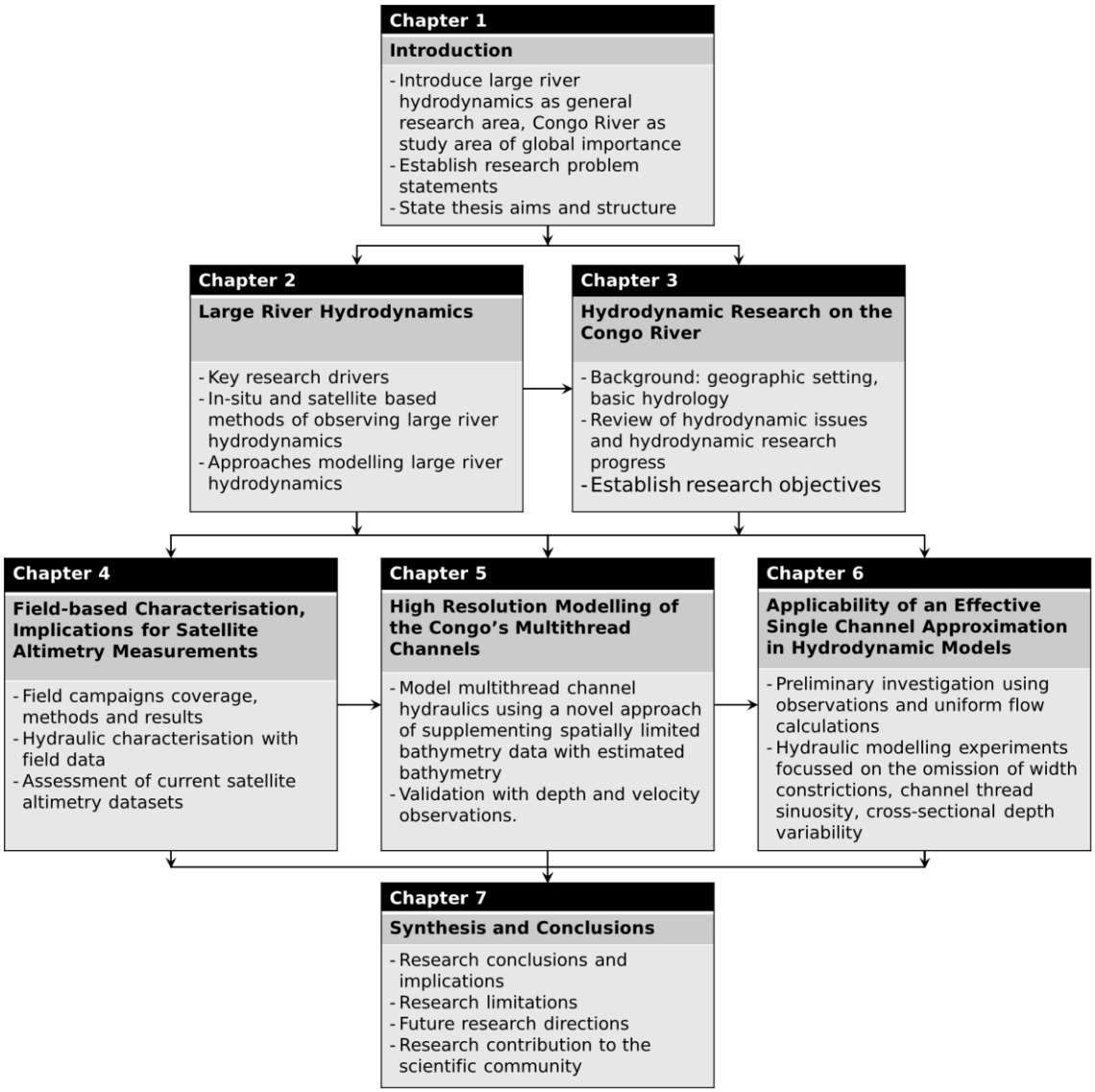

Figure 1-2. Thesis structure

CHAPTER 2
Large River Hydrodynamics

2.1 Definitions

2.1.1 Large Rivers

There are number of published definitions of 'large' rivers in a global context. In one example, Gupta (2007) defines a large river as being over 1000 km long, having a catchment area of $>10^5$ km^2 and a mean annual runoff volume greater than 200 x10^9 m^3. Fielding (2008), defines large rivers as having a channel greater than 1 km wide and 10 m deep. These definitions based on channel size, catchment area or runoff volume are not always satisfactory. The threshold values used in the definitions are subjective, and a lack of reliable global discharge and bathymetric data limits their wider application. Use of globally available data such as catchment area alone is problematic, due to the large variation in catchment runoff rates, resulting for example in the inclusion of relatively small rivers with big catchments in arid regions, and the exclusion of some large rivers with relatively small catchments in tropical regions. Human impacts and river regulation also complicate these definitions.

In this thesis, 'large rivers' are defined simply as being distinct from smaller rivers by some key characteristics. They possess wide channels systems, flow depths of up to 25–50m or more, very high width to depth ratios, and very low water surface gradients (~10 cm/km or less) (Ashworth and Lewin, 2012; Nicholas et al., 2012). They also have low Froude numbers (Amsler and Garcia (1997) suggest typically equal to or less than ~0.3), and therefore have highly subcritical flow conditions. Large rivers often possess extensive floodplain systems, and their channel systems exhibit a range of complex planform patterns that do not conform to the traditional pattern terminologies (Latrubesse, 2008), beyond the fact that they are multichannel to some extent (Carling et al., 2014). Their flood regimes are seasonal, more stable and predictable. Large rivers provide important ecosystem services, supporting biodiversity, freshwater and marine fisheries, and productive agricultural land. They may be primary rivers or tributaries, and their drainage basins often lie in remote regions spanning multiple countries.

Mega rivers are a useful sub-category of large rivers, first proposed by Latrubesse (2008). They are defined as 'very large' rivers, and include the nine largest rivers on earth by mean annual discharge: Amazon, Congo, Orinoco, Yangtze, Madeira, Negro, Brahmaputra, Japura, and Parana. See Table 2-1 for some summary statistics of these mega rivers. The quoted discharge statistics are obtained from in-situ

measurements (rating curves): in the absence of any information on the uncertainty of specific values, an uncertainty in the region of 5-10% can be assumed (Di Baldassarre and Montanari, 2009). The reported sediment flux values are more uncertain. Numerical assessments of the uncertainties associated with the values reported are not available, but recent sediment flux values of 326 Mt/year and 159 Mt/year published for the Irrawaddy and Salween Rivers in Southeast Asia are assigned an uncertainties of ~25% and ~40% respectively (Baronas et al., 2020). Moreover, different measurements on the same river often report variations in excess of 50%: compare for example the Orinoco sediment flux of 74 Mt/year produced by Laraque et al. (2013) with the 150 Mt/year quoted in Table 2-1, and the value of 210 Mt/year published in Milliman and Meade (1983). Milliman and Meade (1983) also give an overview of the potential error sources in large river sediment flux measurements, which is still relevant today.

Table 2-1: The world's nine largest rivers by discharge, known as mega rivers. After Latrubesse (2008)

River	Country to the mouth	Mean annual Discharge (m^3/s)	Drainage area (10^3 km^2)	Sediment flux Q_s (Mt/year)	Sediment yield (t/km^2 year)
Amazon	Brazil	209,000	6100	~1000	167
Congo	DR Congo	40,900	3700	32.8	9
Orinoco	Venezuela	35,000	950	150	157.8
Yangtze	China	32,000	1943	970	499
Madeira	Brazil	32,000	1360	450	330
Negro	Brazil	28,400	696	8	11.5
Brahmaputra	Bangladesh	20,000	610	520	852.4
Japura	Brazil	18,600	248	33b	133
Parana	Argentina	18,000	2600	112	43

Many of the world’s large rivers are located in the tropics due to the intense rainfall here; eight of the 10 largest rivers by discharge globally are tropical rivers (Latrubesse et al., 2005). Tropical rivers in particular are the subject of intense biogeochemical activity. Inland waters are known to emit amounts of trace gases

including carbon dioxide and methane that constitute considerable components of the global carbon budget (Bastviken et al., 2011; Raymond et al., 2013), and emissions from tropical river systems are thought to contribute significantly to this (Richey et al., 2002; Melack et al., 2004; Sawakuchi et al., 2014; Borges et al., 2015). For example, Borges et al. (2015) estimate carbon dioxide equivalent greenhouse gas emissions from the Cuvette Centrale wetlands of the Congo River to be 0.48 ± 0.08 petagrams per year. This number is globally significant, considering that the combined net global carbon sink from oceans and land is currently estimated as 5.7 petagrams per year (Friedlingstein et al., 2019). These systems also facilitate carbon storage by depositing stocks of carbon-rich sediments and contributing to peatland formation through wetland inundation.

2.1.2 Hydrodynamics

In this thesis, the study of river hydrodynamics refers to observing and modelling the dynamic spatiotemporal distribution of several surface water parameters within a river system. These parameters include water flows, surface elevations, depths, velocities, and inundation patterns (i.e. dynamic inundation extent and duration). River hydrodynamics is strongly influenced by terrain, including the topography of river banks and floodplains, the bathymetry of river channels. Terrain also encompasses land surface roughness, which creates flow resistance. Hydrodynamics does not specifically include the study of the hydrological processes that generate river flows, which is a component of the broader field of hydrology. Hydrodynamics is an important component of hydrology however, as it governs the speed of travel and changes in magnitude and duration of river flows as they move down a river system.

2.2 Key Drivers of Large River Hydrodynamic Research

2.2.1 The Proliferation of Space Borne Earth Observation Satellite Data

In recent decades there has been enormous progress in the use of remote sensing techniques to obtain hydrodynamic and topographic information from space borne earth observation satellite instruments (Smith, 1997; Calmant et al., 2009; Yan et al., 2015). This is largely due to a sustained growth in the number of satellite missions, and also the capability and diversity of technologies employed by the instruments. The last decade in particular has seen major advances in the utility of observations of inundation patterns and water surface elevation.

Large rivers are the prime candidates for the application of satellite remote sensing (SRS) to observe hydrodynamics, because they can accommodate the generally lower temporal and spatial resolution of SRS datasets. Conversely, in situ (ground based) observation methods are sparsely applied to large rivers because of scale and

accessibility issues. The data that has become available from SRS has therefore been unprecedented especially in terms of spatial coverage, and has partly driven the increasing study of large river hydrodynamics. Anticipated future advances in spatiotemporal coverage, resolution and accuracy of SRS data will continue to be a key driver of such studies, particularly within the earth science community.

The progress in SRS is continuing to advance what is possible in large river hydrodynamics, and is fuelling research into a wide range of societal issues that entail hydrodynamic observations or predictions on large rivers. These are described below.

2.2.2 Biogeochemical processes

Large river hydrodynamics is a key determinant of globally important biogeochemical processes. Water depths, velocities, and inundation patterns are all hydrodynamic information that are needed to understand the production of trace gases from rivers. Observed or modelled flood extents and durations are used in conjunction with locally measured trace gas evasion rates per unit area to produce estimates of total emissions from river systems. For example, the Borges et al. (2015) estimate of 0.48 ± 0.08 petagrams per year of carbon dioxide equivalent greenhouse gas emissions from the Cuvette Centrale wetlands is the product of a compilation of locally computed trace gas flux values (which are themselves based on local measurements of dissolved concentrations), and a flooded surface area of 360×10^3 km^2 estimated from satellite imagery and terrain data (Bwangoy et al., 2010). In addition, trace gas evasion rates are a function of gas transfer velocity, which is influenced by river channel flow properties including velocity and channel friction. This was demonstrated by Alin et al. (2011) who found there to be a strong positive correlation (R^2=0.78) between gas transfer velocity values and water current velocity measurements on a range of medium and large rivers.

Dynamic inundation processes also play a role in the storage of carbon. Specifically, inundation facilitates the build-up of organic material within soils, which is then unable to fully decompoe and release carbon into the atmosphere (Keddy et al., 2009). Wetlands are a hotspot for this carbon sequestration activitiy, where the abudant vegetation is prevented from fully decomposing and forms peatlands. Despite only occupying 3% of the earth's surface, peatlands make up one third of the total global carbon pool (Page et al., 2011).

2.2.3 Ecological Processes

Hydrodynamic processes are a major control on the ecosystems present within the river channel and on floodplains. Within river channels, the variability in flows, depths,

and velocities provides a diverse range of potential niches that serve as habitats for aquatic organisms. Consequently these organisms are spatially distributed in a highly heterogeneous way that changes temporally with river flow (Crowder and Diplas, 2000; Allan and Castillo, 2007). River channel aquatic habitat models simulate habitat changes with flow, using observations and predictions of water depth and velocity for a range of flows to investigate habitat suitability for various species (Daraio et al., 2010; Jowett and Duncan, 2012).

Biodiversity is highest in large rivers. This is in part because larger rivers can accommodate larger fish as well as small fish, meaning the size range and hence diversity of fish increases as rivers become larger (Vander Vorste et al., 2017). The main reason however is the role of floodplain inundation in large rivers, known as the flood pulse in an ecological context (Junk et al., 1989). In large rivers, many aquatic and terrestrial organisms are adapted to and dependent on regular seasonal inundation for moderate periods. During inundation, aquatic organisms migrate out of the channel and onto the floodplain to use newly available habitats and resources. The floodplain also receives a fresh supply of sediment. As flood waters recede, nutrients, organic matter and newly produced organisms return from the floodplain into the river channels (Johnson et al., 1995). Large river floodplains are therefore highly ecologically productive and diverse environments, especially where inundation duration is sufficient to produce wetland ecosystems. Wetlands are known to be some of the most biologically diverse and productive ecosystems in the world, but are also among the most threatened due to their fragility (Tockner et al., 2008). The importance of floodplain ecological processes and their strong dependence on hydrodynamics is a key motivator of an increasing number of studies involving observations and modelled predictions of floodplain hydrodynamics.

2.2.4 Flood risk

The predictable, slow moving, seasonal nature of large river floods and their often remote, sparsely populated localities dictate that they are regarded as a beneficial ecosystem service as much as they are a natural hazard, with floodplain dwelling communities being adapted to seasonal flood conditions. However, large river floods do pose a risk to human life, property and infrastructure in many cases. Extreme floods events that cause exceptional inundation extents and depths test the resilience of communities and can have catastrophic consequences; Table 2-2 gives some examples of such events over the last 10 years. Flood risk exposure is projected to increase in developing countries where most large rivers are located, because of rapid urbanisation

on floodplains driven by population growth (Di Baldassarre et al., 2010; Smith et al., 2019).

Table 2-2. Studies of Recent Large River Floods

River	Year of flood	Example study
Indus	2010	Gaurav et al., (2011)
Mississippi	2011	Driscoll et al., (2014)
Chao Phraya	2011	Komori et al., (2012)
Amazon	2014	Espinoza et al., (2014)
Brahmaputra	2017	Philip et al., (2019)

Observed and modelled hydrodynamic information is essential for implementing flood risk mitigation measures such as flood risk mapping, flood forecasting and warning, and construction of flood control infrastructure. In the case of large rivers, such information is needed not just for understanding the flood risk posed by the river itself, but also the risk associated with its many tributaries whose hydrodynamic behaviour will likely be strongly controlled by the river they drain into. For example, the influence of the Amazon mainstem hydraulics on its tributaries was observed by Meade et al. (1991) who showed that water surface elevation (WSE) in the Madeira and Purus tributaries can vary by 2-3 m for a given discharge, depending on the conditions in the downstream mainstem. Amazon mainstem backwater effects on the Purus and Solimoes tributaries were also characterised by Trigg et al. (2009), who found the Purus to be more affected of the two, mean water surface slopes from a hydrodynamic model simulation being 4–6 times lower than channel bed slopes during high and low water conditions respectively.

2.2.5 Remote Discharge Measurement

Accurate measurement of river discharge is essential, as it quantifies the amount of water resources available for human use, defines the quantity of water that comes out of bank during flood events, and describes overall catchment response to hydrometeorological processes. Despite the high value of discharge information to society, gauging stations and access to river discharge information has been declining since the 1980s, including on the world's largest rivers (Hannah et al., 2011; Pavelsky et al., 2014). Facilities and accessibility are a particular problem in developing countries (Calmant et al., 2009). The global decline in operational gauging infrastructure is difficult

to quantify because gauge data in many countries is often unavailable to the public. Data sharing restrictions are often present in large river basins as a result of transboundary hydro-political issues (Qaddumi, 2008). However, Hannah et al. (2011) were able to quantitatively assess the decline in North America. They looked at the total number of gauges with >30 years of data that were decommissioned between 1980 and 2004 in the USA and found this number represented 28% of the gauges that were operational in 2005. In Canada the equivalent figure was 16% over a similar time period.

The global Runoff Data Centre database (GRDC, 2019) is the most complete global discharge dataset that is freely available to the international scientific community (Pavelsky et al., 2014). Whilst the database will certainly omit gauges and datasets due to data sharing restrictions, it provides a useful indicator of global gauge data availability over time. The database provides the start and end dates for which data is available at each gauge, enabling an understanding of spatiotemporal changes in data availability. Figure 2-1 maps the global distribution of all gauges that have provided data at some point in time, along with gauges that provided data after 2010. Locations of large river basins (basin area greater than 500,000 km^2) from Lehner et al. (2008) are also highlighted. This map clearly shows the decline in data availability globally, especially in large river basins and in developing countries. The Amazon Basin is somewhat of an anomaly in that it is relatively well gauged, this is because it is the world's largest river and accordingly has received significantly more hydrological research attention than other large rivers. Alsdorf et al., (2016) demonstrate this by showing there is an order of magnitude more scientific publications on Amazon hydrological research compared to the world's second largest river by discharge (Congo). Still, the Amazon Basin gauge data is sparse relative to river basin gauge densities in developed countries, there being eight times the number of gauges per kilometre in the Mississippi Basin than in the Amazon in 2010, based on the data shown in Figure 2-1.

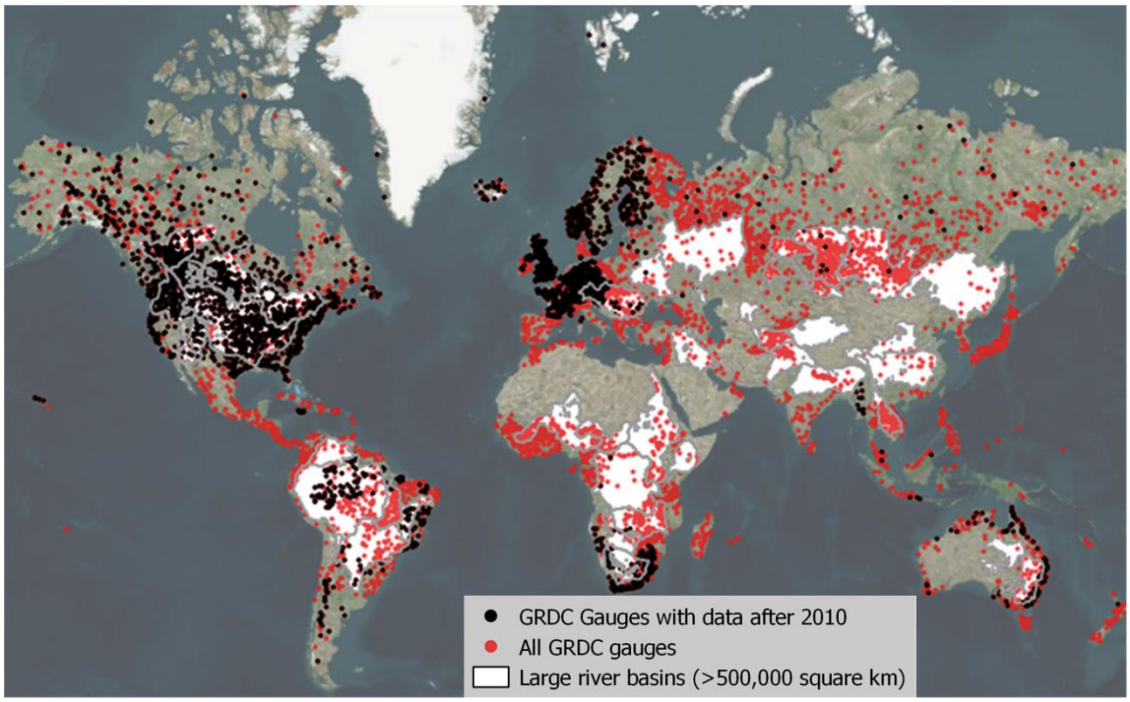

Figure 2-1. Global Distribution of gauges in the Global Runoff Data center (GRDC) database; all gauges are plotted in red, and gauges with data after 2010 are plotted in black. River basins with an area greater than 500,000 km^2 are also highlighted. River basins above 60 degrees northern latitude are not included.

This decline in gauge data availability can be quantified by plotting the number of gauges that provide data in each year (Figure 2-2). This shows the magnitude of the decline in available gauge data since the 1980s. A similar decline is seen specifically in large river gauge data in developing countries, by plotting the number of gauges located in large river basins only (river basin area greater than 500,000 km^2), and outside of North America or Europe. River basins above 60 degrees northern latitude are also excluded. These gauges comprised just 13% of all gauges on average over the last century, but occupy river basins that span approximately 33% of the world's land surface based on the basin delineation of Lehner et al. (2008), which illustrates the sparsity of large river gauges in developing countries relative to global gauge density.

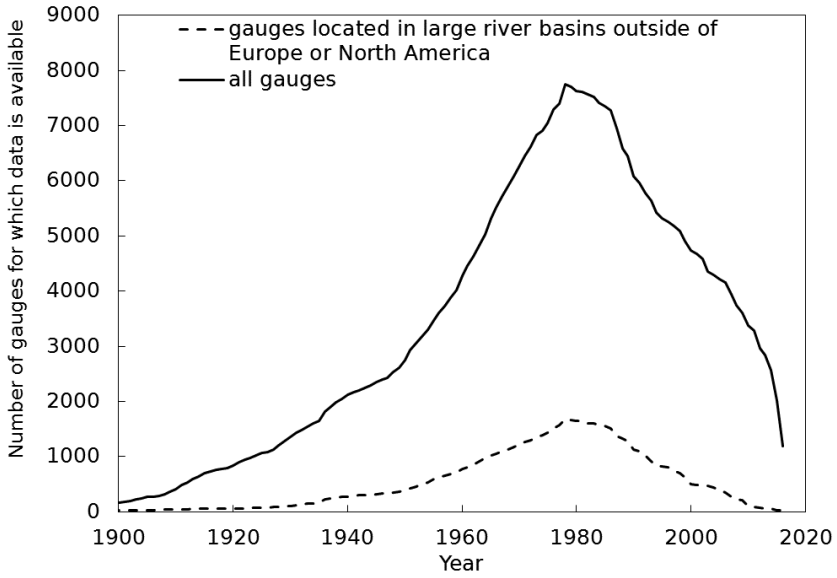

Figure 2-2. Plot of number of gauges that provide data in each year, from the Global Runoff Data Center Database. Total number of gauges in the database are plotted, and compared with number of gauges that are located in large river basins (river basin area >500,000 km^2) outside of Europe or North America and below 60 degrees latitude.

Clearly, improved spatiotemporal coverage of discharge measurements is greatly needed across the globe. Long term river gauging structures such as weirs that are used to obtain discharge from a water level measurement at the critical depth are the dominant flow gauging station in developed nations such as the UK (Centre for Ecology and Hydrology, 2019), but are generally not feasible to construct on larger rivers. Discharge – stage (water level) rating curves developed at a particular river cross section location can be used to derive discharge from regular water level measurements in large rivers, however these require direct measurements over a range of flows for calibration purposes, using a flow measurement device such as an acoustic Doppler current profiler (ADCP) or a current meter. The ongoing need for these direct measurements as a result of river channel geometry and vegetation change over time limits the rating curve methodology to locations with the facilities and conditions to carry out such measurements periodically. Establishing such locations on large rivers can be very challenging, given their remoteness, large channel widths, extensive floodplains, and multichannel nature. These large river gauging difficulties, combined with the increasing capabilities of SRS techniques, has resulted in a concerted effort in research into methods of retrieving discharge from space. The methods involve derivation of useful hydrodynamic observations from SRS, and their subsequent use to predict discharge using hydrodynamic models with a wide range of complexities (e.g. Andreadis et al., 2007; Brakenridge et al., 2007; Durand et al., 2016).

2.2.6 Sediment Dynamics

Hydrodynamic processes are key determinants of sediment transport processes, as they control the size, quantity and locations of sediment that is mobilised, transported, and deposited, and the evolution of river form. Specifically, the initiation of motion, rate of transport, and deposition of sediment is a function of bottom shear stress, which itself is a product of depth, water surface slope and velocity (van Rijn, 1993). These hydrodynamic variables are therefore commonly used to predict sediment bed load and total load transport rates, and erosion and deposition rates (e.g. Le Bouteiller and Venditti, 2014).

The underlying motivations of the study of sediment dynamics include many of the motivations described above. Ecologically, changes in composition and quantity of sediment is important in providing habitat for aquatic and terrestrial organisms within the river corridor (Hauer et al., 2018). Sediment deposition and migration of bed forms results in a changing bathymetry that poses a major risk to fluvial navigation vessels (Guerrero et al., 2013); this is discussed in more detail in section 2.2.7. Channel deposition can increase fluvial flood risk (Slater et al., 2015), whilst insufficient delivery of sediment can increase flood risk and cause land loss in deltaic environments (Twilley et al., 2016).

2.2.7 Inland Waterway Navigation

Inland navigation on rivers is generally the most sustainable mode of transport in terms of energy consumption, greenhouse gas emissions, and infrastructure requirements (Rohács and Simongáti, 2007; Schoemaker et al., 2012). For this reason, navigation is common on large rivers that are deep enough to accommodate the draft of large vessels over long distances. Naturally, vessels must contend with the risk of grounding, particularly when water levels are low. Observations and predictions of dynamic water levels along navigable rivers can help manage this navigation risk and optimise vessel loads (Hemri and Klein, 2017). For example, operational navigation forecasting on Europe's principal inland navigation route, the Rhine River, is known to involve hydrodynamic modelling. Both Hemri and Klein (2017) and Baran et al. (2019) allude to the conversion of runoff forecasts into water level forecasts using a hydrodynamic model in their descriptions of the operational Rhine navigation forecasting procedure used by the German Federal Institute of Hydrology. However, Hemri and Klein (2017) and Baran et al. (2019) both look specifically at prediction of river discharge only in their research, (i.e. do not model hydraulics), and from the available literature, it appears that research relating to forecasting of flow conditions for navigation is primarily focussed on hydrological modelling, and less hydraulic modelling; see also for example,

Demirel et al. (2013) on the Moselle, Western Europe. Some researchers have also used non-physically based modelling techniques such as artificial neural networks to derive navigation water level predictions solely from historical water level data: see the efforts of Fernandez et al. (2010) applied to the Magdalena River, and Figueiredo et al. (2014) on the Tapajos River.

In the context of navigation forecasting, hydrological modelling may be receiving the research attention because it is perceived to be a research challenge of greater magnitude than the hydraulic modelling component. In addition, the discharge values that corresponds to the minimum WSE conditions for navigation along a river reach may be known on well gauged rivers (see e.g., Rötz and Theobald (2019)), in which case local the WSE prediction provided by a hydraulic component is not necessary in the same way that it is for flood forecasting. Regarding this latter point in the context of large rivers, accurate discharge values that correspond to minimum navigable WSE are less likely to be known in the case of large rivers in remote regions where operational gauging is limited (as discussed in section 2.2.5). Moreover, a hydraulic modelling component is often necessary even when only discharge predictions are required, as attested to by Rötz and Theobald (2019) who assessed the performance of different hydraulic model numerical formulations for predicting downstream discharge conditions for navigability.

Ultimately, navigability is not dictated by WSE, but by depth. Detailed knowledge of river bathymetry along navigation routes and its evolution over time resulting from sediment transport processes are therefore important for managing navigation. Accordingly, researchers and practitioners are increasingly utilising hydrodynamic models to predict channel morphological changes that may affect long term navigability on large rivers. On the Rhine River for example, the Dutch navigation authority (Rijkswaterstaat Oost-Nederland) have developed a morphological model to predict future morphological changes and simulate potential measures for mitigating reduced navigability in areas of deposition (Yossef, 2016). Scientific research efforts are relatively rare on large rivers, likely because of the onerous input data requirements of a morphological model such as detailed bathymetry and sediment load data. Rare examples include the efforts of Creech (2014) on the Sao Francisco River in Brazil, which entailed the development of a sediment yield model using the Soil and Water Assessment Tool, and a morphological change model using HEC-RAS covering 1000 km of the river's middle reach. These models were coupled and used to analyse the navigability of the river following various anthropogenic interventions such as dredging and construction of spur dykes. Nicholas et al. (2012) modelled the hydrodynamics of a relatively short 30 km reach of the Rio Parana, Argentina, citing the prediction of

morphological evolution as being the key purpose of the model. In addition, Nicholas et al. (2013) circumvented the need for detailed data by modelling synthetic river reaches that are designed to be representative of large sand-bed rivers. Schuurman et al. (2016) also did so for the Brahmaputra, using such a model to analyse the generalised behaviour of braided river morphodynamics under human-induced interventions including bank protection works and closure of channel threads to improve navigability.

2.2.8 Disease Transmission

Water related diseases encompass water borne diseases, water based diseases, and vector borne diseases. The infection dynamics of water related diseases are linked to climatic, hydrologic and in some cases hydrodynamic drivers across a wide range of spatial and temporal scales (Bertuzzo and Mari, 2017). For example, malaria risk is strongly associated with surface water bodies which serve as breeding sites. Many of these surface water bodies are controlled by river hydrodynamics; the detection and prediction of inundation duration, velocity and depth can be used to determine breeding habitat suitability and hence malaria risk (Smith et al., 2013).

2.2.9 Hydrological Change

Hydrological change may be instigated directly by hydraulic structures that regulate river flows and alter river bed slopes on many of the world's rivers (Grill et al., 2019). Indirectly, changes in hydrological processes are occurring as a result of human activities such as deforestation, agriculture, and urbanisation. Climate change is also having significant hydrological impacts through changes in land cover, rainfall patterns and intensities, and evaporation. There is a need to understand how this hydrological change will affect hydrodynamic processes. Many of the hydrodynamic research drivers discussed above also require to be studied in the context of hydrological change.

2.3 Observing large river hydrodynamics

2.3.1 Discharge Measurements

In situ Measurements

Discharge measurement is challenging on large rivers due to their large spatial scale and difficult access, as outlined in section 2.2.5. Nevertheless, it is possible and necessary given the decline in permanent gauging infrastructure and reluctance of government agencies to share data for political or commercial reasons. The modern established methodology involves use of an ADCP deployed on a boat to directly measure velocity and cross sectional area, and hence discharge. These devices measure velocity magnitude and direction using the Doppler shift of acoustic energy reflected by material suspended in the water column. These measurements produce vertical velocity profiles composed of water speeds and directions at regularly spaced intervals, across the entire river cross section. Morlock (1996) provides a detailed description of the ADCP and its operational principles.

ADCP discharge measurements can also be used in conjunction with a geodetically levelled depth gauge to establish a rating relationship between discharge and WSE. The rating relationship then enables discharge to be measured indirectly in a convenient manner from a depth gauge. This practice has been used by the observation service SO-HYBAM, who conduct hydrological and biogeochemical measurements on the three largest rivers in the world (by average discharge): Amazon, Congo and Orinoco, for scientific purposes (Filizola et al., 2009; Institut de recherche pour le développement, 2019). The majority of their efforts are concentrated in the Amazon Basin where thirteen discharge gauging stations are currently operational. There is one gauging station each in the Congo and Orinoco basins. These stations and their data are all included in the global Runoff Data Centre database.

Remote Sensing Measurements

Dynamic river width, WSE, and water surface slope (WSS) information derived from remotely sensed observations of surface water extent and WSE are the common hydrodynamic variables used to estimate discharge from space. These variables are discussed in section 2.3.4 and 2.3.5 respectively, and their subsequent use in models to obtain discharge is discussed in section 2.4.5.

2.3.2 Bathymetry Measurements

In situ Measurements

Measurements of river depth on large rivers necessitates use of a sonar device mounted on a survey boat, as reported by Wilson et al., (2007) and Trigg et al. (2009; 2012) on Amazon basin rivers and floodplain channels, and Altenau et al. (2017a) on the Tanana River. The sonar devices that were used in these studies are single beam devices that produce point depth information along the vessel track. Complete spatial coverage of river bathymetry cannot be realistically achieved on large river channel systems with single beam devices, necessitating a compromise between survey effort and measurement coverage, and interpolation of the raw sonar data.

Multi-beam echo sounders (MBES) are increasingly being used to achieve complete coverage of river bathymetry. Multiple beams measure water depth across a wide swath perpendicular to the vessel track. A device used by Parsons et al. (2005) to measure dune morphology on the Rio Parana produced a swath width approximately seven times the water depth. Such coverage enables full bathymetric coverage of navigation corridors or discrete river reaches along rivers of up to a certain size (e.g. Schumann et al., 2010; Conner and Tonina, 2014), but full coverage of rivers over hundreds of kilometres with widths in the order of kilometres remains unrealistic even with a MBES. Deployment of multiple MBES devices on different vessels is possible logistically, but is likely to be financially unviable for scientific purposes given individual MBES devices cost in excess of £30,000 (Seafloor Systems Incorporated, 2017)

On the spatial coverage requirements of bathymetry data, it is well demonstrated that channel discharge capacity must be accurately represented in order to model floodplain inundation processes (see for example, Trigg et al., 2009; Dey et al., 2019). When obtaining bathymetry data for hydrodynamic modelling purposes, it is therefore of primary importance to obtain measurements across the full cross sectional width of the channel. This ensures that the channel cross sectional and hydraulic mean depth are known, which govern the discharge capacity of a large river channel, as evidenced conveniently by viewing an equation for uniform flow in an open channel, such as the Manning formula (Manning et al., 1890):

$$Q = \frac{1}{n} A R^{2/3} \sqrt{s} \qquad \text{Eq. 2-1}$$

Where Q is discharge (m^3/s), n is Manning's hydraulic roughness coefficient ($s/m^{1/3}$), A is cross-sectional area (m^2), R is the hydraulic radius (m^2/m) – equal to hydraulic mean depth for a large river, and s is the energy slope (m/m) – assumed equal to the bed slope and water surface slope under uniform flow conditions. Since channel discharge is a product of cross sectional area and mean channel velocity, accurate representation of A is also necessary for reliable model predictions of mean channel velocity, and hence the velocity at which a flood wave travels along a river.

The traditional approach to bathymetric surveys is to take river cross sectional measurements (known as transects) at regular intervals along a river channel. The locations and distance between measurements is dependent on numerous factors such as the apparent variability in channel cross sectional area and width (to ensure sufficient sampling of A and R). Larger rivers are known to require a lower spatial resolution of bathymetry; Samuels, (1990) argues that the required transect space step should scale with channel width. Trigg et al. (2009) looked specifically at the effect of reducing the bathymetry information content on modelled WSE along a ~400 km reach of the Amazon mainstem. They found that simplifying a series of surveyed cross sections to rectangular cross sections by preserving flow cross sectional area and wetted width resulted in only a 0.126 m increase in modelled WSE root mean squared error (RMSE), and when all cross sections were replaced with a single reach average rectangular section and bed slope, modelled RMSE increased by 0.53 m. These RMSEs are a fraction of the Amazon's 12 m flood wave amplitude, leading Trigg et al. (2009) to conclude that quite crude assumptions regarding the Amazon's bathymetry will suffice providing the mean cross sectional area is well approximated. They suggest their conclusions may hold for other large rivers, but it appears this has not yet been thoroughly explored, probably largely because of the unavailability of bathymetry data for many of the world's large rivers. Nicholas et al. (2012) does assess the bathymetric controls on flow conditions in a large river, by modelling steady state hydraulics along a 30 km reach of the Rio Paraná, Argentina. They find large-scale (channel scale) bathymetric features is the dominant control on the spatial distribution of channel velocity, implying fine-scale features such as dunes have little effect on spatially distributed flow conditions.

Model purpose is a determining factor: prediction of low flow conditions requires more bathymetry information than prediction of flood flow conditions, because low flow conditions are more sensitive to bathymetry than flood flows (Garambois et al., 2017). Moreover, studies that require predictions of spatially distributed in-channel flow conditions require greater coverage and resolution compared with studies that only require mean channel flow conditions along the river channel. For example, (Conner and

Tonina, 2014) conclude the spacing between cross sectional measurements should equal the mean channel width for the purpose of predicting spatially distributed aquatic habitat suitability and sediment transport processes, whereas (Castellarin et al., 2009) concludes that for prediction of WSE during a flood, a spacing of 10-20 times the mean channel width (first proposed alongside ten other criterion by Samuels, 1990) is valid. In any case, determining measurement spatial interval is subjective, indeed Samuels (1990) comments on this subjectivity, stating “this selection is part of the art of river modelling and it is likely that no two experts would choose precisely the same location for the cross-sections”.

When surveying large rivers with a boat, the entire river reach being surveyed is usually navigable, and access is more efficient by boat than on land, particularly in remote regions where road infrastructure is lacking. In this scenario, the full cross sectional width can be sampled regularly and with maximum efficiency by diagonally moving from bank to bank in a ‘zig-zag’ manner, as shown in Figure 2-3.

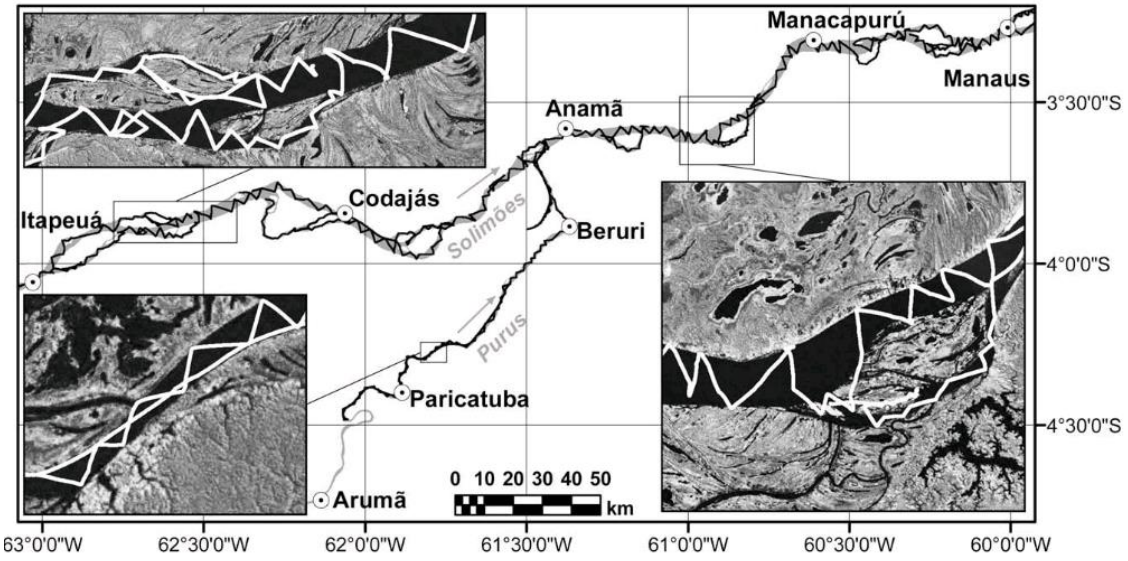

Figure 2-3. Example of sonar collection route on a large river. Taken from the work of Trigg et al. (2009) on the Amazon River.

Acquisition of bathymetry is less straightforward in large multichannel river reaches, where mid-channel islands prevent survey boats from navigating across the full width of the channel belt. In these environments, survey boats must navigate around islands and up numerous channel threads in order to regularly sample the full channel width, greatly increasing the sonar collection route for a given reach length. In the example shown in Figure 2-3, it can be seen that islands are relatively infrequent and the secondary channel threads can be captured with only a moderate amount of additional

track distance. However, when islands are more numerous as is the case for reaches of many large rivers (see Figure 2-4), the necessary track routes are more complex and far longer. As a result, the timeframe and resources required to carry out a complete multichannel bathymetric survey may be beyond what scientific research teams are able to afford, and consequently, there are very few published hydrodynamic modelling studies that involve use of multichannel bathymetry.

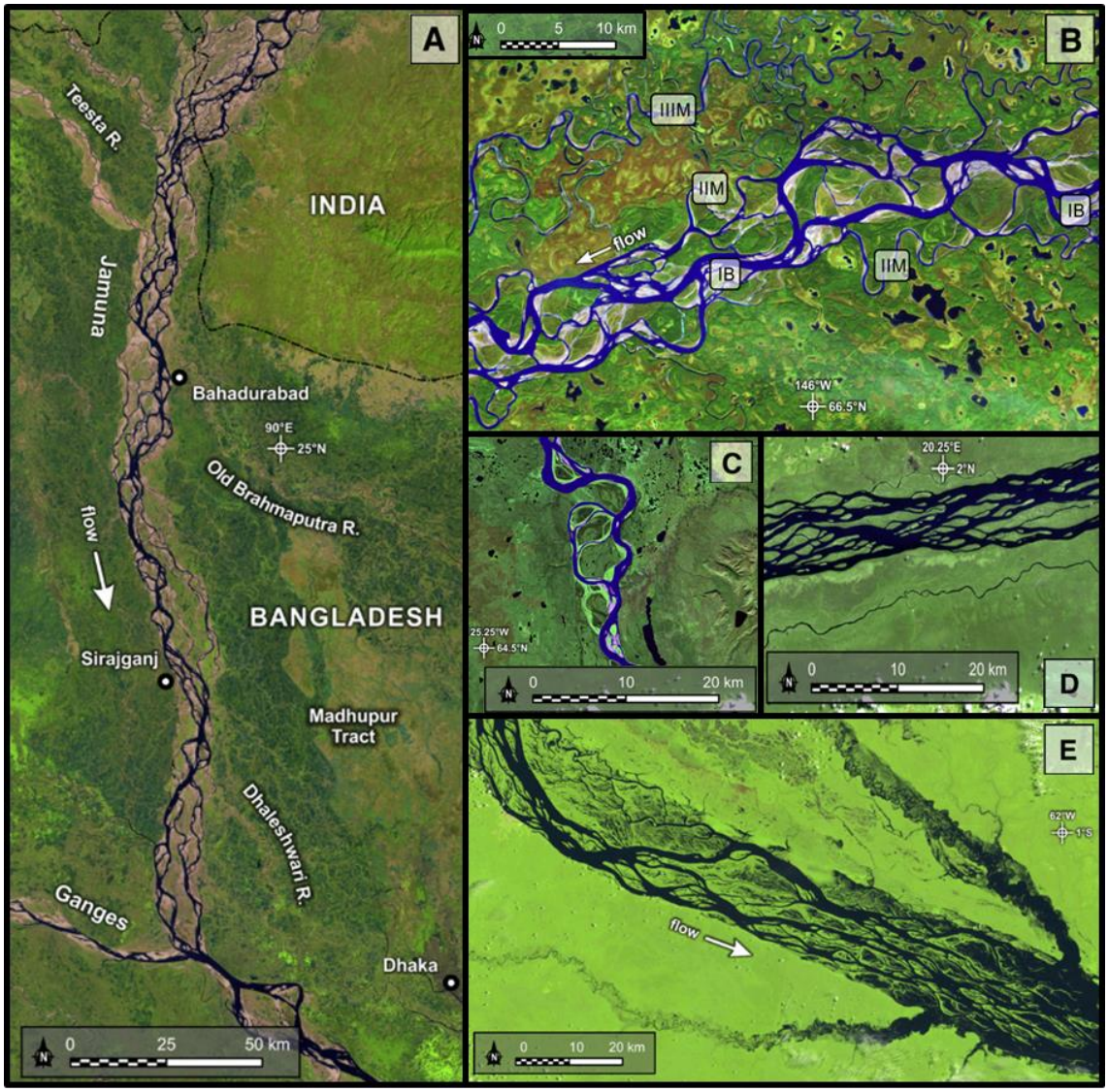

Figure 2-4. Landsat satellite images showing examples of large multichannel river patterns, illustrating difficulties in executing depth measurements across the full channel width: (A) Brahmaputra River in Bangladesh and India; (B) Yukon River in Alaska; (C) Mackenzie River in Canada; (D) Congo River in DR Congo; (E) Rio Negro in Brazil. Individual images taken from Ashworth and Lewin, (2012).

The work of Altenau et al. (2017a) is a rare example of such a study on a 90 km reach of the Tanana River, considered to be medium size based on its 1300 m^3/s mean

discharge during the open water season. A 15 mph average boat speed, 0.5 second measurement interval, and 220,000 total number of measurements reported in the study suggest that a total track length of approximately 740 km was necessary to complete a bathymetric survey of the 90 km study reach (shown in Figure 2-5), with similar spatial coverage to that shown in Figure 2-3. In comparison, a track length for a 90 km long single channel is estimated to be 127 km, derived by applying a Pythagoras calculation to an assumed mean channel width of 1 km and a zig-zag track route aligned at 45 degrees to the stream-wise direction.

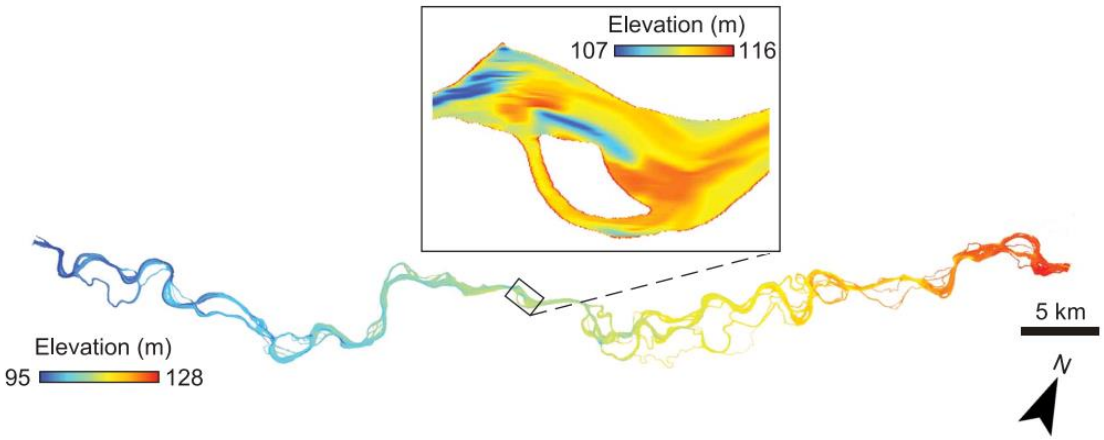

Figure 2-5. Example bathymetry model (BM) of the multichannel Tanana River (first order tributary of the Yukon) developed by Altenau et al. (2017a).

Remote Sensing Measurements

Within the field of river hydrodynamics, bathymetry is generally regarded as being a parameter that cannot be reliably retrieved directly from space (e.g. Bates et al., 2014). Given the difficulty and expense of measuring depths via conventional field methods, and the importance of bathymetry to river hydrodynamic research, this is one of the most fundamental limitations in river hydrodynamics research currently. However, the reflectance of open water to solar illumination is known to be a function of the water depth, the water optical properties and the bottom reflectance (Lyzenga, 1981), implying that depth information can be retrieved from optical imagery for clear waters.

Reviewing the efforts to measure river depth from space, there has been some success with using high resolution optical satellite imagery on short reaches of relatively shallow low turbidity rivers, such as the work of Legleiter and Harrison, (2019). But this study concludes that the sensors and algorithms it employs need to be applied and tested over many tens of hundreds of river kilometres in order to establish credibility. To do this will require generalisation of the relationship between image-derived quantities and water

depth that so far are very localised, and extensive in-situ bathymetry datasets for a wide range of rivers. Moreover, SRS bathymetry retrieval techniques are limited by depth and turbidity and therefore have seen very little application to large rivers, which are associated with areas of deep bathymetry and often relatively high turbidity, particularly in the tropics. Still, detection of only shallow water bathymetry in large rivers would be of value, for example in helping to manage navigation risk, but has seldom been explored. The work of Lopes et al., (2014) is a rare example showing (albeit in a limited way) that it is feasible to use optical remote sensing to estimate bathymetry on a large turbid river (the Congo River). They produced depth estimates from Landsat accurate to within 10%, up to a depth of 14 m using methods devised by Lyzenga, (1981).

Whilst nearly all methods of mapping bathymetry from satellite remote sensing are based on passive, multispectral imagery, Parrish et al., (2019) report that the recently launched ICESat-2 profiling laser altimeter has the ability to retrieve bathymetry. The authors note that ICESat-2 has some advantages over passive methods: ICESat-2 has lower susceptibility to false readings caused by changes in substrate type or other confounding variables introduced by the environment, and does not require reference depths. However, the spatial coverage of ICEsat-2 is clearly inferior to the passive methods, and results so far show a limited maximum depth potential of approximately one secchi depth with a standard deviation of 0.1 secchi depths. Going forward, ICESat-2's performance may improve as its geolocation and calibration are still being enhanced.

2.3.3 Terrain Data

In situ Measurements

Ground elevation data along large river corridors are generally not measured in situ for the purpose of studying hydrodynamics because it is not feasible given the spatial scales involved and the ability of remote sensing methods to capture this variable.

Remote Sensing Measurements

Airborne Light Detection and Ranging (LiDAR) is typically the preferred source of ground elevation data for studying and modelling river hydrodynamics. This is because of its ability to quickly survey large areas at relatively high vertical accuracy (0.05 – 0.2 m), and a high spatial resolution (1 – 5 m) (Sanders, 2007). Crucially, LiDAR is able to penetrate vegetation, which allows the vegetation to be filtered out to yield an accurate bare earth digital elevation model (DEM). LiDAR has been used to map most of the UK and is used routinely in UK flood risk management, but there is little coverage in the developing world because it is expensive to acquire. Much of the LiDAR data that does

exist is not open source; Hawker et al. (2018a) estimate that only 0.005% of the global land surface is covered by open access LiDAR.

Airborne interferometric synthetic aperture radar (InSAR) instruments offer another source of terrain data. Commercial airborne InSAR DEMs typically achieve ~1 m root mean square error (RMSE) and a resolution comparable to LiDAR, but cannot fully penetrate vegetation, and suffer from random noise (Sanders, 2007). Airborne InSAR is potentially cheaper than LiDAR because they can offer a wider swath width than LiDAR (Pinheiro et al., 2020). However, in many parts of the world the resources do not exist to acquire terrain data using these airborne instruments. Instead, reliance is placed on low cost terrain data from space borne instruments.

The Shuttle Radar Topography Mission (SRTM) product obtained from a space borne InSAR mission is generally the most popular source of globally available and free ground elevation data for river hydrodynamics studies. This is because of its superior vertical accuracy, feature resolution, and a lower amount of artefacts and noise compared to alternative data sources such as the ASTER GDEM (Rexer and Hirt, 2014; Jarihani et al., 2015). Despite these advantages over other data sources, SRTM height errors vary between 5 and 9 m (Farr et al., 2007), which limits its application in river hydrodynamics. Height error is spatially heterogeneous however: errors are larger in higher relief terrain than in low relief areas (Sanders, 2007), which is an important factor considering the low relief nature of large river corridors. Much of the height error is due to random noise induced by radar speckles that manifest as spikes and wells, which can be reduced by pixel aggregation when dealing with inundation pattern at the large river scale.

One of the key issues for large river hydrodynamics is the inability of SRTM to fully penetrate vegetation canopies, which leads to overestimation of ground elevations in vegetated areas including large river floodplains, and in turn a failure to recognise inundation processes when utilising SRTM in flood inundation studies. This has led to efforts to create bare earth DEMs by subtracting a component of the vegetation height (e.g. Baugh et al., 2013). More recently, in recognition of the increasing need for accurate bare earth global DEMs, several error corrected derivative DEMs have been created from SRTM. The most comprehensive error removal product to date is the Multi Error Removed Improved Terrain (MERIT) DEM (Yamazaki et al., 2017). MERIT increases land areas mapped with ±2 m or better vertical accuracy from 39% to 58%, and makes significant improvements in flat regions, river networks, and wetlands. However, resolution and accuracy remain a limitation, even for the world's largest rivers. Whilst 2

m is a small proportion of a typical Amazon River flood wave amplitude, other large rivers have much smaller flood wave amplitudes. For example the Congo River annual flood wave amplitude is 3–4 m (O'Loughlin et al., 2013), and the accuracy of the inferred or modelled extent of inundation will be heavily influenced by a 2 m error. Moreover, SRTM's 90 m resolution has been shown to be insufficient to capture floodplain channels that play an important role in the floodplain inundation dynamics of some large rivers such as for the Amazon (Trigg et al., 2012).

Two new open access global DEMs have recently become available: the 90 m resolution TanDEM-X (Rizzoli et al., 2017) and the 30 m resolution ALOS AW3D30 (Tadono et al., 2014). TanDEM-X was recently evaluated in the context of flood inundation by Hawker et al. (2019) who conclude that MERIT can regarded as being slightly more accurate, mainly because it performed better in vegetated land cover. Despite its higher spatial resolution, ALOS AW3D30 was found to have lower accuracy than MERIT and TanDEM-X in describing the topography of a mid-size river with both high and low relief terrain (Tavares da Costa et al., 2019). There are a number of commercial space-borne global DEMs of higher resolution and accuracy than any of the open access DEMs (for example, WorldDEM has a vertical accuracy of 1.4 m (RMSE) and 12 m resolution according to Hawker et al., 2018a), but these products have restricted rights and are regarded as being prohibitively expensive for scientific purposes (Sampson et al., 2016).

Any future effort to produce a global open access high accuracy DEM is likely to comprise existing and newly acquired airborne terrain data in areas where accuracy is most critical, combined with high resolution satellite stereo imagery in areas without airborne coverage (Schumann, 2014). Given the likely costs involved in obtaining such a DEM (Sampson et al. (2016) estimate $7 billion), this is unlikely to happen in the near future, leading Hawker et al. (2018b) to develop an uncertainty approach whereby the effect of topographic uncertainty on hydrodynamic model predictions is explored by simulating multiple plausible DEMs.

2.3.4 Inundation Extents

In situ Measurements

Inundated areas associated with large rivers are generally not measured or monitored in situ because it is not feasible given the spatial scales involved and the ability of remote sensing methods to capture this hydrodynamic variable.

Remote Sensing Measurements

Because of the low spatial resolution requirements of large rivers, their permanent open water extents (i.e. rivers and lakes) are routinely mapped with satellite imagery. Optical products such as Landsat have been used extensively for this purpose, and are now able to produce permanent water body and inundation extent information at the global scale. For example Pekel et al., (2016) used 30 m spatial resolution Landsat data to produce the Global Surface Water Explorer product, which maps the location and temporal distribution of inundation at the global scale over the last 35 years, and provides statistics on their extent and change. Another example is the NASA NRT Global Flood Mapping Product (Policelli et al., 2017), which produces near real time global daily surface and flood water maps at 250 m resolution using data from the Moderate resolution Imaging Spectro-radiometer (MODIS).

A key limitation of optical sensors is that they are unable to see through clouds or at night (Huang et al., 2018). This limitation can be circumvented by using composite images, temporally interpolating, or selecting alternative images captured during representative hydrological conditions, but leads to inaccuracies especially when mapping the spatiotemporal dynamics of a specific flood event that requires higher temporal resolution data during a particular time window. For the purpose of mapping flood dynamics, active microwave instruments provide an alternative or complementary option because their longer wavelengths can penetrate through clouds and they can function at night. Microwave instruments are not always preferable however, as their longer wavelengths limit the resolution of data. Moreover, interpretation of raw microwave data is less straightforward; requiring specific processing algorithms to suit the specific image properties of different products (Schumann and Moller, 2015). As a result, both optical and microwave sensors are well utilised sources of dynamic inundation extent information on large rivers, as demonstrated by the fact that all the rivers that were listed in Table 2-2 have been the subject of multi-temporal dynamic inundation mapping studies using optical and / or microwave products. Details are shown in Table 2-3.

Table 2-3. Examples of Flood Inundation Studies on Selected Large Rivers using Multi Temporal Satellite derived Inundation Extent Information.

River	Example study
Indus	Gaurav et al. (2011), optical
Mississippi	(Li et al., 2013) – optical supplemented with a DEM
Chao Phraya	(Trigg et al., 2013) – optical; (Nakmuenwai et al., 2017) – microwave
Amazon	(Canisius et al., 2019) – microwave
Brahmaputra	(Uddin et al., 2019) – microwave

Penetration of vegetation canopies in order to detect inundation where vegetation is emergent remains a challenging task of satellite imagery. Only certain microwave sensors have sufficiently long wavelength capable of penetrating through dense vegetation, which limits the resolution and availability of suitable datasets. This is a problem on large rivers which often have floodplains that are densely vegetated with diverse species.

Looking specifically at research in the well-studied Amazon basin, Hess et al., (2003) mapped water extents along 1500 km of the central Amazon River and tributaries using 100 m resolution data from L-band JERS-1 synthetic aperture radar (SAR). These maps are seasonal only (i.e. one high water and one low water), and the validation yielded relatively low producer's classification accuracies for certain vegetation classes including 65% for aquatic macrophytes and 55% for flooded woodland. More recently, Canisius et al., (2019) were able use 5 m resolution C-band RADARSAT-2 data to produce multi-temporal (22 images between April 2014 and August 2016) inundation maps including flooded vegetation. However, the spatial extent of mapping was limited to a 100 km reach of the lower Amazon mainstem, and the study also suffered from low producer's classification accuracies (62% for floodplain shrub and 67% for degraded forest). Moreover, this study does not address the issue of the poor ability of the shorter wavelength C-band SAR to penetrate through dense forest canopies. So, it appears that there is still significant room for improvement in the retrieval of inundated areas concealed by vegetation, as asserted by Schumann and Moller, (2015).

2.3.5 Water Surface Elevation

In situ Measurements

WSE is arguably the most necessary hydrodynamic parameter because it is valuable standalone data, and is also required to measure bathymetric elevation and time series discharge data. Accurate in-situ measurement of large river WSE above a reference datum is often not straightforward because of the absence of vertical datum benchmarks or cellular network coverage in the remote regions through which many large rivers flow. This precludes the use of traditional survey equipment or hand-held / consumer grade GPS devices, and requires the use of a survey-grade global navigation satellite system (GNSS) receiver to obtain satellite positioning information. To obtain sufficient vertical accuracy (sub-decimetre) for WSE measurement, a receiver requires the ability to operate on multiple frequencies and receive raw positioning information from multiple satellite constellations. Such a receiver was used in studies of the Tanana River by Altenau et al. (2017b) and Altenau et al. (2017a). With the receiver mounted to a boat, they obtained WSE measurements at regular intervals along a 90 kilometre river reach. They also used the receiver on land to geodetically level a series of depth gauges to obtain WSE time series data. Similar field campaigns have been conducted on Amazon Basin rivers including the Amazon/Solimões, Negro, and Madeira, (Moreira et al., 2012; Moreira et al., 2016; Montazem et al., 2019) where up to 1000 kilometre long reaches were surveyed.

To obtain high precision positional information, the raw data collected by a GNSS receiver must be subject to a correction procedure known as precise point positioning (PPP) (Laínez Samper et al., 2011). In the aforementioned Tanana River and Amazon Basin studies, this correction procedure involved post processing of the raw data using web-based software tools. Such a correction procedure may be unsuitable in situations where internet access is unavailable and there is a need to obtain results in the field. To cater for such a need, alternative real time correction methodologies have been developed by commercial services in recent years, whereby correction information is obtained live by a receiver from a dedicated satellite (e.g. Glocker et al., 2012; Leica Geosystems, 2017; Trimble, 2019). With this live correction information, a receiver is able to obtain high precision measurements in the field.

Remote Sensing Measurements

A growing number of radar and laser profiling satellite altimeters have measured WSE with a vertical accuracy of 0.35 m or less (Frappart et al., 2006; Urban et al., 2008; Jarihani et al., 2013) and are therefore considered suitable for many SRS river

hydrodynamics studies (Domeneghetti et al., 2015). Altimetry satellites function by measuring the satellite-to-surface round-trip time of a radar or laser pulse as they move along their orbital profile, and thus the distance from the satellite to a target surface. The elevation of the target surface can then be obtained by using the precise altitude of the satellite. Spatial resolution, temporal resolution and spatial coverage are the key properties of an altimeter that govern its suitability for a hydrodynamic study. Spatial resolution, i.e. the footprint size of the pulse on the water surface, limits the size of water body that can be accurately measured. Water bodies must be 2–3 times wider than the footprint to ensure WSE is well sampled (O'Loughlin et al., 2016a). For example, the vertical accuracy of 0.28 m quoted for the ENVISAT radar altimeter (Frappart et al., 2006) is only valid for water bodies greater than 1 km wide. This is a major limiting factor in the application of altimetry, as the majority of instruments are radar altimeters and have a footprint of 300 m or larger (O'Loughlin et al., 2016a). The exceptions to this are the laser altimeters including the 70 m footprint of ICESat, and the 17 m footprint of ICESat-2 (Markus et al., 2017).

The orbit of an altimeter and hence its ground track determines the inter-track distance and the repeat cycle; i.e. spatial coverage and temporal resolution respectively. Orbit design involves a trade-off between minimising inter-track distance and repeat cycle. For example, Cryosat-2 prioritises spatial coverage, achieving an inter-track distance of 7.5 km at the equator, but at the expense of a 369 day repeat cycle. In contrast, Jason missions have a 315 km inter-track distance at the equator, but a repeat cycle of 10 days. Cryosat-2 and Jason are at the extreme ends of the spectrum, and Table 2-4 shows the full diversity of past and present altimetry missions in respect of repeat cycle and inter-track distance.

Table 2-4. Summary of Satellite Altimetry Missions, modified from Jiang et al., (2017), ICESat-2 Information from Markus et al., (2017).

Satellite	Period	Repeat cycle (Day)	Equatorial Inter-Track Distance (km)
Skylab	1973–1974		
GEOS 3	1975–1979		
SeaSat	1978	17	
Geosat	1985–1990	17	
ERS-1	1991–2000	35	80
Topex/Poseidon	1992–2005	10	315
ERS-2	1995–2011	35	80
GFO	1998–2008	17	165
Jason-1	2001–2013	10	315
ENVISAT	2002–2012	35	80
OSTM/Jason-2	2008–present	10	315
CryoSat-2	2010–present	369	7.5
HY-2	2011–present	14, 168	
Saral	2013–present	35	80
Jason-3	2016–present	10	315
Sentinel-3A	2016–present	27	104
ICESat-2	2018–present	91	29

Is has been widely acknowledged that the resolution and coverage of these radar and laser altimetry missions needs to be improved upon in order to address many key hydrologic questions, as they miss too many of the world's freshwater bodies and fail to capture them with sufficient resolution (Alsdorf et al., 2007). Attempts to address this have culminated in the use of satellite imagery to obtain WSE information. Imagery alone cannot obtain absolute WSE measurements, but it can yield measurements of WSE change through InSAR techniques with centimetric accuracy (Alsdorf et al., 2007), and can provide shoreline WSEs when combined with terrain data of sufficient accuracy.

InSAR techniques to retrieve relative changes in WSE rely on the double bounce effect that occurs in flooded vegetation. In open water the radar pulses of SARs are reflected away from the antennae because they are not perpendicular to the earth's surface, but the presence of flooded vegetation causes a second reflection (so called "double bounce") from the vegetation surfaces, sending some of the radar pulse back to the antennae (Alsdorf et al., 2000). By comparing the longer wavelength radar information of the two SAR images obtained for the same location at different times, the relative change in WSE can be derived in the form of an interferogram. The relative WSE change values can then be converted to absolute values by using reference WSE measurements. Following the introduction of this technique to the Amazon floodplains by Alsdorf et al. (2000), the technique has been used in over 20 studies of wetland water level monitoring (Mohammadimanesh et al., 2018). Some examples include the work of Lee et al. (2015) who estimated WSE change over a 20,000 km^2 area of flooded forests adjacent to the Congo River mainstem using ALOS PALSAR. These estimates were not multi temporal, only providing the difference between June and December (i.e. low water and high water conditions respectively) on the mainstem, but serve to establish that WSE change increases closer to the Congo mainstem. Jaramillo et al. (2018) looked at degradation of the Magdalena River delta wetlands due to a loss of hydrodynamic connectivity by producing multi temporal interferograms from ALOS-PALSAR (66 between 2007 and 2011), but this was over a relatively small area of 100 square kilometres. Cao 2018 were able to use coarse resolution SAR (SLOS2 ScanSAR) to obtain multi temporal interferograms (timespans of 28-42 days) over a large 75,000 km area of the Amazon floodplains.

InSAR derived WSE change information is of quite limited value on its own, and requires complementary datasets such as absolute WSE information and discharge information in order to maximise its potential for studying river hydrodynamics. For example, Jaramillo et al. (2018) were able to use in-situ river discharge data to supplement their interferograms. Consequently, as Mohammadimanesh et al. (2018) points out, studies have been biased towards favourable conditions, such as availability of gauges or profiling altimetry data, and accessibility. Interferograms are also difficult to validate quantitatively due to a paucity of in-situ data or alternative SRS data.

2.3.6 SWOT: Unprecedented WSE and Complementary Inundation Information

The ability to retrieve hydrodynamic parameters from space-borne instruments has seen remarkable progress in recent decades, but current data sources and methods are still regarded as being insufficient for many key large scale hydrological questions. In an effort to advance progress in answering such questions, the Surface Water and

Ocean Topography (SWOT) Mission is soon to be launched. This is the first satellite mission dedicated to surface water exploration. In simple terms it can be regarded as the surface water equivalent of SRTM, as like SRTM, it will use an interferometric SAR instrument. SRTM only ran for 11 days and was not designed to retrieve surface water, whereas SWOT will run for three years and will use a radar band specifically intended to retrieve surface water.

SWOT will produce four products, including an unprocessed raw pixel cloud product, a pre-processed raster product which contains water extent and WSE information at 100 m or 250 m spatial resolution, and two post-processed products. The post-processed SWOT products will include river centreline nodes at 200 m centres containing WSE and river width information, and 10 km long river reaches containing computed mean water surface slope and estimated discharge (CNES, 2019b). All rivers and lakes wider than 50-100 m will be captured with a repeat cycle of 21 days, with most of the globe being visited at least twice during each repeat cycle. The expected accuracy of the processed WSE products is scale dependent, and is stated as being 10 cm over a 1 km^2 area, and 25 cm over a 250 m^2 area (Biancamaria et al., 2016). Further details are provided in Table 2-5.

Table 2-5. Surface Water and Ocean Topography Mission Science Requirements (Rodriguez, 2016; Biancamaria et al., 2016)

Requirement	Description
Observed areas	All observed water areas detected by SWOT will be provided to end users, but: errors will be evaluated for (250 m)^2 (= 62,500 m^2) water bodies and 100 m (width) x 10 km (long) river reaches or higher. Errors will be characterised for (100 m)^2 to (250 m)^2 water bodies and 50 m to 100 m (width) x 10 km (long) river reaches
Height accuracy	<10 cm when averaging over water area >1 km^2. <25 cm when averaging over (250 m)^2 <water area <1 km^2.
Slope accuracy	1.7 cm/km for evaluated river reaches when averaging over water area>1 km^2
Relative errors on water areas	<15 % for evaluated water body and river reaches <25 % of total characterised water body and river reaches
Mission lifetime	3 months of fast sampling calibration orbit + 3 years of nominal orbit
Rain / layover / frozen water flag	68% or more of the contaminated data should be correctly flagged
Data collection	>90 % of all ocean/continents within the orbit during 90 % of operational time

Coincident WSE and water extent information at the global scale, with the accuracy, spatial and temporal resolutions reported above is expected to yield major advances in hydrology, and will present many new research opportunities especially in data sparse regions. SWOT data resolution and accuracy will surpass the requirements for many large river hydrodynamics applications, and since it was first proposed over a decade ago, research efforts into how to utilise its data have been growing. Much of this research has focused on addressing the limitations of SWOT, which are largely a result of complementary global high accuracy terrain data and bathymetry data being unavailable. Another limitation is the impact of vegetation on SWOT's elevation and inundation extent measurements, which remains poorly understood (Rodriguez, 2016).

This is important because many of the world's large rivers are located in equatorial regions, where vegetation coverage is dense and widespread on floodplains. Many large rivers also interact with heavily vegetated wetlands. Research into SWOT's handling of inland water obscured by emergent vegetation is ongoing.

Another ongoing area of research is SWOT's approach to multichannel rivers. Currently, SWOT discharge estimation algorithms work with reach-averaged hydraulic variables lumped into an effective single channel, and do not attempt to resolve hydraulic conditions in individual channel threads (Rodríguez and Frasson, 2020). However, providing channel threads are over 100 m wide, it should be possible for SWOT to obtain water surface extent, elevation, and slope through individual channel threads, along with inundation patterns and elevations that occur on mid-channel islands. Whether or not this channel thread information would improve upon the discharge estimates derived from lumped effective single channel approach remains to be seen. Besides discharge estimation, these hydraulic observations through channel threads and on mid-channel islands will be of significant value to large river hydrodynamic research.

There is a need to look beyond SWOT and leverage its data long after its three year operational life, bearing in mind that further dedicated inland surface water satellites may not be financially sustainable. This appears to have received limited attention in scientific publications. One possible longer term future strategy for earth observation may involve constellations of identical, low-cost microsatellite altimeters launched by the same rocket (CNES, 2019a). This would reduce development and launch costs and launch costs too for micro-satellites launched by the same rocket, but prompts questions about what the minimum number of satellites needed would be and their distribution in time and space.

2.4 Modelling Large River hydrodynamics

Free surface hydrodynamic fluid flow is described by the Navier–Stokes equations, which are derived by applying the conservation of mass and momentum to describe the motion of a viscous fluid in three dimensions (Douglas et al., 2001). Hydrodynamic modelling traditionally involves applying these equations (or simplifications of) to predict spatially distributed dynamic flow conditions including WSE, velocity, inundation extent, and discharge. The term 'hydraulic model' is often used interchangeably with 'hydrodynamic model', here the interpretation is that the latter term specifically refers to the simulation of unsteady (i.e. dynamic) flow conditions, whereas the former may involve unsteady or steady state flow conditions. Inputs into hydrodynamic models include river flow hydrographs at particular locations, topography and bathymetry, and a hydraulic roughness coefficient. Models are usually calibrated by adjusting the hydraulic roughness coefficient, which may be spatially uniform or variable. Bathymetry is also sometimes treated as a calibration parameter when observed bathymetry data is not available. Flood extent and WSE observations are the most commonly used sources of data for calibrating and validating hydrodynamic models of large rivers, and are now routinely obtained from SRS for this purpose (Grimaldi et al., 2016). Discharge data is also sometimes used to calibrate and validate such models (e.g. Schneider et al., 2017), and although seldom used, observed velocity data can been used in calibration and validation (Nicholas et al., 2012).

Inverse approaches to hydrodynamic modelling are less common, but their use is increasing. They entail a reversal of the traditional inputs and outputs, allowing bathymetry and discharge information to be estimated by using inputs of dynamic inundation extent and WSE information (e.g. Durand et al., 2016). The growth of inverse modelling approaches on large rivers is being driven by a scarcity of in-situ discharge and bathymetry information, combined with the increasing availability of remotely sensed dynamic WSE and inundation extent data. One of the key aims of the SWOT mission is to provide the data to drive inverse models that will estimate discharge (Biancamaria et al., 2016).

Models may serve to inform any number of the hydrodynamic research drivers discussed in section 2.2, but are often developed with a specific purpose in mind. Every model is unique in terms of the purpose(s) it is intended to serve, and several key factors that are discussed in the following sections, namely the available input data, the spatial structure, resolution, and numerical formulation adopted.

2.4.1 Model Numerical Formulations

To model river hydrodynamics the shallow water approximation of the Navier–Stokes equations is usually employed. This approximation assumes that the horizontal length scale is much larger than the characteristic vertical length scale, and the characteristic vertical velocity is small in comparison with the characteristic horizontal velocity. This is implemented mathematically by integrating the Navier-Stokes equations over the flow depth assuming a hydrostatic pressure distribution, which yields the two dimensional (2D) shallow water equations (SWEs). De Almeida and Bates (2013) present the SWEs in the following form:

$$\underbrace{\frac{\partial h}{\partial t}}_{\substack{Conservation\ of \\ mass\ in\ time}} + \underbrace{\frac{\partial q_x}{\partial x} + \frac{\partial q_y}{\partial y}}_{\substack{Conservation\ of \\ mass\ in\ space}} = 0 \qquad \text{Eq. 2-2}$$

$$\underbrace{\frac{\partial q_x}{\partial t}}_{\substack{Local \\ acceleration}} + \underbrace{\frac{\partial}{\partial x}(uq_x) + \frac{\partial}{\partial y}(vq_x)}_{\substack{Convective \\ acceleration}} + \underbrace{gh\frac{\partial (h+z)}{\partial x}}_{\substack{Water\ slope \\ (pressure\ gradient \\ and\ bed\ slope)}} + \underbrace{\frac{gn^2\|q\|q_x}{h^{7/3}}}_{Friction} = 0 \qquad \text{Eq. 2-3}$$

$$\underbrace{\frac{\partial q_y}{\partial t}}_{\substack{Local \\ acceleration}} + \underbrace{\frac{\partial}{\partial y}(vq_y) + \frac{\partial}{\partial x}(uq_y)}_{\substack{Convective \\ acceleration}} + \underbrace{gh\frac{\partial (h+z)}{\partial y}}_{\substack{Water\ slope \\ (pressure\ gradient \\ and\ bed\ slope)}} + \underbrace{\frac{gn^2\|q\|q_y}{h^{7/3}}}_{Friction} = 0 \qquad \text{Eq. 2-4}$$

Where x and y are the two Cartesian directions, t is time, h is water depth, q_x and q_y are the x and y components of the discharge per unit width, $\|q\|$ is the magnitude of discharge per unit width, u, v are the x and y components of the flow velocity, z is the bed elevation, g is acceleration due to gravity, and n is the manning friction coefficient.

Models often employ approximations of the 2D SWEs. These include the local inertial, diffusive, and kinematic formulations where certain terms are assumed to be negligible relative to other terms (Hunter et al., 2007), and / or use of the one dimensional (1D) St Venant formulation whereby the 2D SWEs are width integrated, thus assuming flow to be unidirectional. Their reduced physical complexity means they are computationally faster. Table 2-6 summarises the key simplifications used. Despite continuing advances in computational power, these simplified formulations remain well utilised when modelling the hydrodynamics of large rivers over long reaches. This

includes the use of 1D formulations to model flow in 2D, by decoupling formulae in the *X* and *Y* directions on a 2D orthogonal grid (e.g. Bates and De Roo, 2000; Bates et al., 2010; Jamieson et al., 2012).

Table 2-6. Simplified Formulations of the 2D SWEs.

Formulation	Description	Example large river application
2D SWE	Derived by depth integrating the Navier Stokes equations	Parana (Nicholas et al., 2012)
1D St Venant [1]	Simplifies the SWEs by assuming flow is unidirectional, by width integrating the SWEs.	Amazon (Trigg et al., 2009)
Local inertial approximation	Simplifies the SWEs by assuming the convective acceleration term is negligible.	Zambezi (Schumann et al., 2013)
Diffusive wave approximation	Simplifies the SWEs by assuming the following terms are negligible: - Local acceleration, - Convective acceleration.	Amazon (Rudorff et al., 2014)
Kinematic wave approximation	Simplifies the SWEs by assuming the following terms are negligible: - Local acceleration, - convective acceleration, - Pressure gradient component of water slope term.	Amazon (Wilson et al., 2007)

1. Local inertial, diffusive wave, and kinematic wave formulations are combined with the 1D St Venant approximation in all the examples given for these formulations.

The suitability of each of these simplified formulations for modelling different types of free surface flow conditions has been widely explored for decades (e.g. Ponce et al., 1978; Vieira, 1983; Moussa and Bocquillon, 1996; Tsai, 2003). A key parameter that recurs in this literature and is the Froude number. The Froude number (Fr)

represents the dimensionless ratio of inertial forces to gravity forces acting on free surface flow (Chow, 1959), and is given by:

$$Fr = \frac{U}{\sqrt{g\frac{A}{B}}} \qquad \text{Eq. 2-5}$$

Where U is the mean channel velocity, g is the acceleration due to gravity, A is wetted cross-sectional area, and B is the free surface width. When the Froude number is less than 1, gravity forces dominate the inertial forces, and the flow conditions are termed subcritical. Thus, when the Froude number is sufficiently small, the inertial forces (i.e. the local and convective acceleration terms in the SWE) can be assumed negligible, enabling the local inertial and diffusive wave formulations to be used. Indeed, implementations of such formulations are sometimes referred to as 'low Froude' models (e.g. Garambois and Monnier, 2015).

The local inertial approximation was explored relatively recently by De Almeida and Bates (2013), who benchmarked a local inertial model against a SWE model using four test cases. They evaluated errors in WSE prediction and flood wave propagation speed along a rectangular channel reach experiencing subcritical flow, i.e. a Froude number <1. Errors introduced by the local inertial approximation were found to be relatively low (depth estimation errors were no greater than 4%) for flow conditions with low Froude numbers (0–0.5) and low water surface slopes (less than 3%). Increasing the Froude number alone (up to 0.95) had little effect on errors, but when combined with an increase water surface slope, the errors became more substantial (up to 20% depth error), reflecting an increase in the convective acceleration component of the flow. Errors in flood wave propagation speeds were also found to be substantial for higher Froude numbers. This research implies that the local inertial approximation is suitable for the vast majority of large river flow conditions, because their flow conditions are predominantly highly subcritical and their bed slopes very gentle.

Trigg et al (2009) assessed the effect of a diffusive wave approximation in the context of modelling large river hydrodynamics. Their study involved hydrodynamic modelling of a 575 km reach of the central Amazon River, using both a 1D St Venant formulation and a diffusive wave formulation. Evaluation of both models showed negligible difference between the St Venant and diffusive WSE predictions (average RMSE along the mainstem differed by only 0.025 m, a small fraction of the 12 m high flood wave amplitude). The results were not surprising, as prior to the modelling exercise

the authors had characterised the amazon flood wave as being diffusive, using the methods of Vieira (1983), and Moussa and Bocquillon (1996). These methods were also used by Tuozzolo et al. (2019) to demonstrate that a diffusive wave formulation is suitable for use in a hydraulic model that estimates discharge along a mid-size river in Ohio, USA.

The kinematic wave approximation is more limited in its application, because it neglects the pressure gradient component of the water slope term, thereby assuming that the energy grade line is parallel to the bed slope. Gradually varied flow conditions such as backwaters and flow attenuation are therefore not accounted for, yet are known to occur naturally in large rivers. For example, Meade et al. (1991) quantified backwater effects in the Amazon basin and found that in the lowermost 800 km of the Madeira and Purus tributaries experience falling river stages as much as 2~3 m higher than rising stages at any given discharge. Kinematic wave formulations are now rarely used to model river channel flow conditions. Even within the emerging global flood modelling initiative, where models are used to predict flood inundation extent and depth across the entire world, diffusive wave or local inertial formulations are increasingly being used (Yamazaki et al., 2011; Sampson et al., 2015; Trigg et al., 2016).

2.4.2 Model Spatial Structure

Hydrodynamic models use various spatial structures to implement a numerical formulation. Broadly speaking, these are divided into 1D and 2D categories. Within the hydraulic modelling community the terms ‘1D model’ and ‘2D model’ generally refer to the spatial structure adopted (i.e. not the dimensionality of the numerical formulation), and this terminology is adopted from hereon. Models within the 1D category (usually known as 1D models) implement formulations at nodes containing river channel geometry information, commonly known as cross sections (e.g., Brunner and Bonner, 1994; Havnø et al., 1995). The locations and orientation of nodes are user defined, and may be dictated by where channel geometry data is available. The node cross-sectional information is often interpolated longitudinally to facilitate computations at higher spatial resolution and obtain hydraulic information at locations between surveyed cross sections, and may be extended laterally onto floodplains to enable floodplain flows to be simulated. The assumption that flow is uni-directional is a key limitation of 1D approaches, since flow conditions in rivers are widely 2D, and the direction of flow often unpredictable and highly variable, particularly on floodplains, in sinuous channels, multi-thread channels, and at confluences. All these features are commonly found on large rivers. The 1D approach is further limited by the requirement for the user to define cross section locations and orientation, because it effectively requires the user to determine

the direction of flow, and select what topographic and bathymetric features to represent in the model. These limitations to 1D approaches can be mitigated to a degree, for example, floodplain flows can be represented with an independent set of nodes connected in parallel with the main channel (see for example, the modelling of the Mekong delta reported in Evans et al. (2007)), and thus allowing floodplain velocities, flow direction, and water surface to be modelled independently from the main channel. The floodplain nodes may employ the same numerical scheme as river cross sections, or use a simpler 'storage cell' computation that calculates a flat WSE only (i.e. velocity is assumed zero).

The limitations of 1D approaches can be largely overcome by adopting a 2D approach. The development of 2D approaches (commonly known as 2D models, irrespective of whether the use a 1D or 2D numerical formulation) was largely in response to the widespread availability of spatially distributed topography data afforded by the emergence of airborne and spaceborne remote sensing techniques such as LiDAR and and InSAR (Sampson et al., 2016). 2D approaches entail a continuous representation of topography on a 2D grid or mesh. 2D grids are made up of vertices that form cells, the model formulation being implemented across each vertex. Topographic information is located at each cell centre. Water may move across any cell vertex and therefore in two horizontal dimensions, and is calculated by the model according to the pre-existing hydraulic conditions and the topography. Cell shape varies between different 2D approaches. At their simplest, cells are fixed in orientation, square in shape, and uniform in size, forming a structured grid on which water can flow between cells in either in the X or Y direction. Variants of the square, structured grid have been developed to improve model efficiency (by reducing the number of cells necessary) and /or improve process representation, although they also require additional user intervention. Key examples include curvilinear grids (shown in Figure 2-6) adopted by software packages such as Delft 3D (see for example, Gerritsen et al., 2008) and Mike 21C (e.g., Vested et al., 2014). Curvilinear grids have cells that can be rectangular, curved in shape, variable in size, and their orientation aligned with channel centrelines, effectively enabling a more accurate representation of topography using fewer cells. Unstructured type grids employ cells of different shapes (i.e. a variable number of vertices) and size. Cell shape variability enables cell vertices to be aligned according to the topography in a more flexible way than the curvilinear grid approach, potentially enabling further increases in efficiency and / or process representation (Hoch et al., 2018).

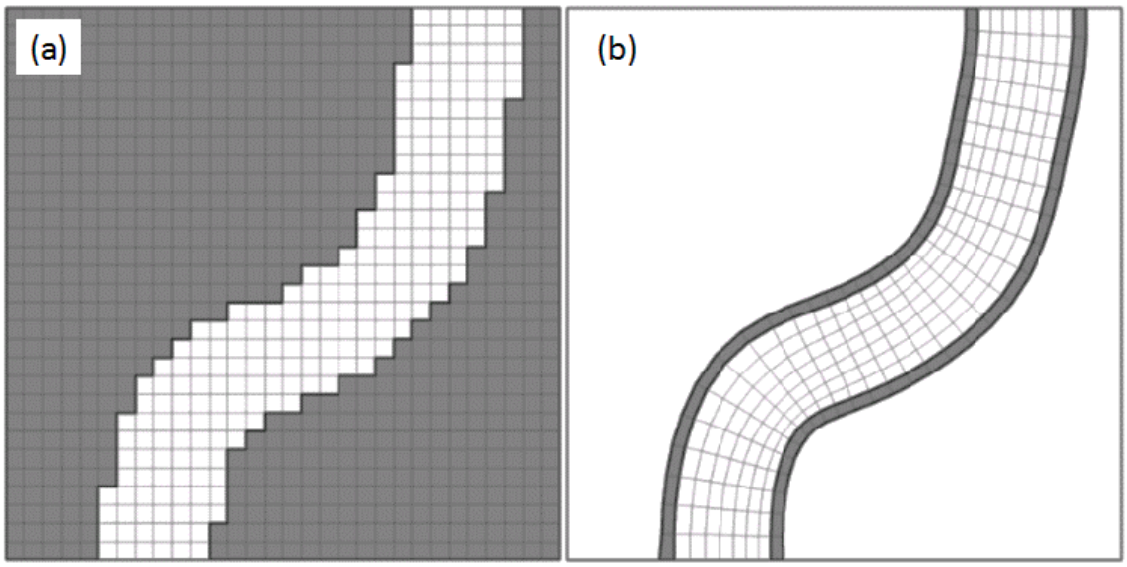

Figure 2-6. Channel representation using: (a) structured square grid; (b) rectangular curvilinear grid. From DHI Water & Environmental (2004).

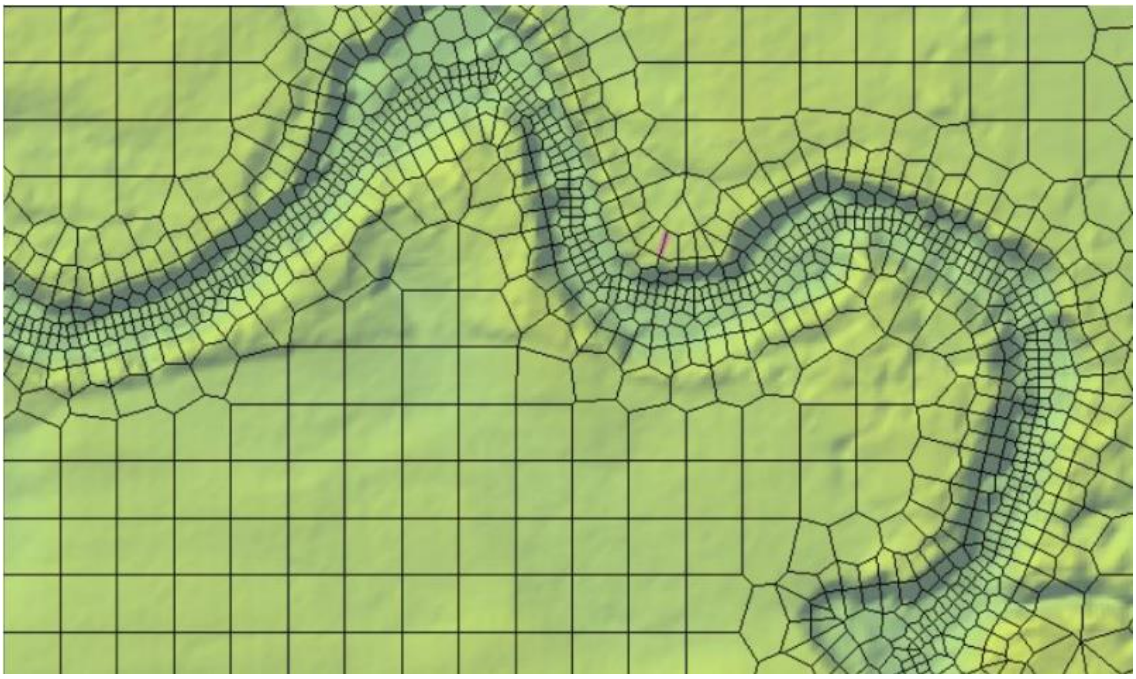

Figure 2-7. The irregular grid shapes of an unstructured grid used to accurately define channel edges and alignment. From Lintott (2017).

Regardless of grid type, 2D approaches require a far greater number of computations than 1D approaches, as a result of the larger number of 2D vertices at which computations are executed, and historically this has hindered the application of 2D approaches at large scales. For example, Alho and Aaltonen, (2008) constructed two

comparative models, using a 1D approach (HEC-RAS model with 29 cross sections) and a 2D approach (TELEMAC-2D with 17,286 nodes), and found The 1D model took five minutes to run, whilst the 2D model took 36 hours to run (approximately 430 times slower). It should be noted that TELEMAC-2D is a full 2D SWE model, and other 2D approaches such as LISFLOOD-FP that use model formulations of reduced dimensionality and neglect acceleration terms are much faster. This was illustrated by Sanyal et al. (2014), who found a LISFLOOD-FP model to run approximately 100 times faster than a comparative TELEMAC-2D model. Generally, the greater run times of 2D models has become less of an issue in recent years, due to advances in computing power. 2D approaches are now adopted even at the largest spatial scale conceivable; i.e. in global flood models (GFMs) (Trigg et al., 2016), albeit at low spatial resolution and using 1D diffusive or local inertial formulations on simple square grids. Simple square grid approaches continue to widely used and actively developed (see for example, the recent improvements to the LISFLOOD-FP code reported by Neal et al. (2018)), largely because of the minimal user intervention they require.

Another key development of 2D approaches has been the emergence of the sub-grid capability, whereby individual grid cells are parameterised with fine scale (i.e. 'sub-grid' scale) topographic information. When model spatial resolution is reduced to manage the computational power requirements of modelling large spatial domains and long timescales, important topographic features and physical processes may be neglected. For example, Yu and Lane (2006a) found that decreasing the spatial resolution of their 2D hydrodynamic model resulted in an increase the rate of flood propagation, and changes in the direction of the propagation. In response to these findings, Yu and Lane (2006b) developed a sub-grid scale treatment, enabling fine-scale topography and hydraulic processes to be represented without increasing computational resolution, thus avoiding the increase in computational expense associated with increasing model resolution. This computational expense is significant: a 50% reduction in cell size (i.e. one cell becomes four cells) will typically increase model run time by an order of magnitude, on account of the increased number of computations and the reduction in time step necessary to maintain numerical stability (e.g. Savage et al., 2016). Unsurprisingly, sub-grid approaches are used in some GFMs (Trigg et al., 2016).

The current versions of LISFLOOD-FP and HEC-RAS are both examples of hydrodynamic model codes that have sub-grid capability, although the two approaches are quite different. LISFLOOD-FP uses a sub-grid procedure to enable channels smaller than individual grid cells to be represented (Neal et al., 2012). Computations separate to the base model of LISFLOOD-FP are carried out at each grid cell vertex using a 1D local

inertial formulation as shown in Figure 2-8, based on input channel cross-sectional information including width, depth, channel frictional coefficient, and shape.

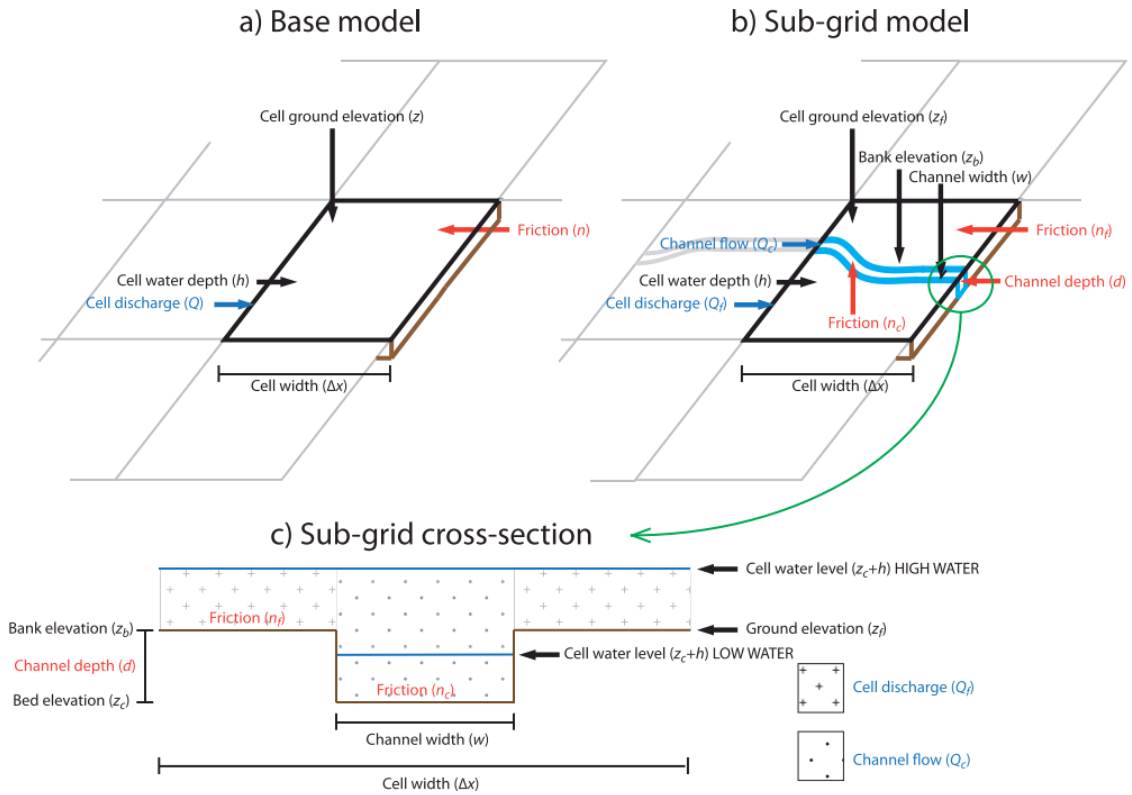

Figure 2-8. Conceptual diagram illustrating sub-grid capability of LISFLOOD-FP model code, enabling channel features smaller than individual grid cells to be represented (Neal et al., 2012): (a) LISFLOOD-FP base model using simple structured square grid; (b)-(c) Separate sub-grid component using 1D cross-sectional information.

The sub-grid approach employed by HEC-RAS is to provide each cell with tabular information that describes the topography within the cell and across each cell edge. To do this, an elevation – volume curve is generated for each cell, and a series of hydraulic property curves are generated for each cell face (elevation vs. wetted perimeter, area, and roughness). This is illustrated in Figure 2-9.

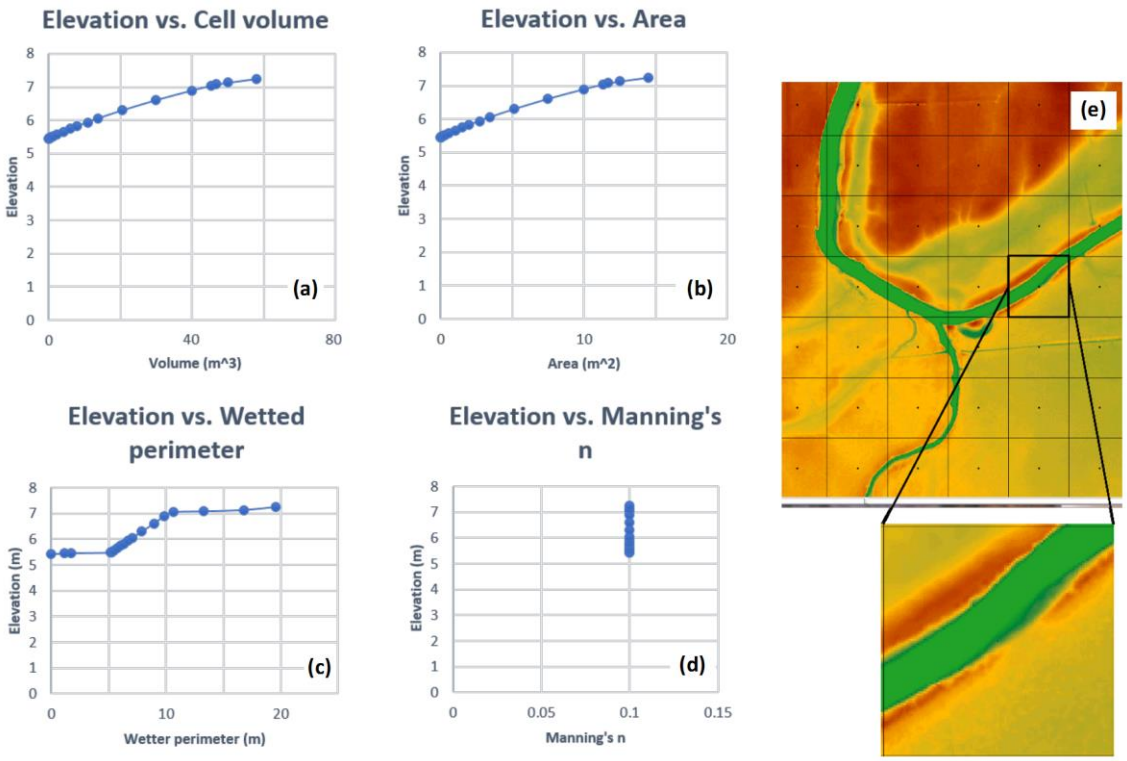

Figure 2-9. Tabular information used in HEC-RAS sub-grid approach: (a) Example cell volume vs. elevation relationship; (b)-(d) examples of the relationships at each cell vertex; (e) example of input DEM information within each grid cell used to generate sub-grid information. From Brunner (2016); Betsholtz and Nordlöf (2017).

2.4.3 Model Discharge Data

Input data into hydrodynamic models include terrain data, hydraulic roughness information, and water surface information used as a downstream boundary condition. Models usually include discharge data as an input, or in the case of inverse modelling approaches, detailed dynamic WSE and free surface width information instead. Rainfall and evaporation data may also be input into a model if they are deemed to significantly affect discharge within the spatial and temporal extents of the model.

Discharge data may be obtained from observations outlined in section 2.3.1, or estimated using a hydrological model. The model purpose may dictate that hydrological modelling to estimate discharge is required; for example, for flood forecasting where model hydrodynamic predictions are required for the future based on current (or forecast) precipitation observations (Cloke and Pappenberger, 2009). Flow estimation using hydrological models is beyond the scope of this thesis, so only a very brief and simplistic description of this topic follows. Hydrological models estimate river flows by calculating the catchment runoff that generates river flow. To calculate runoff, hydrological models use rainfall data as an input, and derive the water that is available for runoff by modelling

hydrological processes such as interception, evapotranspiration, and infiltration (e.g. Hughes, 2013). Surface and sub-surface runoff processes are then modelled to determine streamflow. Modelling the hydrological processes requires several other inputs, such as evapotranspiration information, soil type, land cover, and topography. Streamflow data is required to calibrate and / or validate hydrological models, although if the hydrological model is coupled to a hydrodynamic model, water surface information (WSE or extent) can be used in part (Paiva et al., 2013).

There are many hydrological models available worldwide, and almost as many methods for applying them. Unsurprisingly, the large river hydrodynamic modelling studies that have involved flow estimation have used a variety of hydrological modelling approaches. Examples include the work of De Paiva et al. (2013) and Fleischmann et al. (2018), who used the Modelo de Grandes Bacias (MGB) hydrological model to simulate discharge in the Amazon Basin and Upper Niger River Basin respectively. Schumann et al. (2013) used the Variable Infiltration Capacity (VIC) hydrological model to estimate discharge for input into a hydrodynamic model of the Lower Zambezi River. Hydrological models have also been used to supplement discharge measurements with incomplete spatial coverage, see for example Paz et al. (2011), who used the MGB model to supplement gauged discharge data input into a hydrodynamic model of the Upper Paraguay River Basin.

Use of hydrological models as a source of input discharge data to large river hydrodynamic models is attractive because the inputs required can often be obtained using remote sensing datasets, and are therefore more available than discharge measurements. Key datasets include radar derived precipitation datasets such as those derived from the Tropical Rainfall Measuring Mission (TRMM), other meteorological information required to estimate evapotranspiration including temperature, wind speed, solar radiation and humidity (datasets from the University of East Anglia's Climate Research Unit are an example - see New et al., 2002), and land cover datasets such as that provided by the Climate Change Initiative (Santoro et al., 2017). However, a hydrological model introduces significant source of uncertainty to hydrodynamic model predictions. There is significant disagreement between satellite-derived and in-situ datasets used as hydrological model inputs, errors in precipitation datasets in particular are known to cause large uncertainties (Voisin et al., 2008). Hydrological processes not represented in models may also create significant uncertainty (Schumann et al., 2013).

2.4.4 Model Topographic Data

The vast majority of large river modelling studies that involve out-of-bank flow conditions make use of the globally available SRTM DEM (or a derivative of it) to represent topography, as discussed in section 2.3.3. When inputted into a hydrodynamic model, the model spatial resolution adopted is often significantly lower than the resolution of the DEM, to manage computing resources, and also to reduce elevation error by spatially averaging the SRTM data. SRTM elevation error reduces with spatial averaging in proportion with the reciprocal of the square root of the number of elevation points that are averaged, if it is assumed the terrain is flat and the errors are normally distributed (Rodríguez et al., 2006; Neal et al., 2012). So, if four cells are spatially averaged for example, an elevation error of 5 m at the native 90 m resolution of SRTM would reduce to 2.5 m.

2.4.5 Model Bathymetry Data

The process of preparing bathymetry data for input into hydrodynamic models often involves interpolation of the bathymetry measurements, in either one or two dimensions. 1D methods involve interpolating between cross sectional data in the stream-wise direction in order to obtain one or more cross sections in between the surveyed cross sections. Individual elevation points from each cross section are paired according to their relative location along the cross section, and linearly interpolated (e.g. Evans et al., 2007). This method is usually adopted within a 1D hydraulic model framework, and involves similar assumptions and limitations as those posed by the use of 1D hydraulic models. 2D interpolation methods involve generating a continuous bathymetric DEM, and may utilise one of many well established methods for spatially interpolating terrain data, typically in raster format and in a GIS environment. There has been some research into 2D bathymetric interpolation methods, much of which has focussed on the treatment of river anisotropy. River channel morphology is known to be anisotropic, varying more in the direction perpendicular to the stream-wise direction, and several techniques have been developed to account for it. Solutions include channel fitted coordinate systems (e.g. Goff and Nordfjord, 2004), and directional inverse distance weighting (IDW) (e.g. Merwade et al., 2006).

Particular challenges arise when interpolating multichannel river bathymetry. Use of 1D methods by treating a multithread channel as single thread may neglect significant morphological features such as mid-channel islands and bifurcations, and a hydrodynamic model that does not represent such features will misrepresent in-channel hydraulic processes. This was demonstrated by (Altenau et al., 2017a), who found the

critical success index (CSI) of flood inundation predictions reduced by 47% when multichannel morphology was neglected. Theoretically it would be possible to account for multichannel morphology using a 1D method by implementing the interpolation separately along each individual channel thread, but this would be prohibitively time consuming to apply to the kind of river patterns shown in Figure 2-4 (the apparent absence of any account of this being done in published scientific literature is testament to this). The use of a 2D interpolation method is more realistic for incorporating multichannel morphology into bathymetry, and development of a method of doing so in an efficient manner (i.e. without extensive manual intervention that prohibits application on large scale reaches of rivers with numerous channel threads) has begun to receive some research attention. Specifically, (Altenau et al., 2017a) developed a custom interpolation methodology applicable to a multichannel river with an anabranching planform, and Hilton et al., (2019) developed a novel method of implementing a channel-fitted coordinate system that can incorporate a mid-channel island. Neither of these methods has been generalised for multichannel river modelling problems however, and have only been applied to a specific type of channel pattern or a limited number of channel threads.

As discussed in section 2.3.2, bathymetry cannot be reliably observed using remote sensing techniques, resulting in no bathymetry data for many river reaches. This is particularly true for large rivers in remote regions, where the resources and infrastructure required to undertake bathymetric surveys are not well established, and the spatial coverage requirements of very large, often multi-thread channel systems presents a major undertaking. The bathymetry data gap has led to widespread application of hydrodynamic modelling methods that use limited or no observed bathymetry data to model floods.

At their simplest, these methods do not represent the river channel bathymetry, and allow for the bathymetric volume that is missing from a remotely sensed DEM such as SRTM by subtracting an estimate of the discharge carried by the unrepresented portion of the channel (e.g. Bradbrook et al., 2004). Simply subtracting the estimated channel capacity is clearly not a viable approach when in-channel hydraulic information is required, and is problematic for even the coarsest hydraulic model approach conceivable, for a number of reasons. In addition to the failure of this approach to represent changes in channel capacity along a reach that will strongly control inundation processes (Samuels, 1990), this approach also neglects important physical processes such as transfers of momentum between the channel and the floodplain (Bradbrook et al., 2004). There is likely to be significant error in the estimated discharge magnitude, in

terms of how representative it is of the flow conditions represented by the DEM water surface. Moreover, globally available DEM products do not accurately represent the water surface of channels, and include physically unrealistic vertical steps. This DEM water surface inaccuracy was recently assessed by Langhorst et al. (2019) who concluded that the upcoming SWOT mission will greatly improve upon the river surface elevation profiles provided by existing DEMs. Figure 2-10 (taken from Langhorst et al. (2019)) shows a comparison of observed water surface profiles along the river Po in Italy from different sources, clearly showing these vertical steps.

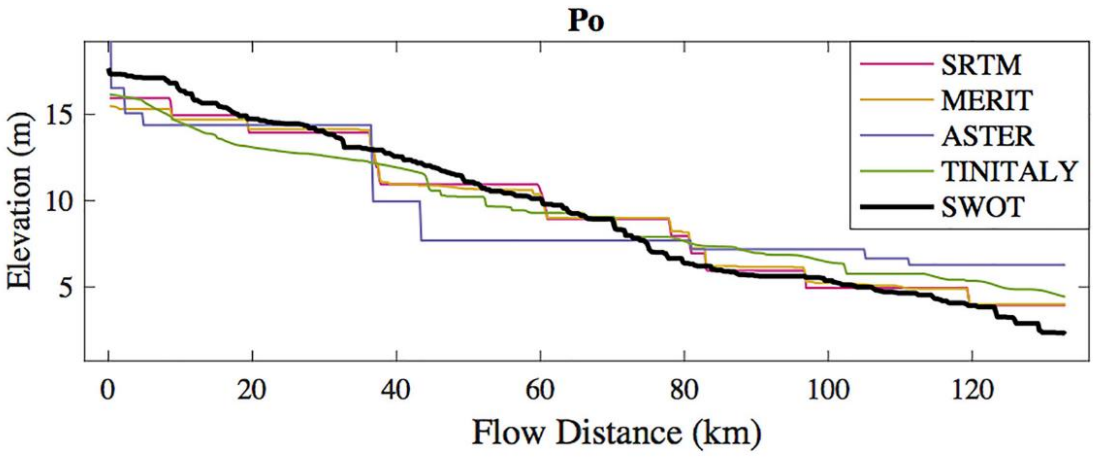

Figure 2-10. Comparison of water surface profiles from different DEMs and simulated SWOT data along a reach of the river Po, Italy. From Langhorst et al. (2019).

In light of these shortcomings of the bank-full discharge subtraction method, it is not surprising that explicitly including channels has been shown to be crucial to the ability of a hydraulic model to simulate large-scale hydrodynamic process such as floodplain dynamics (Neal et al., 2012; Sampson et al., 2015). In order to do so, a considerable number of recent studies have employed various methods of estimating bathymetry on large rivers, including the Zambezi (Schumann et al., 2013), the Niger (Fleischmann et al., 2018), and the Congo (O'Loughlin et al., 2020).

Typically, estimation of bathymetry entails calculation of depth based on remotely observed river geometry such as channel width or upstream drainage area, and an assumed generalised channel shape such as a rectangle, triangle, or a parabola (e.g. Neal et al., 2015). For example, Sampson et al. (2015) present a method of estimating bathymetry designed for application in a GFM. They calculate channel depth from a bank full discharge (assumed equal to a 1 in 2 year return period), a longitudinal slope measured from a DEM, an assumed hydraulic roughness parameter, and uses manning's equation, thereby assuming uniform flow conditions. When implemented, the

model showed a clear improvement in performance compared with models with no channel representation. Neal et al. (2012) developed a similar method, designed for application over large and data sparse areas. They modelled the hydrodynamics of an 800 km reach of the river Niger in Mali with no bathymetry data, by representing bathymetry with two parameters to be calibrated, alongside the hydraulic roughness coefficient. Dynamic WSE and flood extent data are used as model calibration data, and there is no requirement to estimate discharge or assume uniform flow conditions as is the case for the approach of Sampson et al. (2015). Whilst the model showed significant improvement compared to a model without channel representation, the authors concluded that a major inaccuracy in the model's simulation of WSE was due to the use of a global parameterization of the main channel (i.e. assuming the same channel parameters across the entire 800 km model domain).

There are a number of challenges associated with estimating bathymetry. Among these is the joint estimation problem associated with treating both friction and bathymetry as unknowns (Bates et al., 2014). By examining the Manning formula for uniform flow conditions (written in section 2.3.2), it can be seen that the bathymetric component AR trades off against Manning's n such that a whole series of $n-AR$ combinations will provide the correct value of Q. In the context of hydraulic modelling, this means that modelled WSE along a channel may closely match observed values with a channel bed elevation that is represented, for example, as being lower than reality, but is compensated for by increasing the flow resistance, thereby increasing the depth of the flow conditions so as to elevate WSE to the observed value. However, the deep flow conditions result in lower modelled water velocities and an incorrect representation of the speed at which the flood wave travels along the river. Neal et al. (2015) quantified this along a 30 km reach of the River Severn (a mid-size river) in the UK, finding that inflation of Manning's n by 0.015–0.02 in order to compensate for error in channel geometric representation resulted in a delay in flood wave arrival time of 17%. Over longer reaches, the cumulative negative effect of friction on flood wave travel will increase.

Models that estimate bathymetry to simulate the hydrodynamics of large river floods often continue to rely on relatively inaccurate DEM elevations (see Figure 2-10) as a reference from which to subtract an estimated channel depth in order to derive river bed elevation (e.g. Fleischmann et al., 2018). This is increasingly being resolved by using more accurate longitudinal WSE profiles afforded by satellite altimeters (see section 2.3.5). For example, Schneider et al. (2017) used CryoSat-2 WSE information to calibrate modelled channel bed elevations along the Brahmaputra River in Bangladesh,

India and China. A similar approach is also being used in models developed to estimate bathymetry and thereby discharge. In anticipation of the data that SWOT will provide (see section 2.3.6), discharge estimation models seek to utilise remotely sensed dynamic observations of river water surface width, elevation, and slope, to estimate bathymetry and thereby discharge by solving some variant of the Manning formula. Durand et al. (2016) conducted a thorough review of discharge estimation algorithms by testing different algorithms on approximately 20 medium to large rivers, and found over 80% of the single channel rivers estimated discharge within 35% relative root mean square error. Errors were greater on multichannel rivers however, due to use of the gross simplification of the channel geometry to an effective single channel that is necessary to estimate bathymetry.

The apparent necessity of simplifying river channel geometry information for input into hydrodynamic models of large rivers, whether due to a lack of observational data or use of coarse spatial resolution to manage computational resources, remains a key limitation of these models. The methods that are employed to derive the data and the simplified channel geometries that are adopted remain poorly validated: the performance of many channel simplification methods have been assessed simply by comparison with another model that has no channel representation, in order to demonstrate improvement. Moreover, validation using observed data has mostly involved comparing modelled and observed WSE or flood extent, which are a product of multiple sources of error (e.g. floodplain topography, hydrological uncertainty) and therefore do not isolate the bathymetric error. Compounding the significant sources of model uncertainties (discharge, topography, hydraulic roughness, flood extent) with bathymetric uncertainty may not always be a reasonable or defensible approach when bathymetric observations can be obtained, albeit spatially sparse observations that do not conform to traditional bathymetry input data requirements such as those put forward by Samuels (1990).

Very few studies have looked specifically at the effect of simplifying bathymetry on the modelled hydraulics of large rivers using observed bathymetry data. The efforts of Trigg et al. (2009) on the Amazon and (Altenau et al., 2017a) on the Tanana are rare exceptions that have been discussed. Dey et al. (2019) recently assessed the effect of different bathymetric representations on 1-D hydraulic model simulations of four rivers with varying geomorphologic characteristics, and draw the following generalised conclusions: (1) bathymetry must accurately represent channel cross sectional area and channel volumetric storage; (2) in the case of mapping flood extents, any channel shape may be assumed, because accurate in-channel velocity is not essential in this case; (3) the need for accurate modelled in-channel velocities introduces an additional

requirement to represent channel shape in an accurate manner such that the thalweg and wetted perimeter are well represented. These conclusions are not necessarily applicable to large rivers however, as they are based on experiments applied to relatively short reach lengths (10 - 60 km) of small to medium single channel rivers (2–100,000 km^2 drainage area).

2.5 Concluding Remarks

Large rivers can be characterised as having very low water surface gradients (~10 cm/km or less), low Froude numbers (~0.3 or less), very high channel width to depth ratios, and complex multithreaded channel planform patterns. Modelling the hydrodynamics of large rivers can inform many important earth science and development issues, perhaps the most prominent of these being the exposure of populations to flood risk in a changing climate. Flood risk aside, the hydrodynamic processes occurring along large rivers are a key determinant of globally important biogeochemical processes such as the outgassing of carbon dioxide and methane, and maintain some of the world's most biologically diverse and productive ecosystems. In this context, wetlands that interact with large river systems are particularly noted for being biogeochemical and ecological hotspots. Large rivers enable inland water navigation, which is an important and sustainable form of transport across large remote regions often lacking land transport infrastructure. Hydrodynamic modelling is a prerequisite of many sediment dynamics studies, and can also inform the infection dynamics of water related diseases.

In recent years hydrodynamic modelling of large rivers has become increasingly employed in order to exploit the growing number of globally available remotely sensed observations of flood extent, water surface elevation, and terrain data, especially for the purposes of estimating river discharge in light of the continuing decline of in-situ flow gauging. This has resulted in the development of modelling methodologies that are specifically designed for large rivers in remote regions, where in-situ data is absent or limited, but SRS datasets are plentiful. These modelling methodologies manage computational resources by solving efficient approximations of the SWEs that assume the acceleration terms of the momentum equation are negligible – an assumption shown to be widely applicable to large rivers with Froude numbers less than ~0.3. Moreover, sub-grid representations of channels and floodplain topography enable large spatial resolutions to be adopted without significantly compromising the representation of hydraulic processes. These methodologies have significant potential for application globally as new SRS water surface elevation and extent datasets become available. However, such methodologies have a number of unresolved deficiencies, one of which is the representation of bathymetry. The difficulty is the result of a lack of pre-existing

large river channel bathymetry data, the onerous nature of obtaining new bathymetry data, particularly on multithreaded channel systems that prevail in large rivers, and also the non-trivial task of spatially interpolating bathymetry data on multithreaded channels. Large river hydrodynamic modelling methodologies circumvent this data gap by parameterising bathymetry with one or two parameters, and treating these parameters as variables to be estimated and calibrated alongside hydraulic roughness. Calibration involves adjustment of the bathymetry and roughness parameters to fit the modelled water surface to SRS observations of WSE and / or extents.

Several studies have demonstrated the efficacy of this approach, by showing there to be significant improvement upon models that do not represent river channels, or through validation of modelled WSE, extent or discharge, with observed data. There is no doubt that the approach is a valuable tool for hydrodynamic modelling and exploiting SRS datasets, but there is considerable room for more detailed investigation into the performance of the approach in order to improve it. Geometric simplification of the river as a single channel, with a uniform shape, and with a depth and width that is uniform over relatively long reaches, will result in significant misrepresentation of local channel depth, width, slope, and therefore hydraulic processes. Moreover, a lack of hydraulic process representation will result from with neglected morphological features such as bifurcations and mid-channel islands. Thus, the modelled channel hydraulics are likely to be unrepresentative of reality. Whilst calibration schemes can be used to ensure modelled WSE or extents fit observed values by locally adjusting hydraulic roughness in a way that compensates for the bathymetric representation, the modelled channel hydraulics will remain erroneous, and consequently the model will not maintain its performance across its spatial and temporal extents.

Research into improving simplified bathymetric representation approaches could involve investigation of how particular bathymetric simplifications affect modelled channel hydraulics, and thereby identification of simplified representations that preserve channel hydraulics when adopted in place of a bathymetry that is geometrically more representative. This would be of value on large multichannel systems in particular. It would also be useful to investigate the inclusion of spatially sparse measurements of large multichannel river bathymetry in a model, which may not satisfy traditional hydraulic model requirements, but can feasibly be collected on a scientific field campaign. Such measurements could reduce bathymetric uncertainty, and therefore reduce reliance on calibration data such as flood extents which themselves may be highly uncertain or unobservable in environments such as wetlands.

CHAPTER 3

Hydrodynamic Research on the Congo River

3.1 Background

The Congo River is a large tropical river located in Central Africa. Its drainage basin, shown in Figure 3-1, occupies 12% of the entire African continent and straddles the equator, thus occupying significant parts of both the northern and southern hemisphere. No less than nine countries are situated partly or entirely within the basin, with parts of the mainstem and several tributaries forming international borders.

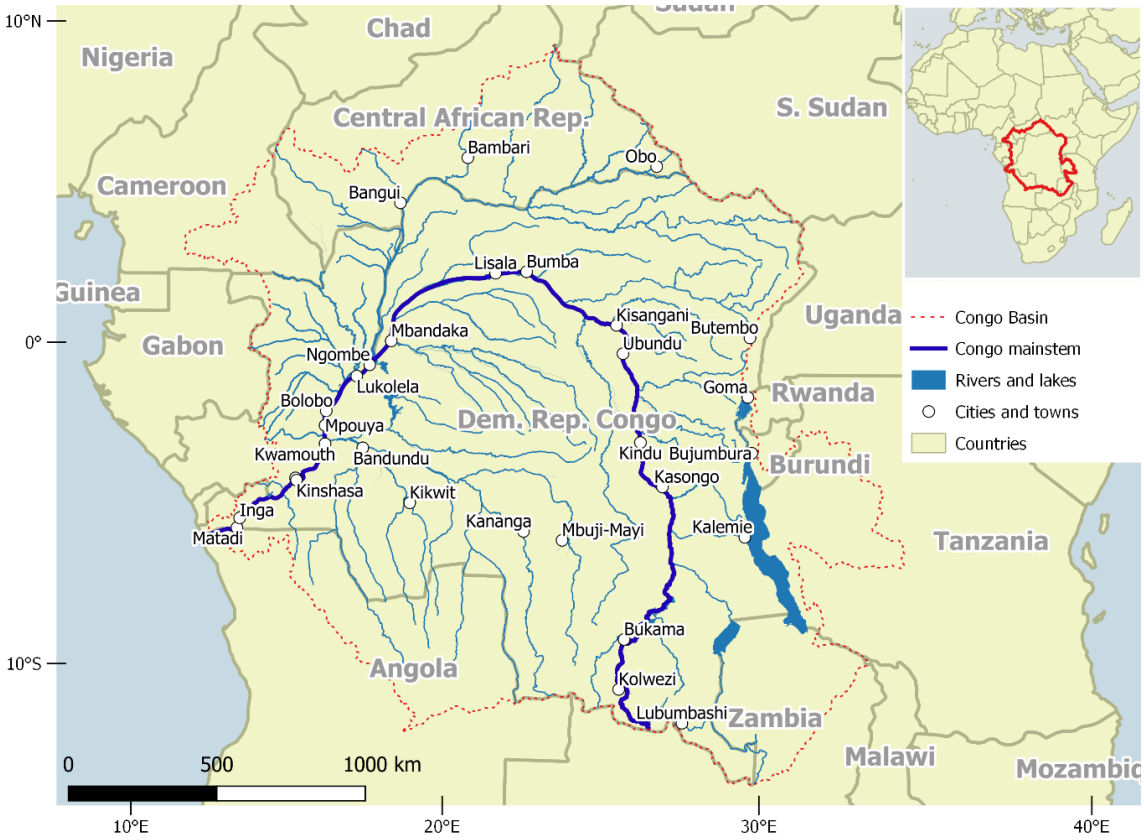

Figure 3-1. The Congo River Basin (CRB), major rivers, cities and countries. Major rivers from O'Loughlin et al. (2013), and CARPE (2017).

Across all metrics of river size, the Congo River ranks near the top of the list of rivers globally. According to Ashworth and Lewin (2012), the Congo ranks second globally by mean annual discharge, catchment area, and channel width. Key river size descriptors for the Congo and comparable rivers are shown in Table 3-1, data for the UK's largest river – the Severn, are also included for scale.

Table 3-1. Discharge, Catchment Area, and channel width Information for the five largest rivers globally (by discharge), all data for these rivers taken from Ashworth and Lewin (2012). The UK's largest River by discharge, the Severn, is also shown for scale, data taken from Centre for Ecology and Hydrology, (2019). Discrepancies between these discharge statistics and those listed in Table 2-1 are explained by measurement errors, long term variability in discharge, and different approaches in accounting for river regulation.

River	Mean annual discharge (m^3/s)	Catchment area (10^6 km^2)	Typical channel width (km)
Amazon	198,100	6.0	2.5
Congo	41,000	3.7	5
Orinoco	34,500	1.0	2.6
Yangtze	27,700	2.0	2.5
Brahmaputra	18,200	0.6	12
Severn	100	0.01	0.06

The Congo River is known for being relatively pristine. Runge (2007) notes that a lack of industrial and agricultural development in the Congo Basin keeps the Congo River relatively unpolluted. Spencer et al. (2016) remarks that the Congo has far fewer dams in comparison to other tropical watersheds such as the Amazon or Mekong and is thus the most pristine major tropical watershed on Earth. Moreover, Grill et al. (2019) showed that the Congo is one of the least modified large rivers on earth according to their assessment of the global distribution of free flowing rivers.

Within the field of hydrologic research, the Congo River is one of the least studied large rivers on earth. By comparing numbers of peer reviewed publications, Alsdorf et al. (2016) asserts that contemporary understanding of the Congo River Basin (CRB) and its hydrology is about an order of magnitude less than that of the world's largest river – the Amazon. A severe lack of contemporary data for fundamental variables such as river discharge (Tshimanga and Hughes (2014), also see Figure 2-1 in subsection 2.2.5) and river channel bathymetry (O'Loughlin et al., 2013; Alsdorf et al., 2016) on the Congo largely explains this lack of research. The scarcity of data is a symptom of the remoteness and large size of the Congo River, and the political instability that has

plagued the region over the last three decades. However this is beginning to change, as researchers are able to make use of SRS data that continues to increase in coverage and resolution, and the CRB region shows signs of improving political stability and security (e.g. United Nations, 2019). This chapter introduces the CRB, identifies the key scientific questions in the CRB that hydrodynamics can inform, and reviews the current knowledge on Congo River hydrodynamics. The intention is to identify opportunities for original research into the hydrodynamics of the Congo River, which can potentially inform wider earth science and hydrologic questions in the CRB, and also hydrodynamic modelling of large rivers generally.

3.1.1 Upper, Middle, and Lower Mainstem Reaches

The Congo River system comprises three distinct reaches: the upper Congo, middle Congo, and lower Congo. The upper Congo, also known as the Lualaba originates in the southeast of the DR Congo near the border with Zambia, at an altitude of roughly 1500 m, and ends at Kisangani. Downstream of Bukama, the upper reach has a relatively low longitudinal gradient (average 12 cm/km according to Robert, (1946)), but features several steep sections of river including the gorge known as Portes d'Enfer near Kasongo, and Boyoma Falls near Kisangani. Therefore only discrete sections of this reach can be navigated by boat. The navigable reaches are also limited to small vessels and become unpassable during the low flow season according to the International Commission of the Congo-Oubangui-Sangha Basin (CICOS, 2015). The reach is predominantly single channel and runs for approximately 2000 km (Runge, 2007).

The Congo Middle Reach (CMR) runs from Kisangani to Kinshasa, occupies the central CRB, and passes through the Congolian rainforests, the second largest rainforest in the world covering an area of approximately 2 million km^2 (Laporte et al., 1998). Figure 3-2 shows a detailed topographic map of the central CRB, and the CMR and its key tributaries. Land cover in the central CRB is dominated by dense tropical evergreen forest, flooded forests, and inundated grasslands (Bwangoy et al., 2010). Through this reach, the mainstem and its tributaries drain a region known as the Cuvette Centrale (which translates to ‘shallow bowl’), a shallow depression occupying the central CRB. The Cuvette Centrale region contains a very large wetland area, the extents of which are shown indicatively in Figure 3-2. The combined area of these wetlands is uncertain: Hughes and Hughes (1992) estimate 190,000 km^2, whereas Bwangoy et al. (2010) estimate 360,000 km^2, but both figures place them fourth in the list of the world’s largest wetlands (Keddy et al., 2009). There are no steep sections of river through the CMR, and the reach is navigable throughout the whole year (CICOS, 2015). The river channel

is almost entirely multithreaded with many large vegetated mid channel islands, and is very wide – measurements from satellite imagery by O'Loughlin et al. (2013) indicate average effective width is in excess of 5 km. Along its ~1700 km length, the CMR accumulates the vast majority of the total Congo river discharge, with contributions from many large tributaries that drain the rainforest and the wetlands, and are also widely navigable. The Oubangui and Kasai are the two largest of these tributaries, with catchment areas of approximately 645,000 km^2 and 890,000 km^2 respectively (Alsdorf et al., 2016). Approximately 270 km upstream of Kinshasa where the mainstem exits the Cuvette Centrale, there is a marked change in channel planform, the channel becoming single thread and ~2 km wide along a 200 km section known as the 'Chenal'. As the river approaches Kinshasa its planform changes again, exhibiting a lake-like widening of the channel known as the Malebo Pool. The downstream end of this pool marks the end of the CMR, and the start of the lower Congo River.

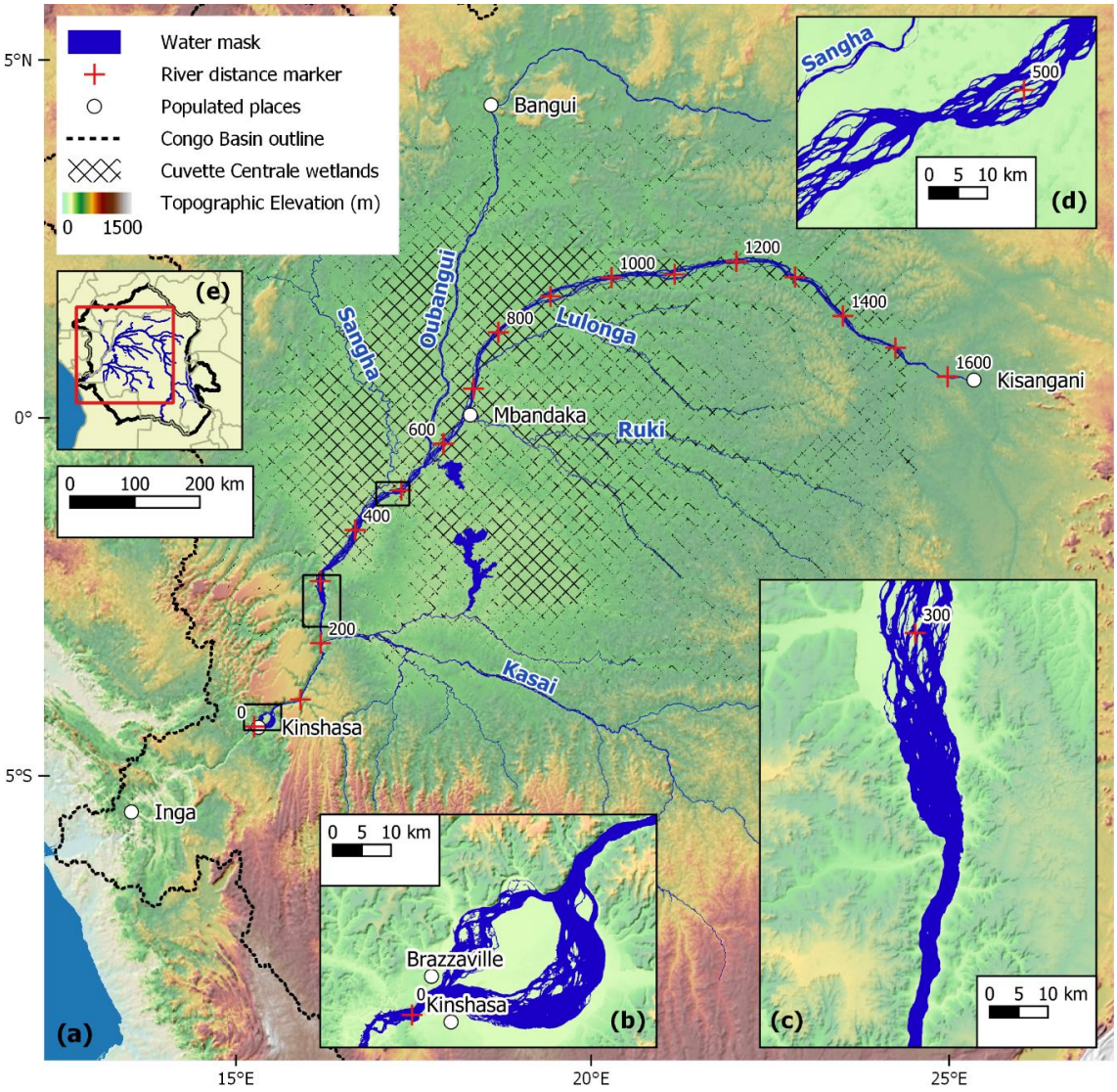

Figure 3-2. (a) Map of the central Congo River Basin showing the Congo Middle Reach (CMR) and key tributaries; (b) Malebo Pool; (c) Start of the Chenal; (d) One of the constrictions; (e) Location plan. Topography data is from MERIT DEM (Yamazaki et al., 2017), water mask is from Landsat data (O'Loughlin et al., 2013), and Cuvette Centrale wetlands extent is from the global tropical wetland distribution map produced by Gumbricht et al. (2017). River distance is measured from outlet of Malebo Pool along a channel belt centreline.

The 500 km long lower Congo has a remarkably steep gradient (approximately 50 cm/km on average) and comprises numerous falls and rapids, making it more characteristic of a mountain headwater stream than the lower course of a large river. This is a result of the Congo's geological history. The uplift of the Atlantic Rise mountain range that runs between the Atlantic Ocean and the Cuvette Centrale (see Figure 3-2) resulted in the Congo River becoming dammed, and the creation of a the Congo Lake

during the Pliocene geological period. The natural dam landform was subsequently breached at the downstream end of Malebo Pool, and the lake was drained in a single, highly energetic geomorphic event (Runge, 2007). The combination of steep gradients and very large discharge along this reach gives rise to one of the deepest documented sections of river in the world (Jackson et al. (2009) measured over 160 m deep in places), and huge potential for hydroelectric power generation – the Inga site alone is estimated to have a potential generating capacity of 40 GW (World Bank Group, 2014; Société nationale d'électricité, 2014).

This thesis focuses specifically on the hydrodynamics of the CMR for several reasons as follows. The CMR presents many research opportunities associated with the hydrodynamic functioning of the Cuvette Centrale and the criticality of fluvial navigation along its channel system. Moreover, the distinctive multithread channel system of the CMR is an example of a channel pattern that poses unique challenges for hydrodynamic modelling, and advances in this regard have the potential to inform hydrodynamic modelling of multichannel systems generally. Additionally, from a practical standpoint, the navigability of the CMR means it is more accessible for obtaining in-situ measurements that are likely to be crucial to the advancement of hydrodynamic research in the CRB.

3.1.2 Basic Hydrology

The climate of the CRB is warm and humid, with a mean temperature of approximately 25 °C and a difference of only 2 °C between the warmest and the coldest months (Bultot, 1977). The average rainfall is about 1800 mm per year in 115 days. The Congo River is the only large river in the world to cross the equator twice, and as a result a substantial part of the CRB is always experiencing the rainy season, giving rise to an average annual downstream hydrograph that is highly damped (Flügel et al., 2015). Seasonal variation in downstream flow is therefore very low: (Wohl, 2007) quantifies this by comparing the coefficient of variation in mean monthly flow for a selection of large rivers including the Congo, shown in Figure 3-3. This shows the Congo's annual variability in flow to be approximately half that of the Mississippi, and considerably less than that of the Amazon River.

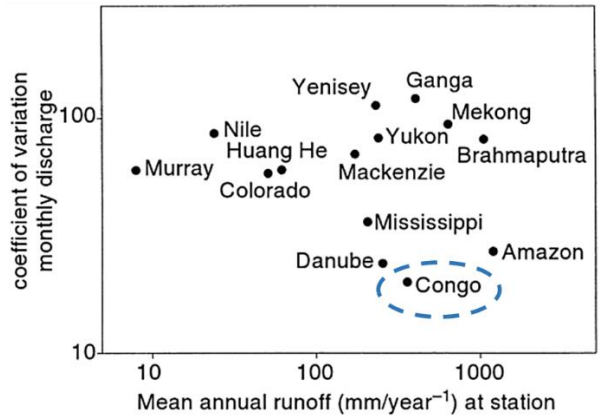

Figure 3-3. Coefficient of variation in monthly discharge versus mean annual runoff for selected large rivers, as an indicator of annual discarge variability (Wohl, 2007).

The main rainy season occurs in the northern sub-basins from July to October, and in the Southern sub-basins from December to March, according to the seasonal movement of the tropical rainbelt (Alsdorf et al., 2016). The flows generated in the northern and southern sub basins are sufficient in magnitude to produce two distinct downstream flood peaks annually, as shown in Figure 3-4. The main flood peak arrives from November to January, and results from the northern sub-basins, particularly the Oubangui. A second, smaller peak then occurs from April to June, generated by the southern sub basins (Runge, 2007).

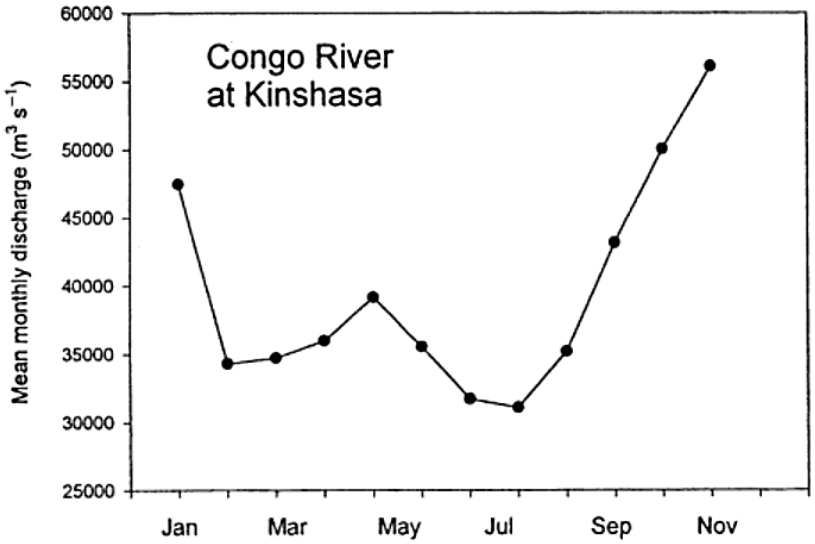

Figure 3-4. The bimodal average annual hydrograph at Kinshasa. Main peak occurs between November and January, seconary peak occurs between April and June. From (Wohl, 2007).

Historical discharge data at Kinshasa shows the Congo's mean annual discharge is relatively consistent inter-annually, which is unsurprising given the location of the CRB with respect to the equator, and the humid tropical climatic zone occupying the centre of the basin (Latrubesse et al., 2005). However, the results presented by Laraque et al. (2001) show a period of significant inter-annual variability in discharge at Kinshasa from the 1960s to the 1990s. As shown in Figure 3-5, they found that discharge was 20% above the long term mean in the 1960s, and was followed by a 5% drop below the long term mean from 1982 to 1993. Analysis of the most recent data has shown discharge measurements from 1996 – 2017 are close to the overall mean annual discharge, indicating a renewal of runoff from 1990 onwards, after almost 15 years of deficit (Laraque et al., 2020). The Oubangui tributary is believed to be largely responsible for this period of high inter-annual variability in discharge, having itself experienced a reduction in discharge of 36% from 1982 to 2013.

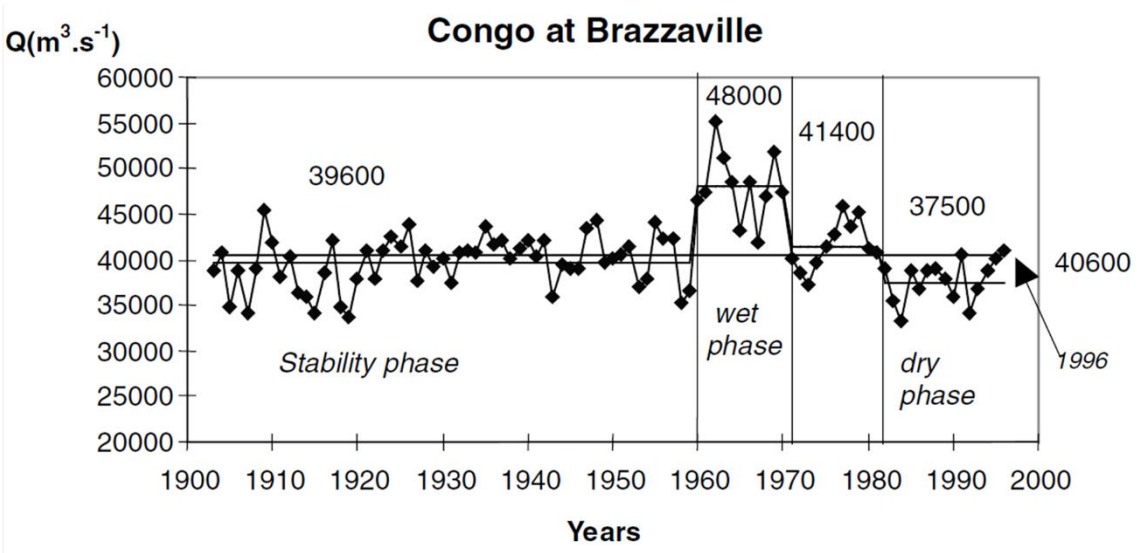

Figure 3-5. Long term annual average discharge at Kinshasa (Brazzaville) showing considerable inter-annual varibility from 1960 - 1993. From Laraque et al. (2001).

Similar to the annual flow amplitude, the flood wave amplitudes along the mainstem and its main tributaries are relatively small in the central CRB. Becker et al. (2014) used ENVISAT satellite altimetry data from 2003 to 2010 to derive river WSE variations within hydrologically similar sub-catchments. Key results, displayed in Figure 3-6, show that average annual amplitude in WSE along the mainstem is approximately two metres between Kisangani and the Oubangui (Figure 3-6b), and increases to three metres downstream of the Oubangui (Figure 3-6c). The amplitude is shown to be four metres along the Oubangui (Figure 3-6d) and two metres along the Kasai (Figure 3-6e). Flood wave amplitudes of similar sized rivers globally are generally larger than this: both

the Amazon and Orinoco rivers have flood wave amplitudes of up to 12 metres (Trigg et al., 2009; Frappart et al., 2015), and Schneider et al. (2017) showed the lower Brahmaputra flood wave amplitude is approximately eight metres.

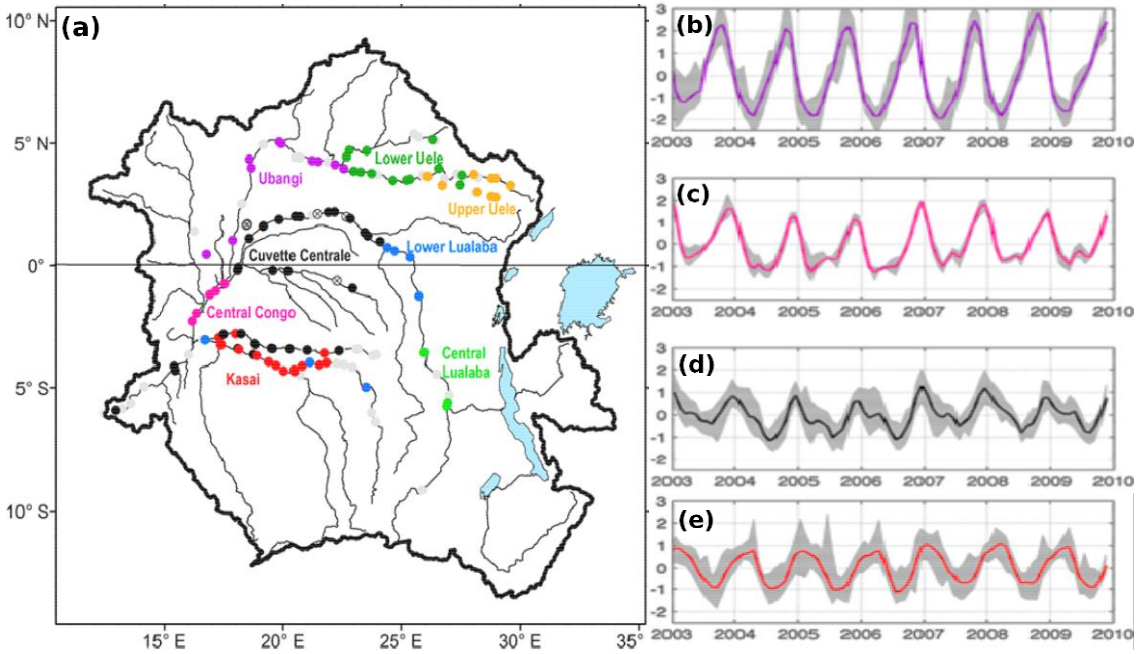

Figure 3-6. Water level fluctuations spatially averaged over major sub-basins of the CRB, from Becker et al. (2014): (a) Plan showing locations of ENVISAT altimetry WSE measurement locations, colour coding indicates sub-basin groups and matches the time series plot colours; (b) Oubangui WSEs; (c) Central Congo WSEs; (d) Cuvette Centrale WSEs; (e) Kasai WSEs. Upper reaches and tributary sub-basins omitted for clarity. X and Y axes of (b) to (e) are time (year) and WSE fluctuation (m) respectively, grey envelopes show 5% and 95% quartile of the mean.

The main annual flood peak does not usually represent a particular environmental risk to people, as inhabitants are well adapted to the predictable seasonal floods. Rather, the deposition of fish and sediment onto the floodplains during the seasonal flood provides a crucial role in regional food security (Comptour et al., 2016; Comptour et al., 2020). However, the impacts of more extreme, low probability flood events that have occasionally occurred on the mainstem and its key tributaries have resulted in significant human fatalities and economic losses (Tshimanga et al., 2016). The positive and negative impacts of mainstem floods are reviewed in more detail in section 3.2.

Hydrodynamic Data

The scarcity of in-situ hydrological data in the CRB is an issue frequently raised by researchers studying the CRB hydrology and hydrodynamics. Tshimanga and Hughes (2014) remark that the lack of adequate data to support hydrological predictions represents serious constraints to water resources assessment and sustainable management in the CRB. Progress in CRB hydrological research has been much slower than for the Amazon Basin, largely due to the lack of in situ data (Lee et al., 2015).

In their review of CRB hydrologic research, Alsdorf et al. (2016) present a useful account of the status of CRB hydrologic measurements that includes discharge, bathymetry, WSE, and water extent data. With respect to discharge, the basin used to be relatively well gauged: prior to the 1960s there were over 400 operational flow gauges. As of 2010 there were only 10 operational flow gauges in the basin (Croneborg, 2013), and flow data after 2010 is only available for one gauge located at Kinshasa / Brazzaville, courtesy of SO-HYBAM (Institut de recherche pour le développement, 2019). Information on the bathymetry of the CMR and its tributaries is scarce. In their review, Alsdorf et al. (2016) reference Marlier (1973) and Stanley (1885), who respectively report that depths through the Chenal are 23 m to 30 m, and 11m to 12m. Marlier (1973) also notes that throughout the navigable portions of the CMR, depths rarely exceed 15 m, and at lower water depths are often less than 2.5 m.

Contemporary hydrologic and hydrodynamic research in the CRB is benefiting increasingly from SRS measurements of WSE, and to a lesser extent, water extent. Satellite altimetry is able to measure WSE on the mainstem and many tributaries (see Figure 3-6 above for example of the use of ENVISAT altimetry data). ENVISAT is one of several satellite altimeters that has measured WSE in the CRB, and data for all these altimeters is now publically available from web-based services such as the Hydroweb database (see for example, Santos da Silva et al. (2010)). This database provides time series data of WSEs on rivers and lakes for up to 10 years, at over 500 locations in the CRB, over 80 of which are located on the CMR (see Figure 3-7). Hydroweb provides processed data including the total number of measurements and standard deviation of each overpass for the following altimeters: ENVISAT, Jason-1, Jason-2, and Sentinel-3A, all of which are described within Table 2-4 in subsection 2.3.5.

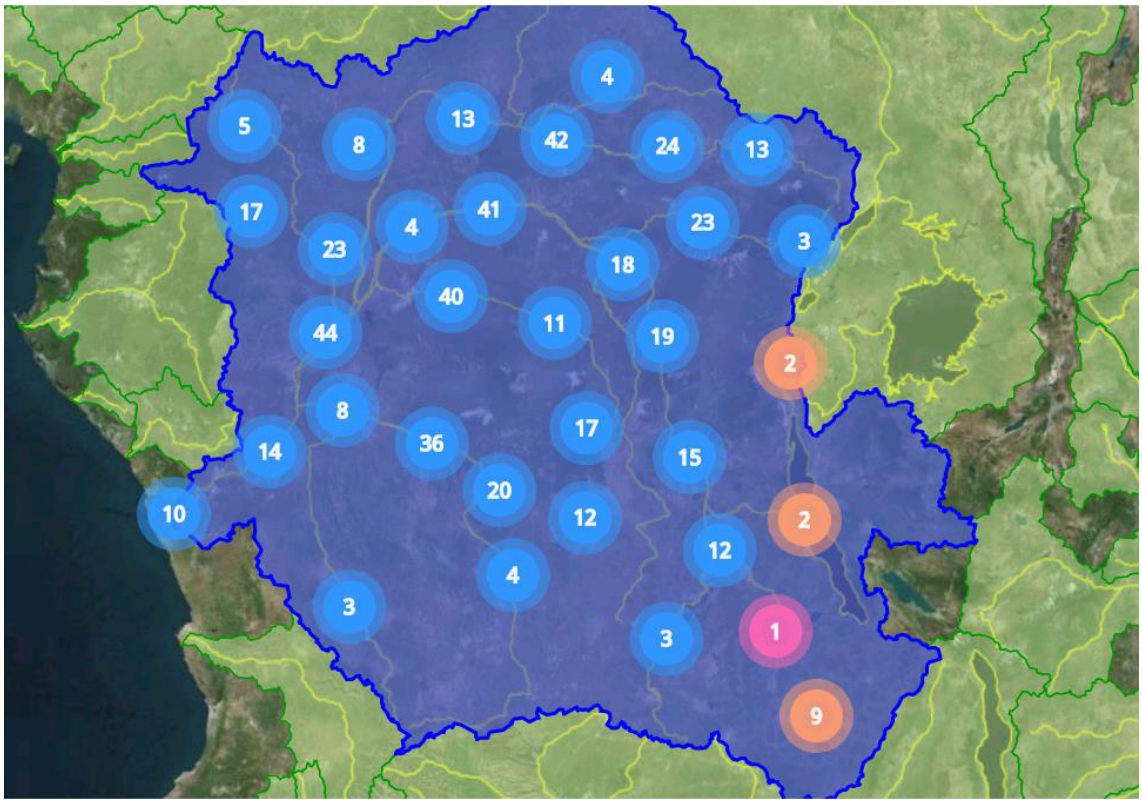

Figure 3-7. Map of the CRB showing the number of overpass locations by altimeters (i.e. number of locations where time series data of river and lake WSE is available). From the Hydroweb database, accessed at: http://hydroweb.theia-land.fr/?lang=en&basin=CONGO.

Information on water extents and their spatiotemporal variability derived from SRS is limited compared to WSE. The use of optical imagery to map extents specifically within the CRB (i.e. excluding global mapping initiatives such as the work of Pekel et al. (2016)) has been limited to permanent water bodies (large river channels and lakes mapped by O'Loughlin et al. (2013)), and the probabilistic assessment of wetland extents by Bwangoy et al. (2010). Analysis of microwave imagery has produced higher resolution information, and has been used to good effect in mapping floodwaters with emergent vegetation, which is the predominant type of flooding in the CRB (Alsdorf et al., 2016). Lee et al. (2015) complemented ALOS PALSAR images with satellite altimetry and the MODIS Vegetation Continuous Fields classification product to produce water extent and depth maps in the flooded forests adjacent to CMR. These maps were produced during high water conditions in December 2006, 2007 and 2008, and have a spatial resolution of 100 m. As shown in Figure 3-8, differences in depth and extent can be seen between each year. Whilst the maps are estimates based on a linear regression model, and subject to significant uncertainty having not been ground truthed, the resulting estimates of absolute floodplain water storage volume showed reasonable agreement with a

separate study that used interferometric SAR (Yuan et al., 2017). They have some potential to be used for calibration and validation of a hydrodynamic model.

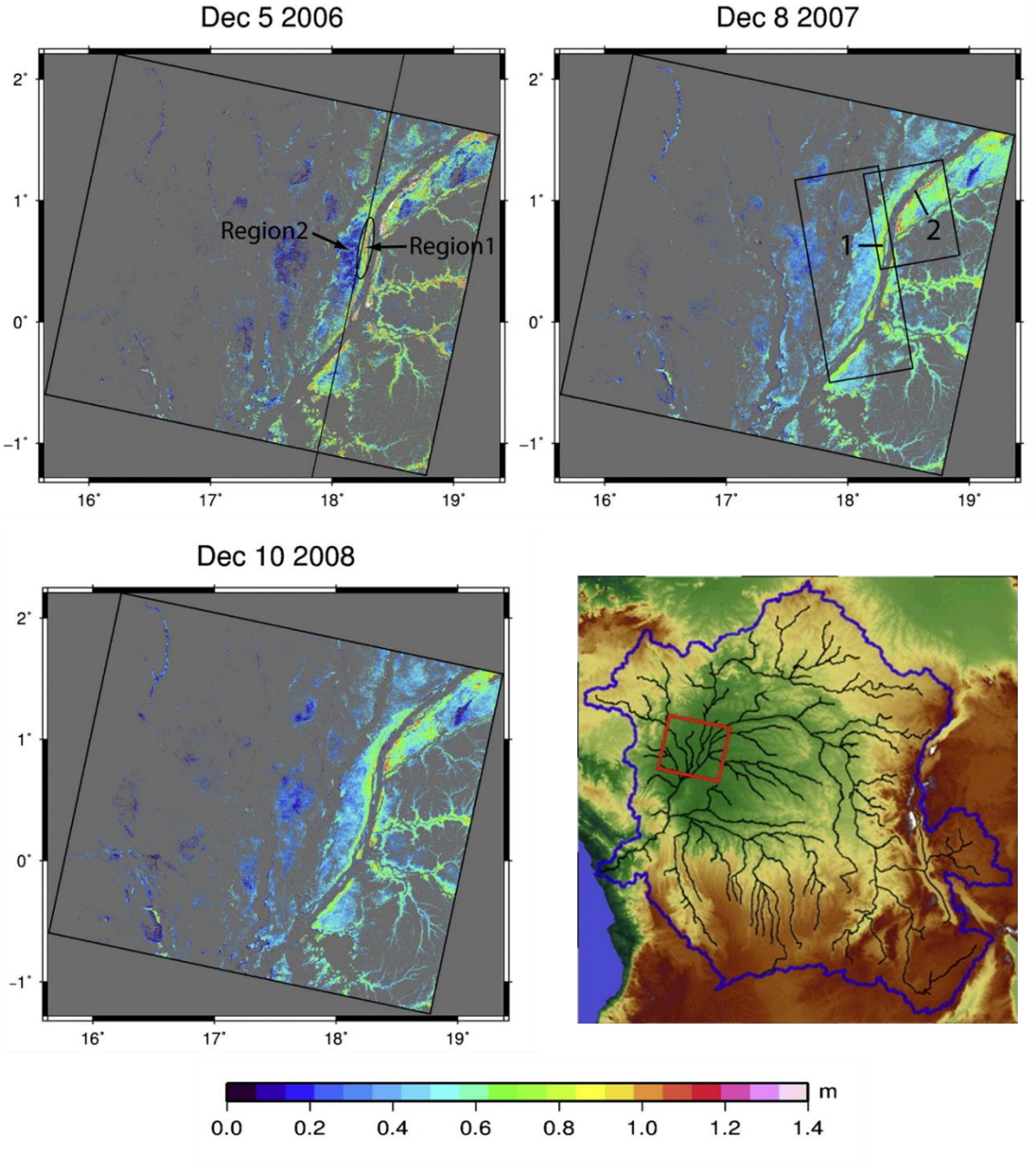

Figure 3-8. Estimates of flood extents and depths in flooded forests along the CMR, using microwave satellite imagery, altimetry, and the MODIS Vegetation Continuous Fields classification product. From Lee et al. (2015).

3.2 Hydrodynamic Issues of Regional and Global Importance

3.2.1 Flooding: Impacts on People Inhabiting the Central CRB

Positive Impacts

Seasonal flooding of the CMR provides a crucial service for the inhabitants of the region. For example, Comptour et al. (2020) provide a detailed account of the flood-recession agriculture (i.e. the cultivation of seasonally flooded land during the dry season) that is practised in the Cuvette Centrale region. The waters of the mainstem and tributaries such as the Oubangui have relatively low acidity and considerable concentrations of sediments, which provide relatively fertile soils on the islands and floodplains that are seasonally flooded. In contrast, large parts of the Cuvette Centrale are inundated primarily by 'blackwater' tributaries such as the Likouala Aux Herbes River or by rain water, giving rise to a soil that is characterised by strong acidity and lower fertility. Comptour et al. (2020) showed this by comparing soil samples from mainstem islands with samples from the floodplain at the confluence of the mainstem and Likouala Aux Herbes River, finding the islands soil properties were more suitable for agriculture; being lighter in texture, having less clay and more sand, more phosphorous, and lower carbon-nitrogen ratios. These more fertile soils are essential for the widespread cultivation of important and versatile primary staples such as cassava.

Fish account for a significant part of animal protein and are a primary source of cash income for rural households in the central CRB (Trefon, 2016). Fishing methods in the CRB are diverse and have been adapted to exploit the inundation dynamics in the basin. Pond fishing is an example of a method that is widespread in the Cuvette Centrale region and is highly dependent on flooding. As water recedes from the floodplain, some fish species that are well adapted to wetland and swamp conditions will seek refuge in the inundated areas of forest that remain. Pond fishing entails the capture of these fish, in some cases by emptying the inundated area by manually scooping water out, or draining water through the removal of man-made bunds (Comptour et al., 2016). The inundated areas may occur naturally or be of human origin, and deliver a great amount of fish both for self-consumption and income generation.

Flood Risk to People

Whilst the seasonal floods that occur along the Congo's mainstem and key tributaries are regarded mainly as being of benefit to inhabitants, high magnitude flood events that are more extreme than the typical seasonal flood are known to have presented a major risk to human life and caused significant economic damage in the central CRB (Tshimanga et al., 2016). The 1999 floods are reported as being the most

severe, but information on this event appears to be limited. The Global Active Archive of Large Flood Events (Brakenridge, 2019) report that 75,000 people were displaced, DR Congo suffered 30 million USD of economic damage, and that Kinshasa, Brazzaville and Bandundu were the most affected population centres. The archive calculates the magnitude of the flood as number 47 out of a total of 3,700 events globally, this magnitude being calculated as the product of the duration, severity, and affected area. The main cause of the flood was the synchronous peaking of both the northern and southern sub-basins, itself caused by unusual rainfall patterns (i.e. heavy prolonged precipitation in both the northern and southern sub-basins). The floods of 1961-62 and 1903 are also noted as being particularly severe, but there is little scientific or journalistic documentation of these flood events.

The most recent annual flood of 2019-20 has caused significant economic damage and loss of life along the Oubangui and the Congo mainstem downstream of the Oubangui confluence. Unusually high water levels were caused by increased rainfall from October to December in the northern sub-basins, particularly the Oubangui (International Federation of Red Cross, 2020). As of December 2019 an estimated 450,000 people had been affected (Emergency Response Coordination Centre, 2019), and the Global Active Archive of Large Flood Events calculates that the event magnitude exceeds the magnitude of the 1999 floods. The situation seems to be receiving more attention than previous damaging floods, with regular bulletins being released by news outlets and aid organisations that include the use of satellite imagery to map flood extents. Figure 3-9 shows an excerpt from one such map, prepared by the United Nations Operational Satellite Applications Programme (UNOSAT) using very high resolution (50 cm) Pleiades-1 satellite imagery. UNOSAT have also used other lower resolution satellite imagery such as Sentinel-1 for mapping these floods at a large scale, but with the caveat that the analysis may significantly underestimate the presence of standing waters in built up and/or densely vegetated areas due to backscattering of the radar signal.

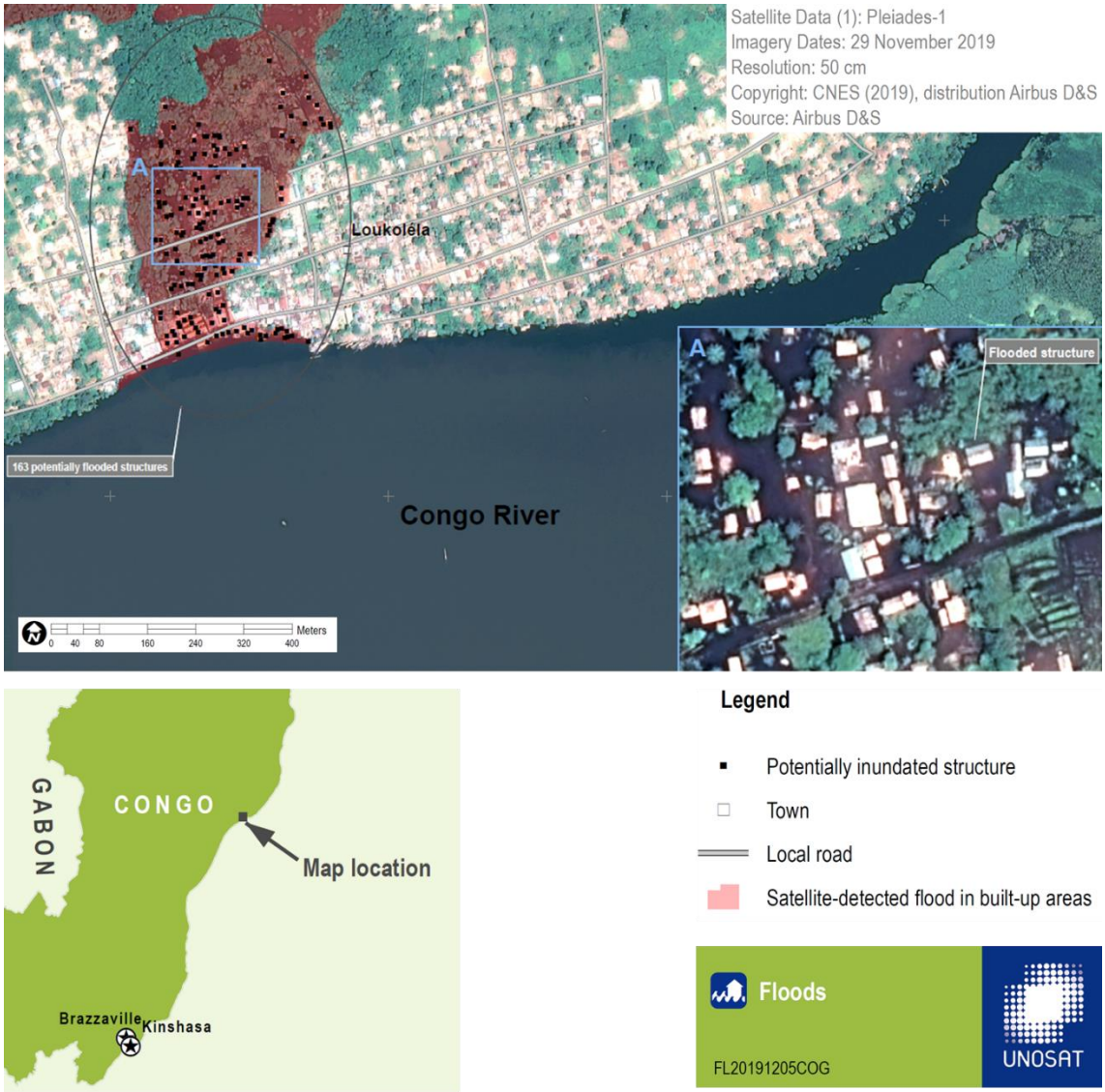

Figure 3-9. Satellite Imagery showing observed flood extents and affected building structures at Loukolela, a town on the right bank of the Congo mainstem, on 29 November 2019. From UNOSAT (2019).

3.2.2 Carbon Cycling

The wetlands of the Cuvette Centrale function as a globally significant source and sink of carbon. As a source of carbon, the wetlands are estimated to produce 0.48 ± 0.08 petagrams per year at present from outgassing of carbon dioxide and methane (Borges et al., 2015), which is approximately 8% of the current net global carbon sink from oceans and land (Friedlingstein et al., 2019). However, this outgassing estimate is based on a value of flooded surface area of 360,000 km^2, which itself is highly uncertain, being estimated from a combination of satellite imagery and SRTM (Bwangoy et al., 2010). The 360,000 km^2 value does not account for seasonal variations in flood extents, and differs

in magnitude by 47% when compared to the 190,000 km^2 value published by Hughes and Hughes (1992).

As a carbon sink, the Cuvette Centrale contains the most extensive peatland complex in the tropics. (Dargie et al., 2017) estimate the peat within the Cuvette Centrale represents total stored carbon of 30.6 petagrams, making it a considerable component of the global peatland carbon pool (Page et al. (2011) estimates this to be 480 petagrams). Potential environmental changes affecting the CRB threaten the preservation of the peatlands. Specifically, Dargie et al. (2019) cite climate and land use change, and human alterations to fluvial processes (e.g. through construction of hydroelectric facilities) as potential threats. Inundation is essential to the preservation of the peatlands; drier conditions in the peatlands or an increase in the frequency of intense dry periods could lead to an increase in decomposition rates and a loss of carbon from the peatland system. The role that fluvial flooding plays in the inundation of the peatlands is currently not well known. Dargie et al. (2017) remark that the peatland inundation may be due to poor drainage and high rainfall, and/or overbank flooding by rivers, but also suggest that they may be predominantly rain fed based on some in-situ observations of WSE. Hydrodynamic observations and research pertaining to the role of fluvial flooding in wetland inundation is reviewed in subsection 3.3.1.

3.2.3 Ecology

Brooks et al. (2011) investigated the status of freshwater biodiversity in Central Africa, noting that the Congo River has the highest species diversity of any freshwater system in Africa, and is second in species richness globally, after the Amazon. Brooks et al. (2011) also found that the richest area of species diversity is clearly defined by the channel of the Congo River and its tributaries the Oubangui River and the Kasai River. (Winemiller et al., 2016) presents fish diversity in the context of potential dam development (see Figure 3-10), noting that there are 1269 known fish species within the basin, 846 of which are endemic.

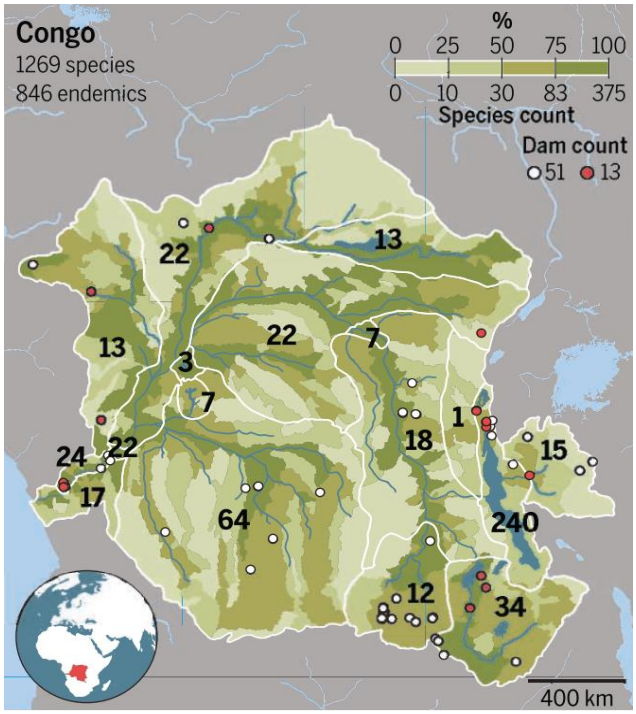

Figure 3-10. Fish Diversity in the Congo Basin, along with dams that are planned (red dot) or under construction / operation (white dot). White lines represent boundaries of ecoregions, black numbers are number of species found only in a single ecoregion. From Winemiller et al. (2016).

The high levels of diversity and endemism in the region apply to both aquatic and terrestrial species. The Central African rainforests of the Congo Basin have the greatest biodiversity on the African continent (Harrison et al., 2016), being home to over 400 mammal species, 1000 bird species, and over 10,000 plant species. The floodplains and wetlands that flank the major channel systems are likely to play a major role in this diversity, because of the important exchanges of water and nutrients that are believed to occur between the channel and the floodplain (Junk et al., 1989; Hughes and Hughes, 1992).

3.2.4 Inland Water Navigation

Due to the severe lack of road and rail transport in central Africa (e.g. Foster and Benitez, 2010), fluvial navigation on the Congo and its tributaries is the main mode of transport in the region. The most important and heavily used navigation routes in the CRB are along the mainstem, the Oubangui, and the Kasai. These routes provide vital connectivity within and between DR Congo, the Republic of Congo, and the Central African Republic (CICOS, 2015). Several other major tributaries are also widely navigable and provide some connectivity to Cameroon and Angola. The degree of navigability, as shown in Figure 3-11, varies by river and reach, according to the

minimum river depths that occur in the low and high water seasons along the established navigation route, and hence the size of vessels that can navigate.

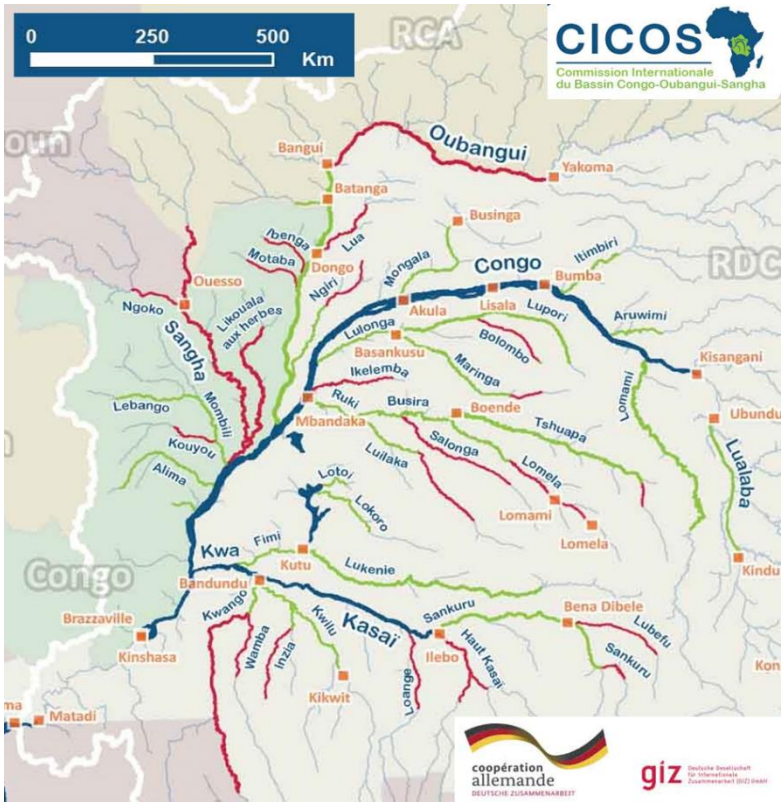

Figure 3-11. Navigable waterways and ports of the Congo Basin, from CICOS (2015). Blue waterways are first category, having a minimum depth of 2 m during high water and 1.3 m during low water. Green waterways are second category, having a minimum depth of 1.3 m during high water and 1 m during low water. Red waterways are third category, having a minimum depth of 1 m during high water and 0.5 m during low water.

Despite the category system that describes minimum river depths along the navigation routes being enforced by the national navigation authorities such as the Régie des Voies Fluviales (RVF) in DR Congo, a significant risk of vessel grounding remains, especially during low water conditions, even on the mainstem (Wood et al., 1986). This is partly because the rivers are predominantly shallow: at low water the mainstem is reported to be often less than 2.5 m (Alsdorf et al. (2016) who references Marlier (1973)). Navigation on the Oubangui River is the worst affected, having become increasingly limited in recent decades. This is one of the most important routes as it connects Bangui in the Central African Republic to the network. Ndala (2009) reports that CICOS have observed a persistent increase in the number of days per year that Oubangui navigation is interrupted due to low depths, from 40 days in the 1970s, to 107 days in the 1980s, to

over 200 days in the 2000's. The observed reduction in mean annual flows on the Oubangui since the 1970's partly explains this (Laraque et al., 2001).

Shallow depths are compounded by morphological changes associated with the erosion and deposition of sediment that is occurring, including deposition along sections of the navigation routes leading to unforeseen shallow depth conditions (e.g. Deltares, 2018). Evidence of this morphological change is visible when viewing changes in surface water extent that have occurred over time. The global water transitions map produced by Pekel et al. (2016), based on more than three decades of Landsat imagery, provides a convenient means to view such change over time, and an extract from this map is shown in Figure 3-12. The water transitions map documents changes in water state between 1984 and 2018, and documents several types of observed transition, indicated by colour. For example, new permanent water surfaces are areas where conversion of a no water place into a permanent water place has occurred, lost permanent being the converse of this. Similarly, new seasonal water surfaces represent areas where conversion of a no water place into a seasonal water place has occurred, lost seasonal water surfaces being the converse of this.

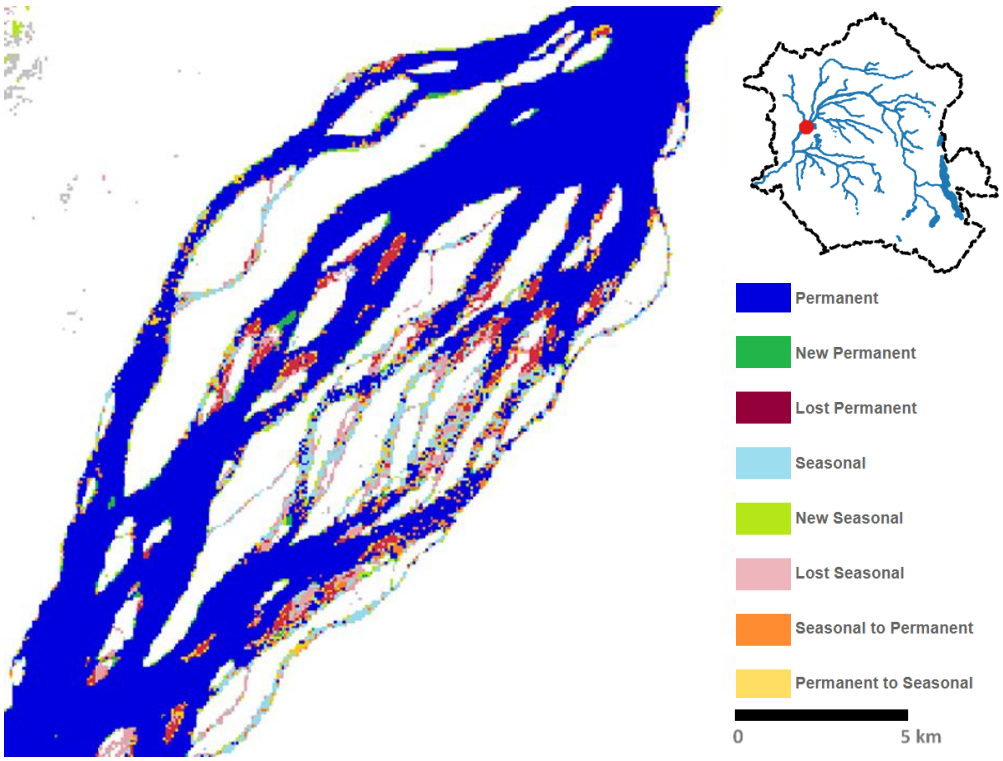

Figure 3-12. Extract of the global water transitions map showing a 30 km long reach on the mainstem Congo near Mbandaka, from Pekel et al. (2016). The new permanent and lost permanent transitions indicate areas of erosion and deposition respectively. Areas of deposition are clearly more widespread than the areas of erosion.

The growth and movement of islands, and the evolution of channel threads is clearly visible in Figure 3-12. Notably, lost permanent areas appear to be the most common transition type, and new permanent transitions are relatively rare here, indicating net deposition has occurred. As is the case with optical satellite imagery, cloud and vegetation cover are likely to cause some localised errors in this map, but the map provides a useful indicator of the overall trends in water transitions on a large river with very gradually varying flow conditions.

Maintenance of river depths along the navigation routes through dredging is not carried out, except localised efforts at major ports, despite the importance of navigation to the region and the serious implications of vessel grounding on a river of such size and remoteness (RVF, personal communication, 2017). The current navigation routes were originally established around 100 years ago during colonial times, and at the time were designed to minimise high risk shallow areas by following the deeper channel threads. These routes have not as yet been revised in response morphological change because of a lack of bathymetric information, but efforts to do so are currently ongoing as part of a wider institutional capacity building project. The European Union is providing the RVF with funds and capacity building through the Fluvial and Lacustrine Navigability Support (PANAV) project (Deutsche Gesellschaft für Internationale Zusammenarbeit, 2019).

3.2.5 Future Environmental Change

A number of human induced and natural changes that are occurring or anticipated have the potential to alter the hydrodynamic functioning of the middle Congo. Significant land use changes are taking place in the CRB, including deforestation resulting from the demand for agricultural land (Norris et al., 2010). In their assessment of future CRB deforestation impacts on regional climate, Akkermans et al. (2013) adopt a “realistic” loss in forest area of 12–20% by the year 2050. Whilst there does not appear to be any research looking specifically at the effects of land use change on river discharge in the CRB, it is generally thought that forests serve to reduce discharge and dampen river discharge variability, because they increase evapotranspiration and canopy interception, and reduce surface runoff rates (Brummett et al., 2009). For example, (Costa et al., 2003) showed that conversion of 19% of catchment area from tropical forest to cropland and pastures resulted in a significant increase in mean annual high-flow season discharge on the Tocantins River in Amazonia (see Figure 3-13 for magnitude). There was no statistical difference in precipitation over the basin during the study period.

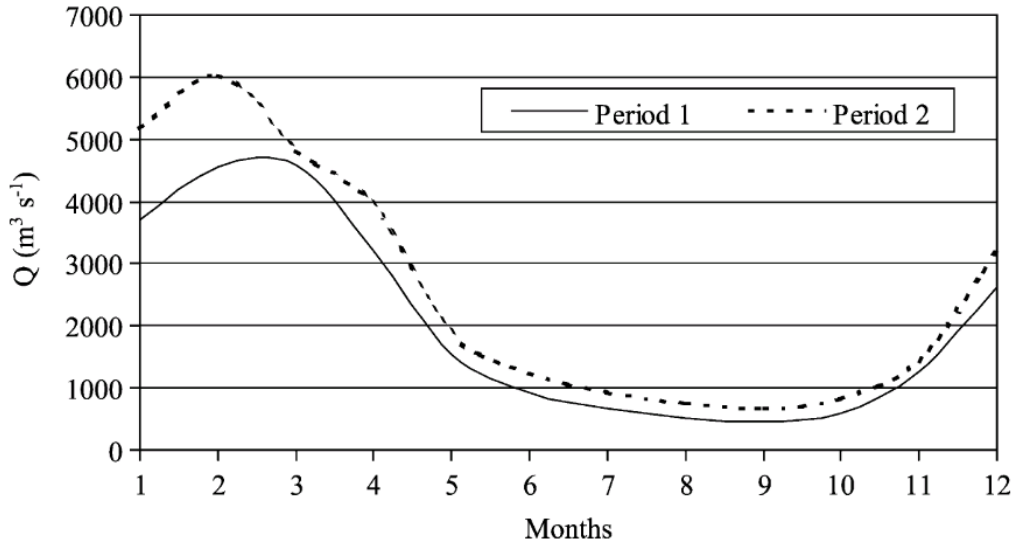

Figure 3-13. Observed changes in mean annual discharge on the Tocantins River in Amazonia (between period 1 and period 2) coincident with conversion of 20% of catchment area from tropical forest to agricultural land. From Costa et al. (2003).

There has been some research into the effects of climate change on hydrological processes in the CRB. Aloysius and Saiers (2017) found that total runoff from the CRB is projected to increase by 5% over the next two decades and by 7% by mid-century, based on hydrological modelling of climate projections using a range of global climate models. However, they note that future projections for both magnitude and direction of change in runoff is strongly influenced by climate model selection, and varies significantly between sub-basins; indeed a reduction in runoff is predicted to occur in northern and southern parts of the basin, driven by a predicted decrease in precipitation. This is in agreement with the findings of Tshimanga and Hughes (2012), who showed there to be a 10% decrease in total runoff for the near-future (2046–2065) in the northern part of the CRB, due to a relatively little increase in rainfall coupled with a consistent and substantial increase in potential evapotranspiration.

The effects of Land use and climate change on discharge in the CRB are inexorably linked, and firm conclusions on their net effect on discharge is likely to be difficult to ascertain, beyond there being clear potential for considerable variability. Conversely, it is clear that a reduction in discharge and its variability will result from the direct human alterations of discharge that may occur, such as abstractions or impoundments of river flows. Water security issues in the regions to the north and south of the CRB have led to proposals for major inter-basin water transfer schemes. One high profile proposal is the Lake Chad inter-basin water transfer scheme, which aims to replenish Lake Chad's diminishing water levels by transferring 4-8% of the CRB mean

annual discharge into the Lake Chad Basin (Dargie et al., 2019; Lake Chad Basin Commission, 2019). The scheme would involve the construction of a canal from a CRB tributary to a Lake Chad tributary, the canal also serving as a new navigation route, to generate hydropower, and provide irrigation in the Sahel region. Feasibility studies were ongoing as of 2016. Extraction of such a large flow rate will have significant effects on hydrodynamic processes, mainly on affected tributaries, and also the mainstem. An inter-basin water transfer has also been proposed to transfer approximately 1% of mean annual CRB discharge into the upper Zambezi Basin (Lund et al., 2007), but the proposal appears to be speculative at this stage, having received little attention in research or the media.

If realised, the proposed Grand Inga hydropower project on the Lower Congo (location shown in Figure 3-1) would have by far the highest generating capacity of any hydropower scheme in the world and provide power to much of the African continent (World Bank, 2014). The scheme is often cited as potentially having a major adverse environmental impact due to alterations of fluvial processes, including within the CMR (Deshmukh et al., 2018; Dargie et al., 2019). Whilst the concerns over the environmental impacts on the lower Congo are clearly valid, the hydrodynamic functioning of the CMR would be unaffected by the scheme, as can be seen from an inspection of elevations. Elevation of the proposed Grand Inga intake reservoir is 205 m aSL (Société nationale d'électricité, 2014), 40 m lower than the typical WSE at the foot of Livingstone Falls which separate the CMR and the lower Congo (Robert, 1946). The flow conditions of Livingstone Falls and the waters upstream will therefore be unaffected by the scheme.

3.3 Progress in Hydrodynamic Research on the Congo Middle Reach

The majority of hydrodynamic research efforts on the CMR appears to be focussed on the subject of inundation of the Cuvette Centrale, and in particular the extent to which the wetlands of the Cuvette Centrale are maintained by fluvial flooding and / or rainfall. This is perhaps not surprising, given the relevance of this subject to biogeochemical and ecological processes, and food security. Research into channel flow conditions is extremely limited, the efforts of O'Loughlin et al. (2013) to characterise the hydraulics of the CMR being the only known example of research that looks specifically at channel hydraulics.

Key Research: Hydraulic Characterisation of the CMR

The work of O'Loughlin et al. (2013) draws predominantly on SRS observations of WSE and water extent, and serves to provide key hydraulic data and understanding required for hydrodynamic modelling. The work involved analysis of a water mask of

permanent water bodies including the CMR and its key tributaries (shown in Figure 3-2) produced from Landsat imagery, and analysis of water surface profiles produced from ICESat altimetry data. The water mask provided detailed planform statistics including river width and number of channel threads through the CMR, and showed that river width is highly variable and cannot be adequately represented with parametrisation methods. An ICESAT derived Water surface Profile (WSP) was used to understand the spatial and temporal variability of water surface slope (WSS) through the CMR, which showed that they were nearly constant over time for the period corresponding to the falling limb (March), low water (June), and the rising limb (November). Marked spatial variability in WSS was observed (between 2 and 8 cm/km), although the average spatial resolution of approximately 50 km (i.e. river distance between WSE observations) may not have been adequate to fully assess spatial variability (Garambois et al., 2017). Finally, O'Loughlin et al. (2013) identified five key hydraulic constrictions where the river width reduces dramatically. These constrictions were attributed as having wide implications for the hydraulics of the middle reach of the Congo, and to be base level controls that affect both the upstream WSE and downstream flows. The authors suggest overbank flow due backwater effects caused by these constrictions could be a major source of water in the floodplain, and may also be the cause of the marked variation in WSS in space. The method of Samuels (1989) was used to derive estimates of backwater lengths upstream of these constrictions, which showed that during low water and high water, 11% and 33% of the total CMR is affected by backwater effects respectively. Such constrictions have been identified in other large rivers: Warne et al. (2002) who cite Hamilton and Lewis (1990) report eight constrictions termed bedrock control points on the Orinoco River, which form substantial but navigable rapids, limit lateral channel migration, modify peak discharge by constricting overbank flow, and cause extensive floodplain inundation.

3.3.1 Flood Inundation Observations

The research into large scale fluvial inundation dynamics is substantially driven by the need for the scientific community to understand the vulnerability of the wetlands to the future changes in rainfall patterns and river discharge regimes that are anticipated (e.g. Dargie et al., 2019). Researchers have also pointed out that the current understanding of large tropical wetland systems is drawn heavily from studies of the Amazon (the ecological flood pulse paradigm (Junk et al., 1989) being a key example of this), leading Alsdorf et al. (2016) to state that, differentiating the Congo from the Amazon could lead to the Congo being considered a new paradigm for other tropical wetlands.

Contrasting views on CMR fluvial flooding emerge from a review of the available literature. In their description of the Cuvette Centrale, Hughes and Hughes (1992) refer

to the area being “inundated, either temporarily or permanently, from the Congo and Oubangui Rivers”. Conversely, Ashworth and Lewin (2012) refer to the Congo as an example of a river that is essentially disconnected from its floodplain for nearly its entire length. Lee et al. (2011) investigated Congo floodplain inundation in detail by comparing channel and adjacent wetland WSEs measured by ENVISAT altimetry. They found that at the two transects retrieved (shown in Figure 3-14), wetland WSE was consistently higher than river WSE, and the wetland WSE range was small compared to the river, leading them to conclude that the connectivity of the Congo River to its floodplain and wetlands is limited compared with the Amazon.

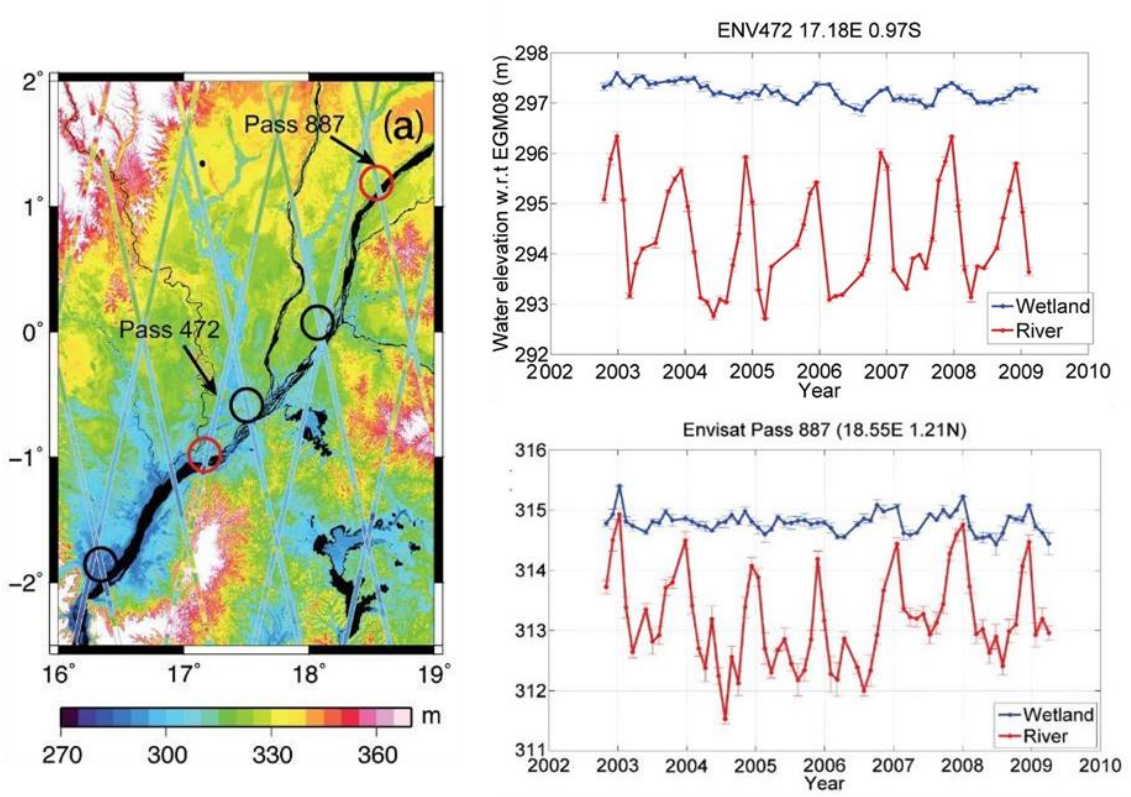

Figure 3-14. ENVISAT altimetry measurements of Congo Mainstem and adjacent wetland WSEs. From Lee et al. (2011).

Figure 3-14 clearly shows that at these transects, the mainstem is not providing the main source of wetland inundation and plays a limited role in inundation dynamics compared to the Amazon. However, channel – floodplain connectivity is evident at ENVISAT pass 887, with the wetland WSE clearly reacting to river WSE during some years. Thus, the wetlands here are not being supplied exclusively by fluvial flooding, but their water levels are being partly controlled by river WSE, through subcritical water surface gradients that run from the wetlands to the river. It is also important to be mindful that, firstly, the non-perpendicular orientation of these two transects results in the

transect measuring the floodplain some distance upstream of the adjacent river, thus elevating wetland WSE to some degree. Secondly, ENVISAT temporal resolution is approximately one month, and is therefore unlikely to capture flood peaks and the full extent of the floodplain interactions that may be occurring.

Dargie et al. (2017) present some evidence that suggests that the peatlands of the Cuvette Centrale seem to be largely rain-fed. Specifically, no obvious fluvial flood wave was seen in one year of continuous in-situ water table elevation measurements across two transects located between the Oubangui and Likouala-aux-herbes rivers, shown in Figure 3-15. Moreover, the low concentrations of calcium observed within the surface peat is consistent with other rain-fed tropical peatlands, and not river-fed peatlands that have much higher calcium concentrations. Obviously this evidence is not conclusive given the limited spatial and temporal coverage of the transect locations, and it remains conceivable that substantial areas of river affected wetlands do exist. The peatland water tables may also be affected by high and low water conditions that occur supra-annually.

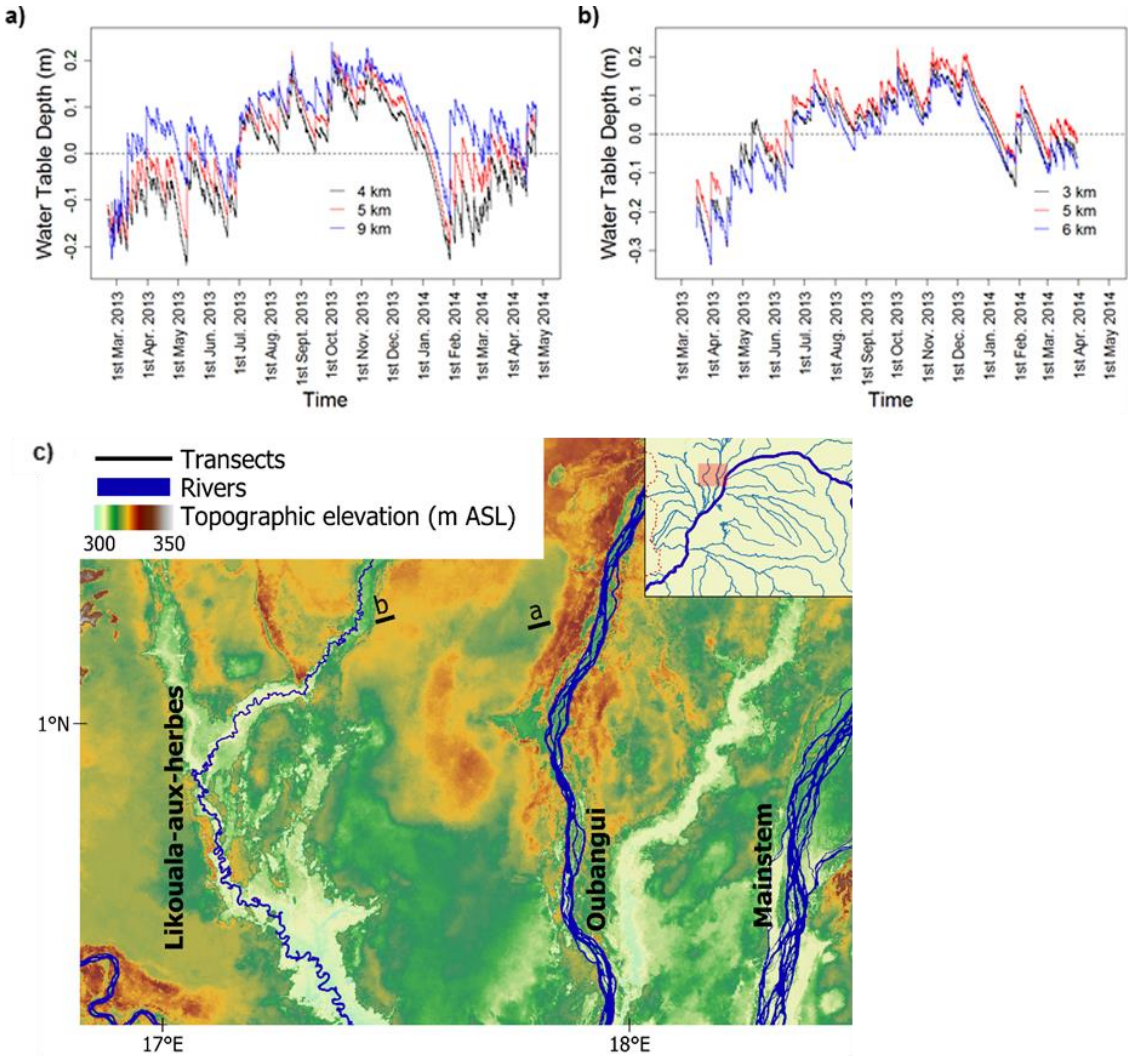

Figure 3-15. (a)-(b) time series of in-situ water-table levels measured at two transects for the time period March 2013 to May 2014 (black, blue and red lines indicate different sample locations along the transects), from Dargie et al. (2017); (c) shows locations of transects and topography from MERIT DEM (Yamazaki et al., 2017).

The water occurrence maps by Pekel et al. (2016) indicate that channel – floodplain interactions along the mainstem Congo and its key tributaries are notably absent when compared with other rivers of similar size. Figure 3-16 shows water occurrence maps for reaches of the Congo, Amazon, and Orinoco (the world's three largest rivers by mean annual discharge).

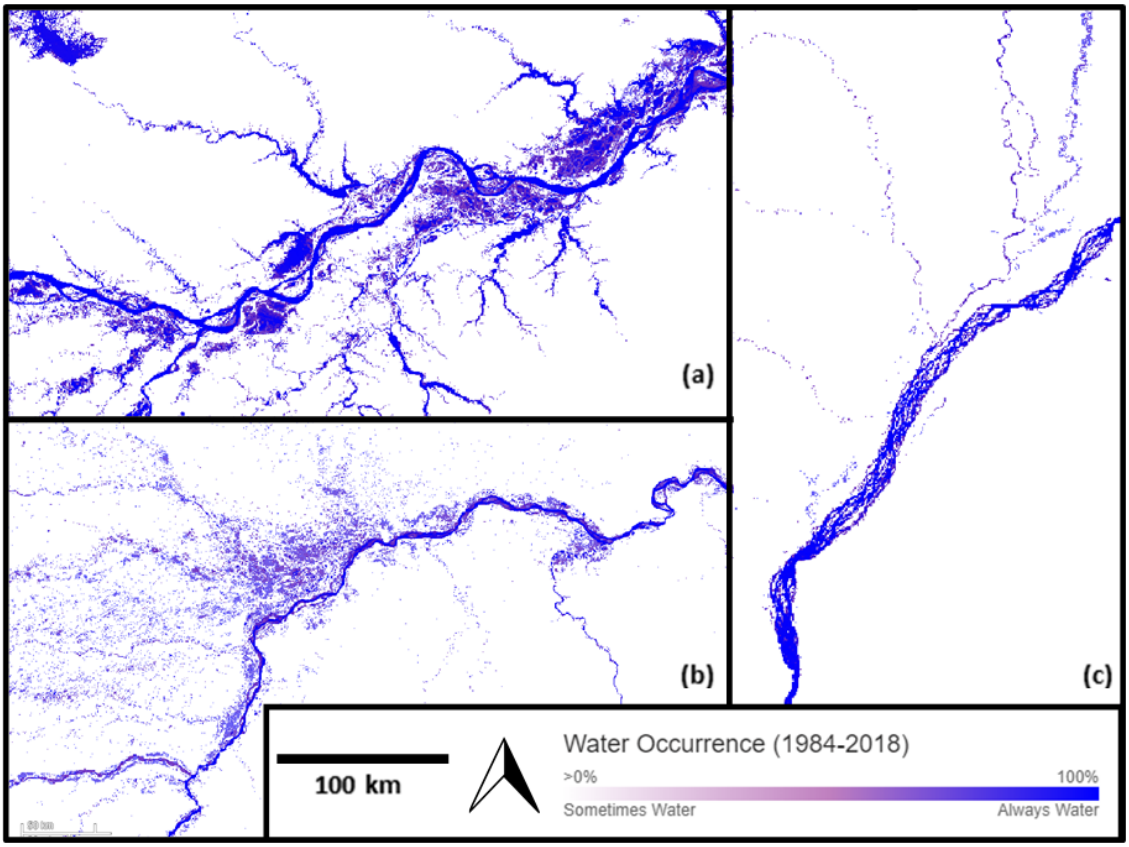

Figure 3-16. Extracts from the Landsat derived water occurrence maps produced by Pekel et al. (2016). Water occurrence maps shows where surface water occurred between 1984 and 2018, and the frequency of that occurrence. River channels are shown to occur 100% of the time, whereas seasonally flooded areas show variability in frequency of occurrence. (a) Amazon mainstem; (b) Orinoco mainstem; (c) Congo mainstem.

Seasonal floodplain inundation is notably absent on the Congo in Figure 3-16c, which somewhat explains the opinion of some researchers that the Congo is essentially disconnected from its floodplain. Yet a brief review of the Landsat imagery covering the Congo during high water shows otherwise. Figure 3-17 shows a Landsat image taken on 23 November 2009, which indicates extensive flooding along both banks of the mainstem in some places. The water occurance maps do not show this inundation, the likely reason for this being that visibility of water is partly obscured by vegetation, which is a known issue with the automated water detection methodology used by Pekel et al. (2016), and indeed satellite based derivation of flood extents in general. Inundation obscured by emergent vegetation is prevalent in the CRB because of the relatively small flood wave amplitudes coupled with the widespread coverage of forests and other tall vegetation types, and satellite-based mapping of inundation is therefore highly challenging here.

Fluvial flooding here is evidently a more subtle process that is distinct from other large rivers such as the Amazon, and to observe and model spatiotemporal variations in WSE and water extent along the CMR, this distinctive characteristic may require higher precision methods than those developed for other large rivers. For example, measuring or modelling spatiotemporal variations in the 3–4 m seasonal floodwave amplitude of CMR may require a higher precision than the Amazon's ~12 m amplitude.

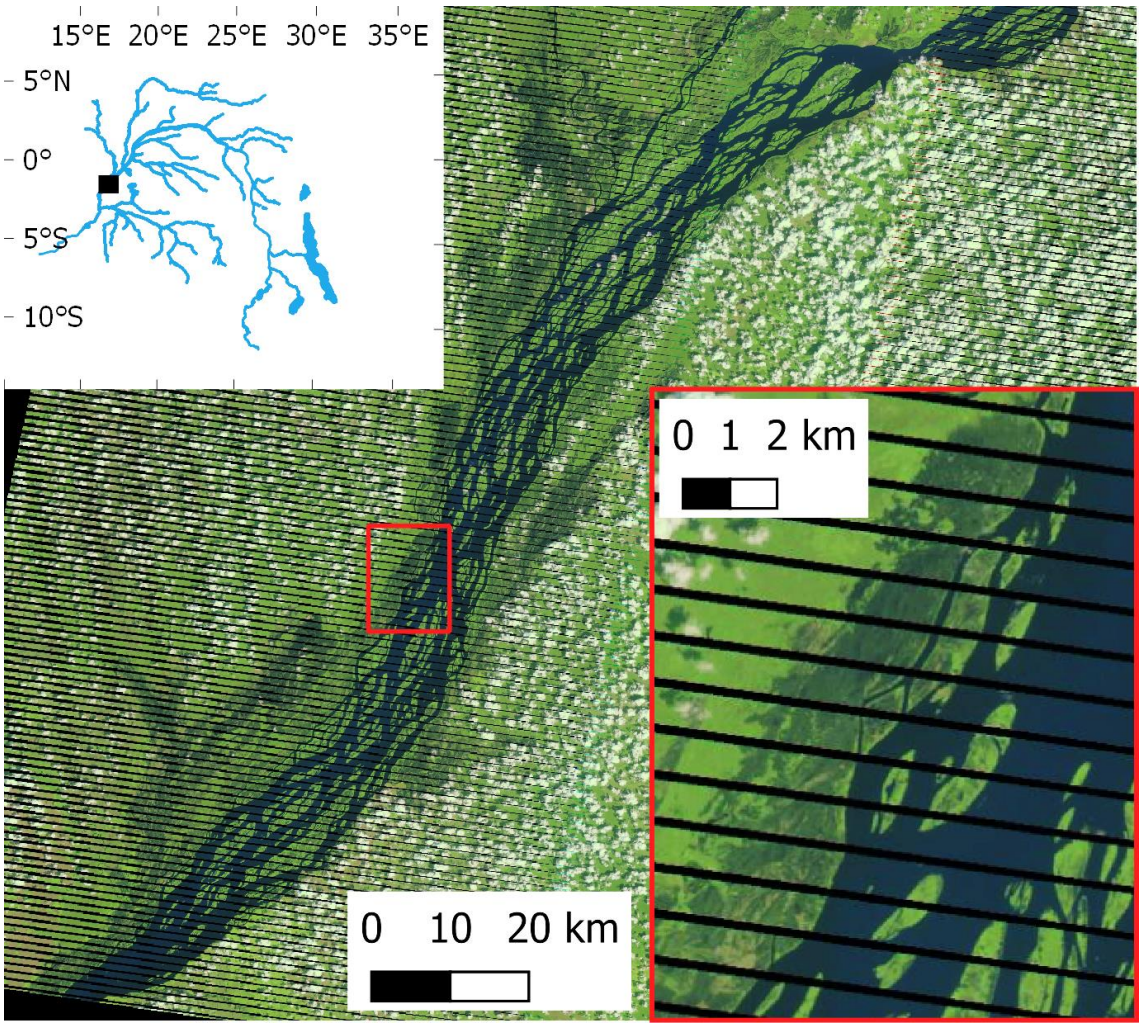

Figure 3-17. Landsat image of the CMR during seasonal inundation, acquired on 23 November 2009. Black stripes are due to failure of the satellite instrument's scan line corrector. Image obtained from the Earth Explorer website: https://earthexplorer.usgs.gov/.

In summary, it is evident that considerable fluvial inundation does occur along the CMR, but it is not the dominant supply of water to the Cuvette Centale wetlands, which in many areas appear to be predominantly rainfed. The extent to which wetland water levels are influenced by river WSE is unknown.

3.3.2 Hydrodynamic Modelling

Hydrodynamic modelling has clear potential to help answer questions over the sources of and controls on flooding in the central CRB, and the spatiotemporal variability it exhibits. O'Loughlin et al. (2020) recently developed a hydrodynamic model for the CMR and its key tributaries, which appears to be the first attempt to produce a hydrodynamic model for the CMR. The model adopted a spatial resolution of 4km, and used the LISFLOOD-FP code that implements a 1D local inertial approximation using a 2D square grid spatial structure. Model inputs comprised terrain data from a vegetation corrected version of SRTM called 'BEST DEM' (O'Loughlin et al., 2016b), river channel width information from Landsat data, and discharge data from five in-situ gauging stations supplemented with discharge estimates from a hydrological model at 12 locations. Calibration entailed simultaneous adjustment of channel friction and channel depth in order to minimise the fit between predicted WSE and observed WSE from ERS-2 and ENVISAT altimetry. At the altimetry overpass locations, the calibrated model predicted altimetry observations of WSE with a bias and root mean square error of 0.2 m and 0.8 m respectively. Two key conclusions were made from the study: (1) that flood wave propagation is not significantly attenuated by floodplain interactions, unlike similar sized rivers such as the Amazon; and (2) significant floodplain interactions occur along almost the entire CMR. These conclusions are broadly supported by the findings summarised in the previous subsection. The study gives insights into the behaviour of river and floodplain flows along the CMR and its tributaries that could not be obtained using either remote sensing data or ground observations alone. However, there is significant potential to build upon and improve these efforts.

Given the scarcity of hydrodynamic data for the CMR (especially bathymetry data), the model necessitated a data sparse methodology similar to that used by Neal et al. (2012), which is discussed in subsection 2.4.5. A key element of this approach is the representation of river channels as a single rectangular channel, using reach-averaged effective width measurements from Landsat (O'Loughlin et al., 2013). Channel depth was treated as a free parameter and is calibrated along with channel friction. The limitations of such an approach to channel representation were highlighted in subsection 2.4.5. In the context of the CMR's multithread channel system and distinctively subtle fluvial flooding processes, these limitations present a number of research needs around representation of the CMR's multithread channel system in hydrodynamic models. Acquiring some in-situ channel hydraulic data is likely to be essential to this.

3.4 Concluding Remarks

It is clear that hydrodynamic research on the CMR is required to inform a range of scientific and developmental questions concerning biogeochemical cycling, ecology, flood risk, food security, fluvial navigation and environmental change. In particular, predictions of dynamic inundation extents are needed to quantify potentially globally significant levels of outgassing of carbon dioxide and methane, determine the dependence of critical wetland and floodplain ecosystems on fluvial flooding, and assess the amount of people and property that are at risk of flooding. In addition, prediction of in-channel flow conditions can help manage fluvial navigation risks associated with shallow depth flow conditions, which emerge particularly during low flows. Furthermore, given the lack of contemporary flow gauging in the CRB, hydrologic research in the basin stands to benefit greatly from the application of satellite-based hydrodynamic observations and models to estimate discharge.

Observations of WSE from satellite altimetry, and hydrodynamic models, will both play a leading role in this hydrodynamic research. However, satellite altimetry has a relatively sparse and inconsistent coverage, and current hydrodynamic modelling approaches to large rivers use poorly verified approximations of channel geometry. These limitations pertaining to sparsity of observations and geometric approximations are not well understood and need to be addressed, particularly on the CMR, which has a complex multithread channel system that requires gross geometric simplification. In addition, the relatively subtle inundation processes here are challenging to observe and therefore require greater accuracy than many other rivers of comparable size.

3.5 Thesis Objectives and Outline

3.5.1 Narrative of Objectives: Research Gaps

Water surface observations from satellite are increasingly being regarded as a sustainable long-term solution to observing large river hydrodynamics, as they can provide near real time monitoring of large rivers in remote and inaccessible regions (e.g. Bjerklie et al., 2003; Schumann et al., 2009). Given its spatial scale, physical inaccessibility, and lack of pre-existing in-situ data, progress in Congo River hydrodynamic research is likely to rely heavily on these satellite observations. However, a comprehensive in-situ hydraulic dataset comprising observations of bathymetry, water surface elevation (WSE), velocity, and discharge is badly needed to complement these satellite observations. An in-situ hydraulic dataset will enable a detailed characterisation of Congo Middle Reach (CMR) channel hydraulics based on in-channel observations. This has not been done previously, yet is essential for understanding the controls on the hydraulic and morphological functioning of the CMR. In particular it will determine the extent to which key morphological features such as width constrictions control hydrodynamics.

An in-situ hydraulic characterisation will also determine the applicability of various approximations that enable satellite observations to be leveraged for hydrodynamic analysis. In particular, WSE from conventional satellite profiling altimeters is one of the most important sources of satellite data in CMR hydrodynamic research (Domeneghetti et al., 2015); yet, the adequacy of satellite altimetry in terms of the spatial density of its coverage is limited (Jiang et al., 2017; CNES, 2020b) and poorly understood. In-situ WSE measurements along the CMR will be invaluable in determining the spatial adequacy of satellite altimetry for capturing the spatial variability of water surface elevation and slope. Quantification of WSE spatial variability is fundamental to the parameterisation of hydrodynamic models and discharge estimation algorithms (Durand et al., 2016; Garambois et al., 2017; Montazem et al., 2019).

The applicability of channel geometric approximations currently being adopted in large river modelling needs to be evaluated in the context of the highly multichannel morphology of the CMR. One approach to doing this is to explicitly include multithread channel bathymetry, in the form of a 2D bathymetry model (see for example Figure 2-5 in Section 2.3.2), in a reach-scale hydraulic model. This multichannel hydraulic model can then be tested alongside a hydraulic model with a simplified geometry such as an effective single channel. Applying the same model parameters and hydrodynamic

boundary conditions to both hydraulic models will enable the consequences of the geometric simplification to be interrogated.

Notably, constructing a bathymetry model of the multichannel CMR will require a novel approach based on spatially limited observed data. The conventional approach to constructing a bathymetry model is to spatially interpolate bathymetry observations that have a relatively dense spatial coverage (Merwade et al., 2008; Altenau et al., 2017a). However, the prerequisite collection of regularly spaced cross-sectional river bathymetry data is a major challenge on the CMR, largely because of the prohibitive resource requirements to cover spatial scale of the CMR (i.e. 5 km wide channels), and the large number of mid-channel islands that prevent a survey boat from navigating perpendicularly across the entire channel. Logistical constraints imposed by personal safety and security concerns in the region must also be considered. Therefore, acquiring bathymetry observations of sufficient spatial density for interpolation is not proposed on this research project. Approaches to creating bathymetry models with spatially limited data are not well researched and need investigation. In addition, multiple mid-channel islands present in large multichannel rivers pose challenges to bathymetry model construction that remain poorly resolved (Hilton et al., 2019).

3.5.2 Thesis Objectives

The aims of the research presented in this thesis are twofold:

1. ***To assess the water surface and in-channel hydraulic conditions along the middle reach of the Congo River, and the capacity of satellite-based observations to determine these conditions.***
2. ***To evaluate methods of channel geometric representation in hydrodynamic models of the Congo's multichannel middle reach.***

The objectives of the research presented in this thesis are as follows:

1. ***To conduct a field-based hydraulic characterisation of the Congo Middle Reach;***
2. ***To assess the spatial adequacy of existing satellite altimetry datasets for capturing the spatial variability of water surface elevation and slope along the Congo Middle Reach;***
3. ***To develop a bathymetry model covering a multichannel reach of the middle Congo, using a novel approach based on spatially limited bathymetry observations;***
4. ***To evaluate geometric simplifications of multithread channel geometry in hydrodynamic modelling of the Congo Middle Reach, using the bathymetry model developed in objective 3.***

3.5.3 Thesis Outline

The three subsequent chapters of this thesis: Chapters 4, 5, and 6, correspond to one or two thesis objectives (described below). Each of these chapters have been prepared as distinct, standalone studies, and therefore include their own introductions, methods, results, discussions, and conclusions sections. However, the chapters have not been prepared in isolation: later chapters generally build upon the findings of earlier chapters, as the research associated with each chapter was carried out consecutively.

Chapter 4 primarily addresses objectives 1 and 2. The methods, results and analysis of two field campaigns along the CMR are presented, and WSE measurements from three satellite altimeters are also retrieved and analysed. The in-situ data includes bathymetry, WSE, velocity, and discharge, and is complemented with river width information from satellite imagery. The analyses provide a detailed hydraulic characterisation of the CMR, and an assessment of the spatial adequacy of satellite altimetry.

Chapter 5 is specific to objective 3, and reports on the construction and validation of a multichannel bathymetry model using a novel approach. The approach involves estimation of bathymetry in channel areas that are outside of the spatial envelope of spatially interpolated observations. The bathymetry model is validated using additional depth observations, and also through 2D hydraulic modelling, by comparing modelled in-channel velocities with observed velocities.

Chapter 6 investigates the applicability of channel geometric simplifications to multichannel CMR hydrodynamic modelling (specifically an effective single channel approximation), and is thus concerned with objective 4. Following its introduction, the chapter begins with a substantial preliminary investigation of an effective single channel approximation. This is followed by a series of hydraulic modelling experiments that draw on the bathymetry model developed in Chapter 6.

Finally, Chapter 7 synthesises the research reported in the three previous chapters. The key findings of the thesis are presented along with limitations of the research, and some potential future research directions are discussed.

CHAPTER 4

Congo Middle Reach Channel Hydraulics: Field-based Characterisation and Implications for Satellite Altimetry

4.1 Introduction

Hydraulic observations from satellite remote sensing (SRS) are expected to play an increasingly important role in the study of large river hydrodynamics globally, as they can provide consistent and near real time monitoring over large areas. In remote regions lacking in situ data, these data are valuable for understanding flood risk, water availability, and for global biogeochemical and ecological processes, because of the role large river floodplains and wetlands play in global fluxes of methane and carbon dioxide (Richey et al., 2002). However, SRS observations are limited by resolution, coverage, and uncertainty and their inability to directly measure bathymetry or discharge. In situ field campaigns can obtain data with denser or more consistent coverage, and target particular locations in space and time. Bathymetry and discharge information can also be obtained; such measurements cannot be obtained directly from SRS, but are key parameters in river hydrodynamics. It therefore remains necessary to complement SRS datasets with in-situ measurements, in order to obtain comprehensive hydraulic datasets and adequately characterise the hydraulic behaviour of large river systems.

Inland open water surface elevation (WSE) measurements derived from satellite altimeters are a primary component of many satellite remote sensing (SRS) studies of large river hydrodynamics. Some key applications have included characterising river hydrodynamics (e.g., Birkett et al., 2002) and calibration and validation of hydraulic river models (e.g., Neal et al., 2012). Moreover, estimation of discharge from SRS at ungauged river reaches combines altimetry estimates of WSE and water surface slope (WSS) with satellite imagery estimates of river width and minimal in situ observations (e.g. Birkinshaw et al., 2014; Bjerklie et al., 2018). These data are fed into hydrodynamic models, often based on simplified flow hydraulics (e.g. assuming uniform flow conditions), in order to derive discharge (e.g., Durand et al., 2016).

A growing number of radar and laser satellite altimeters have measured WSE with an accuracy of 0.35 m or less (Frappart et al., 2006; Urban et al., 2008; Jarihani et al., 2013) and are therefore considered suitable for SRS river hydrodynamics studies (Domeneghetti et al., 2015). However, use of altimetry data in a river hydrodynamics context is limited by data coverage in both time and space, which may be insufficient to

capture key spatiotemporal variations in WSE and WSS. Such variations are important for understanding the hydraulic functioning of river reaches (Garambois et al., 2017; Frasson et al., 2017; Montazem et al., 2019), which is necessary for developing hydrodynamic models and SRS discharge estimation algorithms. In this context, field data can be used to determine the capabilities of valuable altimetry data sets that cover far greater temporal and spatial extents.

The Congo River is one of the world's foremost candidates for SRS, due to lack of in situ data, access, and scale. The ~1,700 km long Congo Middle Reach (CMR) in particular possesses characteristics that are advantageous for the use of SRS datasets with limited coverage and resolution. Here, the river is highly subcritical and has very gradually variable flow conditions in both time and space due to its large size, mild bed slopes, and absence of falls or rapids (Robert, 1946). The channel system is very wide, which also enables satellites to obtain accurate measurements of water surface elevation (WSE) (Frappart et al., 2006). The CMR also represents a global hydrodynamic research priority (Alsdorf et al., 2016), owed to its importance both regionally and globally, for several reasons as follows. It is an important resource for Central Africa, particularly for inland navigation, as it provides a 17,000 km long network of navigable river channels that serve as the main mode of transport in the region (CICOS, 2015). The CMR flows through the Cuvette Centrale wetland region, which functions as a globally significant source and sink of carbon; it contains the world's largest tropical peatland, which combined with above ground flooded forests are estimated to contain 35 petagrams of carbon (Dargie et al., 2017). Flooding in the Cuvette Centrale is clearly important for sustaining these wetlands and peatlands, but also produces an estimated 0.4 petagrams of carbon per year at present from outgassing of carbon dioxide and methane (Bwangoy et al., 2010; Borges et al., 2015). Knowledge of mainstem channel hydraulics is relevant to these carbon and methane fluxes because it is required to simulate flood inundation dynamics, which can improve estimates of flood extent and duration and hence outgassing estimates, and give insights into how susceptible wetlands are to future hydrological variability caused by potential climate and land use changes.

To advance the current scientific understanding of the hydraulic functioning of the CMR, new in situ data has been obtained from two dedicated field campaigns in 2017 and 2019, which combined cover the entire CMR. The data includes elusive discharge and bathymetry measurements, and WSE measurements at targeted locations along the mainstem. An acoustic Doppler current profiler (ADCP), sonar echo sounders, and a high precision GNSS survey instrument were used to collect the data. This chapter reports on the acquisition of this in-situ data. The data is then interpreted in order to characterise

the hydraulic behaviour of the reach, and reveal previously unidentified hydraulic characteristics of the reach. Furthermore, the WSE data is used to explore the spatial adequacy of altimetry for estimating WSE and WSS along the CMR. To do this, key satellite altimetry datasets are analysed alongside the in-situ WSE measurements. Satellite altimetry measurements of the CMR WSE are especially valuable, because the extensive dense forestry that covers much of the Congo Basin makes inundation extents difficult to observe and topographic data subject to large uncertainties.

4.2 Methods: In-situ Data Collection

In the summer of 2017 and 2019, two major field campaigns were conducted on the CMR by boat to acquire the in-situ hydraulic data. Both field campaigns were conducted during the months of July and August, which constitutes the low- flow season for the mainstem and the Kasai River, and the rising limb of the Oubangui River (Becker et al., 2014). The 2017 campaign, covering a 650 km reach between Mbandaka and Kinshasa, is the source of most of the field data that has been used in this thesis. Data from the 2019 campaign, which includes ADCPs and bathymetry along the 1000 km reach between Kisangani and Mbandaka, and WSE measurements along almost the entire middle reach, is only used to a limited extent, as there was insufficient time to fully analyse the data within the designated period of doctoral study. The second field campaign was originally scheduled for summer 2018, but was postponed for a year due to a major outbreak of the Ebola virus in DR Congo. These scientific field campaigns appear to be the first undertaken on the CMR since the establishment of modern hydrographic instruments such as acoustic Doppler current profilers (ADCPs).

4.2.1 Field Campaign Logistics

The Central CRB is an extremely remote part of the world. It is very inaccessible, being severely underserved by all forms of transport infrastructure, and the only reliable means of outside communication is via a satellite communication device. Most settlements have no water or power supply, and no medical facilities. Almost all necessary equipment must be imported from overseas, and cannot be imported at short notice (i.e. in the event of loss or failure of equipment). There are also many risks to health, safety and welfare that are specific to the region and to boat travel. Organising and carrying out the field campaigns involved significant challenges, and their successful completion is regarded as a major achievement, both professionally and personally. Some brief reflections on the fieldwork challenges and achievements are included in Appendix **Error! Reference source not found.**.

The field campaigns were undertaken from within DR Congo, and commenced at Kinshasa in 2017, and at Kisangani in 2019. The methods described below apply to both the 2017 and 2019 field campaigns. Any noteworthy methods particular to 2019 are documented in subsection 4.4.3. Participants included a team made up of approximately 12 researchers and practitioners who are collaborating through the Congo River users Hydraulics and Morphology Project (CRuHM), including staff and students from the University of Kinshasa and RVF (DR Congo), the University of Leeds (UK), The University of Rhodes (South Africa), and the University of Dar-es-Salaam (Tanzania). There was also a team of around eight people involved in crewing the boat and providing logistical support. Two boats were used: a large vessel (Figure 4-1a shows the boat used in 2017) was hired to travel on and provided accommodation for the entirety of the field campaign (a duration of 3–4 weeks). A smaller fibreglass boat with an outboard motor was purchased and used to access shallow water areas and undertake most of the hydraulic measurements. When travelling, the fibreglass boat was tethered to the large vessel.

Figure 4-1. Field campaign boats: (a) Main boat used on 2017 campaign; (b) Fibreglass boat for hydraulic measurements; (c) Boat dining area (and temporary lecture theatre).

4.2.2 High Resolution Study Reach

The 2017 field campaign included a relatively short (70 km long) 'high resolution' study reach along which a denser coverage of measurements was obtained, shown in Figure 4-2. The measurements are intended to provide a more detailed insight into the flow conditions through the multichannel morphology, including localised hydraulic conditions through individual channel threads and morphological features such as constrictions.

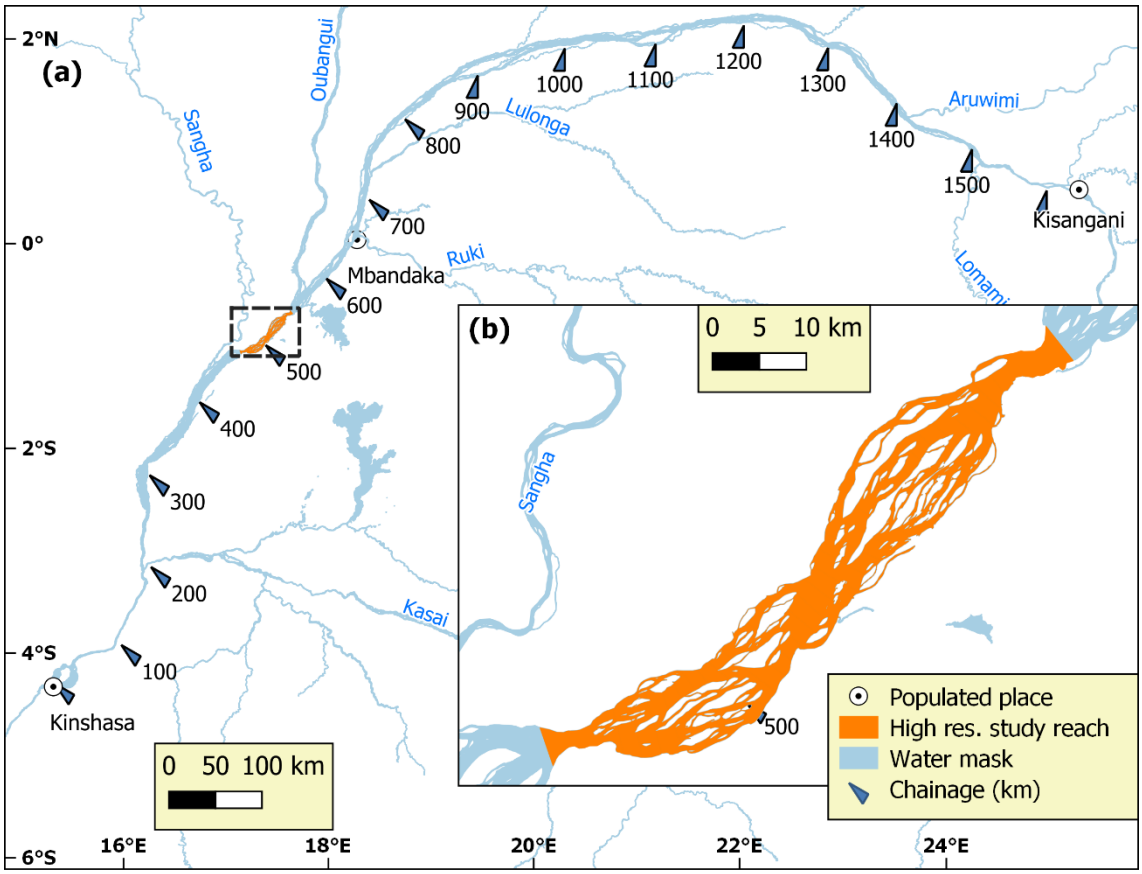

Figure 4-2. High resolution study reach: (a) Location plan; (b) high resolution reach. Water mask from O'Loughlin et al. (2013).

The high resolution reach was selected based on its planform being characteristic of the multichannel CMR; an absence of tributaries, enabling conservation of mass to be assumed; and the presence of single channel sections upstream and downstream, enabling easy full cross-sectional sampling here. This chapter does not look specifically at the high resolution reach in detail, but does make use of the measurements obtained along the reach.

4.2.3 Acoustic Doppler Current Profiler Measurements

An acoustic Doppler current profiler (ADCP) was used to measure depth, velocity, and hence discharge at designated locations. A Teledyne RiverRay was used, which has an operational depth range of 0.4–60 m, which was determined to be sufficient for the CMR. The ADCP was fixed to the side of the fibreglass boat using a purpose made bracket, as shown in Figure 4-3. Routine operational procedures were carried out following Winriver II guidance, including calibration of the ADCP compass and moving bed tests. A minimum of two transects were made at each ADCP site, transect repeatability being a key method of validating measurements.

Figure 4-3. ADCP fixed in place on the side of the fibreglass boat, prior to being fully lowered into the water.

Sites were generally confined to locations at which the channel is single thread and relatively narrow, where complete width of the channel can be surveyed in one bank-to-bank transect. Transects were made at confluences with major tributaries to quantify tributary flows, although this was not possible at some tributaries such as the Oubangui. Here, the complex planform of both the mainstem and the Oubangui necessitates a large number of discrete transects in order to achieve full cross-sectional coverage, which was not achievable within the time constraints of the field campaign.

4.2.4 Water Surface Elevation

Precise measurement of elevation along the CMR is not straightforward due to the absence of cellular networks and sparsity of benchmark elevation references in the region. Fortunately, specialist surveying technologies have been developed for data sparse applications in recent years, and following a review of these, precise point

positioning (PPP) was identified as an appropriate technology for measuring WSE on the CMR. PPP processes measurements from a single surveying instrument, using detailed physical models and corrections, and precise GNSS orbit and clock products computed beforehand (Laínez Samper et al., 2011). Importantly, PPP differs from other precise-positioning approaches like Real Time Kinematic (RTK) in that no reference stations are needed in the vicinity of the user; rather it obtains all its correction information from either the internet or a dedicated satellite. A PPP solution requires that the instrument remain stationary for some time in order to converge due to the need for properly estimating phase ambiguities, but devices that use multiple global navigation satellite systems (GNSS) such as GLONASS, GPS, and Galileo are able minimise this convergence time to around 30-60 minutes. The Trimble R10 used in this research is once such device. This instrument was complemented with the Trimble CenterPoint RTX correction service, which provides the instrument with correction information from a dedicated satellite, enabling processed results to be obtained in the field. Thus, there is no requirement for an internet connection in order to obtain results, which is crucial for fieldwork in the CRB. The EGM96 geoid model was loaded onto the instrument so that elevation measurements would be referenced to this geoid.

Trimble (2019) report that the RTX CenterPoint correction service has a vertical accuracy of 5cm root mean square error (RMSE). This was deemed to be sufficient, as it offers a significant improvement on the accuracy of existing satellite altimetry derived WSE datasets such as ENVISAT, which has a reported accuracy for large rivers of 28cm (Frappart et al., 2006). The device can therefore provide WSE measurements on the CMR with unprecedented accuracy, and more importantly quantify spatial variations in WSE and water surface slope (WSS) with greater precision, and therefore over shorter river reach lengths. A useful comparison can be made here with the planned SWOT mission science requirements: accurate WSS slope measurement is one of the key aims of the SWOT mission, and is required to do so with an accuracy of 1.7cm/km over a 10km long river reach (Biancamaria et al., 2016). In comparison, a pair of WSEs 10 km apart measured with the RMSE of 5 cm proposed in this research, would produce a measured WSS with a RMSE equal to the sum of the WSE measurement errors divided by the reach length, which computes to 1 cm/km. Accurate WSS measurement is particularly important on the shallow sloped CMR; ICESat altimetry measurements processed by O'Loughlin et al. (2013) show WSS may be as low as 2.6 cm/km in places.

To measure WSE along the CMR, the GNSS instrument was deployed at designated shoreline locations. As shown in Figure 4-4, the instrument was setup to

converge on a tripod directly over water if access permitted. Alternatively, the instrument was setup to converge on land, then installed on a detail pole which was positioned over water, or a known elevation above the water surface.

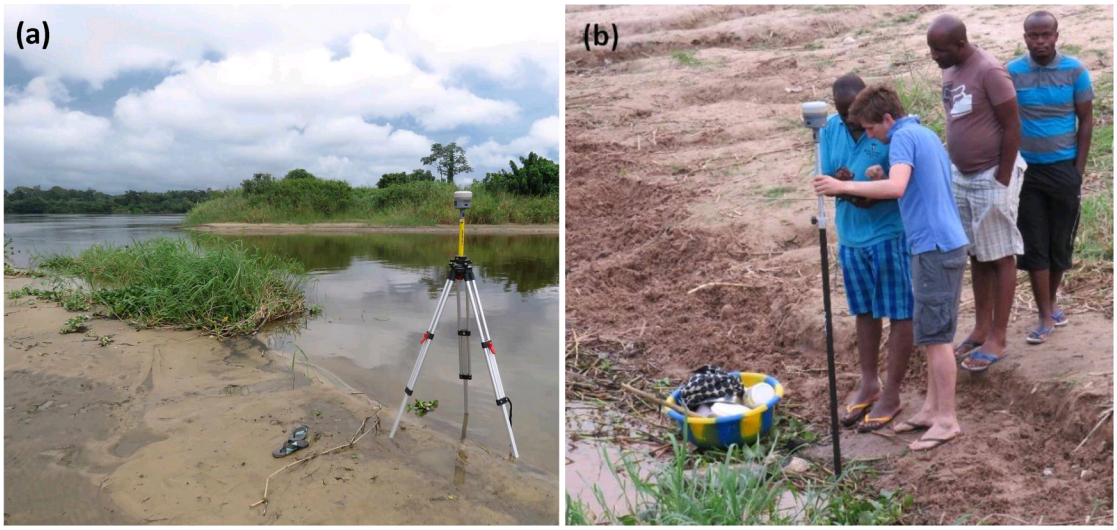

Figure 4-4. Shoreline measurements of water surface elevation (WSE) on the CMR: (a) GNSS instrument measuring WSE directly from a tripod set up over water (b) Use of a detail pole was often necessary to safely position the instrument over water.

In addition to measuring static WSE at shorelines whilst the boat was docked, efforts were made to acquire additional measurements from the boat whilst navigating, in order to reduce the number of boat stopping points required, and increase the spatial density of the WSE measurements. This entailed setting the GNSS instrument up on an area of the boat with a clear view of the sky, such as the roof of the boat, to operate in a continuous measurement mode whereby it measures elevation at set distance or time intervals.

4.2.5 Bathymetry

River depth measurements were made using two Garmin GT22 single beam sonar echo sounders that were set up to provide a spatial coverage density of approximately 2 m distance between measurements. One sonar was installed on the main boat and measured depth whenever the boat was travelling. The main boat followed the established navigation route, and in accordance with the rules set out by the captain, did not deviate from this route. Therefore, the resulting sonar measurement track closely follows the stream-wise direction, covers only one channel thread, and does not provide cross sectional coverage. The other sonar was installed on the fibreglass boat and used at designated locations to survey cross sections and more detailed bathymetry. Specifically, it was used to survey a series of channel threads along the high resolution

study reach, and was also deployed during all ADCP measurements to verify the sonar and ADCP depth measurements were in agreement.

Each of the sonar devices comprise a transducer and a display. The transducers were fixed to the sides of the boats via metal brackets (Figure 4-5), away from any turbulence associated with the engines that were located at the rear of the boats.

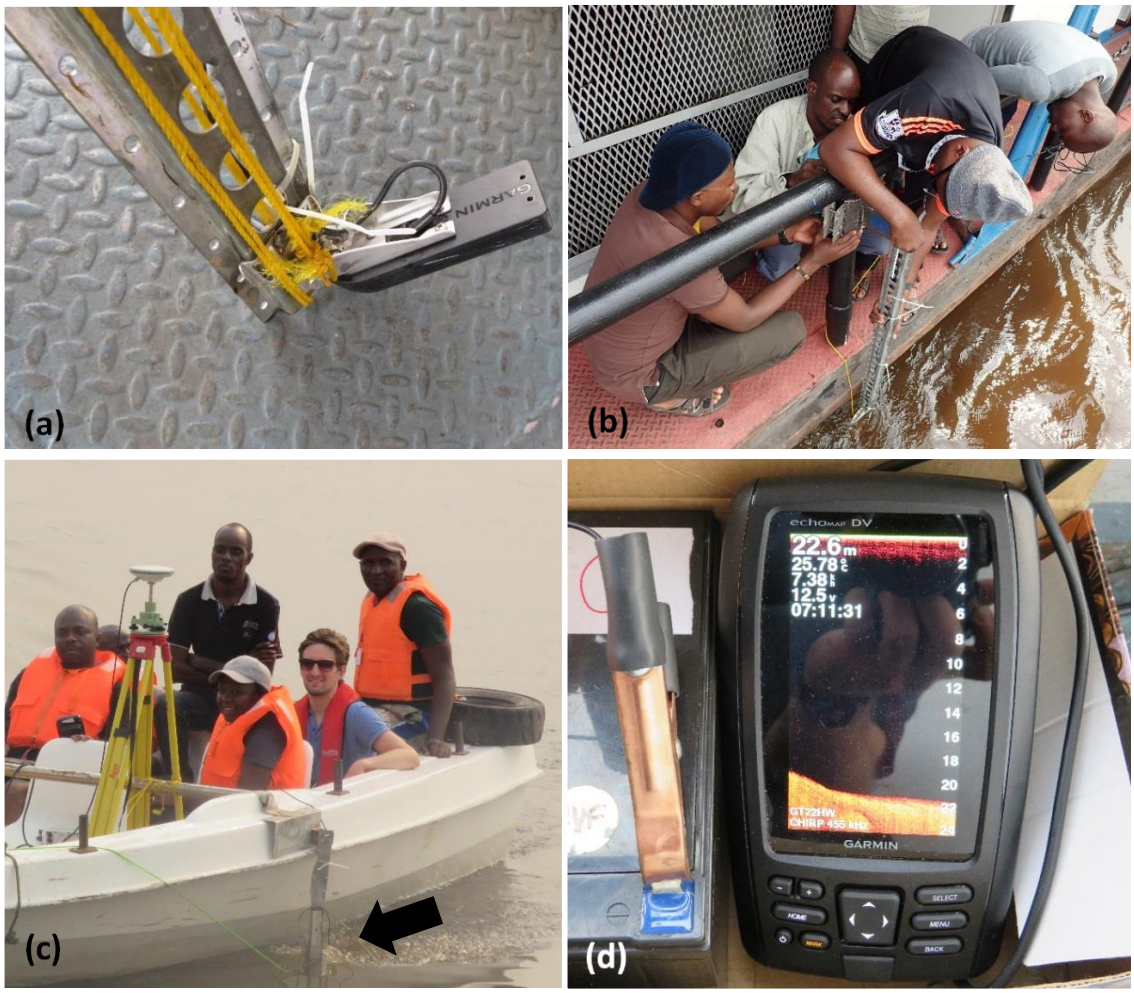

Figure 4-5. The two sonar echo sounders used to measure river depth: (a) one of the transducers fixed to its metal bracket; (b) one of the transducers being installed on side of the main boat; (c) the other transducer in operation, fixed to its metal bracket on the side of the fibreglass boat (transducer is submerged and not visible); (d) one of the sonar displays in operation.

4.3 Methods: Acquisition of Satellite Altimetry Data

In order to assess the spatial variability in WSS captured by satellite altimetry WSE data, longitudinal plots of altimetry derived WSEs along the CMR have been produced. Two periods are considered, July–August representing low flow and

corresponding to the timing of the field campaign, and December–January representing high flow. ENVISAT is the primary data source used for this purpose, it being the most widely used source of WSE in the Congo Basin. The widespread use of ENVISAT is due to its comparatively high spatiotemporal coverage and long temporal record—there are 23 overpasses, known as “virtual stations” (VS), available along the CMR Figure 4-6, that were operational from 2002 to 2010. Each VS has an average temporal coverage of 10 measurements per year. Relevant examples of ENVISAT’s use include studies of wetland inundation dynamics and river/floodplain interactions (Lee et al., 2011), estimation of discharge from space (Kim et al., 2019), and calibration and performance evaluation of a hydrodynamic model of the CMR (O’Loughlin et al., 2020). ENVISAT accuracy for sufficiently wide rivers (~1 km wide) has been shown to be less than 0.3 m (Frappart et al., 2006).

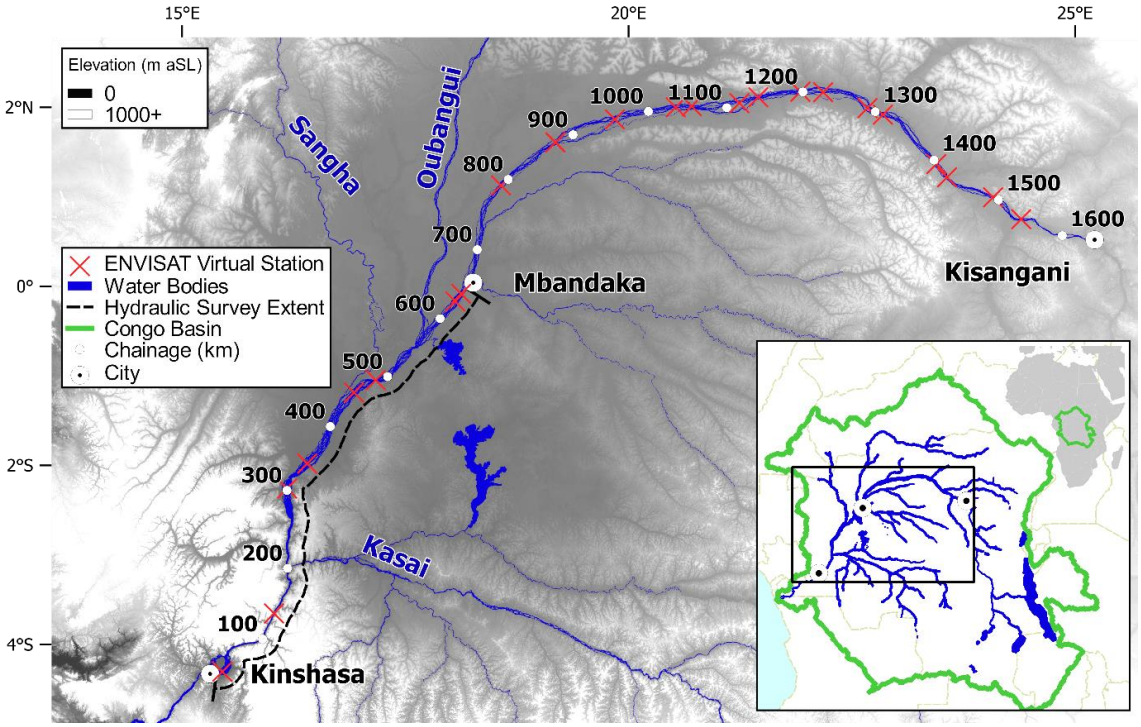

Figure 4-6. Map showing 2017 hydraulic survey extent and mainstem ENVISAT Virtual Station locations (Santos da Silva et al., 2010). Malebo Pool is situated at chainage 0–50 km, The Chenal runs from chainage 50–270 km. Three lateral constrictions in river width are located at chainage 315, 480, and 550 km. Elevations are from MERIT (Yamazaki et al., 2017); water bodies are from LANDSAT (CARPE, 2017; O'Loughlin et al., 2013).

Data from the Sentinel-3A satellite that became operational in 2016 is also obtained for comparison purposes. There is less than 4 years of data at the time of writing, and performance evaluation is limited, although a recent study on the Niger River

reported improved performance of Sentinel-3A compared with well- established altimeters including ENVISAT (Normandin et al., 2018). However, it was operational during our field campaigns so is of use for comparative purposes. ENVISAT and Sentinel-3A data sets have been obtained from the Hydroweb database (Santos da Silva et al., 2010). Published ICESat data (Zwally et al., 2012; O'Loughlin et al., 2016a) has also been used for comparative purposes, although its use is limited in this study because ICESAT data are unavailable during July, August, or January and its lack of repeat passes produced only single measurements in time.

4.4 Results

4.4.1 Water Surface Profiles from Satellite Altimetry

CMR water surface profiles (WSPs) that are representative of seasonal low and high flow were derived by plotting the mean average of all WSEs recorded during July and August, and December and January (low flow and high flow, respectively) at each ENVISAT VS. This plot is shown in Figure 4-7. WSS calculated for each pair of WSEs was also computed, and these are plotted, along with effective river width derived from Landsat imagery (O'Loughlin et al., 2013).

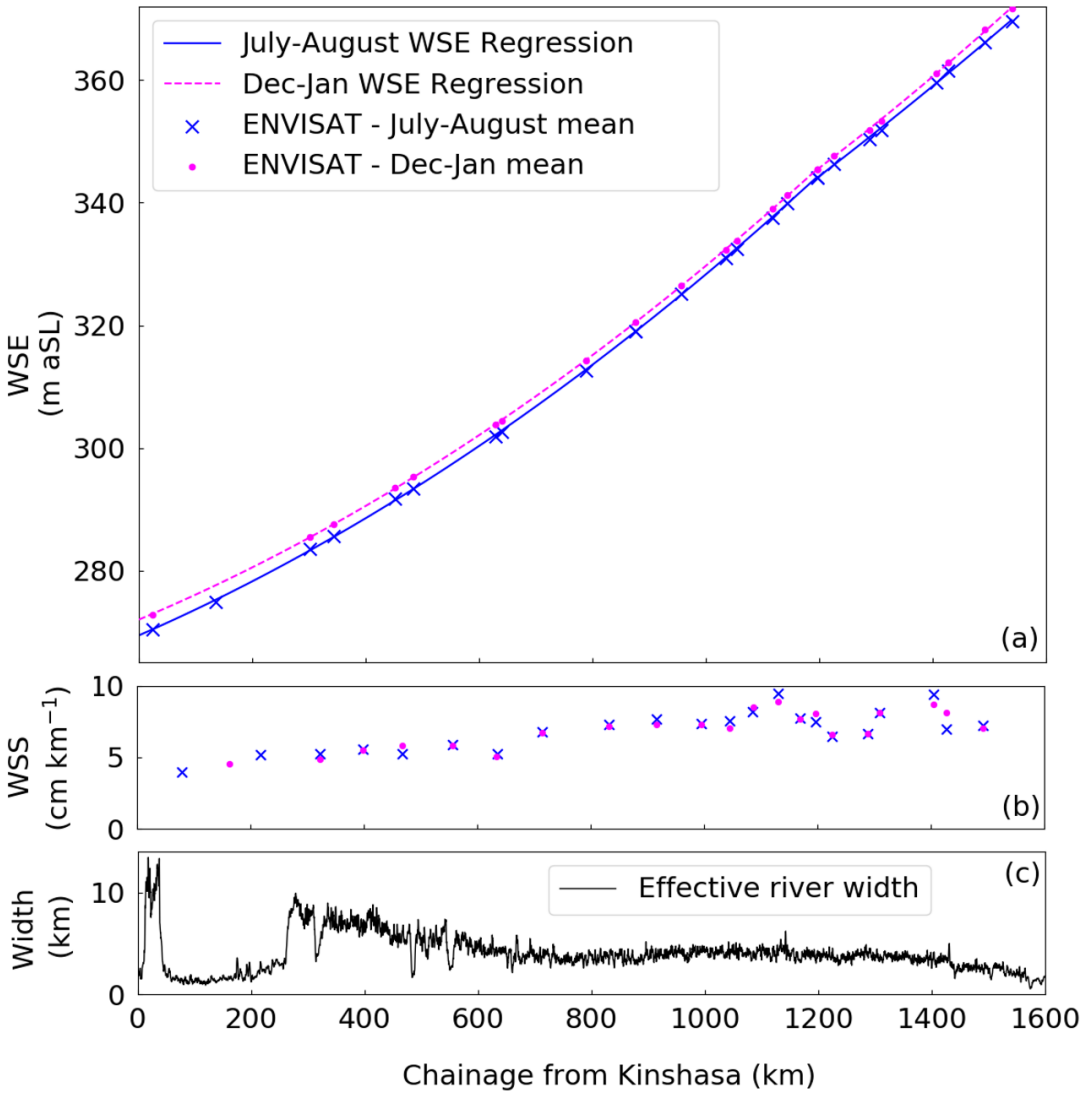

Figure 4-7. Longitudinal sections through the CMR: (a) mean ENVISAT water surface elevations (WSEs) for July–August (low flow) and December–January (high flow), each with second-order polynomial curves fitted between chainage 0–1,200 km and 1,200–1,600 km; (b) low and high water surface slopes (WSS) calculated for each pair of mean WSEs; (c) effective river width derived from Landsat Imagery (O'Loughlin et al., 2013).

Interrogation of the ENVISAT data reveals that 1,200 km of the middle reach WSE from Kinshasa to approximately the upstream maximum extent of the Cuvette Centrale is well represented by a second- order polynomial regression, describing a gradual flattening of the slope in the downstream direction. For low- flow WSEs, maximum regression residual is 0.36 m, and RMS is 0.19 m. For high- flow WSEs, maximum regression residual is 0.26 m, and RMS is 0.15 m. From 1,200 to 1,600 km the WSS becomes more variable. Based on a separate second- order polynomial, maximum regression residual for low flows is 0.55 m, and RMS is 0.30 m, and for high-

flow WSEs, maximum regression residual is 0.36 m, and RMS is 0.24 m. The results are broadly in agreement with those of O'Loughlin et al. (2013) who computed CMR WSS for the month of June using ICESat altimetry, and found WSS to reduce from 9 cm/km to 3 cm/km in the downstream direction. These results suggest that 1200 km of the CMR has a highly predictable WSP, with very little variability in WSS. However, it is not known whether the density of spatial coverage is sufficient to identify more localised variations in WSS that may exist. The in-situ measurements are used to investigate this in section 4.5.

4.4.2 2017 Field Campaign Results

The 2017 field campaign was executed on a trip between Kinshasa and Mbandaka between 28 July and 16 August 2017. The spatial distribution of WSE, ADCP, and bathymetry measurements acquired are shown in Figure 4-8.

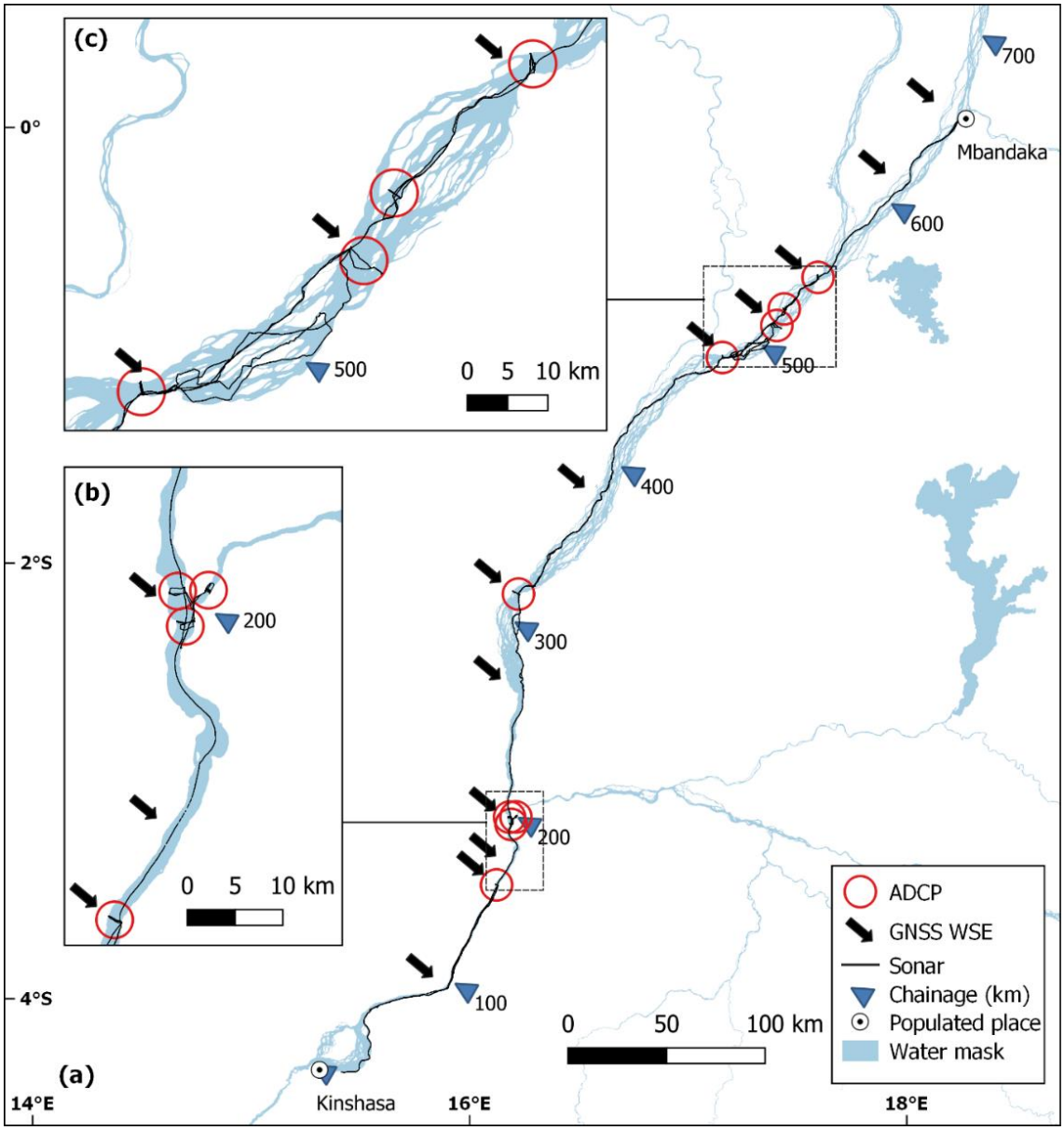

Figure 4-8. Spatial coverage of WSE, ADCP and bathymetry measurements acquired in 2017 field campaign. "Chainage" is river distance measured upstream of Kinshasa. Malebo Pool is situated at chainage 0–50 km, the Chenal runs from chainage 50–270 km. Three lateral constrictions in river width are located at chainage 315, 485, and 550 km. Water mask is from O'Loughlin et al. (2013). Localised finer scale plots at (b) the Kasai confluence and (c) the 2017 high resolution study reach are shown in order to clearly display areas of high density measurements.

ADCP Measurements

ADCP transects were acquired at eight sites on the mainstem, plus one transect on the Kasai. Between chainage 270 km and 650 km, where the study reach is multichannel, most ADCP sites were located at sections where the channel is relatively narrow and single-thread. There are two exceptions to this at chainage 515 km and 525 km, both obtained as part of the high resolution study reach measurements (Figure 4-8c) that aim to sample hydraulic conditions more representative of the multichannel CMR. The chainage 515 km site is at a 5 km wide section of channel; and the chainage 525 km site is a single channel thread that conveys approximately 50% of the total channel discharge. The ADCP discharge measurement at chainage 160 km was within 1% of a discharge measurement made at Kinshasa on the same day using an established rating relationship (Institut de recherche pour le développement, 2019). ADCP measurement precision was also checked with transect repeatability tests at each site, which showed measurement variability to be no greater than 2%. ADCP results are shown in Table 4-1.

Table 4-1. ADCP Results from 2017 Field Campaign. Values are the mean values for all transects; Std Devs are the standard deviations of the transects at each site.

ID	Site name	Chainage (km)	Date (dd/mm)	No. of transects	Discharge (Q) (m^3/s)	Std Dev of Q (m^3/s)
1	Kunzulu	158	30/07	2	28,967	451
2	Kwamouth DS	197	04/08	2	29,265	86
3	Kasai	199	03/08	3	7,255	98
4	Kwamouth US	200	03/08	3	22,408	94
5	Bolobo	317	06/08	2	22,419	118
6	Lukolela	485	08/08	3	19,761	164
7	Clock Point	515	10/08	2	20,955	426
8	Single ch. thread	525	10/08	2	9,846	199
9	Ngombe	547	11/08	2	22,473	193

ID	Transect width (m)	Mean depth (m)	Velocity (V) (m/s)	Std Dev of V (m/s)	Flow area (m^2)	Mean bin size (m)	Q at Kinshasa[1] (m^3/s)
1	1540	16.8	1.12	0.01	25,872	1.1	28,830
2	1905	12.7	1.21	0.06	24,205	1.8	28,490
3	606	12.7	0.95	0.03	7,696	1.1	28,520
4	1851	12.9	0.94	0.03	23,860	1.3	28,520
5	4119	7.2	0.76	0.02	29,702	1.4	27,910
6	1757	11.7	0.96	0.01	20,585	1.3	28,710
7	5083	5.0	0.82	0.04	25,592	1.4	29,210
8	1865	6.1	0.87	0.01	11,382	1.4	29,210
9	2468	11.8	0.77	0.03	29,204	1.2	29,580

1. On same date that ADCP was taken, obtained from SO-HYBAM website: https://hybam.obs-mip.fr/data/

Static WSE Measurements

Static GNSS WSE measurements were obtained at 12 shoreline locations along the CMR. Where possible, measurement locations were selected to obtain coverage of key morphological features such as confluences and width constrictions. Efforts were also made to retain a relatively consistent spatial interval between measurements, but this was not always possible, due to restrictions on where it was permissible or convenient to dock the boat. Precision of the GNSS static measurements was checked by measuring the elevation of an historic benchmark structure multiple times over a three day period, which gave a standard deviation of 3.4 cm. Static measurement precision checks were also carried out by repeating measurements at each WSE measurement location, and computing their standard deviations. This was no greater than 6.4 cm. Measurements are summarised in Table 4-2.

Table 4-2. Static GNSS WSE Measurements from 2017 Field Campaign.

Date (dd/mm)	Site name	Chainage (km)	WSE to EGM96 (m)	WSE to EGM08[1] (m)	No. of Obs.	Std Dev of WSE
29/07	May Ndombe	98	273.18	273.20	3	0.020
29/07	Kunzulu	158	274.82	274.77	1	0.000
31/07	Kunzulu	158	274.81	274.76	6	0.064
01/08	Mfumunzale	169	275.08	275.01	3	0.019
05/08	Kwamouth	199	275.60	275.50	5	0.012
05/08	Sandy Beach	264	279.34	279.13	7	0.016
06/08	Bolobo	315	283.47	283.25	9	0.028
07/08	Bokombo	383	287.65	287.50	6	0.010
08/08	Lukolela	485	292.56	292.42	3	0.007
10/08	Bweta	516	294.28	294.22	2	0.023
10/08	Ngombe	547	295.90	296.25	3	0.001
13/08	Mikuka	613	299.78	300.21	3	0.010
16/08	Mbandaka	659	302.26	302.63	4	0.030

[1.] Conversion from EGM96 to EGM2008 done using web-based conversion tool by Karney (2014), accessed at: https://geographiclib.sourceforge.io/cgi-bin/GeoidEval

Continuous WSE Measurements

Continuous measurements of WSE (approximately 50–100 m spacing) from the roof of the moving boat were mostly unsuccessful in 2017. All attempts but one were abandoned when large step changes in WSE measurements (up to one metre) were observed, indicating that the instrument had lost its satellite convergence, likely because the vertical movements of the boat (pitching, rolling, and heaving) were too severe. This did not happen on one 50 km reach however, located at the entrance to the Chenal, between chainage 260 km and 310 km. When in continuous measurement mode, the instrument vertical tolerance settings were set by Trimble to be 10 cm (i.e. double that of the static measurements), so accuracy is lower. This accuracy was verified by comparing the measurements at the downstream and upstream ends of the reach with static mode measurements, which showed differences of 5 cm and 11 cm respectively here. The plotted raw measurements, contained in Appendix A.2, showed a large amount of noise however, which is attributed to vertical and tilting movements of the instrument due to boat movements. The additional error in WSE associated with boat movements is not straightforward to quantify and little guidance on this could be found in published literature or obtained through personal communication with Trimble's technical team. Altenau et al. (2017b) estimated such an error occurring from a similar instrument setup by applying a Gaussian filter to the raw water surface profile and calculating the root-mean-square error (RMSE) between the raw measurements and the Gaussian filtered profile. They noted that the sample window size over which to apply the filter was selected to eliminate noise, but preserve sub-kilometre scale features. Attempts were made to apply a Gaussian smoothing filter to the data presented here in a similar manner, these are documented in Appendix A.2, and for a window size of 75 measurements, gave a RMSE between the raw measurements and Gaussian filtered profile of 6 cm. When combined with the instrument RMSE of 10 cm, this gives a total error of 16 cm for these measurements.

Bathymetry Measurements

The bathymetry measurements comprise cross sectional measurements at each ADCP site, stream-wise measurements along the navigation route, and a combination of stream-wise and 'zig-zag' tracks through a series of channel threads on the high resolution study reach (Figure 4-8c). Bathymetry measurements were verified by interrogating all crossover points (where depth was measured twice within 5 m horizontally) along the high resolution study reach. This is documented in Appendix A.3, and gave a standard deviation of 0.34 m or 8%.

All sonar measurements of depth were converted to bed elevation values by subtracting them from local WSEs that were derived by linearly interpolating the GNSS WSE measurements. This was carried out in the QGIS open source geographic information system (GIS) application (QGIS Development Team, 2019), and entailed firstly creating a centreline of the channel by applying a Voronoi tessellation (e.g. Nyberg et al., 2015) to a version of the water mask created by O'Loughlin et al. (2013) without any islands included. Regularly spaced points were then created along this centreline, and these points were then assigned a pair of GNSS WSE values according to the nearest upstream (WSE_{us}) and downstream (WSE_{ds}) values. Then, all points were assigned a chainage (C_{interp}) using the QGIS Linear referencing plugin, and subsequently assigned an interpolated WSE value (WSE_{interp}) by applying the following formula:

$$WSE_{interp} = WSE_{ds} + \left\{\left(\frac{C_{interp} - C_{ds}}{C_{us} - C_{ds}}\right)(WSE_{us} - WSE_{ds})\right\} \quad \text{Eq. 4-1}$$

Where C_{ds} is the chainage of WSE_{ds}, and C_{us} is the chainage of WSE_{us}. Finally, each sonar measurement was assigned its nearest WSE_{interp} value using a nearest neighbour spatial join, and sonar bed elevation computed by subtracting sonar depth from WSE_{interp}. Results of the stream-wise bathymetry measurements resampled at 50 km reach intervals are summarised in Table 4-3.

Table 4-3. Stream-wise bathymetry measurements resampled at 50 km intervals.

Chainage (km)	Mean bed elevation (m ASL)	Mean depth (m)	Max depth (m)	Std Dev of depth (m)
0	261.0	9.0	15.7	2.3
50	256.9	14.8	36.3	7.5
100	252.0	21.5	50.3	10.2
150	253.9	20.9	45.0	7.4
200	261.8	15.3	39.9	7.6
250	271.1	8.4	26.7	5.4
300	275.3	7.0	22.2	3.9
350	278.7	7.1	19.7	3.1
400	280.6	8.0	19.7	3.4
450	283.5	7.6	19.2	2.9
500	285.7	8.0	32.0	5.6
550	287.7	7.9	32.7	5.2
600	291.4	7.6	23.7	3.5
650	292.9	8.5	31.8	4.5

4.4.3 2019 Field Campaign Results

The 2019 field campaign was executed on a trip between Kisangani and Kinshasa between 30 July and 26 August 2019. Results from this campaign used in this chapter include WSE information at select locations only, derived from continuous GNSS measurements. In 2019, continuous GNSS measurements of WSE were more successful than in 2017, because a more stable platform for the GNSS instrument was provided by a barge that was pushed by the main boat, as shown in Figure 4-9. This was a reliable setup, and continuous GNSS WSE measurements were made along multiple reaches. Only a limited amount of the data acquired is used in this chapter, for the purpose of verifying aspects of the 2017 data analysis. Raw data, shown in Appendix A.2, shows a significant reduction in noise compared to the 2017 continuous measurements, due to improved stability of the barge over the 2017 boat roof setup.

Boat movement error was estimated to be 3 cm thereby resulting in 13 cm total error, by using the same method as for the 2017 measurements.

Figure 4-9. GNSS instrument set up on the barge being pushed by the main boat, for continuous WSE measurements on 2019 field campaign.

4.4.4 Hydraulic Characterisation with In-situ Measurements

In order to characterise the hydraulic behaviour of the reach surveyed, the static GNSS WSEs, ADCP discharge and velocity, and bathymetry measurements along the study reach are plotted longitudinally in Figure 4-10. The WSEs have been linearly interpolated piecewise to produce a water surface profile (WSP), shown in Figure 4-10a. Stream-wise bathymetry measurements depicting the river bed elevation profile have been plotted alongside this WSP, at two scales: 5 km, and 50 km. By averaging the bathymetry measurements over a 5- km interval (typical river width) and a 50- km interval (reach scale), localized variability is removed, which enables better interpretation of bed slopes and river depths at this scale. Standard deviations of the 5- km intervals express the variability in depth within each interval. Mean cross sectional bed elevations from ADCPs are also plotted. WSS are calculated for each WSE pair, and plotted in Figure 4-10b. Complementary hydraulic information from ADCP measurements including river discharge and mean channel velocity are plotted in Figure 4-10c and Figure 4-10d respectively.

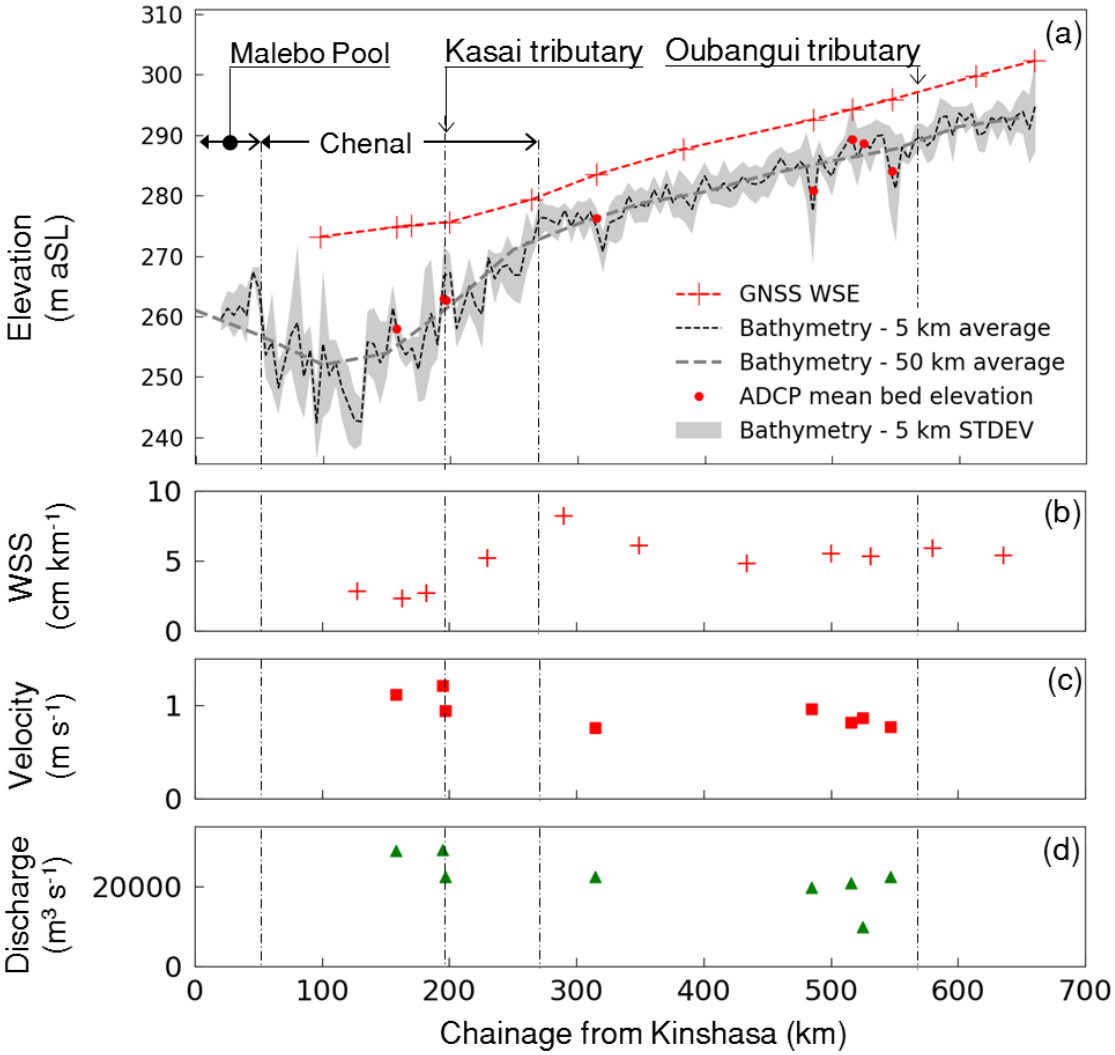

Figure 4-10. Key field campaign results plotted longitudinally: (a) static GNSS water surface elevations (WSEs), stream-wise bathymetry measured with sonar and averaged over 5- and 50-km intervals, and mean cross sectional bed elevations from ADCPs; (b) water surface slope (WSS) calculated from each WSE pair; (c) acoustic Doppler current profiler measured cross-sectional average velocities; (d) acoustic Doppler current profiler measured discharge (including individual channel thread measurement at chainage 525 km). STDEV denotes standard deviation.

Along the reach between chainage 300 km and 650 km, referred to as the multichannel reach for the remainder of this chapter, the in situ WSE behaviour is as shown by the ENVISAT measurements. WSS is highly regular (5–6 cm/km), most notably through chainage 485–610 km where there are four WSE measurements, and the river includes significant morphological features including two major width constrictions and the Oubangui confluence. The 50 km bathymetry shows that bed slope is relatively constant and almost parallel to the WSP, and that depth remains constant

across major confluences including the Oubangui. The 5 km bathymetry shows significant variability, some of which appears to correlate with changes in width. Specifically, the bathymetry locally deepens at chainage 315, 485, and 550 km, where the river width is constricted. Three of the ADCPs were acquired at these constrictions, and their mean bed elevations verify this increase in depth at constrictions, particularly at chainage 485 and 550 km, where mean depth is 12 m. Moreover, the two ADCPs obtained at chainage 515 km and 525 km where the river channel width is more typical of the reach show mean channel depth (channel thread depth at chainage 525 km) to be 5–6 m, which is relatively shallow. Measured mean cross- sectional velocities along the multichannel reach are in the range of 0.75–0.95 m/s, and do not appear to vary with channel depth or width.

Marked changes in channel geometry and hydraulics is evident at approximately chainage 300 km, where the CMR exits the Cuvette Centrale and enters the Chenal. As the river planform changes to being narrow and single-thread at chainage 270 km, the WSS varies considerably, initially steepening to 8 cm/km as it approaches the entrance to the Chenal and causing especially shallow river depths here. The WSS then flattens after entering the Chenal and reduces to only 2 cm/km downstream of the Kasai confluence. The 50 km bathymetry is variable and consistently differs from the water surface slope. In the 50 km reach upstream of the Kasai confluence, the bed slope is 19 cm/km, before flattening out and eventually becoming negative in the 50 km reach upstream of the Malebo Pool. Hydraulic mean channel depth is 13 m upstream of the Kasai confluence, and shows no increase immediately downstream, but does increase to 17 m over a distance of 50 km. Velocities are in the range of 0.94–1.2 m/s, and show a considerable flow acceleration occurs across the confluence with the Kasai.

Continuous WSE Measurements

In linearly interpolating between the WSEs piecewise, the water surface profile has been approximated as being planar between WSE measurements, which may neglect variability in WSS that manifests between measurements and result in significant WSE errors. To assess this planar approximation, high resolution WSPs have been derived from processing continuous WSE measurements. The processing involved firstly checking the raw data for any evidence of loss of convergence or permanent shifts in the instrument's position on the boat (i.e. large vertical step changes in WSE), which would invalidate the measurement set. Raw measurements were then resampled to 5 km resolution to reduce measurement errors. The Gaussian filtered raw measurements have not been used for this purpose, as they still show some error in WSE (some vertical steps

could not be removed, irrespective of the window size used). In adopting a 5 km resolution, the error in WSE is estimated to reduce from 12–16 cm to 1.5–2 cm, by assuming the error is normally distributed and thereby assuming error reduced proportional to $1/\sqrt{n}$; n being the number of measurements, typically equalling 75 per 5 km. With regards to WSS, a combined WSE error of 4 cm across a 5 km reach present a 2 cm /km error , which is significant given WSS on the CMR is typically only 5-6cm/km. Thus WSS cannot be reliably obtained from the 5 km WSEs. Nevertheless, they serve the purpose of validating the planar approximation between static WSE measurements.

Figure 4-11 shows continuous WSE measurements acquired in 2017 at chainage 270–310 km, plotted on a sub-plot of Figure 4-10a.

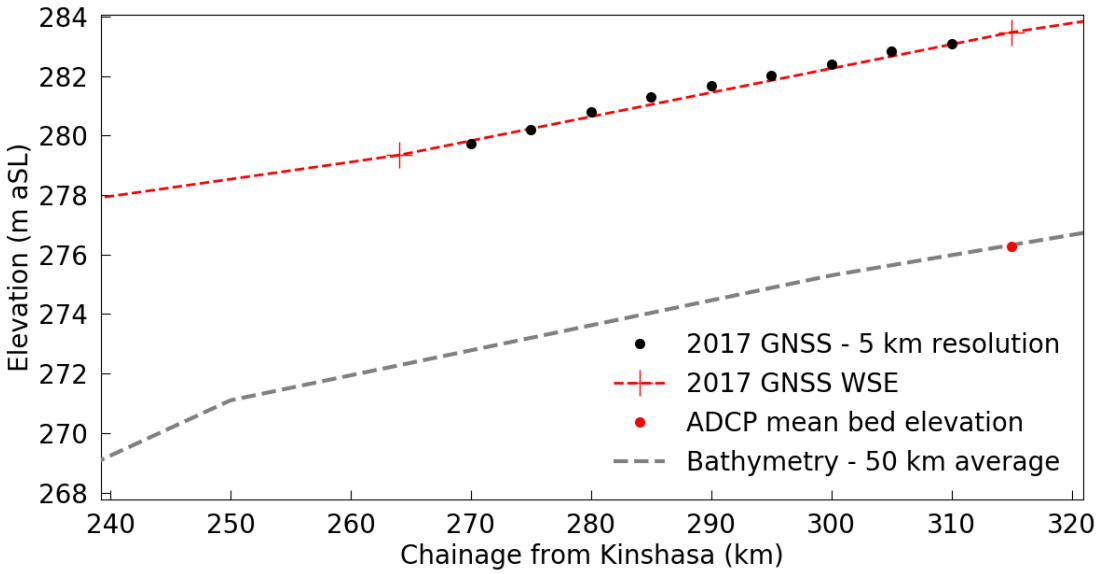

Figure 4-11. Continuous WSE measurements obtained in 2017, resampled at 5 km intervals, plotted on a sub-section of Figure 4-10. 5 km bathymetry omitted for clarity.

From Figure 4-11 it can be seen that the planar approximation results in a small error (maximum 0.25 m) along this reach, as a result of the finer scale curvature that is captured at the 5 km resolution. Similar results are seen in the continuous WSE measurements acquired in 2019. The high resolution WSP plotted in Figure 4-12 was acquired during 2019 along a 150 km reach that includes the Oubangui confluence, the width constriction at chainage 550 km, and the width constriction at chainage 485 km. The error resulting from the planar approximation is also small (again, maximum 0.25 m). Note that a static GNSS WSE measurement at chainage 620 km was omitted from this analysis, as it is not considered reliable. An assessment of this measurement is included in Appendix A.4.

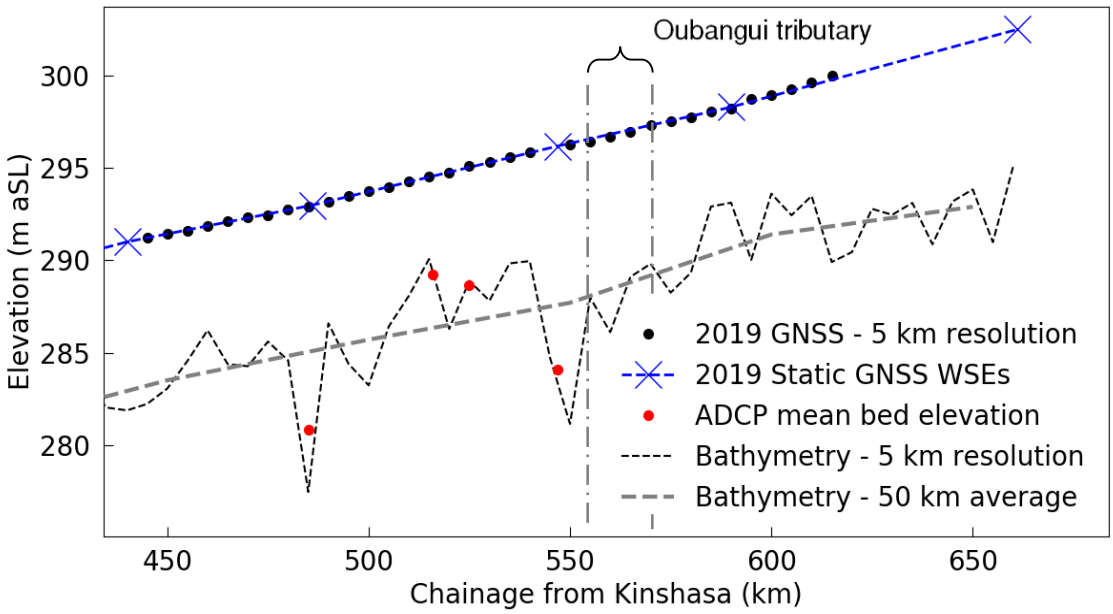

Figure 4-12. Continuous WSE measurements obtained in 2019, plotted on a sub-section of Figure 4-10. 2017 GNSS WSEs and Std-Dev. of 5 km bathymetry omitted for clarity. Oubangui tributary label indicates 20 km lateral inflow width, i.e. where the left and right banks join the mainstem.

A high resolution WSP was also acquired through 150 km of the Chenal, including its entrance, and is shown in Figure 4-13. Errors resulting from the planar approximation are again small (a maximum of 0.27 m). Figure 4-13 also confirms the WSS variability observed at the Chenal entrance in 2017. These results show that the planar approximation between static GNSS measurements spaced on average 50 km apart is an acceptable assumption for most hydrodynamic applications, including flood inundation and fluvial navigation. This may not be the case for measurements with a less dense and inconsistent spatial coverage, however.

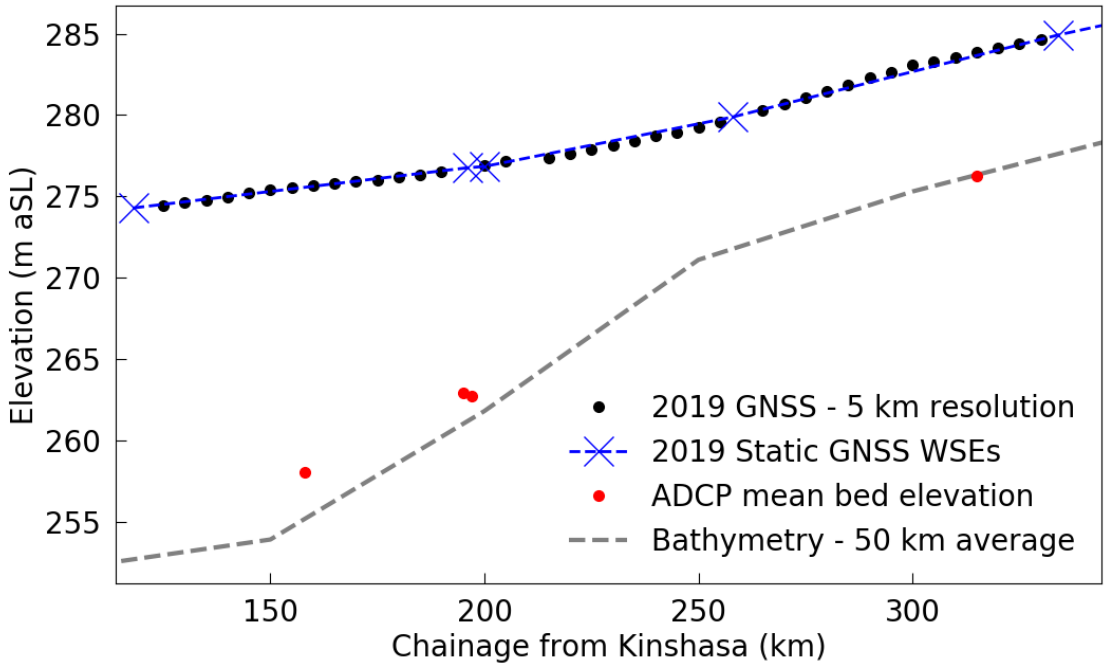

Figure 4-13. Continuous WSE measurements obtained in 2019, plotted on a sub-section of Figure 4-10. 2017 GNSS WSEs and 5 km bathymetry omitted for clarity.

4.5 Analysis and Discussion

The in-situ measurements provide significant new insights into the hydraulic functioning of the CMR. Through the multichannel reach, the almost parallel nature of the bed slope and WSS indicates that flow conditions are close to being uniform longitudinally. Significant morphological features including channel width constrictions and the Oubangui confluence do not appear to cause any appreciable longitudinal non-uniformities in WSS, known classically as gradually varied flow (GVF) profiles (e.g. Chow, 1959). This observed lack of WSS variability is surprising given the diverse and complex planform of the multichannel reach, and contradicts previous expectations, based on relatively sparse WSE observations and very limited knowledge of bathymetry, that the constrictions in channel width and Oubangui confluence cause widespread backwater effects (i.e. a 'M1' GVF curve) up to 60 km long during low flows (O'Loughlin et al., 2013). Of the small velocity variations that were observed through the multichannel reach (Figure 4-10c), velocities at two of the three width constrictions surveyed are lower than the wide multichannel values. Only the chainage 485-km constriction velocity shown to be slightly higher than the multichannel values. This shows the width constrictions do not cause significant flow accelerations during low flows, that mass is conserved predominantly by a local increase in channel depth, and that the channel bed is adjustable through these constrictions.

Whilst greater WSS variability during higher flow conditions is not discounted, and may occur as a result of bank and island topographic effects that manifest during inundation, the observation that bathymetry does not generate WSS variability is applicable to all flow conditions, since water surface is most sensitive to bathymetry during low flow conditions (e.g. Garambois et al., 2017; Frasson et al., 2017). The observed absence of bathymetric controls on WSE is significant, as it implies that a relatively coarse and simple physical representation of bathymetry coupled with a spatially uniform river channel friction may suffice in hydrodynamic models for predicting water surface dynamics. This has been demonstrated in other large rivers such as the Amazon (Trigg et al., 2009), but is an important finding on a morphologically complex multichannel river where obtaining a full bathymetry data set is challenging.

The significant change in hydraulics and specifically WSS at the entrance to the Chenal has not been noted before. The drawdown of the WSP at the Chenal entrance is converse to the backwater conditions that were thought to occur here (O'Loughlin et al., 2013), and appears to be caused by a steepening of the bed slope, known otherwise as a negative bottom slope break (Montazem et al., 2019). Downstream of the Kasai confluence, the flattening of the slope indicates backwater conditions, with the Malebo Pool acting as a downstream hydraulic control and marking the commencement of supercritical flow conditions downstream. At the Kasai confluence, the flow acceleration and absence of any immediate increase in channel depth or cross sectional area is a behaviour widely observed at confluences (Robert, 2003), albeit mostly on small to mid-size rivers. Confirmation that such a large-scale confluence conforms to classic river confluence behaviour is valuable, given aspects of large river confluences have been shown to behave differently to smaller systems; one example being the apparent absence of channel scale 'secondary' (i.e. lateral cross channel) flows in large river confluences (Parsons et al., 2007).

4.5.1 Satellite Altimetry Performance

Accurate WSE and WSS information is important for characterising the hydraulic behaviour of river reaches for a range of hydrodynamic purposes, including derivation of discharge. The 2017 GNSS WSP, and the complementary discharge and bathymetry information, provide an opportunity to assess the performance of satellite altimetry with respect to estimation of WSE, WSS, and discharge. Of particular interest is the WSS variability at the Chenal entrance, which is notably absent in the ENVISAT WSPs plotted in Figure 4-7, and in the ICESat WSS assessment of O'Loughlin et al. (2013). Because of its location immediately downstream of the Cuvette Centrale, the Chenal entrance is ideally located for providing highly valuable wetland outflow data. Moreover, the

physiography of the river in this location is conducive to obtaining requisite measurements of river width, in the sense that it is single channel, does not possess extensive vegetated floodplains that obscure water extents in much of the CRB, and has a relatively stable planform morphology (Pekel et al., 2016). To examine the performance of satellite altimetry, water surface profiles from three satellite altimetry datasets (mapped in Figure 4-14) have been plotted longitudinally in Figure 4-15, along with the 2017 GNSS WSP.

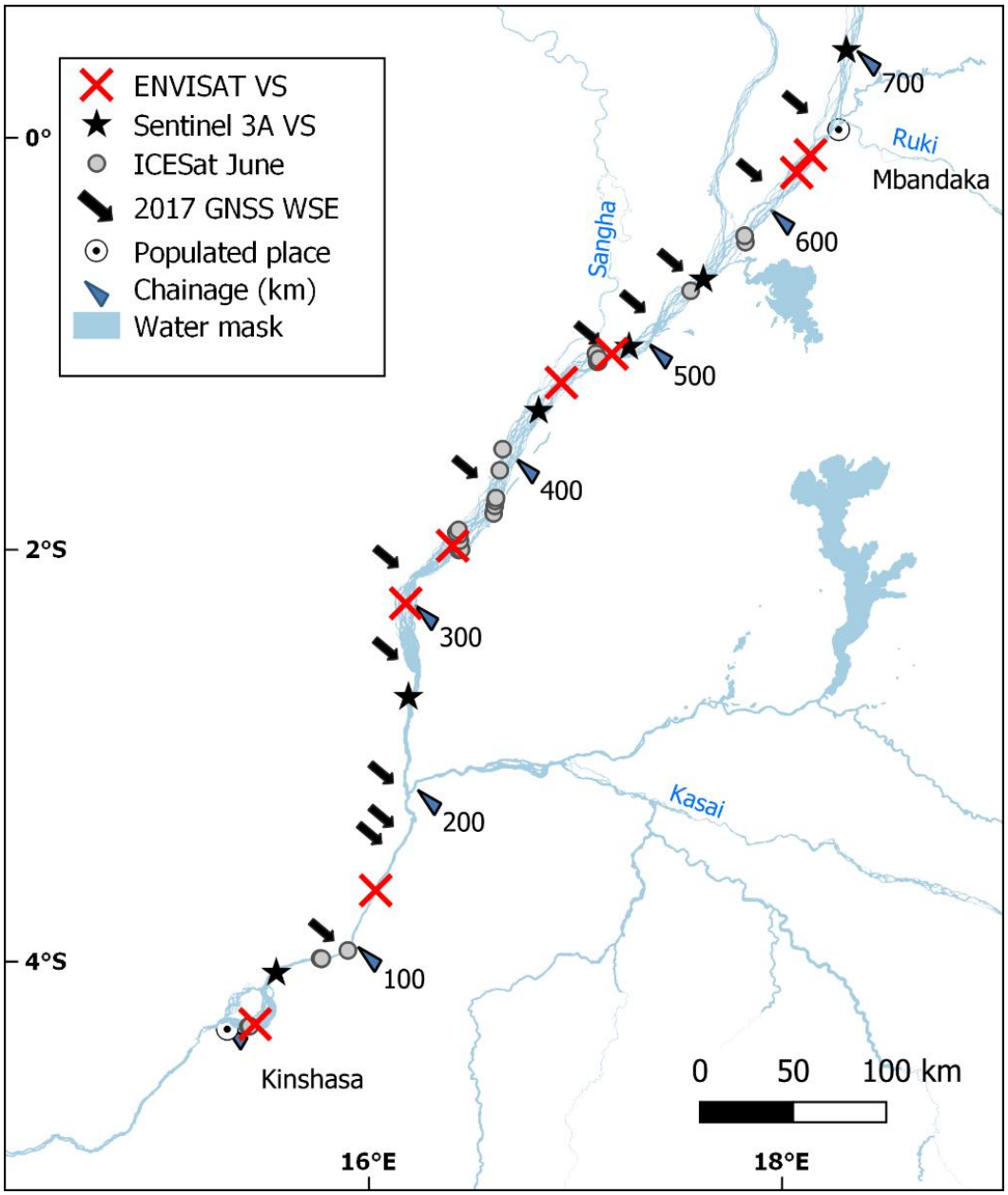

Figure 4-14. Locations of satellite altimetry measurements along the 2017 field campaign reach. ICESat from O'Loughlin et al. (2016a), Sentinel-3A and ENVISAT from Hydroweb (2019).

An initial comparison between the ENVISAT and 2017 GNSS data showed that the GNSS WSEs were consistently lower than the mean low- flow ENIVSAT WSEs plotted in Figure 4-7, which resulted in use of the minimum July–August ENVISAT WSE at each VS instead of the mean. The plotted minima are shown to be highly representative of conditions during the field campaign, consistently lying close to the GNSS WSP. The use of minima instead of mean had no noticeable effect on the regression analysis; repeating the regression analysis for the ENVISAT minima gave a standard deviation of 0.25 m and max residual of 0.56 m for chainage 0–1,200 km.

Alongside ENVISAT, data from the Sentinel-3A altimetry mission is also plotted. As the mission has only been operating since 2016 and is currently operational, WSEs representative of the 2017 field campaign were obtained by temporally interpolating measurements made by the satellite around the field campaign period. The plotted values show reasonable agreement with the GNSS WSP, with a maximum deviation of 0.60 m, which is partially due to the use of temporal linear interpolation between data points that are up to 3 months apart. In addition, June ICESAT measurements for three separate years are plotted, temporal averaging not being possible due to ICESat not making repeat overpasses at the same location. The ICESat measurements show greater deviation from the GNSS WSP, which is explained by the river's slightly different hydrodynamic conditions in June (Becker et al., 2014), and the variability of WSE over a monthly period.

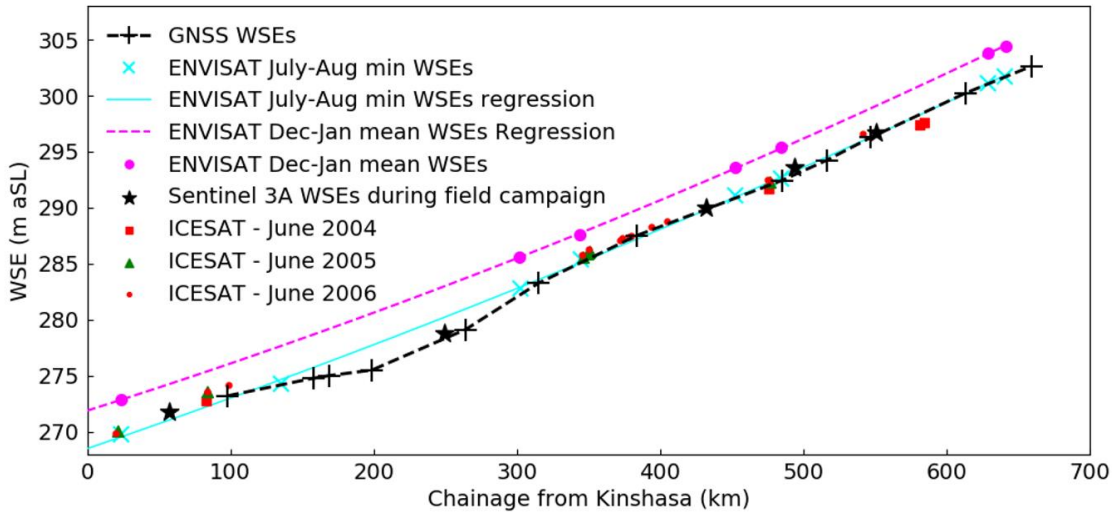

Figure 4-15. Plot of 2017 static GNSS WSEs and comparative low-flow altimetry WSEs from ENVISAT, Sentinel-3A, and ICESAT. High-flow (mean December and January) ENVISAT WSEs are also shown to convey the magnitude of flood-wave amplitude. GNSS WSEs are linearly interpolated piecewise. Sentinel-3A WSEs are linearly interpolated temporally to derive WSEs during 2017 field campaign.

Through chainage 325–650 km, the ENVISAT WSP closely matches the GNSS WSP, maximum deviation from the GNSS WSP being only 0.30 m at chainage 345 km. WSE pairs from ENVISAT and other repeat-pass profiling altimeters with a similar or greater density of spatial coverage (ENVISAT has a mean spacing of 70 km here) can therefore be spatially interpolated to derive longitudinally distributed WSE information. Another important implication is that estimates of WSS at a given location, based on WSE pairs, will be relatively independent of the particular locations of the two WSEs. Consequently, hydrodynamic models used to estimate discharge from WSE, WSS and width information should not show altimetry mission dependence: i.e. altimetry datasets with different overpass locations should provide consistent modelled estimates of discharge along a reach, without the necessity for model friction and bathymetry parameters to be recalibrated to a particular WSE dataset. Altimetry mission-independence is recognised an important quality for a hydrodynamic model to have (e.g. Paris et al., 2016), as it precludes the need for elusive calibration data such as in-situ discharge to be obtained concurrent to each altimetry dataset.

Through chainage 100–325 km, a different picture emerges. Much of this reach is a blind spot for ENVISAT and ICESat missions, which is a result of the orientation of the river being almost parallel to that of the altimetry missions and receiving no overpasses. Consequently, these altimeters do not detect the spatial variability in WSS. Due to insufficient spatial coverage, the low flow ENVISAT WSP overestimates WSE by 2 m between chainage 200–270 km, which is equivalent to over half of the annual flood-wave amplitude defined by the ENVISAT low and high flow WSPs. If the closest available pair of ICESat measurements are linearly interpolated, the overestimate is 2.9 m for the June 2005 measurements. Notably, there is a Sentinel-3A overpass at chainage 250 km, and measurements here identify that there is WSS variability at the Cuvette Centrale outlet. The overpass locations are not sufficient to fully describe the WSS, but are sufficient to define the WSE, and provides additional validation of the 2017 GNSS measurements.

Quantifying the effects of Altimetry WSE and WSS errors

The ENVISAT and ICESat overestimates of WSE could propagate upstream in hydrodynamic flood models and affect inundation predictions in the Cuvette Centrale and along the Kasai. Errors in either WSE or WSS that are present in all altimetry datasets would also affect modelled estimates of discharge through the reach. By applying Manning's equation to the river reach between chainage 200–270 km, the impact of the

WSE and WSS errors can be quantified in discharge terms. Manning's equation for uniform open channel flow conditions can be written as follows:

$$Q = \frac{1}{n} A R^{2/3} \sqrt{s} \qquad \text{Eq. 4-2}$$

Where Q is discharge (m^3/s), A is cross sectional area (m^2), n is Manning's hydraulic roughness coefficient ($s/m^{1/3}$), R is the hydraulic radius (m^2/m), and s is the WSS or the bed slope (m/m). By approximating flow conditions as being uniform and modelling the channel as rectangular with a bed elevation from the 50 km bathymetry plot (Figure 4-10), an in-channel n value can be derived using values of Q and WSE obtained from the field campaign. Q values can then by re-calculated using the previously derived value of n and values of s and WSE from the altimetry measurements. The calculation process is documented in Figure 4-16.

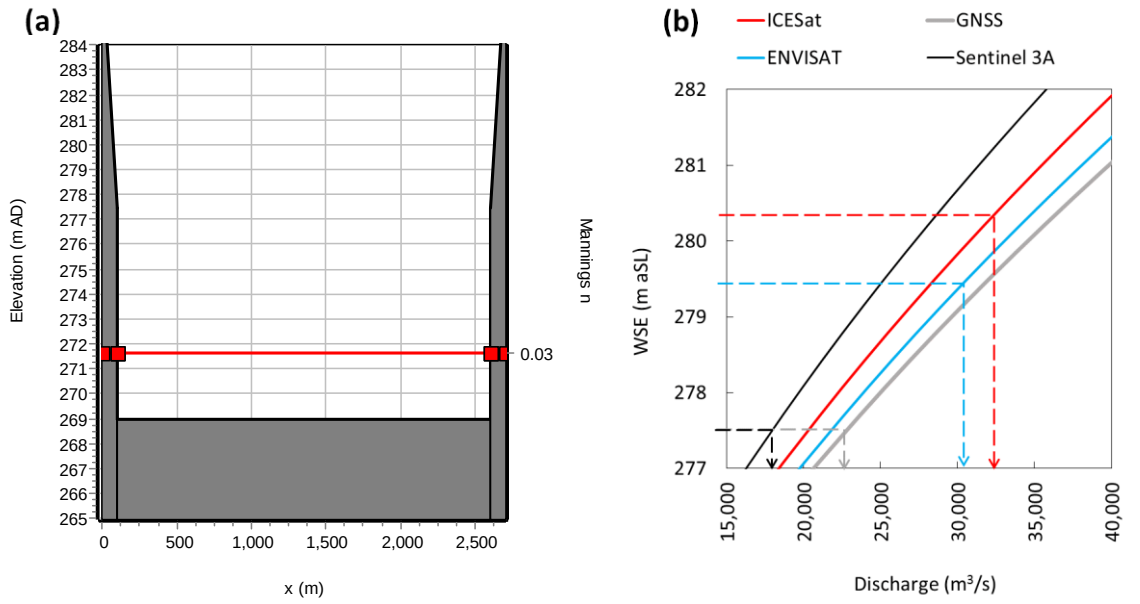

Figure 4-16. Discharge calculations for different WSE datasets: (a) Assumed channel geometry at Chainage 235 km, red line indicates manning's n value. Channel width is obtained from Landsat water mask (O'Loughlin et al., 2013), bed elevation is from 50km bathymetry data (Figure 4-10), above water bank side slopes modelled as 1 in 10 according to SRTM data (Yamazaki et al., 2017); (b) Calculated Q–H rating relationships resulting from the modelled channel geometry and the WSS values for each WSE dataset. Q–H relationships calculated using normal depth calculator tool within the Flood Modeller software package (Jacobs, 2019).

The initial calculation using the GNSS WSEs produced a manning's *n* value of 0.03, which is considered broadly consistent with published values for large low gradient rivers (e.g. Arcement and Schneider, 1984; Trigg et al., 2009). Other pertinent resulting parameters include a velocity of 1.0 m/s, which is close to the value of 0.95 m/s observed immediately upstream of the Kasai confluence, and a Froude number of 0.12, which illustrates the highly subcritical nature of this river. *Q*–*H* curves were then calculated for each altimetry WSE dataset according to their WSS estimates, and *Q* values corresponding to each altimetry WSE value were then derived. Calculations are summarised in Table 4-4.

Table 4-4. Results of discharge calculations for each WSE dataset.

WSE dataset	WSE at Chainage 235 km (m aSL)	*n*	*WSS* (cm/km)	*Q* (m^3/s)	*Q* difference (m^3/s)	*Q* difference (% abs)
GNSS	277.5	0.03	5.8	22,400	0	100%
ENVISAT	279.5	0.03	5.3	30,200	7,800	135%
ICESAT	280.4	0.03	4.6	32,800	10,100	145%
S3A	277.5	0.03	3.6	17,800	-4,600	79%

The discharge calculations reveal large discrepancies between the altimetry datasets from each other as well as from the field data: the Sentinel-3A discharge estimate is approximately half that of ENVISAT. Consequently, hydrodynamic models used to estimate discharge from WSE, WSS and width information will show a high level of altimetry mission dependence through this reach.

The lack of hydraulic visibility through the Chenal with satellite altimetry is surprising given the size of the Congo River and the range of altimeters that have measured the Congo's WSE. Such undetected spatial variations in WSS are likely to exist on other large rivers. The Surface Water and Ocean Topography (SWOT) mission will address this knowledge gap; SWOT's KaRIN interferometer will measure WSE with sub-kilometre spatial resolution at least once every 21 days (Biancamaria et al., 2016), providing more than sufficient WSE information for capturing WSS variability observed here. However, beyond SWOT's 3 year operational lifetime, it is likely that profiling altimetry instruments with limited spatial coverage densities will need to be relied on to

monitor WSE from space (CNES, 2019a). Furthermore, complementary river width information will not be available to the same extent as SWOT data. To obtain sufficient hydraulic visibility for measurement of variable WSS through river reaches, these altimetry instruments will need to provide a higher spatial coverage density than that currently offered by repeat pass altimetry instruments, by either reducing the distance between overpasses, or improving their consistency. As demonstrated by the findings presented here, this is true for even very large, highly subcritical river reaches whose water surface profiles are commonly assumed to vary linearly between sparsely spaced altimetry WSE measurements (e.g. Birkett et al., 2002; O'Loughlin et al., 2013; Paris et al., 2016). Long or non-repeat orbit profiling altimeters can offer a denser spatial coverage or higher- accuracy WSE data than VS data, and can be useful for parameterizing, calibrating, and validating hydraulic models and WSS measurements, particularly where the spatial coverage of VSs is inadequate. For example, the CryoSat-2 satellite altimeter provides dense spatial coverage with an inter-track distance of 7.5 km at the equator (Schneider et al., 2018), and the recently launched ICESAT-2 altimeter is expected to provide higher accuracy WSE information that can validate measurements of WSE and WSS from other altimeters (Escobar et al., 2015). However, the lack of temporal resolution in long or non-repeat pass altimeters (Jiang et al., 2017 reports 369 days for Cryosat 2) limits their use for the generation of WSPs, and the monitoring of changes in WSS over time that is necessary for measuring discharge from space.

4.6 Concluding Remarks

The first hydraulic research field campaigns in recent decades have been completed the middle reach of the Congo River, and have provided a rare opportunity to study the hydraulics of a large, complex planform river system. A large scale hydraulic characterisation has shown that the majority of the 650 km long summer 2017 study reach is characterised by only very gradual spatial changes in WSS (5–6 cm/km) and velocity (0.75–0.95 m/s) during low flows, neither of which are affected by changes in bathymetry, despite its highly diverse and multichannel nature. These results show that a relatively coarse and simple physical representation of river bathymetry may be sufficient for use in hydraulic models used to simulate water surface dynamics here, and potentially along reaches of other large multichannel rivers. However, this characterisation does not hold for a 150 km long reach located at the outlet of the Cuvette Centrale, where changes in bathymetric bed slope cause WSS to vary spatially from 2 cm/km to 8 cm/km. Pre-existing altimetry data sets perform poorly at estimating WSE and WSS in this reach; an ENVISAT- derived WSP deviates from field measurements by up to 2 m due to insufficient spatial resolution, which represents approximately half

the annual flood wave amplitude, or a 35% difference when used to compute discharge. These findings are unexpected for a reach of the world's second largest river that is hydraulically highly subcritical, and shows SWOT's high resolution measurements will provide major new insights into surface-water-topography features on even the world's largest rivers.

The data and analysis presented in this chapter are the first key steps in understanding this river, and enabling the development of hydraulically correct river models for this, and potentially other similarly large and morphologically complex systems. Further progress toward this may be achieved through numerical hydraulic modelling experiments used to identify effective representations of large multichannel river bathymetry in such models, and investigate water surface behaviour during differing flow conditions. This work also presents opportunities for testing the ability of discharge estimation algorithms to translate SWOT WSE measurements into discharge in large multichannel rivers; the in situ hydraulic data presented here may serve as a priori information and validation data.

CHAPTER 5
High Resolution Modelling of Multi-threaded Congo River Channels

5.1 Introduction

Quantification of river hydrodynamic processes is a key component of many earth science and engineering studies. For example, quantitative information on the rate at which flood waves propagate along river systems, channel – floodplain fluxes, and the extents and duration of inundation are required for many ecological, biogeochemical, and flood risk studies (Junk et al., 1989; Richey et al., 2002; Bastviken et al., 2011; Raymond et al., 2013; Bates et al., 2014). Quantifying hydrodynamic processes is required to inform the planning and design of river infrastructure, and also to assess low flow conditions, which control the navigability of river channels as inland waterways and habitat suitability for aquatic species (Jowett and Duncan, 2012; Remo et al., 2013). Numerical hydraulic models are widely relied on in this context (Richey et al., 1989; Bates and De Roo, 2000; Crowder and Diplas, 2000; Schumann et al., 2013).

There is considerable interest in modelling the hydrodynamics of the Congo River. Quantifying channel – floodplain interactions and the extent to which the Cuvette Centrale wetland inundation dynamics is controlled by river channel processes. Answering these important earth science research questions (Jung et al., 2010; Lee et al., 2011; Alsdorf et al., 2016) is necessary in order to understand the vulnerability of these wetlands to anticipated changes in fluvial processes. These changes in fluvial processes may be induced by in-channel hydraulic structures that regulate river flows and alter bed slopes (e.g. Grill et al., 2019), or by land cover and climatic changes that impact hydrological processes and hence river flows (e.g. Coe et al., 2009). Sufficient representation of in-channel hydrodynamic processes is of fundamental importance in order to accurately quantify the flow carrying capacity of channels, the onset and duration of inundation, and fluxes between channels and floodplains in large river systems (Trigg et al., 2009; Dey et al., 2019). However, such representation is challenging in the Congo, where satellite based observations of inundation extent and WSE that are often used to estimate or calibrate channel flow parameters in hydrodynamic models (Schumann et al., 2009) can be difficult to obtain, because the majority of the inundation in the Congo Basin occurs underneath dense vegetation canopies (Hughes and Hughes, 1992; Pekel et al., 2016).

Inland waterway navigation is crucial to many of the countries that make up the Congo Basin (CICOS, 2015), but can be dangerous where river depths are shallow and could benefit from dynamic water level predictions afforded by a hydrodynamic model. The in-situ stream-wise depth measurements reported in Chapter 4 along 350 km of the established mainstem navigation route provide useful information on navigation risk. As shown in Figure 5-1, depths of less than 2.5 m were detected frequently. A depth of 2.5 m represents a minimum depth requirement commonly adopted on navigable waterways, such as on the river Rhine where restrictions are placed on all vessels when this depth is encountered (Hemri and Klein, 2017). Moreover, future hydrological changes due to variations in climatic forcing or anthropogenic activities are anticipated and the impacts of these changes on low and high water conditions needs to be properly assessed.

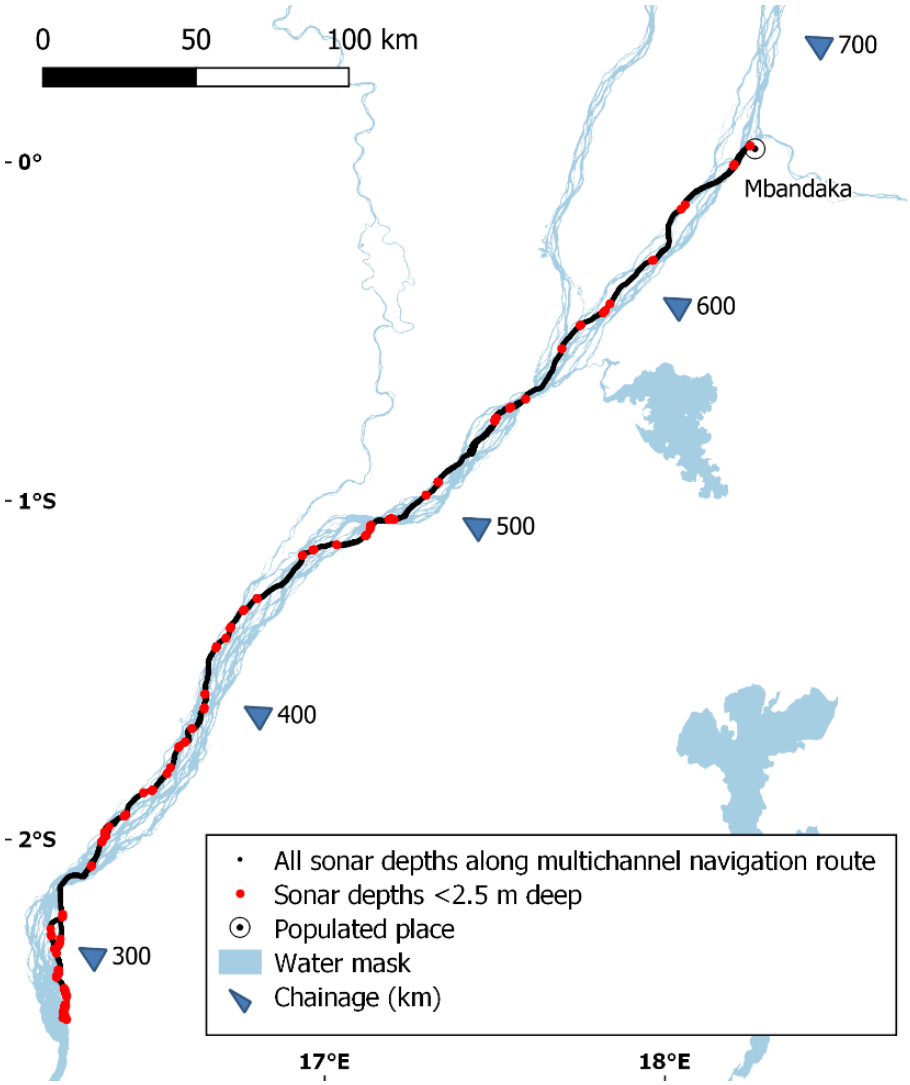

Figure 5-1. Sonar depth measurements from summer 2017 field campaign along a 350 km long multichannel reach. Depths of less than 2.5 m are frequently encountered.

The Congo Middle Reach (CMR), ~1,700 km between Kisangani and Kinshasa along with associated tributaries, is a low gradient, highly multichannel planform system in which numerous individual channel threads flow around large and mostly heavily vegetated islands. Complex river planforms of this nature are often represented using simplifications, due to a paucity of channel geometry information and a need for computationally efficient models (Neal et al., 2012; Neal et al., 2015). One such simplification is to represent multi-channel systems with an effective single channel, as was used by (O'Loughlin et al., 2020) to simulate basin scale hydrodynamics of the Congo at 4 km resolution. Channel geometry was approximated as rectangular using effective width information from a 30 m resolution water mask. Channel depth and friction were both treated as parameters to be estimated, and the modelled water surface was calibrated to observed water surface elevation (WSE) information obtained from satellite radar altimetry. The model simulated channel water surface elevations across the domain with a bias and root mean square error (RMSE) of 0.185 m and 0.842 m respectively, and demonstrated that interactions between channels and floodplains did occur along some of the channels modelled. Similarly, Garambois et al. (2017) used an effective single channel approach on a reach of the multichannel Xingu River, a first order tributary of the Amazon. They found that the use of a temporally varying effective friction parameter (higher friction during low flow conditions) was necessary to account for the flow partitioning among individual channel threads that occurred during low flows but not during high flows, and is not represented by the effective single channel model. This approach was further developed by Garambois et al. (2020) by using a stage dependent friction parameter in an effective single channel hydraulic model of the Xingu River.

It has been demonstrated that hydraulic models of large multichannel rivers can be improved by explicitly representing individual channel threads in such models (e.g. Altenau et al., 2017a). Unlike effective single channel approaches, individual thread planform representation provides a hydraulic model with local in-channel flow path information and hence more accurate stream-line distance. Moreover, by representing individual channel threads, islands are also represented, enabling their inundation to be accurately simulated, thus capturing dynamic changes in flow paths and total wetted perimeter such as those observed by Garambois et al. (2017). Furthermore, there may also be a need for velocity or discharge information through an individual channel thread, to inform local interventions such as dredging, to maintain navigability.

Large multi-channel river model studies that incorporate explicit representation of channel threads are rare due to the difficulties in obtaining the data required and the computational expense of such models. Obtaining bathymetry data is particularly

onerous as it cannot be reliably obtained remotely, and in-situ methods require navigation of each individual channel thread. Nicholas et al. (2012) modelled the hydrodynamics of the main channel of a 30 km reach of the Rio Paraná, Argentina. The reach is predominantly single channel, but some Islands along the reach create multichannel conditions in some places. Three hydraulic model codes, varying in complexity and dimensionality, were used to demonstrate the potential for reduced complexity hydraulic models to predict flow conditions in such a river. A separate study on the multichannel Tanana River by Altenau et al. (2017a) entailed a comparison between hydraulic models that used various levels of model resolution and dimensionality (i.e. both one and two dimensional model spatial structures). They conducted a major field campaign to obtain detailed water surface and discharge information, and a full bathymetric survey of all navigable channel threads that was converted to a 2D spatially distributed bathymetry model (Figure 2-5). They concluded that regional and global-scale hydraulic models can be improved by explicitly representing individual channel threads, rather than using a single effective channel. Thus, there is interest in doing so on the Congo River.

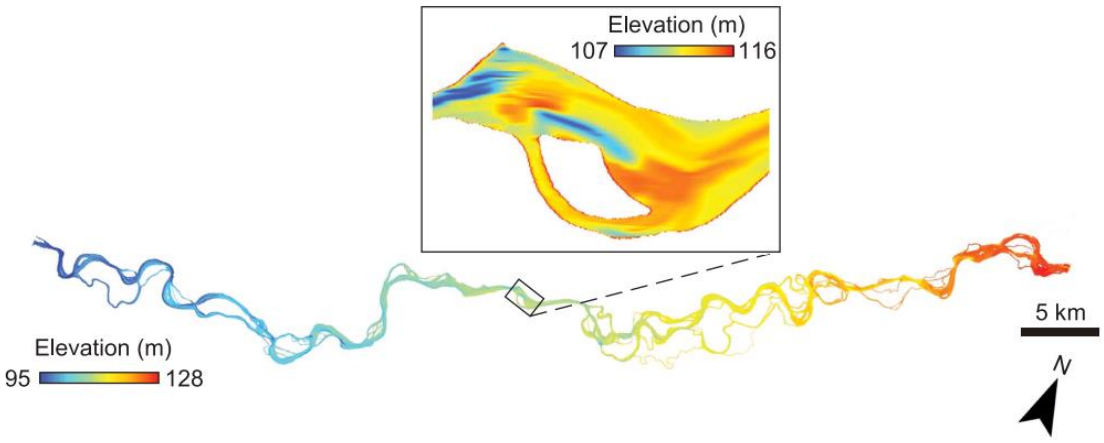

Figure 5-2. Example bathymetry model (BM) of the multichannel Tanana River (first order tributary of the Yukon) developed by Altenau et al. (2017a).

Pre-existing bathymetry data available for Congo River scientific research is very limited, and for a scientific field campaign to obtain a full bathymetric survey along a reach of the Congo is highly challenging, given the spatial scale of the Congo and the many islands that prevent the bank-to-bank movement necessary for complete cross sectional coverage. It is therefore feasible to survey only a small fraction of the Congo's multichannel bathymetry, which can be sufficient for use in coarse 1D hydraulic models that use single effective channels, but not for models that explicitly represent individual channel threads and require complete bathymetric representation. This is problematic,

given there is a need to explicitly model the hydraulics of individual channel threads on this river. This chapter reports on the development and implementation of a hydraulic model covering a 70 km multichannel reach of the CMR. The model explicitly represents individual channel threads, by using spatially limited bathymetry data that covers only a small fraction of a limited number of channel threads. The aim of the study is to demonstrate the ability of a hydraulic model to predict hydraulic conditions in the individual channel threads of a large multichannel river, when bathymetry data used in the hydraulic model is spatially limited to an amount that is feasible to obtain. Doing so will help to answer important questions about bathymetry data requirements for studying the hydrodynamics of large multichannel rivers. Such a model will potentially be a useful tool for investigating bathymetric representations such as effective single channel approximations that are needed to simulate large scale hydrodynamics in an efficient manner. Here, a feasible amount of bathymetry refers to what can be obtained within constraints relating to timescale, the limited accessibility of the Congo River, and budget.

To achieve this, the study comprises the following key components, applied to a 70 km long multichannel reach of the Congo mainstem that was surveyed in high resolution in the 2017 field campaign. First, a novel approach is implemented, which derives a complete bathymetry model (BM) from spatially limited in-situ depth measurements that cannot be directly interpolated across most of the reach because of their sparsity. The BM method interpolates the depth measurements where possible, and supplements this with estimates of bathymetry where it cannot be interpolated. Second, a geometric validation exercise is performed whereby sections of the BM that are estimated are compared with a validation dataset of in-situ depth measurements. Third, a hydraulic validation is carried out. This entails construction of a 2D hydraulic model using the BM, and a comparison of observed and modelled depth-averaged velocities. In addition, a second hydraulic model is constructed using a BM containing no observed depth measurements, in order to assess the benefit that results from the inclusion of the depth measurements.

5.2 Data and Methods

The bathymetry model (BM) is created along a 70 km long study reach on the Congo mainstem approximately 100 km downstream of Mbandaka, and immediately downstream of the Oubangui confluence, as shown in Figure 5-6. The study reach planform is characteristic of the entire middle reach with respect to its width and number of channels. It is well suited to this study because of an absence of tributaries along the reach enables discharge to be assumed approximately constant, and three single

channel sections exist on the reach, enabling cross-sectional sampling of the full river width at these locations without having to navigate around islands.

It was necessary to develop a novel BM approach, as there is no apparent existing method that will produce a spatially distributed BM of a multichannel river from such sparse river depth data. A review of the literature identified the multichannel bathymetry interpolation method developed by Altenau et al. (2017a) to hold most promise, but this was deemed unsuitable for application here, on the grounds that it requires a spatial density of depth measurements sufficiently high such that when interpolated, the entire channel bathymetry can be derived. From Figure 5-6, it can be seen that the depth data available is not sufficient in its spatial density to produce a complete BM from interpolation alone. For example, many channel threads have zero coverage, particularly in the upstream half of the study reach. The novel BM approach developed here therefore employs a method of estimating depth in channel areas that are not in sufficient proximity to depth measurements. This estimation follows an initial routine interpolation of measurements in those channel areas which do lie within sufficient proximity to depth measurements.

5.2.1 Review of Methods of Estimating River Channel Depth

To estimate depths in regions with no measurement coverage, an evaluation of possible relationships between river planform information and river depth was initially carried out, which would potentially enable prediction of depth based on the remotely sensed planform information available. Classic multichannel river channel thread and bar ordering schemes such as those published by Bristow and Best (1993) or Bridge (1993), shown in Figure 5-3, state that multichannel rivers have a hierarchy of primary channel threads that are relatively deep, and relatively shallow secondary (and in some cases tertiary) channel threads that cut across mid channel bars or islands.

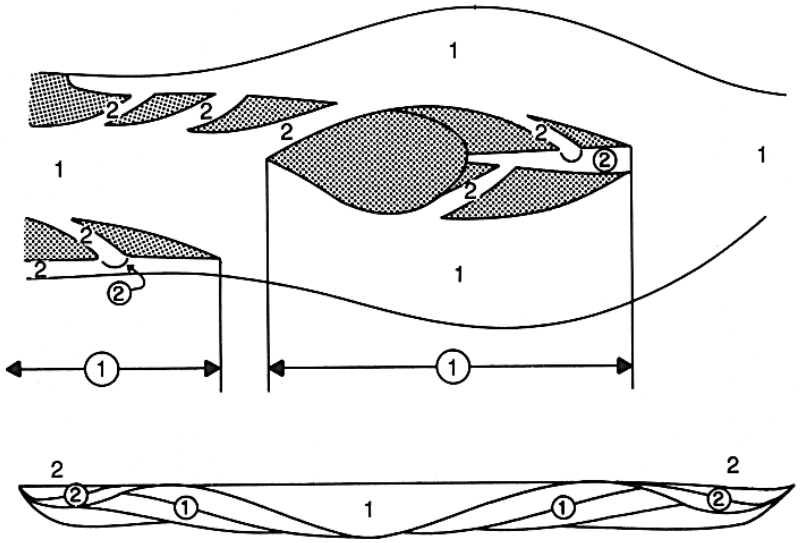

Figure 5-3. Channel thread and bar / island ordering scheme proposed by Bridge (1993). Numbers in circles refer to bars, other numbers refer to channels. Cross section (lower figure) is from a channel thread confluence region, where a central channel (1) is bounded by side bars with cross bar channels (2). Figure is from Bridge (1993).

There is no automated means of assigning ordering to individual channel threads, but it is relatively simple to generate proximity to river bank information using routine GIS analysis. Given their mid channel locations, the shallower secondary channel threads are likely to be located further away from river banks than the deep primary threads. Evidence of this channel ordering behaviour was investigated by examining the sonar data in detail, and was identified in six channel thread cross sections that were clearly identifiable as primary and secondary channel threads. This is shown in Figure 5-4.

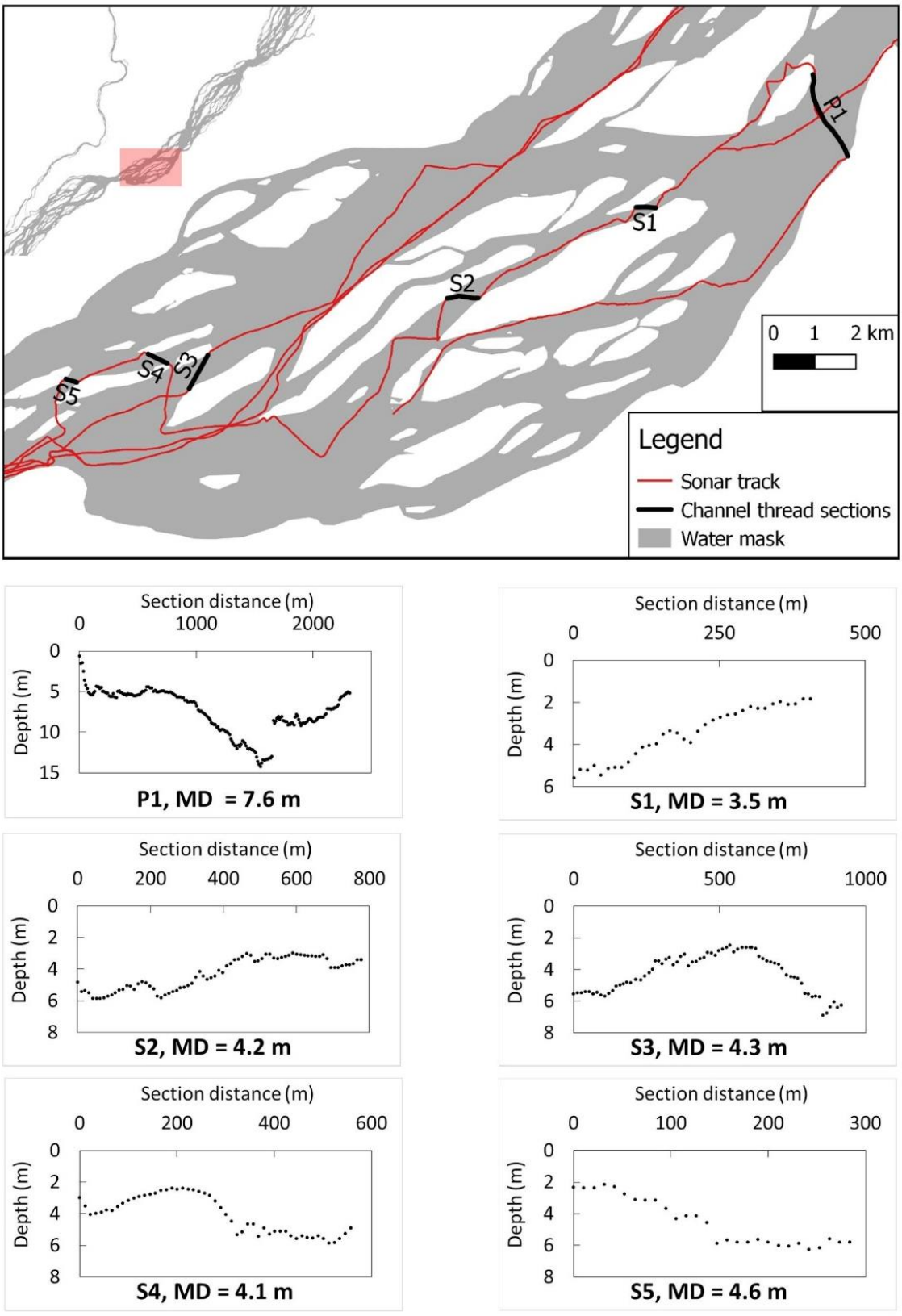

Figure 5-4. Sonar derived sections across a Primary Channel Thread (P1) and five Secondary Channel Threads (S1-S5). Each section is labelled with its mean depth (MD).

To obtain a specific relationship between distance from bank and channel depth that could be used to predict depth, measured depths were plotted against their distance from the nearest channel bank (excluding island banks), with depths averaged over 100 m distance from bank intervals. Results, shown in Figure 5-5, show no discernible relationship.

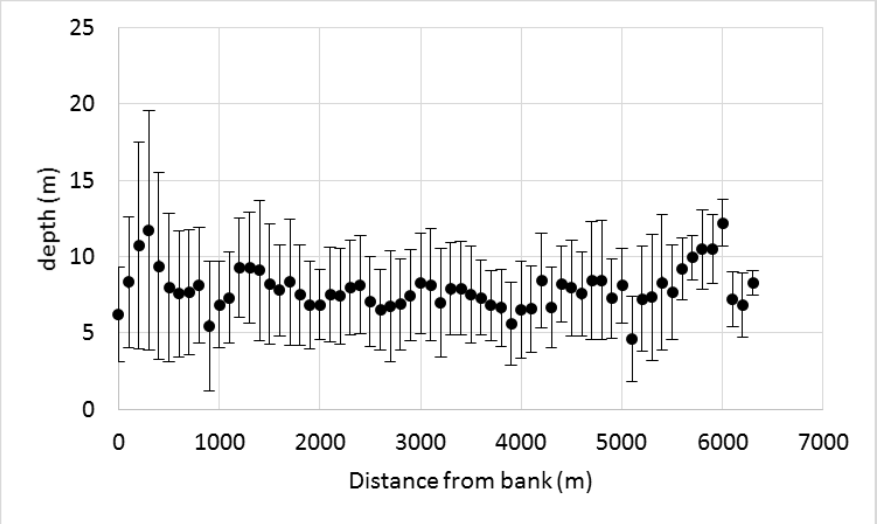

Figure 5-5. Mean of sonar depth measurements at distance from bank intervals of 100 m. Error bars show standard deviation of each mean value.

In the absence of any information on depth variability across the channel belt (i.e. direction perpendicular to flow), depths are estimated assuming a series of rectangular channel threads with constant depth across the channel belt. To estimate such a depth, and its longitudinal (stream-wise) variation with channel belt width (i.e. the deepening where the channel narrows) that was observed in Chapter 4, a uniform flow calculation is was used. Specifically, Manning's equation for uniform flow was applied to calculate channel depth at regularly spaced longitudinal intervals, by using the channel width at each interval derived from a satellite-derived water mask, channel flow from in-situ discharge measurements (assumed constant along the study reach), and slope information from WSE measurements. Whilst assuming uniform flow conditions in this way will not produce the high frequency variations in depth observed at the 5 km scale in Chapter 4, flow conditions were found to be close to uniform at the large scale, with 50 km resolution profiles of bed slope and water surface being near to parallel. The uniform flow depth assumption is therefore determined to be appropriate. A simpler approach whereby channel belt cross sectional area is assumed to remain constant and thus enabling depth to be directly derived from width was dismissed because the

Acoustic Doppler Current Profiler (ADCP) results presented in Chapter 4 show marked random variability in cross sectional area.

5.2.2 Description of Novel Approach to Bathymetry Modelling

The inputs into the BM comprise any direct observations of depth that are available, along with a water mask to define channel planform, a reach average discharge, and a complementary water surface profile obtained by applying a planar water surface approximation to WSE measurements. In this application, these inputs (shown in Figure 5-6) were obtained through a combination of remote sensing and in situ measurements. The water mask was derived from 30 m resolution Landsat data (O'Loughlin et al., 2013), and measurements of discharge, WSE, and depth were obtained in situ using an ADCP, a Global Navigation Satellite System (GNSS) instrument, and a single beam sonar respectively. WSE was measured with a 5cm RMSE, and standard deviation of river depth measurements was 0.35 m at all crossover points where depth was measured twice. Discharge was measured with a maximum variability of 2% based on transect repeatability tests. The in situ measurements were collected during a field campaign in August 2017, further details of which are reported in Chapter 4.

The BM method is implemented in a raster grid using the QGIS open source geographic information system (GIS) application (QGIS Development Team, 2019). The BM method interpolates the sonar measurements, and then combines the interpolated areas of channel with estimates of un-surveyed depth based on uniform flow calculations using the discharge, WSE, and river width information.

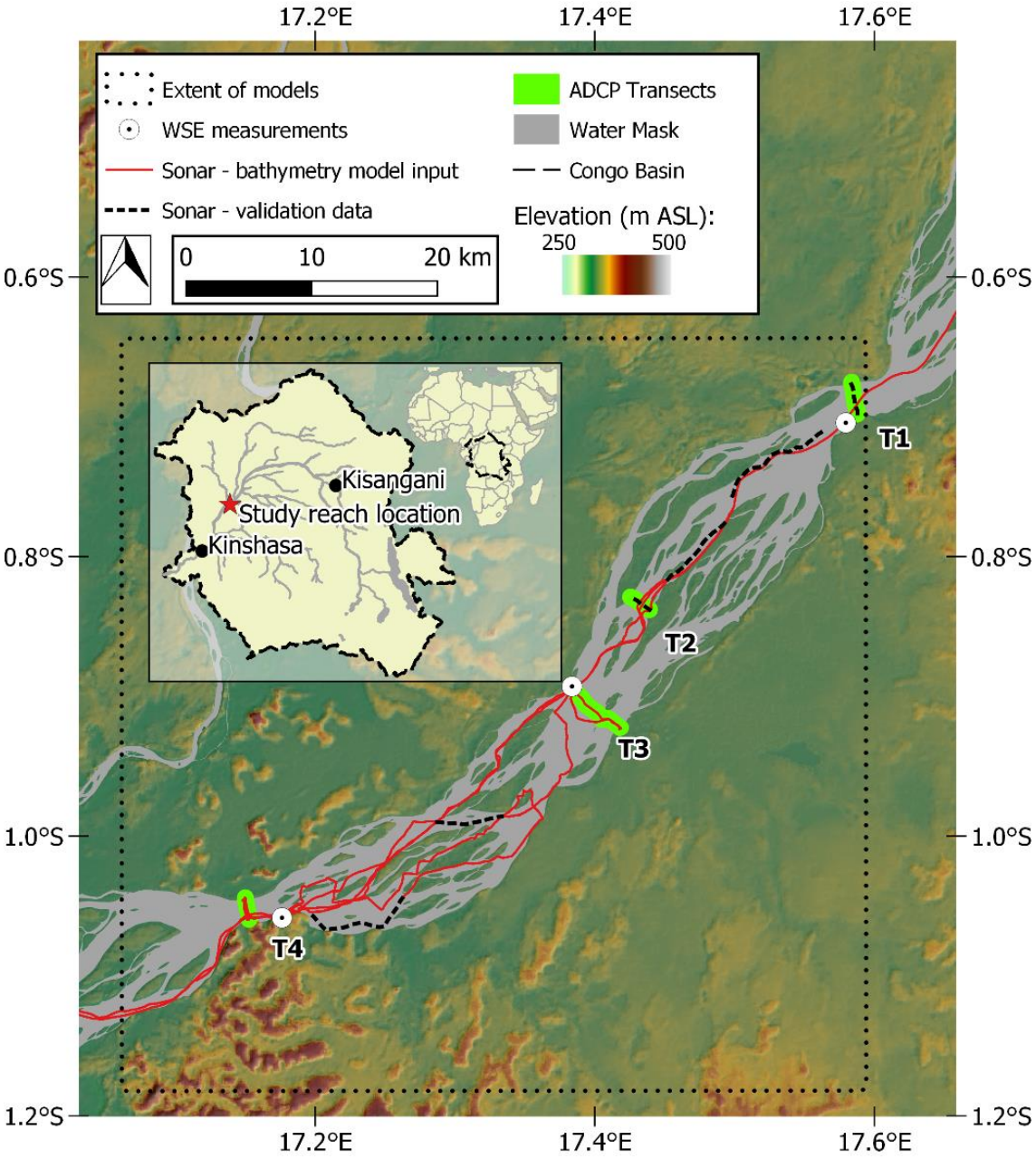

Figure 5-6. Location Plan showing field data, including sonar data input into BM, sonar data used in BM geometric validation, GNSS WSE measurements, ADCP transects, and Landsat water mask (O'Loughlin et al., 2013). Extent of models indicates the spatial extent of the hydraulic models, BM spatial extent is the mainstem water mask within this rectangular extent. Terrain elevations shown are from the MERIT DEM (Yamazaki et al., 2017).

The raw sonar data comprises georeferenced depth measurements made at approximately 3 m intervals. These measurements were collected from 8–11 August 2017 using two boats, and cover a total track length of approximately 200 km. The points

were initially re-sampled on a 10 m raster grid. The sonar data shows dune features with amplitudes in of up to 5 m in the deepest areas, but such features have complex 3D geometries (e.g. Parsons et al., 2005) and their representation in the bathymetry model was viewed as unviable given the depth estimation process described below. Thus, Gaussian smoothing was used to remove dune scale features, as shown in Figure 5-7. Exclusion of dunes was determined to be appropriate because the BM is not required to produce accurate fine-scale 3-D distributed velocity information, and is only required to produce larger scale depth-averaged velocity that is controlled predominantly by large-scale topography in large low gradient rivers, as demonstrated by Nicholas et al. (2012).

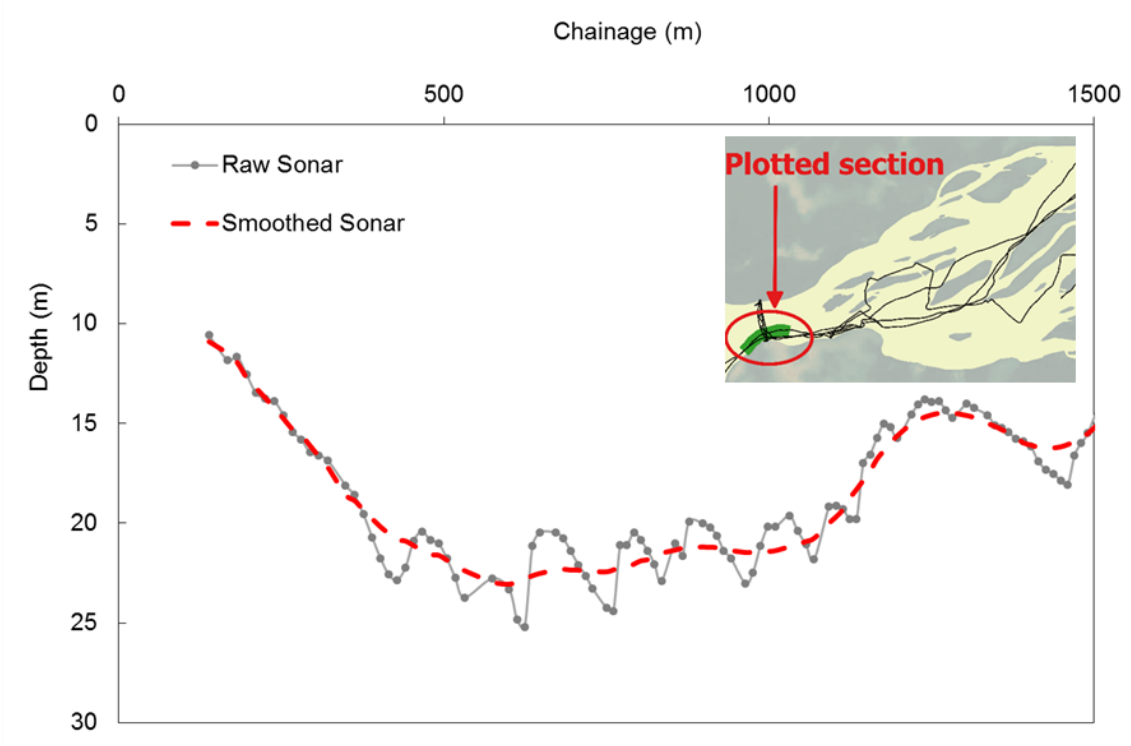

Figure 5-7. 1.5 km section of in-situ sonar data before and after Gaussian smoothing filter applied.

The entire bathymetry modelling process is set out in Figure 5-8. A written description of the process follows, which includes regular references to specific panels of Figure 5-8 to aid the description.

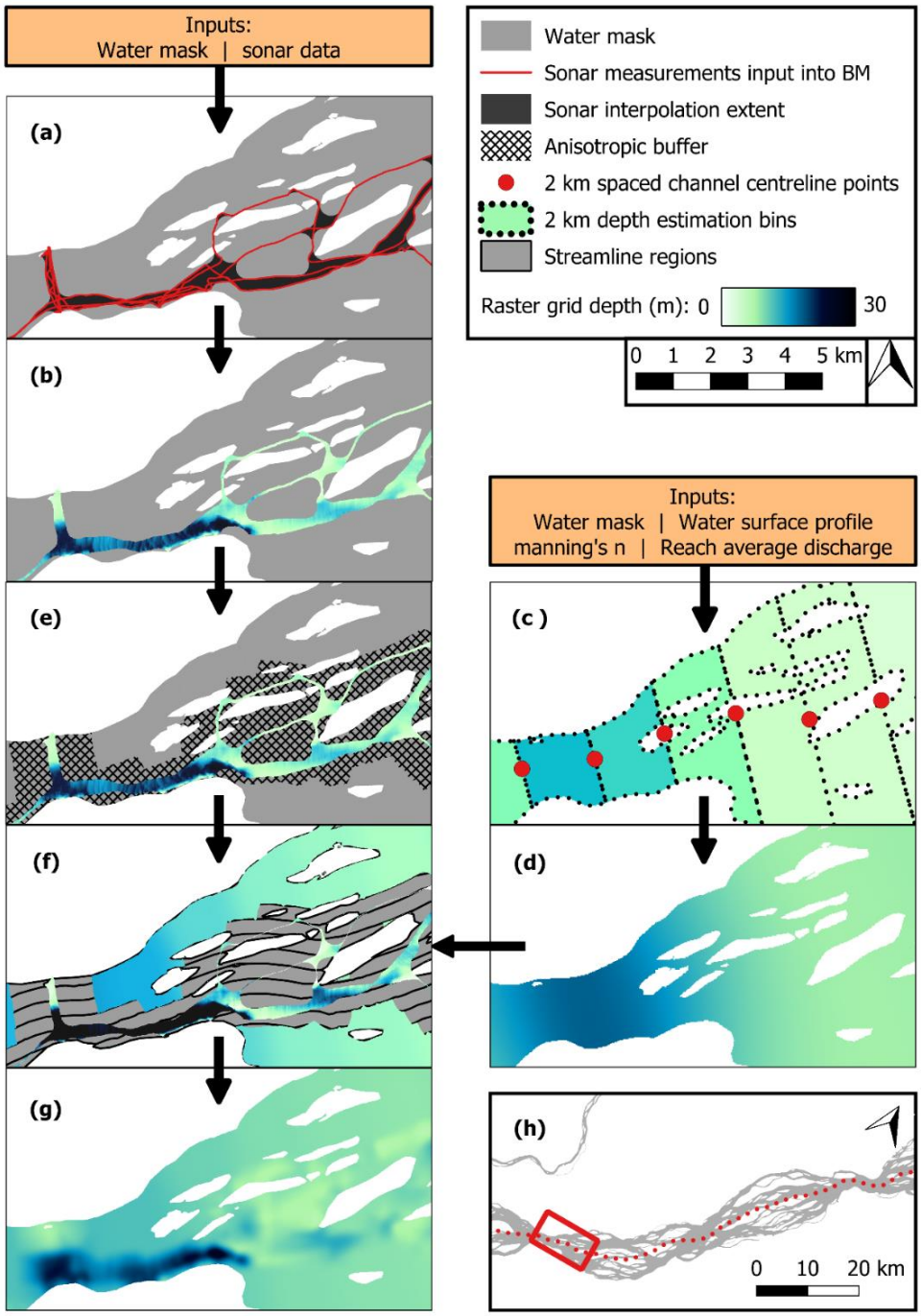

Figure 5-8. Bathymetry modelling process: (a) raw sonar and sonar interpolation extent; (b) resulting interpolated sonar; (c) estimated residual depth in each 2 km polygon prior to smoothing; (d) smoothed estimated residual depth grid (e) anisotropic buffer around interpolated sonar; (f) Merging of interpolated sonar and estimated residual depths: estimated residual depths from (d) are imported to areas outside of the interpolated sonar and anisotropic buffer area, the buffer area is then populated by using anisotropic interpolation (i.e. inverse distance weighting spatially constrained by the streamline regions); (g) Final depth grid resulting from anisotropic interpolation of interpolated sonar and estimated residual depths; (h) plan showing locations of panels a–g.

Interpolation of Sonar Data

Prior to interpolating the raw sonar data, it was first necessary to generate an interpolation extent (Figure 5-8a), in order to spatially constrain the sonar interpolation to regions suitable for interpolation to occur, i.e. regions that fall within a predefined range of two sonar data points. This was created by using the System for Automated Geoscientific Analyses (SAGA) expand and shrink raster algorithm (Conrad et al., 2015), which expands a raster grid around its border by a specified number of cells (expansion radius), then shrinks only where edges remain present. This expand and shrink algorithm was applied to the raw sonar raster grid, an example showing the expansion and subsequent shrinkage results are included in Appendix B.1. Note that the values of the grid cells resulting from this SAGA algorithm were not populated using the algorithm; the algorithm's use here is only to define the plan area extent within which the subsequent interpolation is carried out. A 250 m expansion radius (0.2 km^2 area) was used in the implementation of the SAGA algorithm, based on an assessment of the variability shown by the sonar data. This assessment involved sampling the raw sonar data on a series of orthogonal grids of different resolutions, and showed that mean standard deviation of the depth measurements exceeded 1 m across a grid size greater than 450 m (corresponding to an area of 0.2 km^2 derived from the 250 m interpolation range). A standard deviation error of 1 m was determined to be suitable for the interpolated sonar, as this is expected to be below the bed elevation error associated with the assumptions used in the estimated depths; namely that depth is equal to the channel normal depth and is constant across the entire channel belt width.

Inverse distance weighting (IDW) was used to interpolate the raw sonar data. IDW is one of several commonly used methods of spatial interpolation, and is based on the assumption that unknown values can be approximated by a weighted average of observed values within a circular search radius, a higher weighting being given to points that are closer. Directional influences in the data, also known as anisotropy, may also be accounted for by adopting elliptical search areas that give higher weighting and a larger search radius to observations located along a prescribed direction (Tomczak, 1998). In more conventional bathymetry interpolation situations where the entire channel can be derived from point observations, it has been shown that allowing for anisotropy can considerably reduce interpolation errors (e.g. Merwade et al., 2006). Essentially, river depth varies less in the stream-wise (longitudinal) direction than in the transverse direction, and can therefore be predicted more accurately by prioritising the use of upstream and downstream measurements over transversely located measurements. Here, anisotropy has not been considered in the interpolation of the sonar data, given

the likely small size of the error compared with errors resulting from the estimated depths. However, anisotropy has been considered in the process of merging of interpolated sonar data and estimated depths, and is discussed below therein. In BM applications with a significantly greater coverage of sonar data, it may be necessary to consider anisotropy in its interpolation.

IDW is a simple and accessible interpolation method, and was identified as an appropriate method for this particular application of the BM. Other interpolation methods commonly used in spatial interpolation including basis spline (B-spline) and ordinary kriging were considered. Spline methods interpolate a surface by generating a series of parametric functions to fit sparse observations, these functions being bicubic B-spline functions in the case of B-spline interpolation (Lee et al., 1997). Spline interpolation methods are known for producing smoothly varying surfaces and are therefore commonly used to interpolate gently varying properties, but are poorly suited to sparse and variable measurement coverage (Wasser and Goulden, 2017) and was therefore not selected here. Ordinary kriging is a geostatistical method that is similar to IDW in that it weights the surrounding measured values according to their proximity to derive a prediction for an unmeasured location. However, ordinary kriging uses a more sophisticated weighting for the surrounding measured values, and employs the spatial correlation between sampled points as well as proximity. The spatial correlation is determined by fitting a variogram model to the observed semi-variance between measurements of varying proximity (distance). Kriging can also provide estimates of the uncertainty surrounding each interpolated value. Whilst more sophisticated and potentially offering improved performance (Merwade et al., 2006), the added complexities of kriging introduces considerable computational burden and requires a greater number of user inputs. These inputs include the selection of an appropriate variogram model, which depends on an in-depth assessment of the raw data in order to characterise the spatial autocorrelation of the bathymetry. The sparsity of the raw sonar data here precludes such an assessment, and led to ordinary kriging being discounted in this application of the BM. Nevertheless, all three interpolation methods mentioned above were explored by applying them experimentally to a test section of sonar data. Results of the three methods were compared and revealed no reason to select the ordinary Kriging or B-spline methods over the IDW. The comparison is contained in Appendix B.2.

The interpolation calculation was performed using the Geospatial Data Abstraction Library (GDAL) IDW algorithm (GDAL/OGR contributors, 2020), based on the following formula for interpolated grid values Z:

$$Z = \frac{\sum_{i=1}^{n} \frac{Z_i}{r_i^p}}{\sum_{i=1}^{n} \frac{1}{r_i^p}} \quad \text{Eq. 5-1}$$

Where Z_i is a known value at point i, r_i is the search radius from the interpolated grid node to point i, n is the number of points within the search radius, and p is a weighting power. Here, the default p value of 2 most commonly used in applying IDW (Merwade et al., 2006) was adopted, along with a search radius of 250 m (i.e. the same as the SAGA algorithm expansion radius).

The spatial extent of the IDW interpolation was controlled by the aforementioned interpolation extent. Without this interpolation extent, the IDW would simply interpolate across all areas within the search radius, thus producing erroneous results in areas where there is insufficient data to interpolate (effectively extrapolating in these areas). Example IDW results with and without the interpolation extent are shown in Appendix B.3 for information. The resulting interpolated bathymetry (Figure 5-8b) covers 4% of the total study reach channel plan area in this application.

Estimation of Depth

To estimate depth, the water mask is divided into 2 km long sub reach polygons, as shown in Figure 5-8c. An interval of 2 km was chosen as it is sufficiently small to capture local changes in river width and therefore represent commensurate changes in river depth that are known to occur, particularly at width constrictions. Polygons were created using 2 km spaced points along a channel belt centreline, this centreline was generated using a Voronoi tessellation procedure (e.g. Nyberg et al., 2015). The mean effective width of each polygon, w is derived by dividing its plan area by its 2 km length, and this is then used in the uniform flow calculation. The calculation uses a re-arranged version of manning's formula (Chow, 1959) and the wide channel approximation (i.e. hydraulic radius is equal to flow depth), yielding the following formula:

$$\overline{d} = \left(\frac{Qn}{ws^{1/2}}\right)^{3/5} \quad \text{Eq. 5-2}$$

Where $\overline{d}$ is mean channel depth; w is mean effective channel width; Q is the observed channel discharge of 21,000 m^3 /s; s is the mean observed water surface slope through the reach of 5 cm/km; and n is the manning friction parameter and is assigned a constant value of 0.03 based on guidance in Arcement and Schneider (1984), and values used on other large anabranching rivers (Latrubesse, 2008).

As the depth resulting from this calculation represents the mean depth across the channel belt, it is necessary to adjust this depth to a 'residual depth' value to allow for any interpolated sonar data that exists within the polygon. Simply using the mean channel depth, $\overline{d}$ in the BM would give spurious results, particularly where there is a significant amount of sonar data but only for a part of the channel width. This is illustrated in Figure 5-9, which shows a hypothetical scenario where sonar observations have been obtained for the deep part of the channel but not the shallow part.

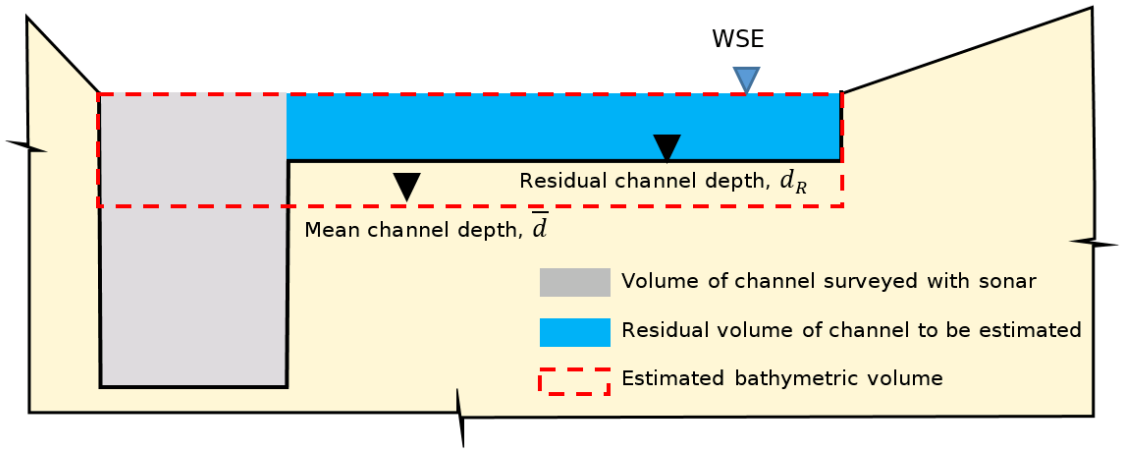

Figure 5-9. Illustration of channel residual depth calculation within a depth estimation polygon, for a hypothetical case where the deep part of the channel has been surveyed but the shallow part has not.

Accordingly, an estimated residual depth value is used in the estimated bathymetry, and is derived as follows.

Estimated bathymetric volume, V is calculated from the polygon length, l (2 km here), $\overline{d}$ and w:

$$V = lw\overline{d} \qquad \text{Eq. 5-3}$$

A residual bathymetric volume, V_R is calculated from volume of interpolated sonar, V_s and V:

$$V_R = V - V_S \quad \text{Eq. 5-4}$$

A residual channel plan area, P_R is calculated from the plan area of interpolated sonar, P_S and the total channel plan area P:

$$P_R = P - P_S \quad \text{Eq. 5-5}$$

Residual depth, d_R is calculated from, V_R and P_R:

$$d_R = V_R / P_R \quad \text{Eq. 5-6}$$

Further illustration of the residual depth calculation is given in Appendix B.4 by way of an example calculation for a hypothetical channel section.

The resulting estimated residual depth raster grid (Figure 5-8c) is then smoothed using a Gaussian filter to remove physically unrealistic step changes in depth between each polygon, shown in (Figure 5-8d).

Merging of Interpolated Sonar Data and Estimated Depths

To merge the estimated depths and the interpolated sonar, we first generate a buffer around the latter, depicted in Figure 5-8e. The buffer is offset from the edge of the interpolated sonar by 1 km parallel to, and 0.2 km perpendicular to the stream-wise direction. These offset values maintain the interpolation extent of 0.2 km^2 introduced previously, and are determined using an anisotropy ratio of 0.2 that accounts for the greater bathymetric variability transverse to the flow direction than along the flow direction. The sonar data are too sparse for direct derivation of a site specific anisotropy ratio here, so we adopt the value of 0.2 used in a bathymetry anisotropy study by Merwade et al. (2006), and by Wu et al. (2019) on the lower Mississippi.

Streamline regions generated from the channel belt centreline are used to define the stream-wise direction, these are shown in Figure 5-8f. The use of multichannel centrelines was explored and are shown in B.5, but they were found to produce hydraulically unrealistic flow paths for the CMR multichannel planform, notably at channel thread junctions where the centrelines resulting from the Voronoi tessellation are perpendicular to one another in some locations. When compared with a single channel belt centreline it is not evident that the more complex multichannel centreline

provides any improvement in defining stream-wise direction and may even introduce error.

Grid cells located outside of the interpolated sonar and its buffer are populated directly with the estimated depth raster shown in Figure 5-8d. The buffer area is then filled using IDW computations performed within each streamline region, and the resulting raster grid is passed through a Gaussian filter to remove physically unrealistic step changes in depth between each streamline region. The final depth grid (Figure 5-8g) is converted into a BM by subtracting it from a WSE raster grid to yield a bed elevation grid. The WSE raster grid is obtained by interpolating the three GNSS WSE measurements and assuming a planar water surface approximation.

5.2.3 Hydraulic Modelling

The BM was used in a steady state hydraulic model in order to assess its hydraulic performance, by comparing depth averaged modelled velocities with those observed with an ADCP during the field campaign. A 2D hydraulic model was built and run using HEC-RAS (v5.0.3), developed by the US Army Corps of Engineers at the Hydrologic Engineering Center. The steady state flow conditions observed during the August 2017 field campaign were simulated, which represents seasonal low flow. The inflow boundary comprised a reach average discharge value obtained by taking the mean of three ADCP transects executed at the upstream, downstream and central parts of the study reach. The standard deviation of discharge across these transects was 5%, indicating a small spatial or temporal variation in discharge, the transects having been measured within a four day window. A fixed WSE was imposed as a downstream boundary condition, derived by spatially interpolating the GNSS WSE measurements. A spatially uniform value of manning's *n* was used, and it was assumed that no out of bank flows occur by representing ground elevation outside of the water mask as infinitely high. This assumption is based on personal observations that were made whilst travelling by boat on the river during the flow conditions simulated. Flow conditions were simulated using the full shallow water equations solver. A simulation time of four days was adopted, and initial flow depth conditions derived from a preliminary model run were used. All model results were extracted from the final model output, by which time model inflow and model outflow were equal.

The BM was resampled to 100 m prior to being imported into HEC-RAS as a 2D flow area, and was subsequently meshed in HEC-RAS at the same resolution as the BM. The HEC-RAS 2D sub-grid capability that parameterises topography within individual grid cells (described in subsection 3.3.2) was not utilised because the modelling process

was originally developed for a different model code (LISFLOOD-FP), which does not have the same sub-grid capability. HEC-RAS was originally used only to verify the LISFLOOD-FP model results, but during this verification exercise, large discrepancies were found between the velocity predictions by each model. By comparing the results of both models to the observed velocity, it was apparent that LISFLOOD-FP was producing significantly different velocity results at certain locations, which led to the adoption of HEC-RAS. It is not known why LISFLOOD-FP velocities deviated from observations and HEC-RAS model results at some locations. It is possible that errors were introduced in the procedure used to extract and process velocity information from the LISFLOOD-FP results, although this could not be confirmed. An account of the superseded LISFFLOOD-FP modelling results is contained in Appendix B.6. The resolution of 100 m was adopted for the BM following experimental use of 50, 100, and 200 m resolution versions of the BM in the hydraulic model, which took 130, 15, and 2 minutes to run respectively. This showed that increasing to 200 m resolution appreciably affected WSE prediction (WSE results are shown in Figure 5-10): the widths of narrower channel threads become significantly over-represented as minimum 200 m wide, and thus over-represent channel capacity and result in a reduction in water levels.

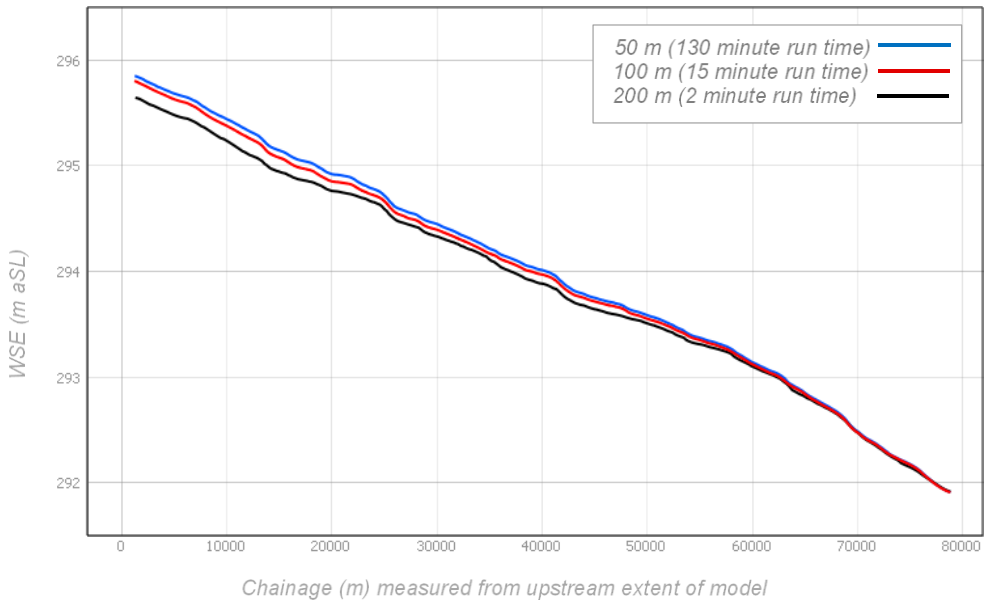

Figure 5-10. Longitudinal plots of modelled WSE predictions for different model resolutions.

To isolate the effect of the sonar data on hydraulic model performance, the base hydraulic model described above was revised by using a bathymetry derived solely from estimated depths, i.e. excluding all sonar data, and using only the uniform flow

calculation of mean channel depth described in Equation 5-2. Results of this estimated bathymetry (EB) hydraulic model were then compared with the base hydraulic model to assess the hydraulic effects of the sonar data.

5.3 Results

5.3.1 Geometric Validation

Geometric validation of the BM was carried out by comparing it against a separate validation dataset comprising five sections of sonar data that were not included in the BM, as shown in Figure 5-11.

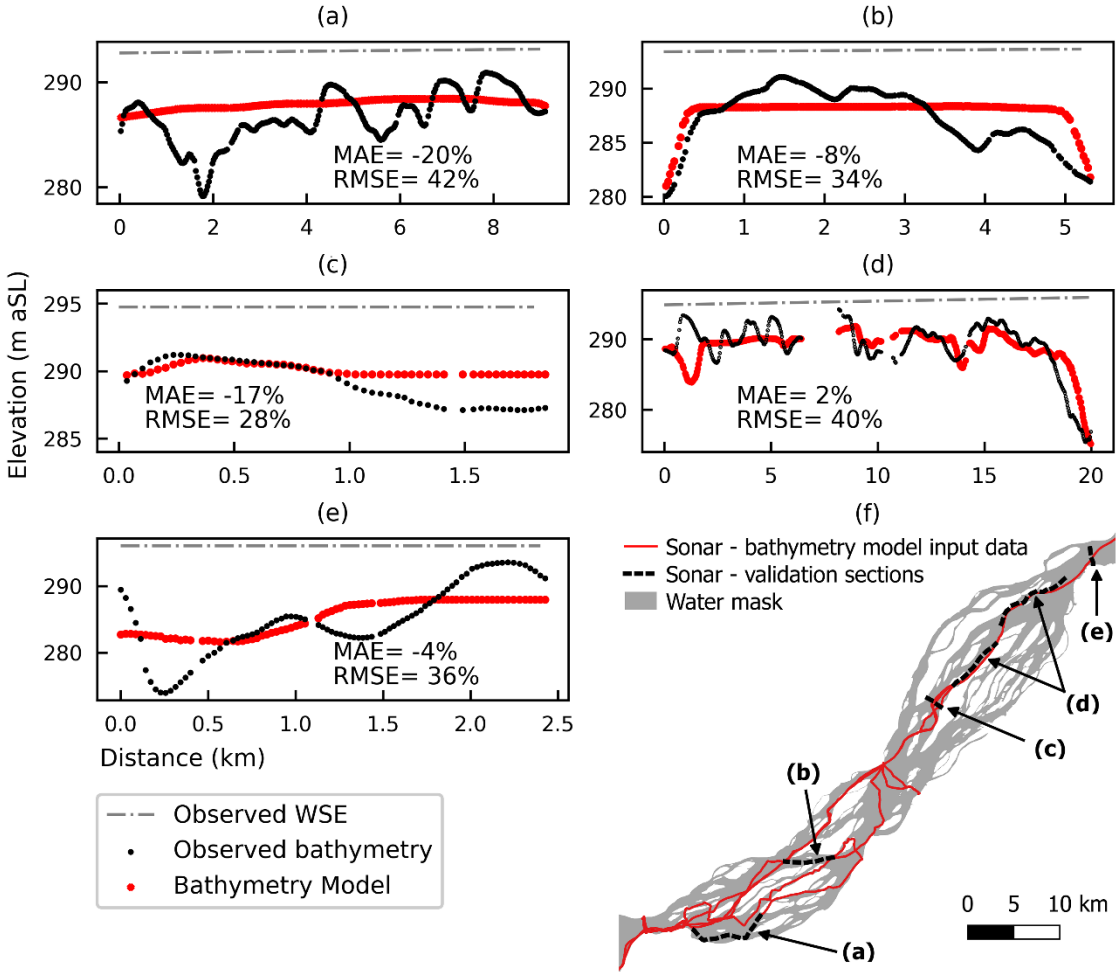

Figure 5-11. Bathymetry model (BM) geometric validation: (a)-(e) plots of bathymetry model bed elevations compared with sonar validation data, measured WSE also shown, X and Y axis titles apply to all axes; (f) Map showing locations of validation sections.

From the validation process, the RMSE values are relatively high, on account of the considerable local variability in depth that cannot be predicted by the estimated depth component of the BM. However, mean absolute errors (MAE) are relatively small,

showing that the EB provides a relatively good estimate of large-scale bathymetry. The BM produces a small underestimate in average depth at all but one of the validation sections, the exception being at section d (Figure 5-11d). Here, sonar data incorporated into the BM runs close and parallel to the section, influencing the BM and producing a very small mean overestimate of depth.

5.3.2 Hydraulic Validation

The base hydraulic model and EB hydraulic model were calibrated separately by incrementally varying manning's *n* and selecting the value that produced the minimum RMSE of modelled WSE at the three observed locations shown in Figure 5-6. The calibrated base hydraulic model produced WSEs with a RMSE of 0.09 m at the three observed locations using a manning's *n* value of 0.03, and the EB hydraulic model calibration yielded a RMSE of 0.03 m with a manning's *n* value of 0.028. The small difference in manning's *n* results from differences in the bathymetry representation. Nevertheless, both these *n* values are broadly consistent with published values for large low gradient rivers (e.g. Arcement and Schneider, 1984; Trigg et al., 2009), and are closely aligned with the value of 0.03 computed at chainage 235 km of the CMR in subsection 4.5.1. Figure 5-12 shows an illustration of the velocities predicted by the calibrated base hydraulic model, with topography also shown for context.

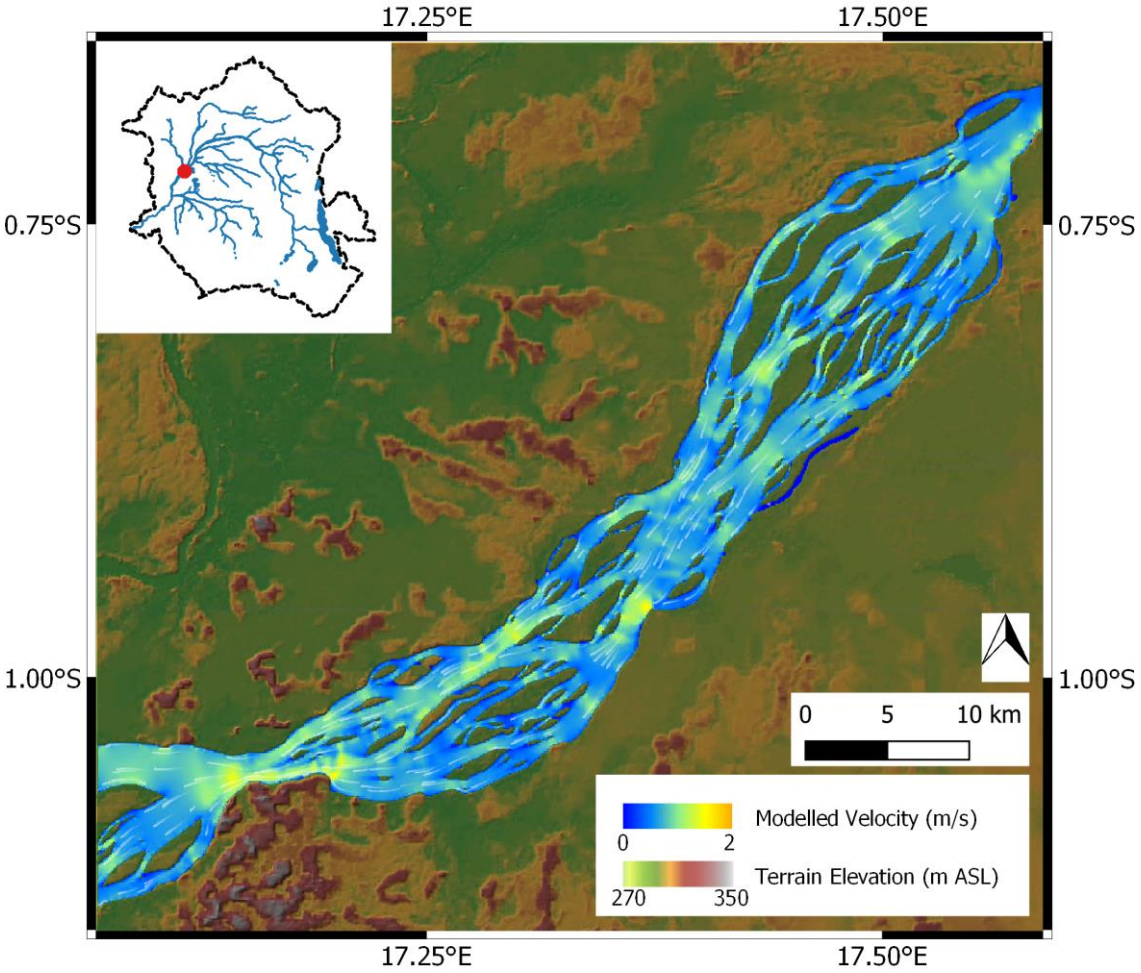

Figure 5-12. Channel velocities predicted by base hydraulic model. White lines indicate local direction of flow, produced by the HEC-RAS particle tracing function. Terrain elevation (Yamazaki et al., 2017) shown for context only, and is not represented in the model DEM.

Depth averaged velocities predicted by both models are compared to observed values at the four ADCP transect locations, as shown in Figure 5-13 and summarised in Figure 5-14.

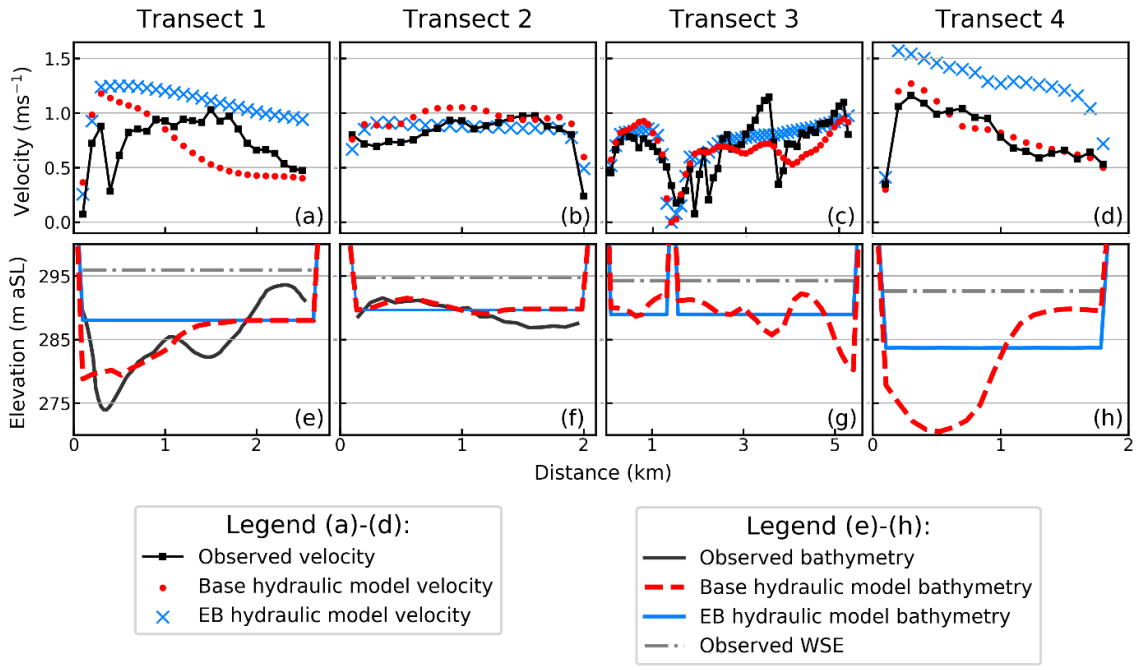

Figure 5-13. Modelled and observed bed elevations and velocities at ADCP transects: (a)-(d) velocities; (e)-(h) bed elevations. Observed bed elevations are only shown at locations where the cross-sectional observations are not used in the base hydraulic model. Transect locations are shown in Figure 5-14(c) below, and also in Figure 5-6. Results for both the base hydraulic model (sonar data included), and the EB hydraulic model (sonar data excluded) are shown.

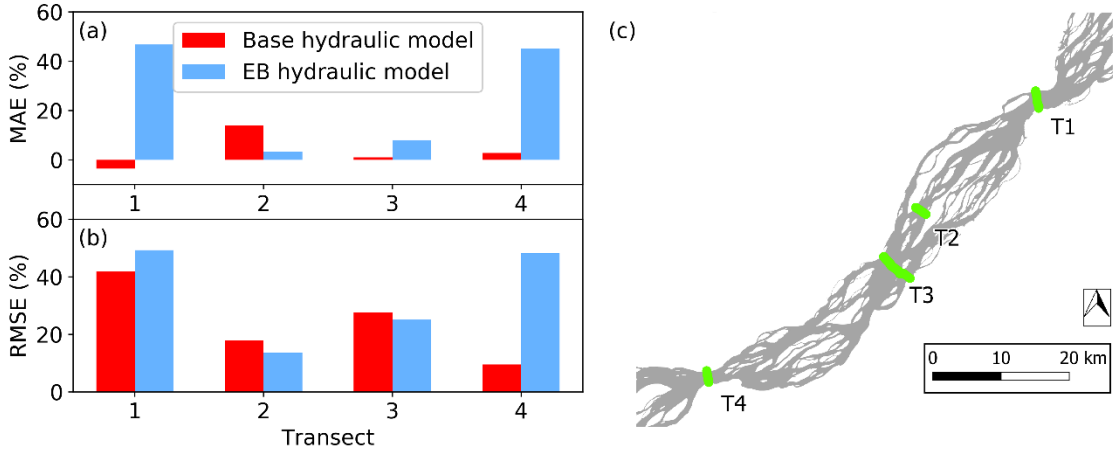

Figure 5-14. Summary of velocity prediction errors in both the base hydraulic model (sonar data included), and the EB hydraulic model (sonar data excluded): (a) Mean absolute errors (MAE); (b) Root means square errors (RMSE); (c) Transect locations.

The base hydraulic model produces small MAEs at transects 3 and 4, and this is expected as the BM contains full cross sectional sonar data at these locations. The

RMSE is also small at transect 4, but is notably greater at transect 3 due to the complex flow patterns seen here, the model being unable to reproduce the high variability in the velocity across the section. Transects 1 and 2 also have relatively small MAEs, despite cross sectional sonar data being absent in the BM at these transects. The longitudinal sonar track running through these transect cross sections provides useful information on channel geometry, particularly at transect 1 where the BM is able to obtain cross sectional information from the sonar track that cuts diagonally across the channel, shown in Figure 5-11(f). However, RMSE is very high at transect 1, partly because the longitudinal sonar does not fully define the channel shape, and also because of its close proximity to the model upstream boundary that imposes flow intensity uniformly across the section. The low RMSE at transect 2 is attributed to the uniformity of the observed velocity profile here.

The value of the sonar data is evident both at transect 1 and 4, as the EB hydraulic model significantly overestimates mean channel velocity due to shallow bathymetry at these locations. The EB hydraulic model performance improves at transect 2 and 3 because here the estimated depths are a much closer match to the observed mean channel depths. Unexpectedly the EB hydraulic model narrowly outperforms the base hydraulic model at transect 2 in both MAE and RMSE, on account of the estimated mean channel depth here closely matching the observed value. The base and EB hydraulic model under-predict discharge at transect 2 by 13% and 18% of the observed value of 9850 m^3/s, respectively. EB hydraulic model RMSE is also slightly lower at transect 3, although visual interpretation of the velocity plots here shows the base hydraulic model better predicts the peaks and troughs in velocity across the right hand side of the section. The value of the 2D planform representation is also demonstrated by the cross-sectional velocity gradient produced by the EB hydraulic model at transect 4, despite the horizontal river bed representation across the channel.

5.4 Discussion

With the exception of transect 1, the base hydraulic model predicted velocity RMSEs are low considering the limited observed bathymetry data used in the model. They are not substantially greater than those seen in comparable large river modelling studies that use full bathymetry datasets (e.g. Nicholas et al., 2012). Base hydraulic model velocities diverge from observations notably at transect 3, where flow conditions are more complex due to numerous shallow areas across the section. A similar increase in modelled velocity error is also reported by Nicholas et al. (2012) where more complex flow conditions exist. Increasing the spatial coverage of observed bathymetry data used, and the spatial resolution at which it is represented, would likely improve modelled

velocities to some degree, but the level of improvement would be limited by the assumption that the frictional coefficient is spatially uniform. Such an assumption is necessary, because the high resolution data needed to quantify the spatial variations in river bed grain size and fine-scale bed form geometry that govern hydraulic roughness cannot be realistically obtained.

5.4.1 Performance of Estimated Bathymetry

Low MAEs are observed in the velocities at transect 2, and in depths at section (a) and (b) of the geometric validation. These areas use limited or no sonar data and rely on the estimated depths, indicating that the uniform flow assumption and the friction coefficient used in the estimated depths characterise these locations well. The low MAEs in the EB hydraulic model velocities at transects 2 and 3 also demonstrate the efficacy of the estimated depths. Moreover, the error in discharge prediction through the transect 2 channel thread increased only marginally for the EB hydraulic model, to 18%. However, the EB hydraulic model performed poorly at transects 1 and 4, where the river channel is laterally constricted and the channel deepens significantly. Here, the observed mean depths are 3–4 m deeper than those predicted by the estimated depths, as shown in Figure 5-13(e) and (h). Whilst the estimated depths do predict a considerable increase in depth at these constrictions, the underlying uniform flow assumption does not predict the full extent to which the bed has locally adjusted through erosion in order to maintain morphodynamic equilibrium. As a result, the EB hydraulic model overestimates mean velocity here by over 40%. WSE predictions also appear to be affected by this under-prediction of depth; as shown in Figure 5-15, recalibration of the EB hydraulic model manning's *n* value was necessary to compensate for a mild backwater effect that amounted to a RMS difference in WSE of 0.2 m and a maximum difference of 0.4 m.

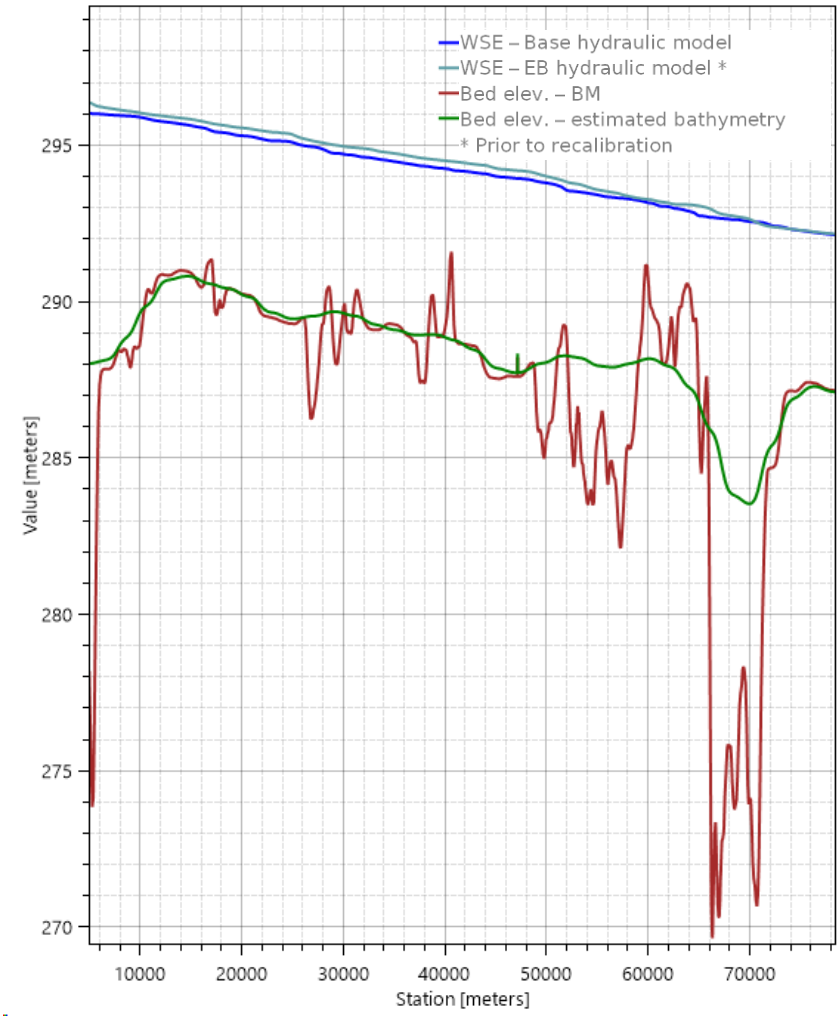

Figure 5-15. Longitudinal water surface profiles resulting from base hydraulic model, and EB hydraulic model prior to recalibration. Note, the plotted BM bed elevation profile is not the cross-sectional average bed elevation.

A WSE error of 0.4 m is small relative to the Congo's 3-4 m annual flood wave through this reach (Becker et al., 2014), and shows WSE to be relatively insensitive to bathymetric representation. In contrast, Altenau et al. (2017a) found WSE to be more sensitive to bathymetric representation on the multichannel Tanana River, a 0.26 m RMSE in distributed WSE predictions arising predominantly from relatively small errors (0.89 m RMSE) in bathymetric representation. Nevertheless, these findings highlight that major misrepresentation of cross sectional area at the constrictions arising from simplified representations of bathymetry, could appreciably affect WSE predictions during high flow conditions when backwater effects are more likely to exist.

5.4.2 Implications for representation of bathymetry in Hydraulic Models of the CMR

These findings have implications for representation of bathymetry in hydraulic models of the CMR and other low gradient multi-thread channel systems. General flow conditions within the multichannel reaches can be relatively well predicted by a hydraulic model that uses estimated bathymetry derived from a simple uniform flow calculation. The use of spatially limited observed data was shown to be of limited benefit to hydraulic model predictions, although more observations of flow conditions through individual channel threads are needed to confirm this more thoroughly. In contrast, at single channel reaches where the channel is laterally constricted, bathymetry is more variable and strongly influences local flow conditions, demonstrating that observed cross sectional data here is of major benefit to model performance. However, observed data is only required locally, as evidenced by the accurate prediction of flow conditions where bathymetry in the upstream and downstream reaches was estimated.

The application of the BM in a hydraulic model to simulate flow conditions through individual channel threads using only a small fraction of observed channel bathymetry will be of interest to scientists and practitioners who require local channel hydraulic information, but do not have the resources available to survey thousands of kilometres of channel bathymetry. When supplemented with a suitable land surface DEM, the BM may be used in a hydrodynamic model to simulate dynamic changes in flow paths and flow resistance as islands become inundated. Physically realistic depths in individual channel threads will prevent significant errors in mean channel velocities. Flow path lengths, dynamic changes in flow resistance, and mean channel velocity can substantially affect the rate at which flood waves move along a river system, so their representation is of relevance to modelling of large scale flood inundation dynamics and wider earth science questions such as the quantification of fluvial contributions to wetland inundation in the Cuvette Centrale (Alsdorf et al., 2016). Accurate representation of the cross-sectional areas of the lateral constrictions is also of importance in this context, to correctly simulate potential backwater conditions during high flows that could affect WSE and therefore the onset, duration, and extents of floodplain inundation. Such a hydrodynamic model may also serve as a base model for experiments of more coarse resolution models that employ effective single channel representations, which are necessary to simulate large scale hydrodynamics in a rapid manner.

5.5 Concluding Remarks

A novel approach has been developed for producing a spatially distributed 2D bathymetry model (BM) of a multichannel river, using only spatially sparse bathymetry measurements combined with river width information, and measurements of WSE and discharge. In areas of the channels where observed bathymetry data are unavailable, and the position is too remote to be directly interpolated from where there are bathymetry observations, the method estimates the depth based on river width, discharge and water surface slope, by assuming uniform flow conditions. The method has been applied to a 70 km long reach of the Congo River mainstem that was the subject of a field campaign in August 2017. Bathymetry observations that were collected along a 200 km long sonar track were used in the BM, but these amount to only 4% of the planform area of the reach.

The key findings are that depths in the wide multi-thread reaches of channel are well approximated by the uniform flow assumption: geometric validation showed the BM average MAEs and RMSEs in depth across four sections in these reaches were 9% and 36% respectively. Moreover, when a version of the BM without any observed bathymetry was used in a hydraulic model, MAEs and RMSEs in predicted velocity at two cross sections averaged 6% and 19% respectively, and discharge through an individual channel thread was predicted to within 18% of the observed value. However, the uniform flow assumption led to large errors in channel depths and local flow conditions where the river flows through single thread channels that are laterally constricted. At two such locations, average MAEs and RMSEs in modelled velocity were 46% and 49% respectively when observed depth data were not used. Inclusion of the observed cross-sectional depth information improved these values to 0% and 26% respectively, confirming the value of observed cross sectional data local to the section combined with the uniform flow depth estimates in the upstream and downstream sections.

This study has shown that there is value in explicitly modelling the hydraulics of individual channel threads of large multichannel rivers with very sparse bathymetric observations. The BM will form a key component of the next research steps into representing the bathymetry of the CMR in hydrodynamic models. Such research will entail experimentation with coarse resolution effective single channel representations frequently utilised in large scale hydrodynamic models, which must parameterise the dynamic effects of channel and island geometry on flow hydraulics.

From a review of the literature, it is apparent that the approach used here to model multichannel bathymetry is novel. The specific components of the BM process

use established methods: interpolation of sparse sonar data using IDW is a routine operation in flood modelling; estimation of bathymetry by assuming uniform flow conditions has been adopted by other researchers (see for example the channel depth estimation method set out by Sampson et al. (2015) that uses Manning's equation). However, the two components are seldom used in tandem. The novelty comes from the unique approach of combining these two distinct components, one satellite-based, the other based on in-situ data, in a 2D environment. This kind of complementary approach will be important for making satellite-based approaches more locally relevant (Fleischmann et al., 2019), and increasing their uptake in decision making.

CHAPTER 6

Effective Single Channel Approximations in Hydrodynamic Models: Applicability to the Congo Middle Reach

6.1 Introduction

In-channel river flow conditions strongly influence the extent of channel – floodplain interactions and the speed at which flood waves travel (e.g. Trigg et al., 2009; Paz et al., 2011; Hoch et al., 2018; Dey et al., 2019). Therefore, channel flow conditions along the Congo Middle Reach (CMR) are linked to the numerous physical processes and risks in the Congo River Basin pertaining to floods or lack thereof. The magnitude, frequency, and duration of floods influences ecological health, the preservation of sequestered carbon (particularly in peat), the outgassing of globally significant amounts of carbon dioxide and methane, food security, and flood risk to people (Borges et al., 2015; Dargie et al., 2019; Laraque, 2019; Comptour et al., 2020). Channel flow conditions also influence fluvial navigability and sediment transport processes (Fernandez et al., 2010; Mushi et al., 2019). Hydrodynamic models that simulate channel flow conditions are an important tool in quantifying these risks and processes, and representation of in-channel geometry and flow conditions is crucial to these models. For example, modelled in channel water surface elevation and its rate of change over time will strongly influence the extent and duration of seasonal inundation predicted in the Cuvette Centrale wetlands, and therefore the amount of carbon dioxide and methane emission that are predicted through outgassing from inland waters.

In developing a hydrodynamic model, a key question that arises is how to represent the multithread channel geometry of large rivers such as the CMR (Figure 6-1). This question is therefore highly pertinent to large river modelling generally: of the world's ten largest rivers, nine have a channel pattern that is predominantly 'anabranching' (Latrubesse, 2008). Here, anabranching refers to a particular pattern of multichannel river whereby vegetated or otherwise-stable alluvial islands divide flows at discharges up to bank-full (Nanson, 2013).

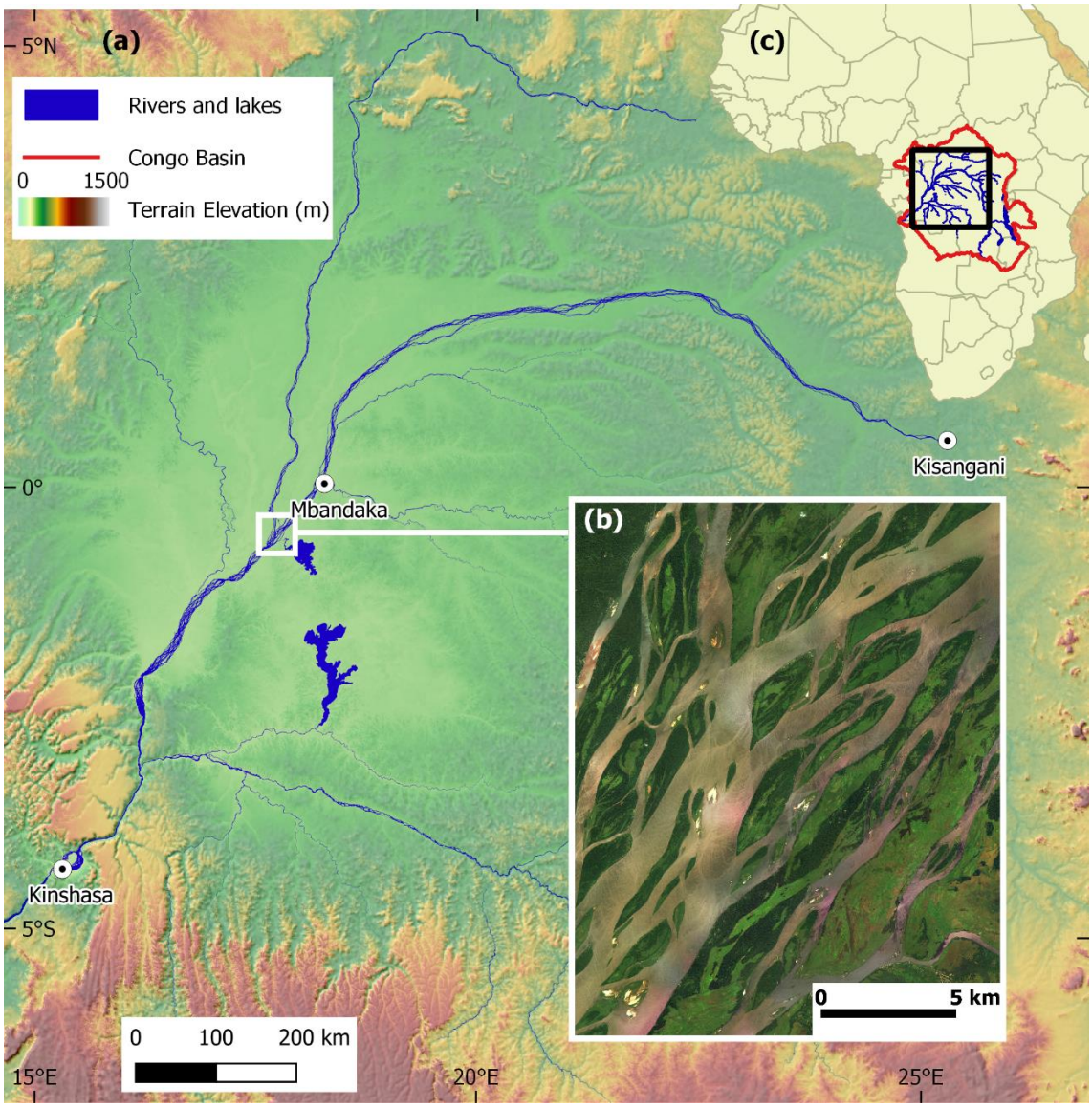

Figure 6-1. The Congo River: (a) The central Congo Basin, showing the mainstem middle reach that flows from Kisangani to Kinshasa, major tributaries, and terrain elevations; (b) Satellite image showing characteristic multichannel planform that persists for almost the entire middle reach; (c) Location plan within the extent of the African continent, showing country boundaries. Rivers and lakes water mask from O'Loughlin et al. (2013), Terrain elevations from MERIT DEM (Yamazaki et al., 2017); satellite image from Bing (© 2020 Microsoft Corporation © 2020 DigitalGlobe © CNES (2020) Distribution Airbus DS).

Clearly the answer will depend to some extent on the availability of data. For example, bathymetry data comprising a limited number of coarsely-spaced cross-sections sampled at single thread sections will preclude the representation of cross sectional variability in channel bed elevation, and necessitate the use of a constant cross-sectional bed elevation profile. The particular requirements of the model such as the accuracy and spatiotemporal resolution of its outputs will also influence the approach

to channel representation: a model that is required to predict spatial variability in velocity across the channel will require cross-sectional variability in bed elevation to be represented. However, a question relevant to reach scale and basin scale models serving a variety of purposes is whether a simplified effective single channel (ESC) can be adopted. Such simplifications are commonly adopted in large scale hydrodynamic models (Neal et al., 2012; Schumann et al., 2013; Rudorff et al., 2014; Schneider et al., 2018), and involve representation of channel geometry along a discrete reach with a single mean cross-sectional depth, a simple shape such as a rectangle, curved bed or triangle, together with a constant bed slope. ESCs enable use of 1D channel models and minimise the requirements for model resolution, thereby minimising the required resolution of input data. This results in faster models, greater potential for automation in model building and calibration, and therefore more opportunity for ensemble or optimisation approaches that allow for the sparsity of data and high levels of uncertainty inherent in CMR input data (Tshimanga and Hughes, 2014; O'Loughlin et al., 2020).

Use of an ESC approximation to represent in-channel hydraulic processes has been shown to provide considerable improvements in hydrodynamic model performance over models that do not represent channels (e.g. Samuels, 1990; Bradbrook et al., 2004; Neal et al., 2012; Sampson et al., 2015). However, ESC approximations of large rivers are not well validated against more detailed hydrodynamic models that represent spatially distributed channel bathymetry. This is particularly true in the case of multichannel rivers. The specific hydraulic consequences of such a simplification are therefore not well understood. To some extent, this is because ESC approximations have mainly been used in situations where no channel hydraulic data has been available, preventing an assessment of the specific impacts of the approximation on hydrodynamic model performance. Here, the applicability of an ESC approximation to the CMR is evaluated.

By adopting an ESC on the CMR, several features of the channel geometry will be neglected or misrepresented, which will lead to some misrepresentation of channel hydraulic conditions. As a result, ESCs cannot be used in situations that require estimation of the cross-sectional distribution of channel velocities, and their use is regarded as being limited to the prediction of water surface dynamics (extent and elevation). Accordingly, this research investigates the effects of ESC representations on Water Surface Elevation (WSE) and its spatial and temporal variability. The objective of the research is to characterise and quantify the hydraulic consequences of an ESC approximation, and ultimately determine its suitability for use in modelling the hydrodynamics of the CMR.

The subsequent sections of this chapter are structured as follows. Section 6.2 begins by setting out research assumptions and identifying four key components of an ESC approximation to a real multichannel bathymetry. The remainder of section 6.2 documents a preliminary investigation of the hydraulic consequences of each of these four components (without the use of hydraulic modelling), based on an analysis of available observations of the CMR and application of the Manning formula for uniform flow conditions. Section 6.2 concludes by identifying a series of hydraulic modelling experiments. The modelling experiments are designed around the validated steady state base hydraulic model documented in Chapter 5. Section 6.3 documents the methods used in these hydraulic modelling experiments, and section 6.4 reports their results. Discussions and conclusions follow in section 6.5 and 6.6 respectively.

6.2 Preliminary Investigation of an Effective Single Channel Approximation

6.2.1 Assumptions

For the CMR, an effective single channel that uses a rectangular cross-section is a logical choice of channel shape, given the lack of channel width change over the bi-annual flood cycle that is apparent from satellite imagery, implying steep riverbanks (Pekel et al., 2016). The observations of channel depth plotted against their distance from a bank in Figure 5-5 (Chapter 5) also support a rectangular approximation, as they show no pattern of increasing channel depth with the distance from nearest bank. A rectangular ESC is therefore assumed initially, which is described by the following three channel geometry parameters that are fixed over a discrete reach length: bed slope, width, and depth. Variations in channel shape are considered however, specifically in subsection 6.4.2. The length of an individual reach, akin to the spacing between traditional 1D river cross-sections, may be any value, and may vary for each of the three geometry parameters. Some accounts of reach lengths adopted in recent studies are given in the literature, for example, on the Niger River, Neal et al. (2012) use a ~1 km reach length over which channel width and depth are sampled, and sample bed slope across a 15 km reach length. On the upper Niger River, Fleischmann et al. (2018) use a fixed channel depth, width and slope across unit-catchments that are on average 150 km^2 in area, or an indicative river length of 14 km if river length is assumed to be the diameter of a circle with this mean catchment area. In the only known hydrodynamic model of the CMR, (O'Loughlin et al., 2020) report use of a constant depth between ENVISAT WSE observations that have an average and maximum longitudinal spacing of 70 km and 170 km (it is not clear what reach length was used to represent width and bed slope). They also derive the channel geometry of each individual reach through a

calibration process, whereby channel depth (or related parameters such as hydraulic radius) is calibrated to observations of relatively low spatial resolution. WSE observations from satellite altimetry are commonly used for calibration; reach-averaged discharge may also be used. In the CMR, ENVISAT altimetry has the greatest spatiotemporal density and coverage, and is therefore most likely to be used for calibrating channel geometry. It is therefore assumed that an ESC approximation will involve calibration of channel friction to observations of WSE.

This research also assumes that the simplification of a real multichannel bathymetry into an ESC comprises the following individual components:

1) Neglecting morphological features that manifest as localised stream-wise changes or irregularities in channel width, depth, or bed slope;
2) Merging of individual channel thread that have their own sinuosity into a single channel, thereby neglecting the variability in sinuosity of the individual channel threads;
3) Neglecting cross-sectional depth variability by adopting a constant and simple cross-sectional shape (constant depth for a rectangular ESC); and
4) Neglecting seasonally inundated mid-channel islands.

To investigate the hydraulic consequences of an ESC, this research evaluates each of these components individually. If they are evaluated in a combined manner, they may ‘counteract’ each other to some extent, and obscure certain hydraulic consequences.

6.2.2 Omitting Channel-Scale Morphological Features

The averaging of channel geometry over a discrete reach, and its derivation through calibration to observations of WSE spaced on average 70 km apart, will result in a channel geometry that omits local variations in channel-scale morphology. Therefore, the ESC will smooth the water surface profile (WSP) according to the observations used for calibration, and may omit morphological features that cause the water surface to deviate considerably from a smoothed WSP. For large sub-critical rivers, including multichannel rivers, these morphological features can be characterised as either constrictions, or breaks in bed slope (Frasson et al., 2017; Montazem et al., 2019). Tributaries can also produce variations in the WSP, in the form of backwater profiles. The omission of these features will neglect the WSP variations they cause, which manifest as backwater or drawdown gradually varied flow profiles, examples of which are shown in Figure 6-2.

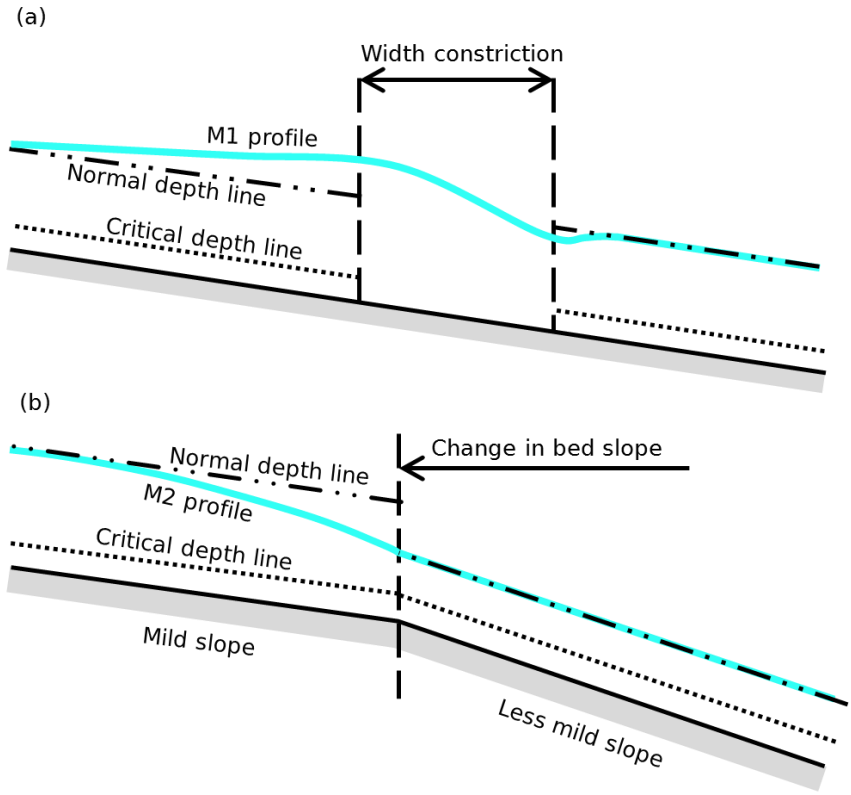

Figure 6-2. Example gradually varied flow profiles resulting from morphological features in a large sub-critical river, with water surface shown in blue: (a) a constriction causing a backwater effect, (b) an increase in bed slope causing a drawdown effect. Adapted from Chow (1959) and Moglen (2015).

The hydraulic characterisation documented in Chapter 4, based on observed low flow conditions along the CMR between Kinshasa and Mbandaka (Chainage 0–650 km) provides insight into the presence of WSP variations caused by morphological features. The entrance to the Chenal (chainage 270 km) constitutes a significant morphological feature, where a drawdown curve is known to occur due to a steepening of the bed slope. Any channel representation will need to represent this bed slope change in order to correctly model the WSE. This location aside, no significant WSP variations were identified: between chainage 270–650 km, WSE observations showed no significant changes in Water Surface Slope (WSS), and the error in WSE resulting from WSP linearization (i.e. piecewise linear interpolation between measurements on average 50 km apart) was found to be no greater than 0.3 m.

Water surface profile analysis between Mbandaka and Kisangani

The reach between Mbandaka and Kisangani (chainage 650–1650 km) was not analysed with in-situ data in Chapter 4, coincident bathymetry data not being available for a full hydraulic characterisation. Looking at the terrain along this reach (Figure 6-3),

no significant landforms indicative of morphological changes are visible, unlike between Kinshasa and Mbandaka, where the river cuts through the Bateke Plateau and changes its planform and bed slope as a result. River widths analysed by (O'Loughlin et al., 2013) showed channel width variability to be small compared with the major width constrictions that are present between Kinshasa and Mbandaka.

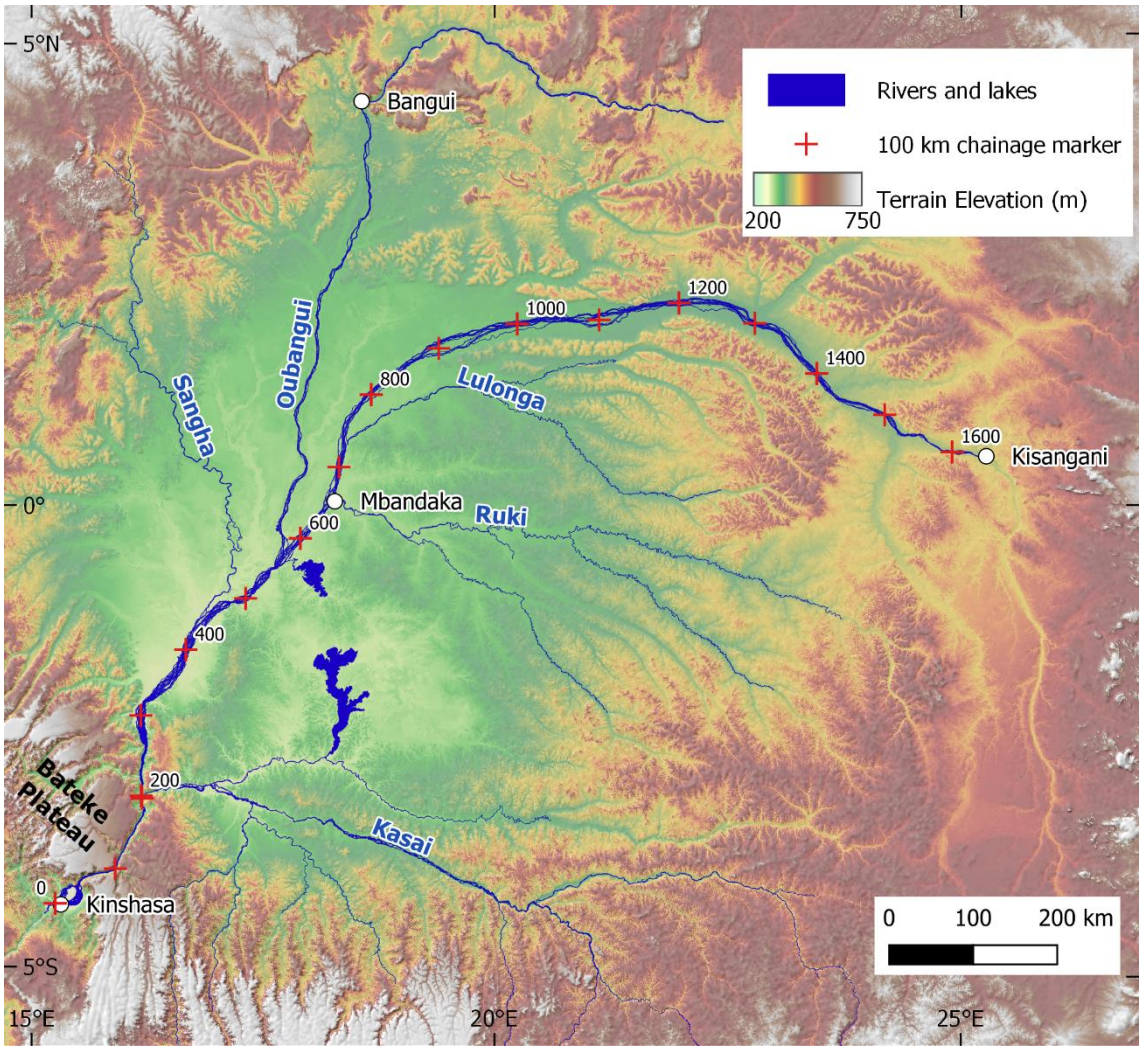

Figure 6-3. Terrain of the Central Congo Basin. Elevation data from MERIT DEM (Yamazaki et al., 2017), Water mask from Landsat data (O'Loughlin et al., 2013).

ENVISAT WSE data analysed in Chapter 4 shows no marked WSP variations between Mbandaka and Kisangani. However, the relatively large spacing between ENVISAT observations may not resolve more localised variability in WSS. Therefore, GNSS observations obtained during the 2019 field campaign have been processed here to obtain a more accurate and higher resolution WSP. Figure 6-4 and Figure 6-5 show the static GNSS measurements of WSE and the resulting WSS, along with continuous GNSS measurements of WSE re-sampled at 5 km intervals.

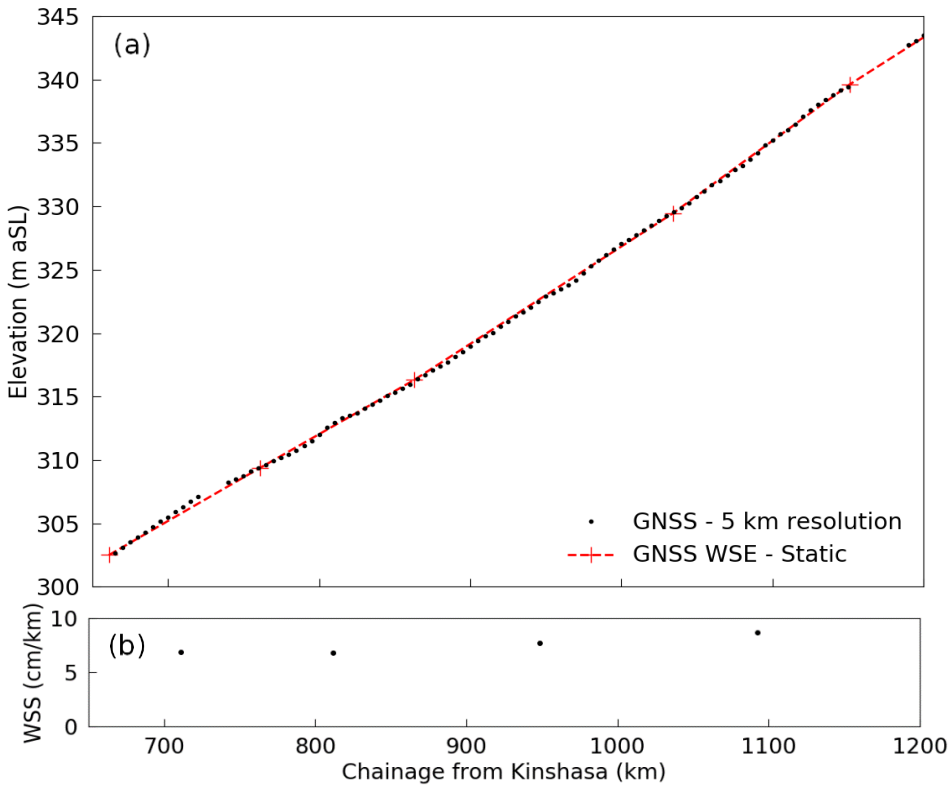

Figure 6-4. 2019 in-situ WSEs, ch. 650–1200 km: (a) WSPs; (b) WSS from static WSE.

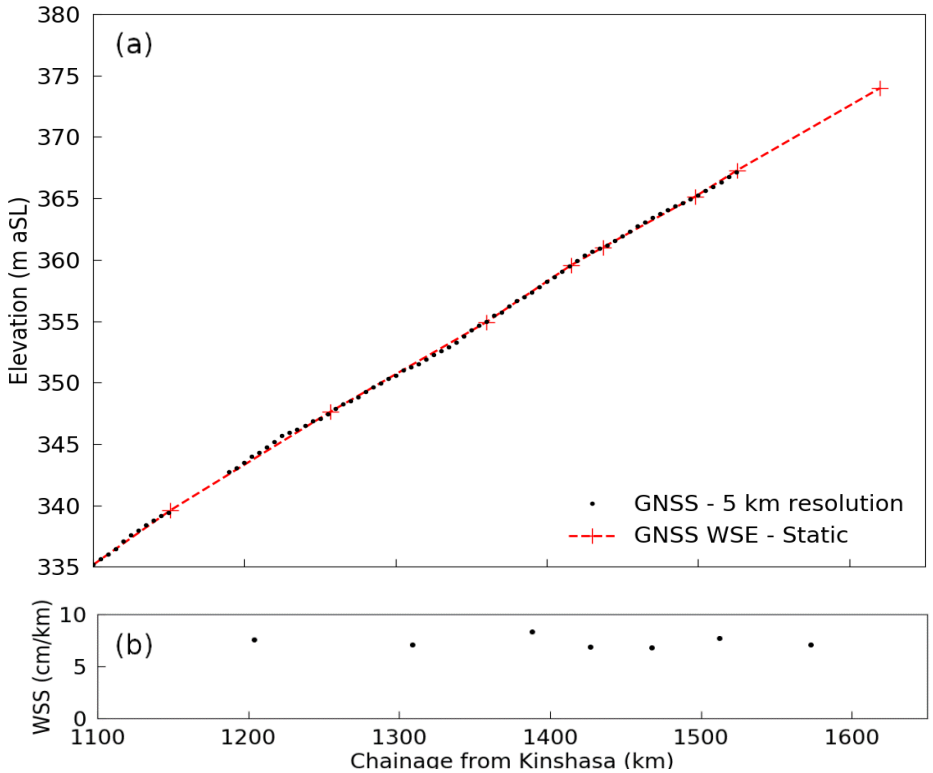

Figure 6-5. 2019 in-situ WSEs, ch. 1100–1650 km: (a) WSPs; (b) WSS from static WSE.

Static WSEs and their slopes are in agreement with the ENVISAT analysis: between chainage 600–1100 km the water surface gradually flattens in the downstream direction, whilst upstream of 1100 km this trend ceases, and WSS fluctuates between 7 and 9 cm/km. There are no significant variations in the static WSP. The 5 km WSEs capture the finer scale variations in the WSP. Most of these variations show a deviation from the linearly interpolated static WSEs no greater than 0.3 m, as was found for the reach between Kinshasa and Mbandaka. However, at two locations, the 5 km measurements show the WSP to deviate from the static WSP by up to 0.5 m. One of these locations, chainage 725 km, is at the confluences with the Lulonga River, and is therefore explained by the backwater effect from these tributaries. However, there are no tributaries, terrain features, or planform features that explain the cause of the WSP variation at chainage 1225 km, which suggests it is caused by the bathymetry. No bathymetry data are currently available to investigate this in further detail. Additional WSP variations are also visible, but due to closely spaced static WSE measurements, they are not identified in the comparison between static and 5 km measurements. Therefore, to estimate the error resulting from the 5 km WSP being smoothed, the 5 km WSEs collected along the multichannel CMR were split into five sub-reaches on average 220 km long. WSEs within each sub-reach were then resampled at an interval of approximately 70 km, and second order polynomials fitted to each set of resampled WSEs, in order to represent a smoothed WSP. The regression analyses showed RMSE across all sub-reaches to be 0.15 m, and identifies three WSP variations where the WSE error exceeds 0.3 m by a considerable margin. Graphical results of the regression analysis is located in Appendix C.1.

Morphological features affecting WSE during high flow

Since the analysis of in-situ observations are based on low flow conditions only, the analysis will not include any WSP variations that form during high flows as a result of bank topography. Such variations would manifest in the form of a constriction effect (i.e. an upstream backwater effect produced by a reduction in cross-sectional flow area as shown in Figure 6-2a), caused by a topographic barrier that locally forces flood flows through the width of the main channel, whilst upstream and downstream flows are able to inundate the floodplain. Their occurrence will be determined by floodplain topography, which is subject to significant uncertainty based on currently available elevation datasets, and cannot therefore be thoroughly investigated in this study. However, high flow constriction effects are most likely to be present at the river width constrictions, because a given loss of floodplain cross-sectional flow area will be forced through a smaller cross-sectional flow area, as illustrated in Figure 6-6.

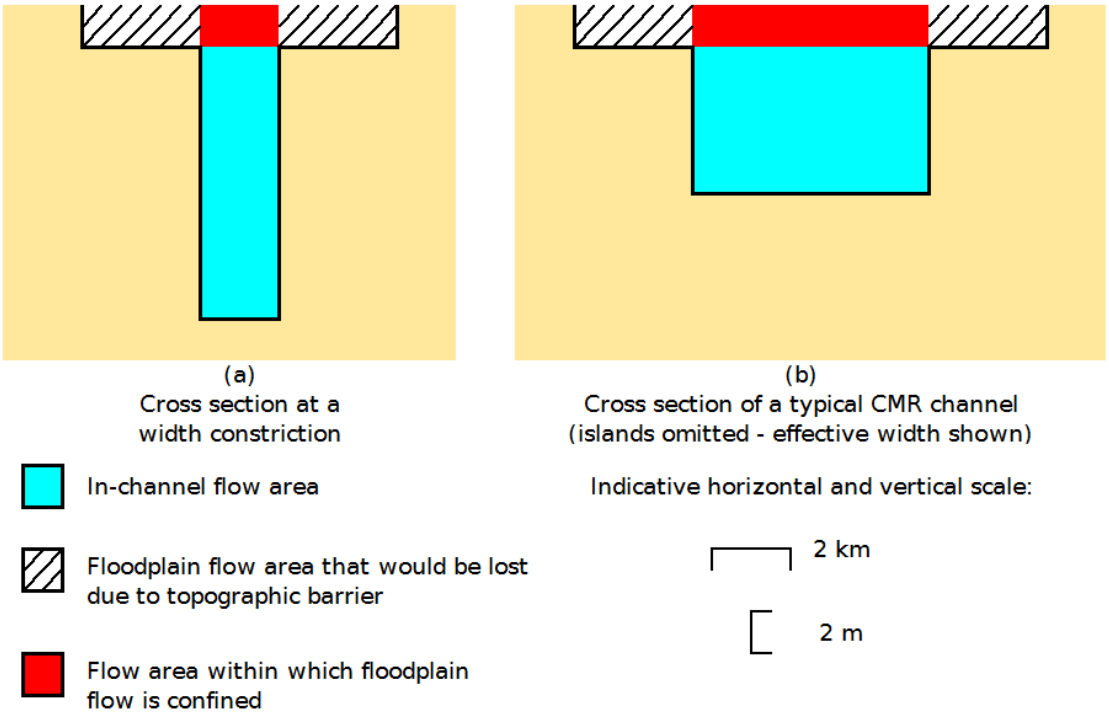

Figure 6-6. Explanation of why high flow constriction effects caused by topographic barriers are most likely to be present at width constrictions: (a) at a width constriction, the cross-sectional area of floodplain flow is constricted to a smaller area (shown in red) due to the narrower width of the channel; (b) at a typical channel width the wider channel provides a much larger cross-sectional flow area (red area) for floodplain flow to occupy. Channel dimensions assume a 4 m high flood wave amplitude and a 2 m river bank height above low flows.

Whilst the analysis presented in Chapter 4 showed the width constrictions produce no backwater effects during low flows, these width constrictions are known to be located at outcrops of high land (O'Loughlin et al., 2013), which have been identified as iron rich conglomerates from field observations (M. A. Trigg, personal communication, 2020). A backwater effect may develop here during high flows when these outcrops act to confine the flow to within the channel. Further insight into the three width constrictions within the multichannel reach can be gained by examining MERIT elevation data (Yamazaki et al., 2017) and Landsat images during inundation, all of which are shown in Figure 6-7.

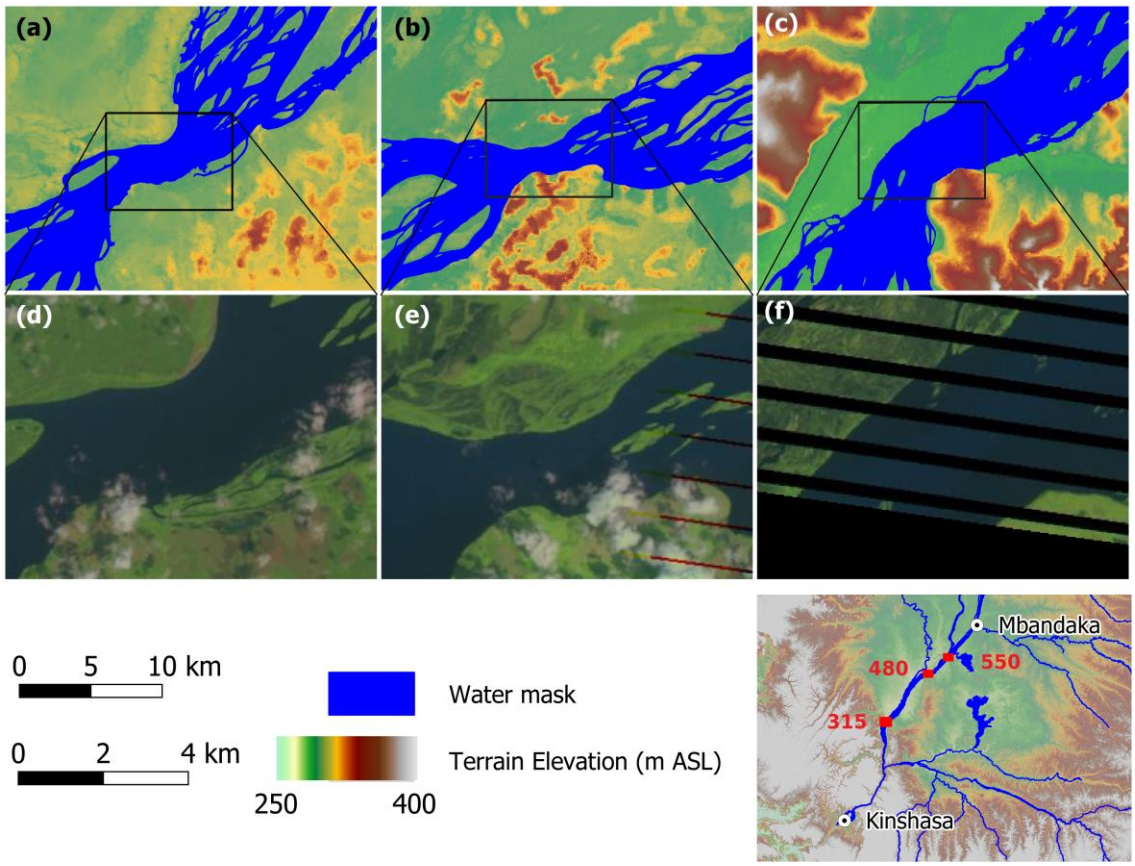

Figure 6-7. Three main width constrictions along the multichannel CMR: (a) – (c) show terrain elevations at Chainage 550 km, 480 km, and 315 km, (d) – (f) show corresponding Landsat images during high flow season (23 November 2009). (a) and (d) indicate left bank inundation, (b) and (e) indicate right bank inundation, (c) and (f) indicate right bank inundation. Landsat images obtained from the Earth Explorer website: https://earthexplorer.usgs.gov/; water mask from O'Loughlin et al. (2013); terrain elevations from MERIT DEM (Yamazaki et al., 2017).

All three width constrictions appear to be flanked by high terrain only on one bank. In all cases, elevations on the opposite bank are consistent with upstream and downstream bank elevations, and Landsat images during the high flow season show evidence of connectivity between the channel and floodplain (assuming the flooding that is visible is fluvial). This indicates that no constriction effects will develop here during high flows. To affirm the absence of backwater effects at the width constrictions, the calibrated hydraulic model can be used to simulate high flow conditions through the width constriction at chainage 480 km. This width constriction constitutes the most extreme reduction in river width, and is therefore the most likely to generate a backwater effect.

6.2.3 Merging Individual Channel Threads

The conversion of several individual channel threads to a single channel will neglect the sinuosity of individual channel threads, and in turn neglect a component of the flow path lengths along which water travels. For a given hydraulic roughness coefficient, this reduction in flow path lengths is expected to give rise to an artificial increase in the channel's hydraulic efficiency (i.e. the flow it can convey for a given water surface). A hydraulic modelling experiment is required to determine the magnitude of this increase in hydraulic efficiency.

A single channel will also neglect the sides of the numerous individual channel threads and the component of the wetted perimeter they represent, but this is negligible given the extremely high width/depth ratios of the CMR: the ratio is over 1000 at the acoustic Doppler current profiler (ADCP) measurement at chainage 515 km. Assuming 10 channel threads with a mean depth of 6 m are neglected, the omission of 20 channel banks amounts to 20x6 = 120 m of neglected wetted perimeter. For a typical CMR effective width of 5 km, this amounts to a negligible error in wetted perimeter of approximately 2.5%, affirming the assumption that wetted perimeter is approximately equal to wetted width.

6.2.4 Omitting Cross-sectional Depth Variability

An ESC represents the channel with a single depth, omitting the variability in the cross-sectional depth that occurs in natural rivers. A channel with a variable depth produces a greater mean channel velocity (and therefore flow) than an equivalent channel with a constant depth. This is due to the development of higher water velocities across the thalweg where the water is deepest and furthest away from the river bed that generates flow resistance (e.g. Douglas et al., 2001). Therefore, a channel with a constant cross-sectional depth can be regarded as being less hydraulically efficient than a channel with a variable cross-sectional depth, even if it has the same cross-sectional area, width, wetted perimeter, bed slope, and roughness coefficient. To investigate this in the context of the CMR, discharge – stage ($Q-H$) relationships were computed for three multichannel scenarios, shown in Figure 6-8: (a) a channel with seven equally deep threads; (b) a channel with one moderately deeper thread; and (c) a channel width one very deep thread. With the exception of the distribution of depth across the channel threads, the adopted geometry of each channel is identical. The adopted parameter values are listed in Table 6-1 and are broadly representative of the CMR based on the in-situ observations presented in Chapter 4.

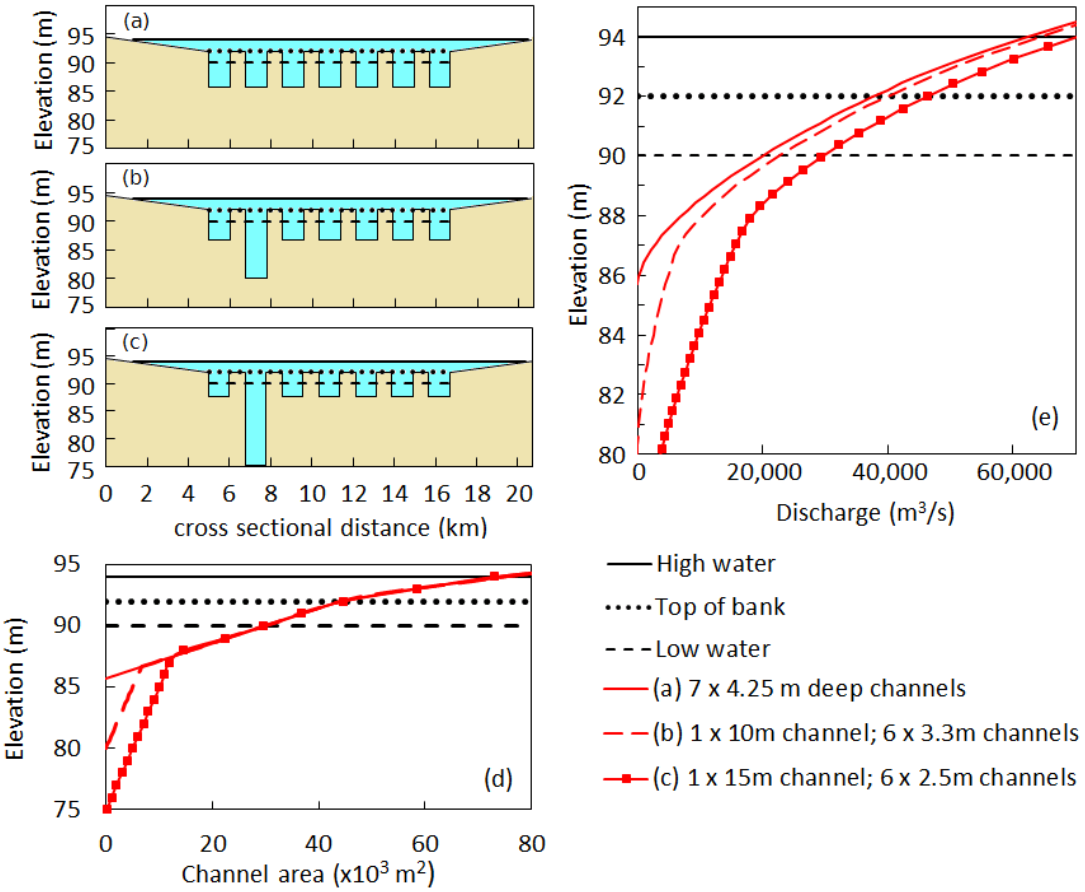

Figure 6-8. Q–H curves for three channel geometries that are geometrically equivalent aside from the distribution of depth across the channel: (a) channel with constant depth distribution; (b) one deep channel thread and six equally deep threads; (c) one 15 m depth channel thread and six equally deep threads; (d) Plot of channel elevation versus cross-sectional area for each geometry, demonstrating geometric equivalence; (e) $Q - H$ curves calculated using normal depth calculator tool within the Flood Modeller software package (Jacobs, 2019). Elevation is above an arbitrary datum.

Table 6-1. Parameters common to all three of the channels shown in Figure 6-8. Values are representative of the multichannel CMR.

Value	Parameter
7	Effective channel width at or below top of bank level (km)
1	Channel thread width (km)
11.7	Total channel width (km)
0.6	Ratio of effective channel width to total width
29,750	Cross-sectional area measured below low water level (m^2)
4.25	Mean channel depth below low water level (m)
5	Bed slope (cm/km)
7	Number of channel threads
0.028	Manning's *n* below top of bank
0.1	Manning's *n* above top of bank
1 in 2000	Floodplain transverse slope
2 m	Bank height above low water
4 m	Flood wave amplitude

Figure 6-8 shows that the 10 m deep channel thread in section (b) produces only a small increase in hydraulic efficiency compared to the channel with a constant depth. However, when the channel thread depth is increased to 15 m as in section (c), the difference in stage response is significant: for a given flow, the equivalent channel section with a constant depth generates a much a higher WSE, particularly during low flow conditions. As expected, the computed mean channel velocities are greater when the channel geometry contains a deep thalweg. At low water, velocities are: 0.68 m/s in section (a); 0.76 m/s in section (b); and 0.99 m/s in section (c).

In conclusion, if a channel possesses a thalweg of sufficient depth relative to its mean channel depth, the omission of the thalweg will result in an artificial increase in channel hydraulic efficiency, according to uniform flow formulae. To ascertain whether neglecting CMR channel depth variability would lead to the introduction of a significant reduction in hydraulic efficiency, a more detailed assessment of channel depth variability

in the CMR can be undertaken, and combined with a hydraulic modelling experiment based on the calibrated base hydraulic model.

6.2.5 Omitting Seasonally Inundated Mid-channel Islands

The simplest approach to representing islands would be to ignore islands completely and adopt a channel with a width equal to the total mean channel width. In this approach, a shallower effective channel depth would be needed to maintain the correct channel cross-sectional area, which would lead to a reduction in hydraulic efficiency caused by a significant over-estimation of channel wetted width (and wetted perimeter). Effective channel widths in the CMR are on average approximately 60% of total channel width, and as low as 30% of total channel width over one 100 km reach (O'Loughlin et al., 2013). Neglecting islands would therefore over-estimate width and wetted perimeter by 40% on average, and by up to 70% along one particular reach. It is therefore likely to be necessary to incorporate the islands into the in-channel geometry by using the effective channel width. This can be confirmed by quantifying the hydraulic effects of over-estimating channel width, through comparison of the $Q-H$ relationship of the channel geometry presented in Figure 6-8(a) with that of a channel with the islands omitted. This comparison is plotted in Figure 6-9, and shows a fundamental difference in the stage response of the two channels within the range of the flood wave amplitude, despite its cross-sectional area being the same at top of bank elevation.

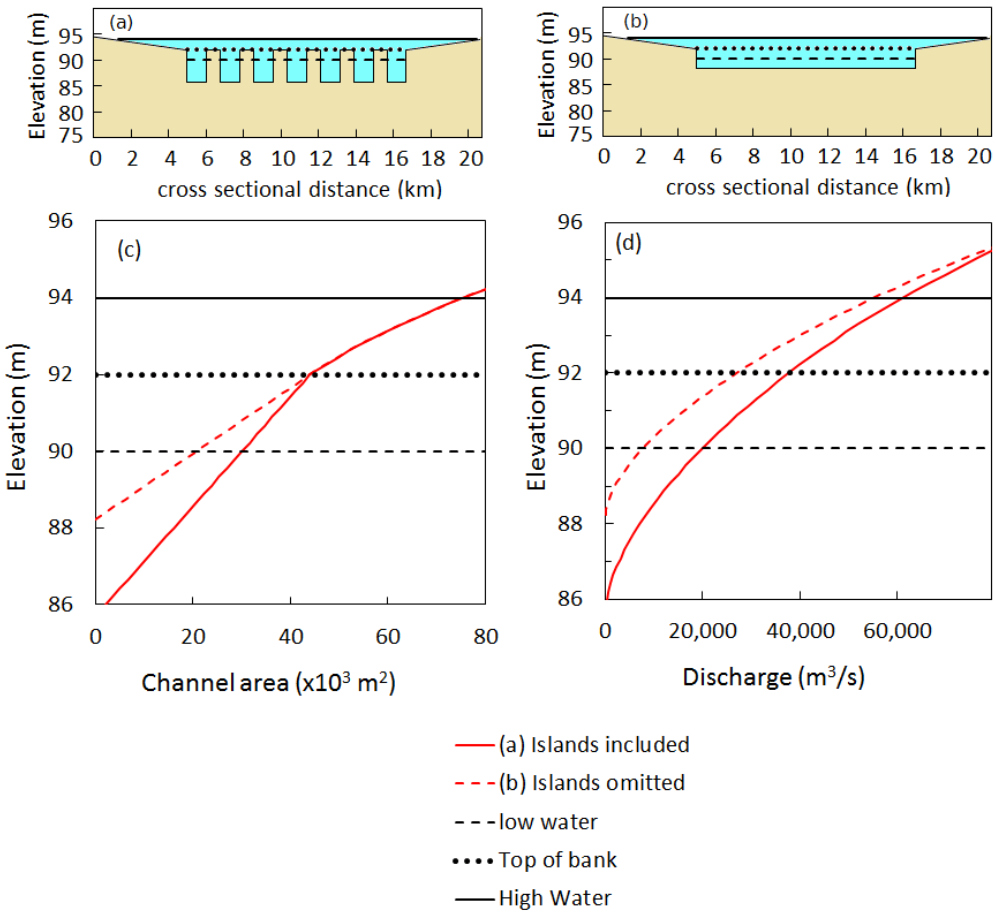

Figure 6-9. Q–H curves for channels with islands included and omitted: (a) channel with islands included; (b) channel with islands omitted and channel bed elevation raised to maintain the same cross-sectional area; (c) Plot of channel elevation versus cross-sectional area for each channel; (d) Q–H curves calculated using normal depth calculator tool within the Flood Modeller software package (Jacobs, 2019). Elevation is above an arbitrary datum.

Another consideration with respect to representation of islands is how to represent high flow when inundation of the islands occurs. Based on personal field observations (e.g. fishing villages on ~2 m stilts) and the observations of others (e.g. Comptour et al., 2020), CMR mid-channel islands are known to seasonally inundate. Model codes that are usually associated with effective single channel approaches such as that of LISFLOOD-FP, in which channels are represented as 'sub-grid' features within a 1D channel model domain (discussed in subsection 2.4.2), are not able to represent islands explicitly, as the entire width of the channel must be represented within a single cell (i.e. a single terrain elevation value). Given the very large plan area that the islands occupy within the channel, they will constitute a significant component of total fluvial inundation along the CMR, and their inundation should therefore be modelled explicitly

in the same way as a conventional floodplain. Moreover, failure to represent the island inundation process will misrepresent several hydraulic processes. Most significantly, the volume of water that would otherwise inundate the islands would be erroneously contained within the channel, and / or routed onto the floodplain (if there is connectivity with the floodplain), as illustrated in Figure 6-10. Panel (a) of Figure 6-10 shows a simplified definition of multithread channel geometry, and the three flow components: channel, floodplain inundation, and island inundation. In panel (b), the channel is represented with a 1D ESC based on effective channel width, and the floodplain is represented with a 2D domain. However, the islands are not represented, and the island inundation volume is conveyed by the channel and floodplain, resulting in erroneous predictions of inundation and / or WSE. In panel (c), islands are included within the 2D floodplain domain, enabling inundation extent and WSE to be correctly simulated.

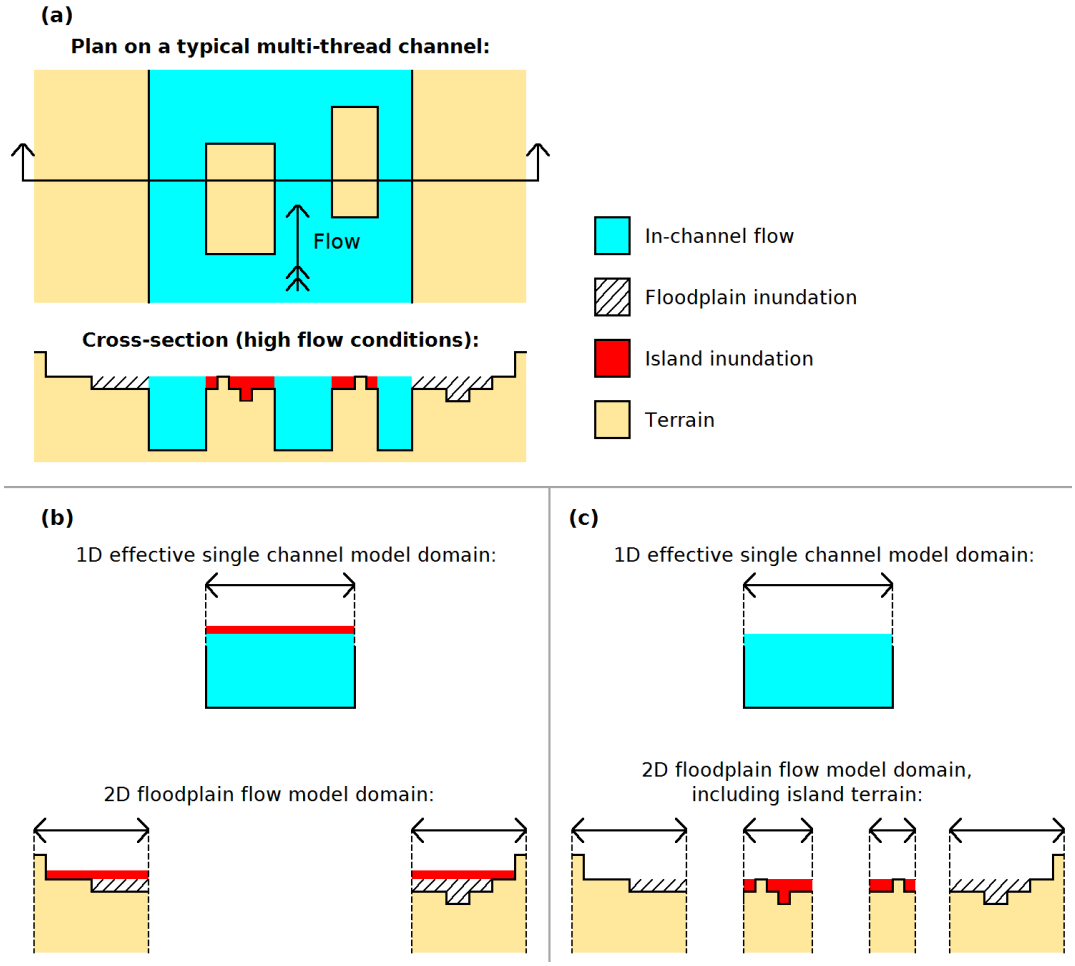

Figure 6-10. Modelling island inundation when using a 1D ESC domain coupled to a 2D floodplain domain: (a) Simplified definition of channel geometry, floodplain, island, and channel flow components, and legend; (b) islands excluded from 2D domain, resulting in water being erroneously contained within the channel and routed onto the floodplain; (c) Explicit representation of islands within the 2D floodplain domain.

Omitting island inundation would also neglect complex changes in channel hydraulic efficiency that occur with increasing WSE as islands inundate. Island inundation reduces flow path lengths as water flows begin to follow a more direct route (i.e. the channel threads begin to close), giving rise to some increase in hydraulic efficiency. However, the islands are heavily vegetated and represent a significant increase in hydraulic roughness, countering this increase in hydraulic efficiency. The net hydraulic effect of island inundation is therefore not straightforward to predict or parameterise and will be highly dependent on the actual elevation of the islands, which adds support to the argument that island inundation should be modelled explicitly. This would entail the incorporation of island terrain into a DEM within a 2D model domain, and use of a water mask to define the spatial extent of the 1D model domain that employs the single effective channel, as shown in Figure 6-10c.

Hydrodynamic models developed for certain purposes such as estimating discharge, which do not require information on inundation, may warrant a different approach in which the island inundation process is lumped within an effective friction parameter that varies in time and space. For example, Garambois et al. (2017) parameterised multichannel river island and floodplain inundation along a reach of the Xingu River (first order tributary of the Amazon) using a stage varying friction parameter and a compound channel shape, and were able to do so using an unusually high spatial and temporal density of WSE data from ENVISAT, complemented with modelled discharge. The primary intention of this study is not to investigate such an approach, as the hydraulic observations during a range of flows that would be required to do so are unavailable. Therefore, no model experiment is proposed to look specifically at island inundation.

6.2.6 Use of Hydraulic Roughness to Compensate for Channel Geometry Errors

The Manning's hydraulic roughness parameter, *n* is commonly treated a parameter to be calibrated, and as such, will compensate for omissions in channel geometric representation arising from an ESC, to some extent. The limitations of using calibration schemes that vary the hydraulic roughness parameter locally to fit WSE are reviewed in subsection 2.4.5, in the context of using *n* to compensate for errors in cross-sectional area and depth. Here, cross-sectional area is assumed to be known, and errors specific to channel geometric representation are investigated.

The effect of varying the *n* value of a channel on modelled flow conditions can be visualised by plotting a channel's $Q-H$ curve. Essentially, changing *n* will change the slope of the curve, but does not alter the H axis intercept of the curve, which is controlled

by the channel's depth. An increase in *n* will steepen the curve, producing greater H values for a given Q. Therefore, adjustment of a constant *n* value may not enable an ESC to sufficiently reproduce the stage response of the actual channel. This is illustrated in Figure 6-11, which plots the two $Q-H$ curves for a channel (a) including islands, and (b) omitting islands. These are the same two $Q-H$ curves as those plotted in Figure 6-9. A third curve, (c) is also shown, for the case where islands are omitted, and the *n* value has been adjusted to reproduce the top of bank WSE to that of curve (a). The adjustment entailed a reduction in *n* of 30%, from 0.028 to 0.020, and is analogous to the calibration of *n* to an observed WSE.

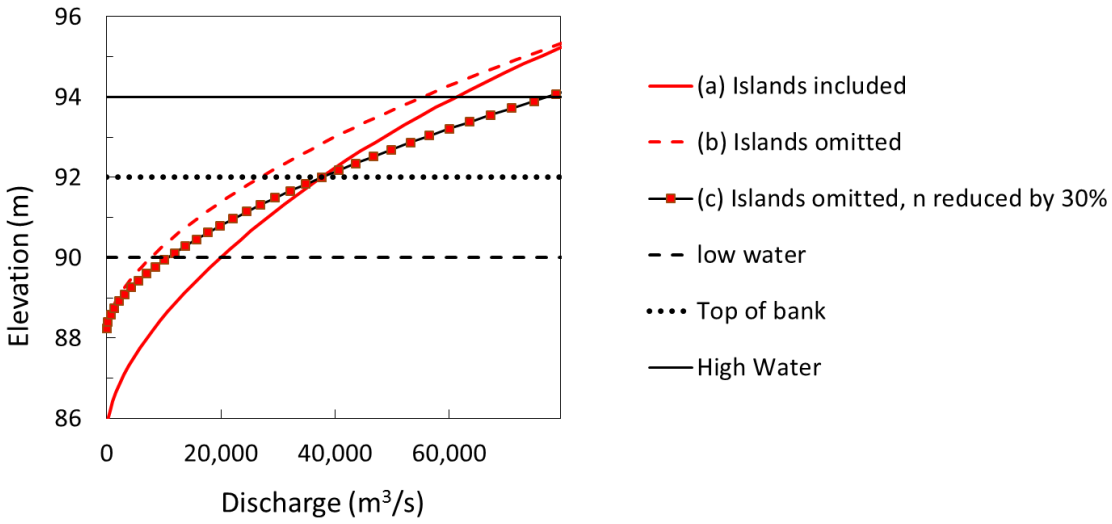

Figure 6-11. Q–H curves illustrating the use of n to compensate for significant misrepresentation of channel geometry (the omission of islands in this case).

The omission of islands has already been shown to produce a fundamental change in the stage response of the channel within the range of the flood wave amplitude, and it is not surprising that a simple reduction of a constant *n* value does not adequately correct this error. However, it does provide an effective illustration of the limitations of varying *n* locally to fit WSE: the model with islands omitted will correctly predict the WSE for which *n* has been calibrated, but will not do so across a range of flows. In Figure 6-11, *n* is calibrated to the top of bank WSE of 92 m, resulting in a large underestimate of WSE during high flow, and a large overestimate of WSE during low flow. Had *n* been calibrated to the high flow WSE, the low flow error would be even larger. Allowing *n* to compensate for large errors in channel geometry also has implications for modelled flood wave propagation; flood wave speed being a function of water velocity and channel depth (Chow, 1959).

A hydraulic roughness parameterisation that varies in time or with WSE would enable a more effective adjustment of a channel's $Q-H$ curve. For example, curve (c) in Figure 6-11 could be more effectively adjusted to match curve (a) by adopting a lower *n* value at low water, and a progressively higher *n* value as WSE increases and approaches high water. Garambois et al. (2017) use this approach in the ESC model they develop for a reach of the multichannel Xingu River. However, flow and WSE data of a high spatial and temporal density is required to ascertain an appropriate distribution of *n* values in time or across a WSE range. In addition, such an approach adds further complexity to the model calibration process. Accordingly, there is interest in retaining a more conventional hydraulic roughness scheme in which *n* varies in space, but not in time or with WSE.

6.2.7 Summary of Preliminary Investigation

Simplification of the CMR multichannel bathymetry to an ESC has been broken down into four specific geometric omissions that each influence channel hydraulic conditions in different ways. These geometric omissions comprise: channel-scale morphological features, individual channel threads, variability in cross-sectional depth, and mid-channel islands. The hydraulic effects of these features have been notionally characterised, and a series of hydraulic modelling experiments has been identified in order to quantify and investigate these effects further. Mid-channel islands are not investigated with a dedicated model experiment here, as their inundation constitutes a significant component of inundation along the CMR, and as such they should be represented explicitly. Therefore, three geometric omissions due to a single channel representation are investigated here, and are each investigated with a modelling experiment:

- **Width constriction at high flow (WC):** any WSP variations that develop at channel-scale morphological features during high flow would be most pronounced at the major width constrictions as backwater effects. To confirm the absence of constriction effects during high flows, high flow conditions are simulated through the most pronounced width constriction at chainage 480 km, using the base hydraulic model.
- **Merging Individual channel threads (MT):** the erroneous increase in hydraulic efficiency introduced by converting individual channel threads to an ESC is investigated by comparing the base hydraulic model with a single thread channel version of the model. Creation of a single channel version of the base hydraulic model is possible through conversion of the bathymetry model (BM) to an ESC with equivalent cross-sectional area and width.
- **Cross-sectional depth variability (XSV):** The BM does not fully represent variability in depth across the multi-thread channels, as bathymetry has largely been estimated based on the assumption that the entire channel cross-sectional width is constant. By adding synthetic thalwegs to the BM based on a characterisation of CMR thalweg geometry, a hydraulic model will quantify the potential reduction in hydraulic efficiency resulting from the omission of cross-sectional depth variability.

The model experiments make use of the base hydraulic model and associated DEM – i.e. the bathymetry model (BM), which are developed and validated in Chapter 5.

6.3 Methods: Hydraulic Modelling Experiments

The conceptual methodology used in the model experiments entails the use of the base hydraulic model, constructed using HEC-RAS-2D, to test the effect of the three aforementioned geometric omissions resulting from an ESC. Before setting up the model experiments, four initial model tests were first carried out, these being necessary to develop and test the conceptual methodology used in the model experiments. These initial tests are documented below.

6.3.1 Initial Model Tests

Test 1: Diffusive Wave Approximation

This test was done to confirm whether the diffusive wave solver in HEC-RAS can be used for all model experiments. The diffusive solver is more numerically stable and computationally faster, and its use will therefore allow the modelling experiments to be completed more efficiently. HEC-RAS-2D uses the diffusive wave solver by default, but Brunner (2016) recommends a test model run using the full Saint Venant solver to verify there is no difference between the results produced by each solver. Using both solvers to run the base hydraulic model shows almost zero change in modelled WSE (see Figure 6-12), confirming the diffusive wave approximation can be used with negligible effect on modelled hydraulics. This not surprising; a diffusive approximation is generally appropriate for Froude numbers of less than 0.3 (Garambois and Monnier, 2015), and the Froude number computed from the velocity and hydraulic depth measured by the ADCP at chainage 515 km is 0.12. Thus, from hereon, all models utilise the diffusive wave solver in HEC-RAS-2D.

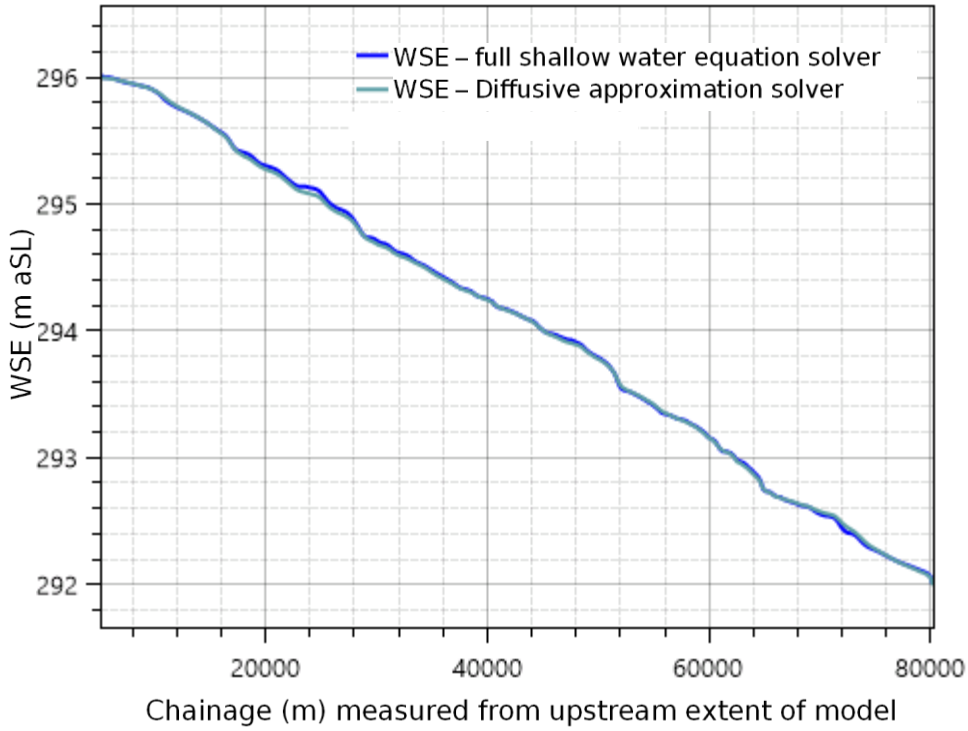

Figure 6-12. Modelled WSPs when shallow water equation solver and diffusive approximation solver used to run base hydraulic model.

Test 2: Representation of Floodplain and Island Terrain

The BM precludes any inundation of islands or floodplain terrain by not representing topographic elevations (all elevations outside of the water mask are set as infinitely high). However, modelling island and floodplain inundation during high flow conditions is necessary for certain model experiments, such as the simulation of the width constriction hydraulics at high flow. Accordingly, island and floodplain terrain can be represented in a model DEM by using elevation data from the MERIT DEM (Yamazaki et al., 2017). There is significant uncertainty in this elevation data, and it is therefore not intended to provide a prediction of inundation extent. It is only used to obtain physically realistic modelled in-channel hydraulic conditions during high flows. Figure 6-13 shows a 'BM plus MERIT' DEM that has been derived through the addition of MERIT elevations to the BM by populating all raster grid cells outside of the water mask with values from the MERIT raster file.

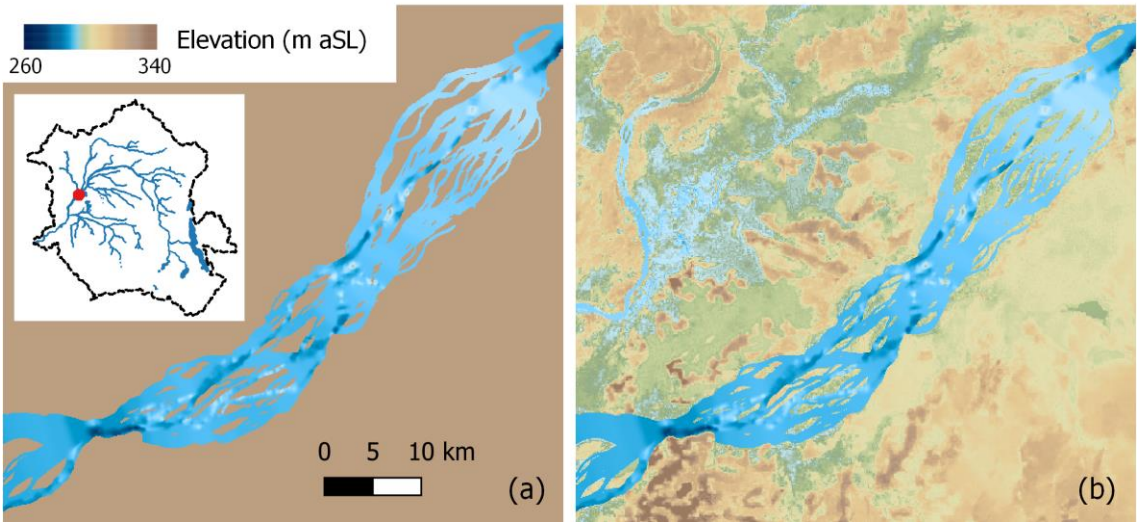

Figure 6-13. (a) DEM derived directly from bathymetry model (BM); (b) 'BM plus MERIT' DEM derived from BM and MERIT elevation data (Yamazaki et al., 2017).

The BM plus MERIT DEM was used in the hydraulic model to simulate the low flow conditions observed during the 2017 fieldwork. All parameters are the same as those used in the base hydraulic model (listed in Table 6-2), except for the use of the BM plus MERIT DEM, and the Manning's *n* values.

Table 6-2. Base hydraulic model parameters.

Value	Parameter
21,000 m^3/s	Steady state discharge simulated. Average of three values observed along the modelled reach during 2017 fieldwork.
291.91 m aSL	Downstream boundary condition. Fixed WSE value from value observed during 2017 fieldwork.
291.91 m aSL	WSE value used for Initial conditions within HEC-RAS-2D flow area (equated to downstream boundary condition).
4 days	Model simulation time
100 m	Spatial resolution (cell size)

The floodplain and island terrain *n* value was set to 0.1 to represent a forested floodplain (Arcement and Schneider, 1984). The channel *n* value was set to 0.032, obtained by calibration to the observed WSE, which is 0.002 (7%) greater than the base

hydraulic model value, because of some inundation introduced by the inclusion of the floodplain and island terrain. This inundation is shown in Figure 6-14.

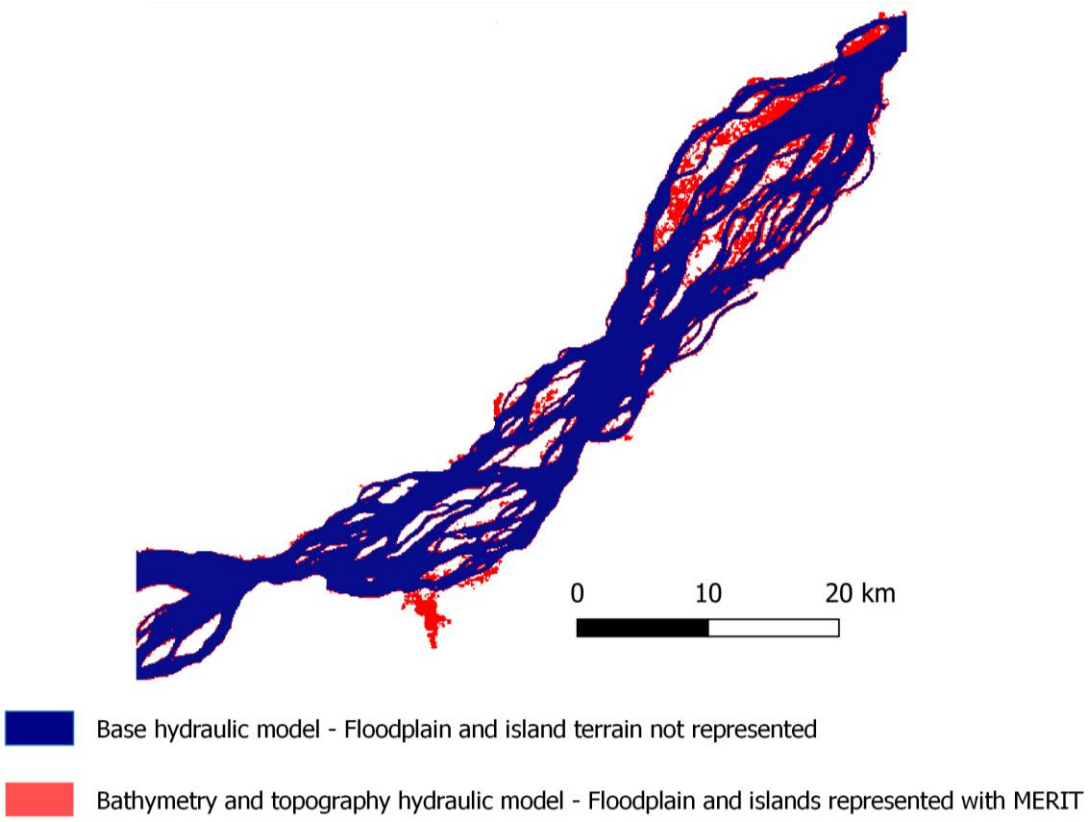

Figure 6-14. Modelled water extents resulting from the base hydraulic model overlaying those resulting from a model using the 'BM plus MERIT' DEM. Note that large areas of floodplain inundation clearly disconnected from the main channel water extent were manually removed from this figure, as they result from the spatially constant initial WSE condition applied to the 2D flow area and are not relevant to the simulated hydraulics of the reach. For a version of this figure without these irrelevent inundated areas of floodplain removed, see Appendix C.2.

Test 3: Simplification of Channel bathymetry to a constant depth and bed slope

In this preliminary model test, mid-channel islands and spatially distributed channel bed elevations in the BM are replaced with a constant channel depth and a uniform bed slope. Channel bed elevation is derived by subtracting a fixed depth value from a planar approximated water surface raster grid (itself derived from observed WSE), and by ensuring the overall volume in the channels is the same as the BM. Variability in total channel width is retained. The two DEMs are shown in Figure 6-15.

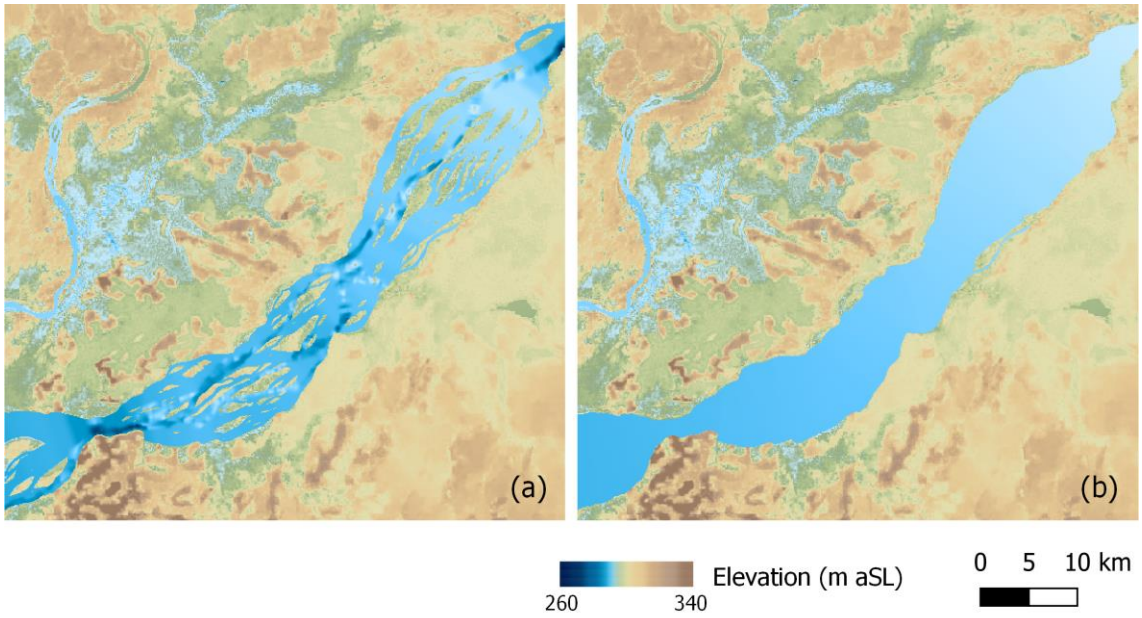

Figure 6-15. Replacement of mid-channel islands and spatially distributed channel bed elevations with a constant channel depth and a linear bed slope: (a) channel bathymetry in BM; (b) channel bathymetry simplified to a linear bed slope. Topographic elevations shown in both sub-plots are those obtained from MERIT DEM.

Simplifying the bathymetry as shown in Figure 6-15 should produce a clear and obvious effect on modelled WSE: use of a simple linear bed slope in this way severely under-represents channel cross-sectional area at the width constrictions, and therefore produces a marked constriction effect. Topography is represented in the linear bed slope DEM to prevent physically unrealistic channelization of any floodplain flows resulting from the constriction effect. WSE and velocity results of this model test are shown in Figure 6-16 and Figure 6-17 respectively, clearly confirming a constriction effect that manifests a backwater curve, raising the upstream WSE by more than 1 m in the immediate upstream 20 km reach. These results are as expected and mainly serve to confirm that the model is operating as anticipated.

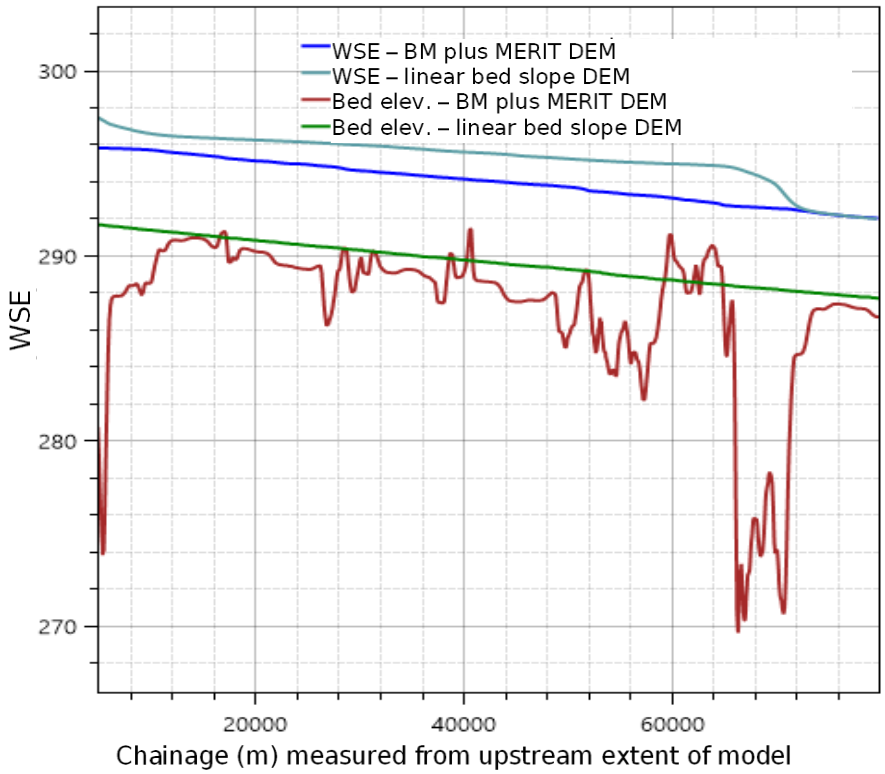

Figure 6-16. Longitudinal profile through modelled WSEs, showing the constriction effect generated resulting from a linear bed slope bathymetry.

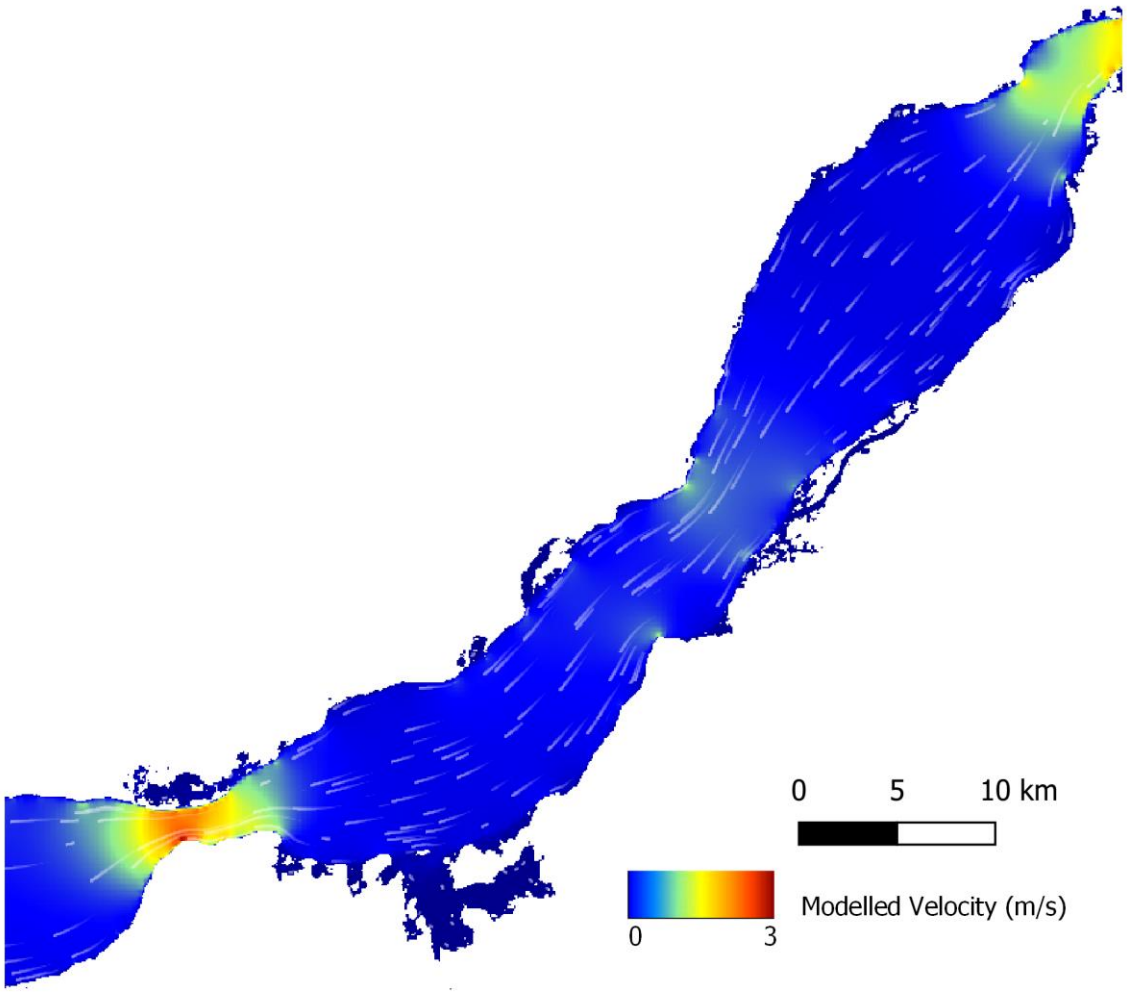

Figure 6-17. Modelled velocities during low flow conditions, resulting from linear bed slope bathymetry.

Test 4: BM Cross-sectional Depth Variability

Bathymetric representation in the BM is mostly estimated assuming the channel cross-sectional depth to be constant and is therefore assumed not to include any cross-sectional variability. However, variability is represented locally, where cross-sectional bathymetry has been ingested into the BM. For the BM to be considered a base model for an experiment where cross-sectional depth is synthetically added, the assumption that the BM is hydraulically analogous to a bathymetry with no such variability needs to be validated. This validation is also required for the single channel experiment, since the effect of merging channel threads should be isolated, and not combined with any cross-sectional depth variability effects.

To validate the assumption of cross-sectional depth variability being absent from the BM, the BM was modified to remove all cross-sectional variability, using the following procedure. The average of the BM bed elevations within each 2 km depth estimation polygon (shown in subsection 5.2.2) were calculated, and bed elevations of each cell set according to the average value. A Gaussian filter was then used to remove physically unrealistic steps in the bed elevations between the depth estimation polygons, yielding a uniform-cross-sectional depth DEM shown in Figure 6-18. Bathymetric equivalence was verified by confirming the total bathymetric volume of the uniform cross-sectional depth DEM was equal to the BM.

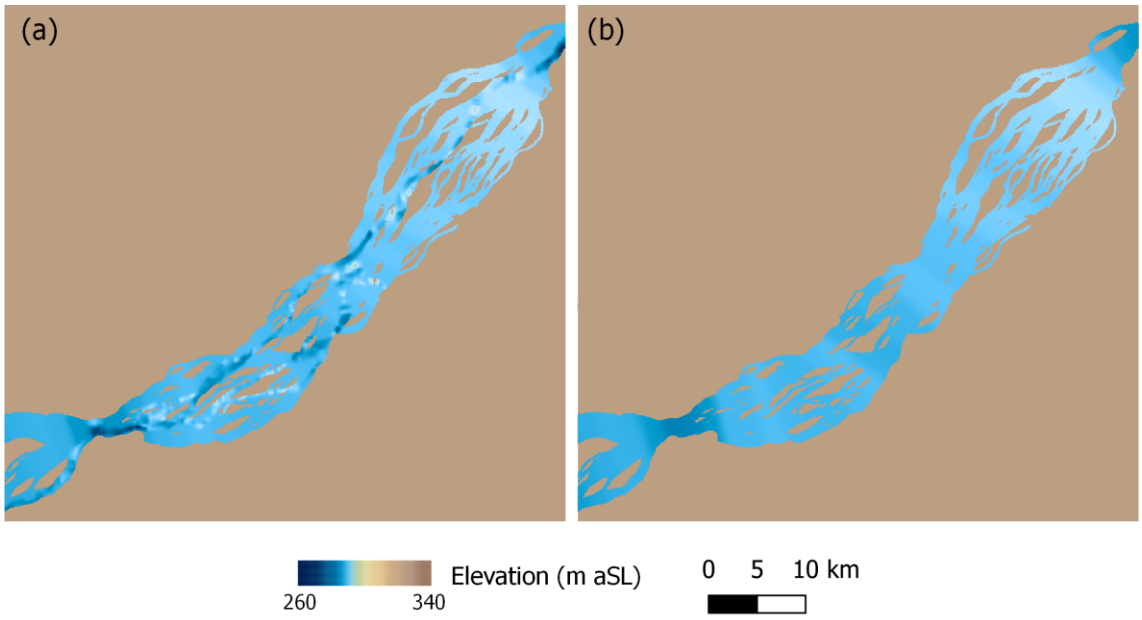

Figure 6-18. Removal of all cross-sectional variability in depth from the BM: (a) BM; (b) BM with all cross-sectional variability removed.

Hydraulic equivalence was tested by modelling both the BM and the uniform cross-sectional depth DEM using the base hydraulic model. The resulting WSPs are shown in Figure 6-19. Whilst some small localised differences in WSE are visible (maximum 150 mm difference), there is no significant difference in hydraulic efficiency at the channel scale, which would manifest as an increasingly large WSE difference in the upstream direction (i.e. a change in reach-averaged WSS). The BM can therefore be assumed to have no cross-sectional variability for the purpose of the modelling experiments.

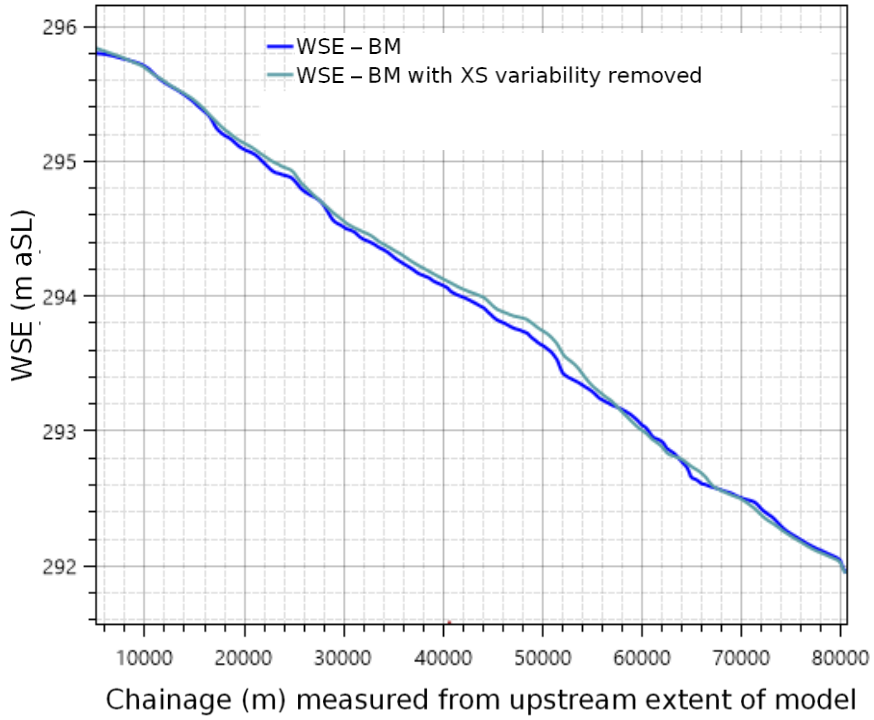

Figure 6-19. WSPs for BM, and DEM with all cross-sectional depth variability removed.

6.3.2 Model Experiments Setup

Experiments CT and XSV each comprise three variants as listed in Table 6-3, in order to evaluate the effect of the geometric simplifications. Control denotes the case without the simplification to the channel geometry; Simplified is the case with the channel geometry simplified; Simplified and Recalibrated is the channel simplified and the Manning's roughness coefficient recalibrated to the low flow observed WSP. Experiment WC only requires a control variant. The two channel simplifications are represented by changing the model DEM, preparation of these DEMs are described below within this subsection.

Table 6-3. Schedule of hydraulic model experiments. Experiments are denoted as follows: width constriction at high flow (WC); merging of individual channel threads (MT); and Omitting Cross-sectional Depth Variability (XSV).

Variant	Experiment		
	WC	MT	XSV
Control (C)	WC-C	MT-C	XSV-C
Simplified (S)	-	MT-S	XSV-S
Simplified and Recalibrated (SR)	-	MT-SR	XSV-SR

Experiment 'MT': Merging of Individual Channel Threads

This model experiment requires an equivalent single thread channel DEM, as shown in Figure 6-20. The parameter values used to create this single thread channel DEM include a constant width of 5.3 km equal to the mean effective width of the BM; and a constant depth of 5.6 m calculated as the BM volume divided by plan area. The planform alignment of the single thread channel is derived from the centreline of the BM, and depths were converted to bed elevations by subtracting depth from the planar approximated water surface raster grid. Conservation of channel volume was checked with a GIS-based raster volume calculation, which showed the two channel volumes to be within 1% of each other.

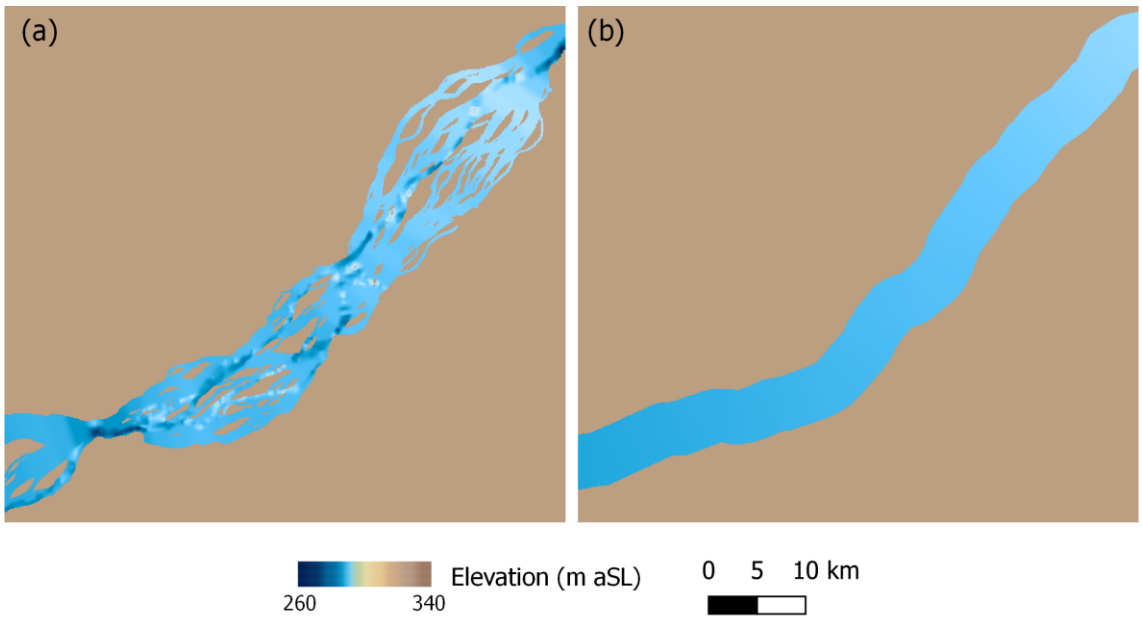

Figure 6-20. (a) DEM derived directly from BM; (b) Equivalent single thread channel DEM.

Experiment 'XSV': Omitting Cross-sectional Depth Variability

It has been established that if channel cross-sectional bathymetry varies sufficiently from the mean cross-sectional depth, the assumption of a constant mean cross-sectional channel depth will cause a substantial reduction in channel hydraulic efficiency. Some cross-sectional variability in depth is represented in the BM, i.e. where observed bathymetry data has been used. However, most of the bathymetry has been estimated assuming the channel cross-sectional depth to be constant. Therefore, to investigate CMR cross-sectional variability in bathymetry using a hydraulic model requires this variability to be added into the BM. The variability is most effectively represented as synthetic thalwegs: thalweg depth is known to be in excess of 15 m (approximately three times the mean depth) based on the observed ADCP transect at chainage 515 km, and will therefore represent the largest deviation in mean cross-sectional depth. Negative depth variability (i.e. shallow bathymetry) is not considered, it being limited to the value of the mean depth (approximately 5 m at chainage 515 km ADCP). Moreover, the non-linear increase in flow velocity with depth means that positive depth variability has a greater effect on channel hydraulic efficiency than negative depth variability.

The adopted geometry for the synthetic thalwegs is shown in Figure 6-21, and is based on a trapezoidal shape with a 200 m wide bottom width and 1 in 25 side slopes, as per the observed thalweg at chainage 515 km (highlighted in Figure 6-21a). This ADCP transect also shows that the CMR has multiple thalwegs that form within individual channel threads, hence the adoption of two thalwegs within the DEM. Thalweg planform alignment was manually digitised. Thalwegs are positioned centrally within channel threads so that they are accommodated within the width of the channel thread as much as possible. One thalweg follows the same channel threads as those followed by the navigation route during the 2017 field campaign. The second thalweg route was user determined, and was chosen as the route that was judged to have the most consistently wide bank to bank width, thus minimising local reduction in thalweg cross-sectional area where the channel thread width is narrower than the thalweg top width. At the width constrictions, both thalwegs align with the observed thalweg represented in the BM.

The thalwegs were generated with a series of 100 m spaced thalweg depth points shown in Figure 6-21c. These points were then converted to bed elevations within a raster grid, which were subsequently burned into the BM. Thalweg elevations were only burned into the BM when the thalweg bed elevation is less than the BM elevation. Elevations within the resultant DEM were then raised by a derived value of 1.3 m (as can

be seen in Figure 6-21f), in order to maintain the same bathymetric volume and mean cross-sectional depth as the BM.

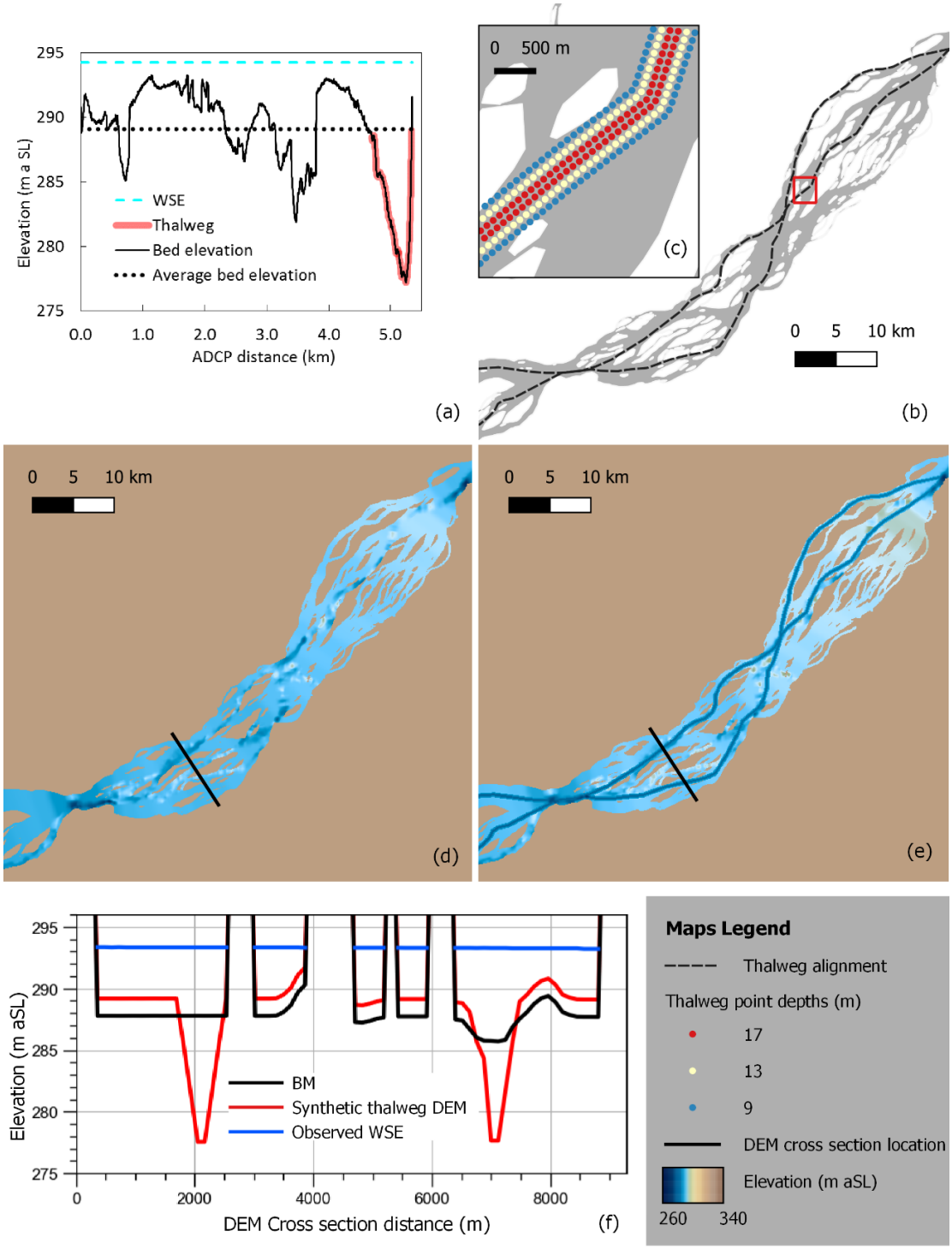

Figure 6-21. Development of a synthetic thalweg DEM: (a) ADCP transect at chainage 515 km, with adopted thalweg geometry highlighted; (b) location of modelled thalweg; (c) creation of thalweg geometry with 100 m spaced points, prior to conversion of depths to bed elevations; (d) BM; (e) thalweg DEM; (f) DEM cross-section showing BM and synthetic thalweg DEM.

The thalweg depth of 17 m is based on an assessment of maximum occurring depth along available sonar transects that traverse across the entire multithread channel belt, which were obtained in the 2017 field campaign. These are shown in Figure 6-22. Deeper thalwegs observed at other cross-sectional ADCP transects are not used in this assessment, as they are all located at width constrictions where the channel is more incised and is therefore uncharacteristically deep relative to the majority of the multichannel CMR bathymetry.

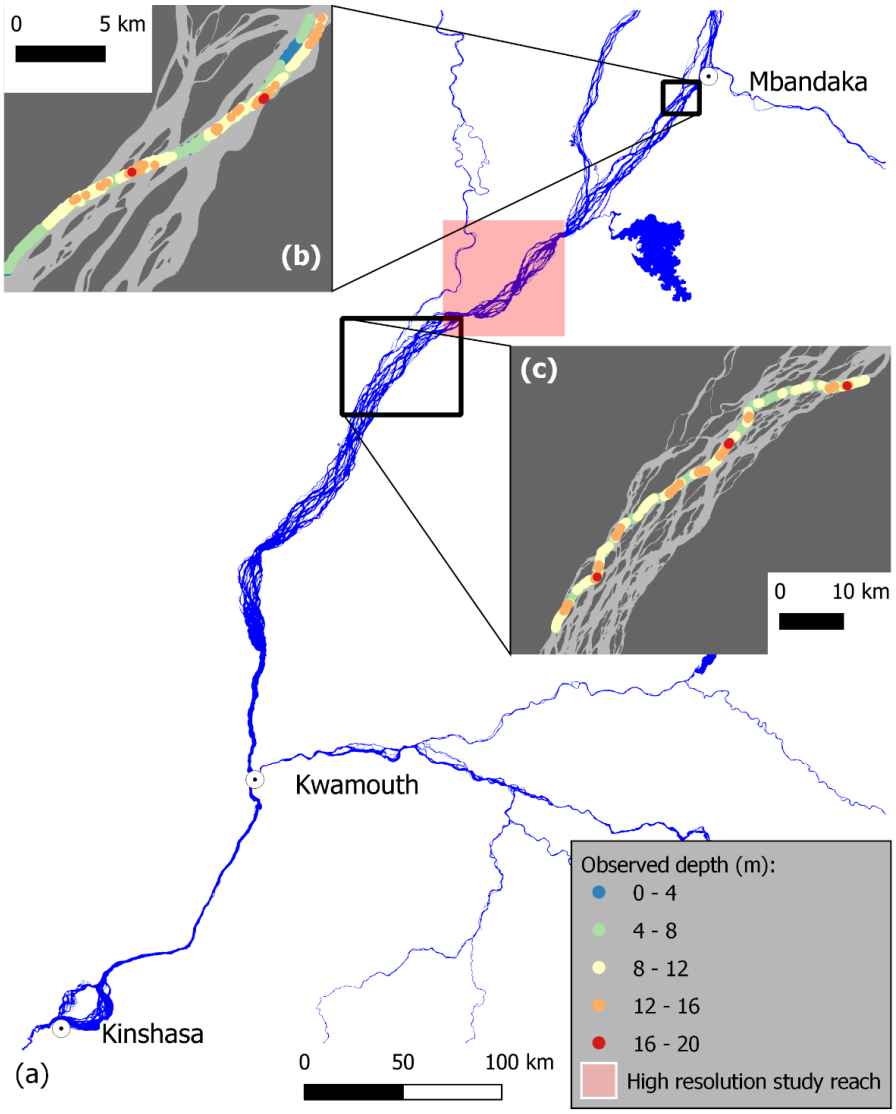

Figure 6-22. Assessment of maximum multichannel thalweg depth, based on acquired sonar depth observations that traverse across the entire multithread channel belt: (a) Location plan; (b) multichannel transect 1 (includes two tracks – one going upstream, one going downstream); (c) multichannel transect 2. Plotted depths shown are resampled at 100 m resolution and show the maximum depth to be 17 m. Maximum depth of the raw sonar measurements is 19 m. Note: depth values are plotted such that larger values overlay smaller values, to highlight maximum depths.

With the thalwegs included, the combined area of the cross-section below the mean depth equates to 36% of the total cross-sectional area at chainage 515 km. For the ADCP transect at this location, the cross-sectional area below the mean depth is 26% of total cross-sectional area. Therefore, based on the observed depth data, the thalweg DEM is representative of an estimated upper limit of positive depth variability in the CMR, in terms of both maximum channel depth and the combined area of the positive depth variability. For this reason, increasing the number of thalwegs beyond two is not considered.

6.3.3 Model Run Parameters

Model run parameters for each experiment are detailed in Table 6-4 below, including boundary conditions, initial conditions, floodplain representation, resolution, and run time. Steady state model runs were completed first, and were followed by unsteady model runs. For experiments MT and XSV, all steady state run parameters are the same as those used in the calibrated base hydraulic model derived in Chapter 5 (also listed in Table 6-2). Experiment WC simulates both low flow and high flow conditions in steady state, so that any constriction effect particular to the high flow conditions can be observed. Different model parameters are therefore required.

Table 6-4. Model run parameters for each experiment

Parameter	Experiment		
	WC	MT	XSV
Floodplain and island representation	MERIT DEM, Manning's n = 0.1	Not represented	Not represented
Initial conditions (fixed WSE)	291.91 (low flow) 295.30 (high flow)	291.91 m	291.91 m
Spatial resolution (cell size)	100 m	100 m	100 m
Steady state inflow boundary	21,000 m^3/s (low flow) 50,000 m^3/s (high flow)	21,000 m^3/s	21,000 m^3/s
Steady state downstream boundary	Normal depth slope = 3.7 cm/km	Fixed WSE = 291.91 m	Fixed WSE = 291.91 m
Steady state simulation time	4 days	4 days	4 days
Unsteady inflow boundary	-	Synthetic hydrograph[1]	Synthetic hydrograph[1]
Unsteady downstream boundary	-	Q-H boundary[1]	Q-H boundary[1]
Unsteady simulation time	-	210 days[1]	210 days[1]

[1.] Derived below and plotted in Figure 6-25 below

Derivation of the parameters for the steady state high flow model run and unsteady flow model runs are described below.

Derivation of Steady State Model Run Parameters for Experiment WC

This experiment involves simulating steady state high flow conditions with the base hydraulic model. No in-situ observations of high flow conditions have been obtained, so such conditions have been derived as follows. Seven years of WSE time series data from an ENVISAT overpass located at chainage 480 km (shown in Figure 6-23) show that peak WSE that has occurred here is 296.6 m aSL (to the EGM 96 geoid), on 26 December 2002. The peak WSE value is approximately 4 m above the in-situ observed WSE during low flow conditions and is not significantly greater than the annual maxima observed in other years.

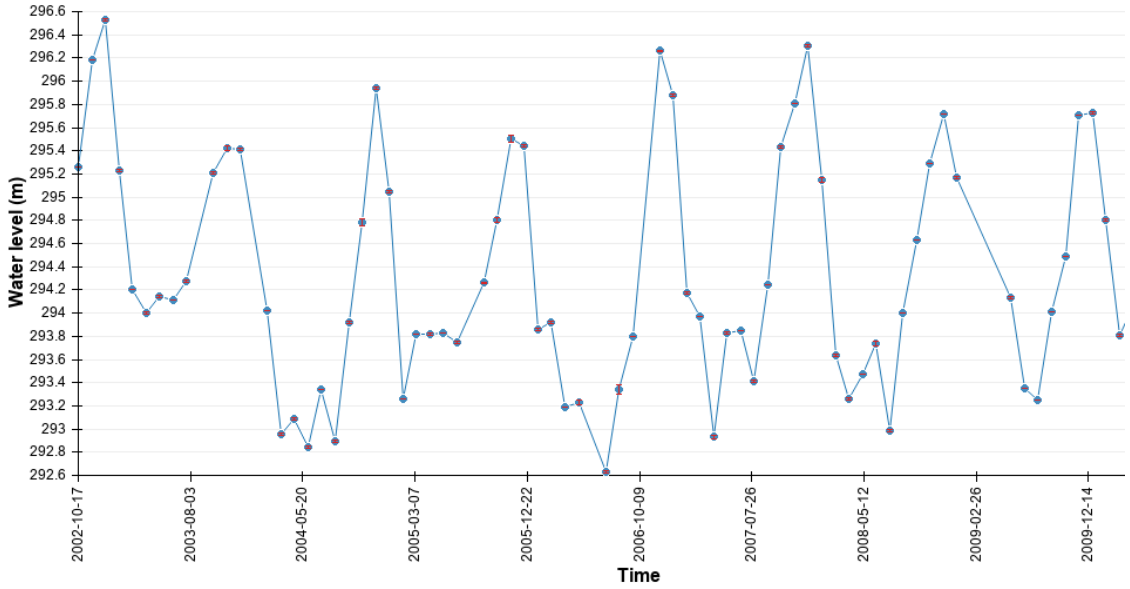

Figure 6-23. ENVISAT WSEs at Chainage 480 km. WSEs shown are referenced to the EGM 2008 geoid. Plot obtained directly from the Hydroweb database (Santos da Silva et al., 2010): http://hydroweb.theia-land.fr/. Note the in-situ observed WSE value during low flow conditions is 292.42 m aSL.

This WSE was then converted to a river discharge of 50,000 m^3/s. This discharge was obtained by running a hydraulic model simulation with a gradually increasing discharge, the BM plus MERIT DEM (Figure 6-13b), and a normal depth boundary condition to cater for the unsteady flow conditions. A normal depth slope value of 3.7 cm/km was used, which was determined by calibrating the slope value to match modelled WSEs with observed WSEs for the steady state 2017 fieldwork conditions simulation. Initially, the WSS value of 5 cm/km observed during the 2017 fieldwork was used, but this resulted in significantly lower modelled WSEs in the vicinity of the boundary condition, as shown in Figure 6-24. This lowering of the WSE is attributed to the 6.4 km cross-sectional width at the boundary condition, which is considerably wider than the

mean. For a given discharge and slope, a larger channel width will result in an underestimate of WSE based on a normal depth calculation.

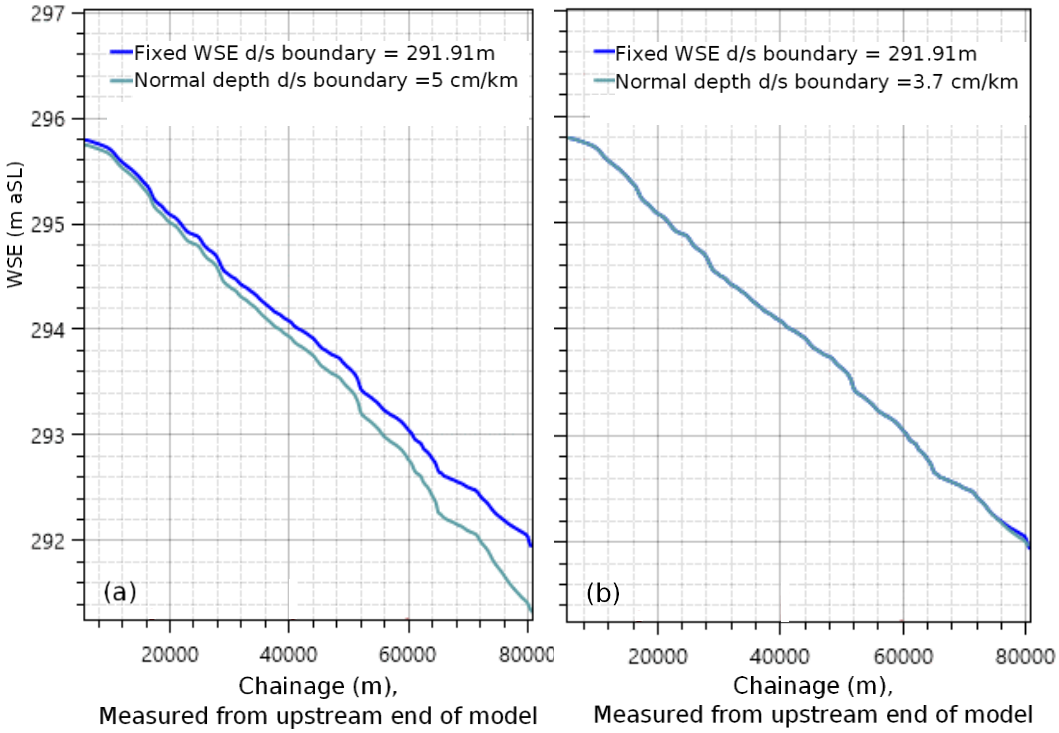

Figure 6-24. Modelled WSPs for a fixed WSE downstream (d/s) boundary, and a normal depth slope boundary: (a) normal depth slope set to observed WSS of 5cm/km; (b) normal depth slope of 3.7 cm/km, calibrated to observed WSE at boundary condition location.

Unsteady Model Run Parameters

To investigate the hydrodynamic behaviour of the channel simplifications associated with experiments MT and XSV, unsteady model runs simulating the seasonal flood wave are necessary. As observed times series discharge data are not available at the study reach, an inflow boundary in the form of a synthetic flood wave hydrograph has been derived, along with a suitable *Q–H* downstream boundary condition. This is shown in Figure 6-25.

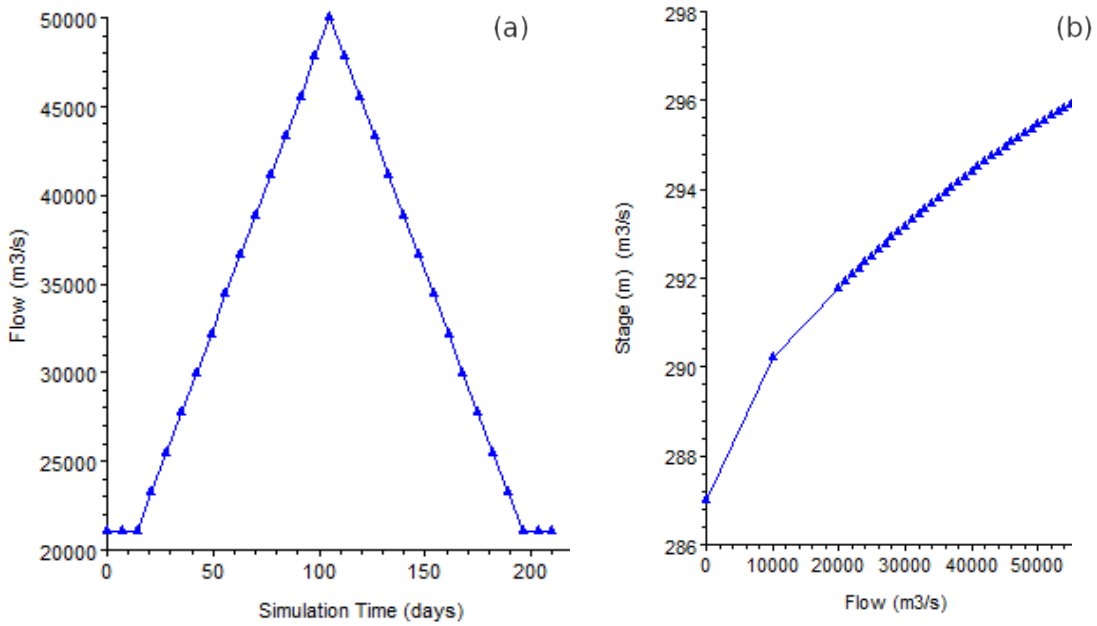

Figure 6-25. Unsteady model boundaries used in hydrodynamic simulations: (a) Inflow hydrograph representing annual flood wave; (b) Q–H relationship used for downstream boundary.

The inflow has been modelled with a 50,000 m^3/s peak, equal to the established steady state peak flow. The hydrograph has been modelled as a triangular in shape with an equal rising and falling limb duration of 90 days, based on water level time-series in the central Congo River derived by Becker et al. (2014) using ENVISAT altimetry. The hydrograph is designed to be representative of a typical annually occurring flood wave in the CMR in terms of the flow amplitude and rate of rise and fall, but is not intended to represent a real flood wave. The *Q–H* relationship was derived by first simulating the inflow hydrograph using the same model parameters as those used for experiment WC steady state high flow model run (see Table 6-4), from which *Q–H* time series information at the downstream end of the model was extracted.

6.3.4 Refinement of Model Calibration Approach

In the hydraulic modelling experiments, recalibration of Manning's *n* to compensate for the channel geometric simplifications is carried out based on low flow WSE observations only. This may not represent the calibration approach commonly adopted for ESC models, in which *n* is calibrated to minimise RMSE according to WSE observations across a range of flows. Moreover, calibration approaches that allow channel shape to be calibrated as well as *n* are increasingly being used. This is explored in section 6.4.2, mainly by testing different channel shapes using Manning's equation.

6.4 Results

6.4.1 Modelled WSEs

Results comprise modelled WSEs for each of the model runs listed in Table 6-5. Steady state results are shown as longitudinal profiles in Figure 6-26. Unsteady results are shown with *Q*–*H* curves extracted from the upstream end of the model, plotted in Figure 6-27.

Table 6-5. Model runs for each experiment. Each run comprises a steady and unsteady model, unless noted otherwise.

Experiment	Experiment Description	DEM	Channel *n* value
WC-C[1]	Width constriction at high flow	BM plus MERIT DEM	0.032
MT-C	Merging of individual channel threads: Control	BM	0.030
MT-S	Merging of individual channel threads: Simplified	Single thread channel DEM	0.030
MT-SR	Merging of individual channel threads: Simplified and *n* recalibrated	Single thread channel DEM	0.036
XSV-C	Omitting cross-section depth variability: Control	Thalweg DEM	0.038
XSV-S	Omitting cross-section depth variability: Simplified	BM	0.038
XSV-SR	Omitting cross-section depth variability: Simplified and *n* recalibrated	BM	0.030

[1.] No unsteady model run: only steady state low flow and high flow runs

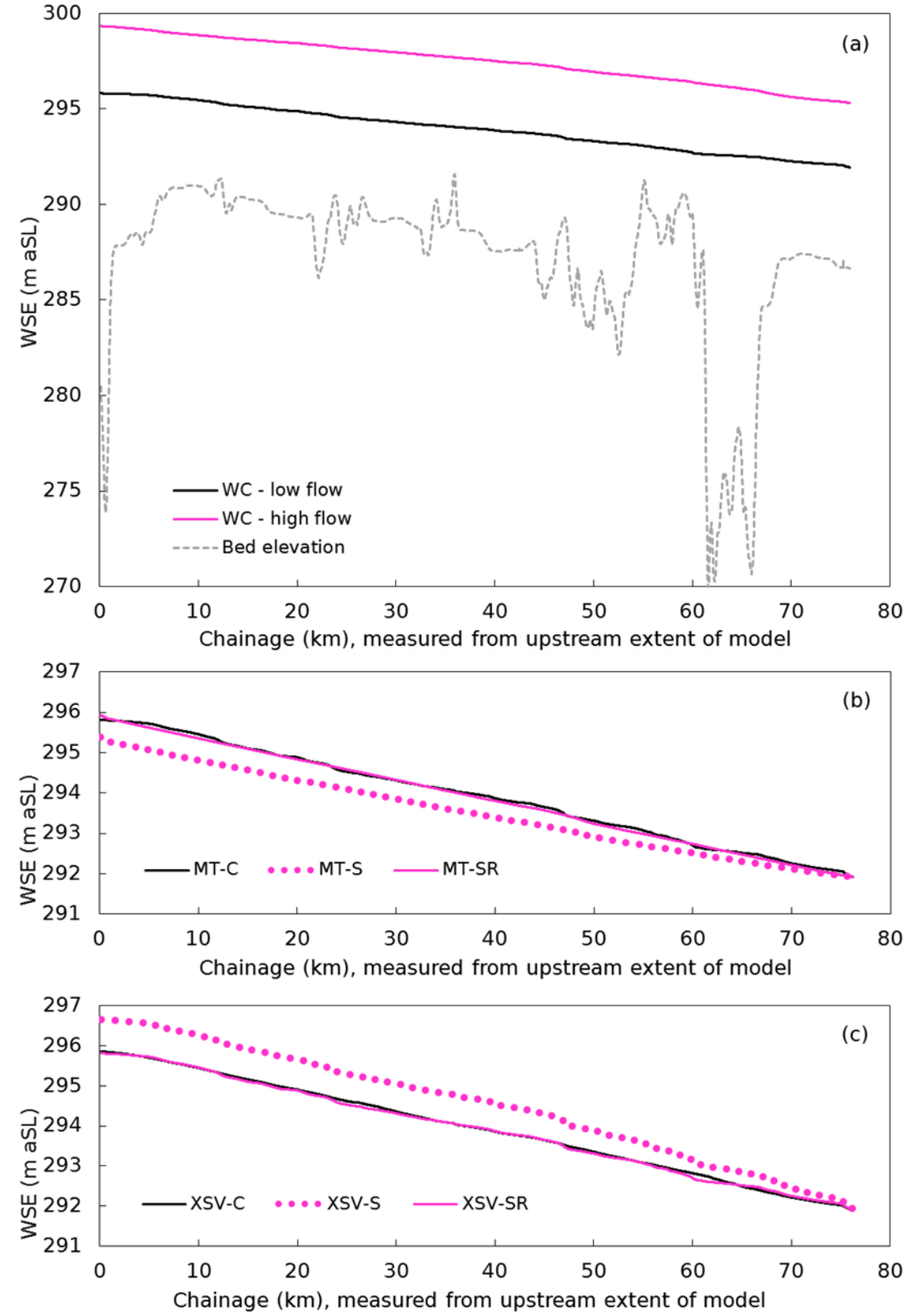

Figure 6-26. Steady state modelled WSPs, low flow conditions unless stated otherwise: (a) Experiment WC, low flow and high flow model runs, bed elevations also shown to indicate width constriction location; (b) Experiment MT model run; (c) Experiment XSV model runs. Manning's n values of all model runs are listed in Table 6-5.

The steady state high flow WSP (Figure 6-26a) shows there to be no constriction effect present through the width constriction at chainage 480 km, confirming the findings of the review in subsection 6.2.2. Results of the two channel geometry simplifications are also as expected. Merging of the channel threads increases the channel hydraulic efficiency, resulting in a 15% reduction of the reach averaged WSS, and requires a recalibration of the model amounting to an *n* value offset of +0.006. Removal of the cross-sectional depth variability has the opposite effect, but of a similar magnitude (22% increase in WSS), requiring a model recalibration amounting to an *n* offset of -0.008.

The modelled response of WSE to a range of flows resulting from unsteady simulations based on the synthetic CMR flood wave event are shown in Figure 6-27, in the form of *Q–H* curves extracted at the upstream end of the model. These *Q–H* curves show how the recalibrated models perform across the full range of CMR flows. All curves plotted consist of a rising and falling limb, and show a small amount of hysteresis behaviour, this being indicated by the looped profile of the curves.

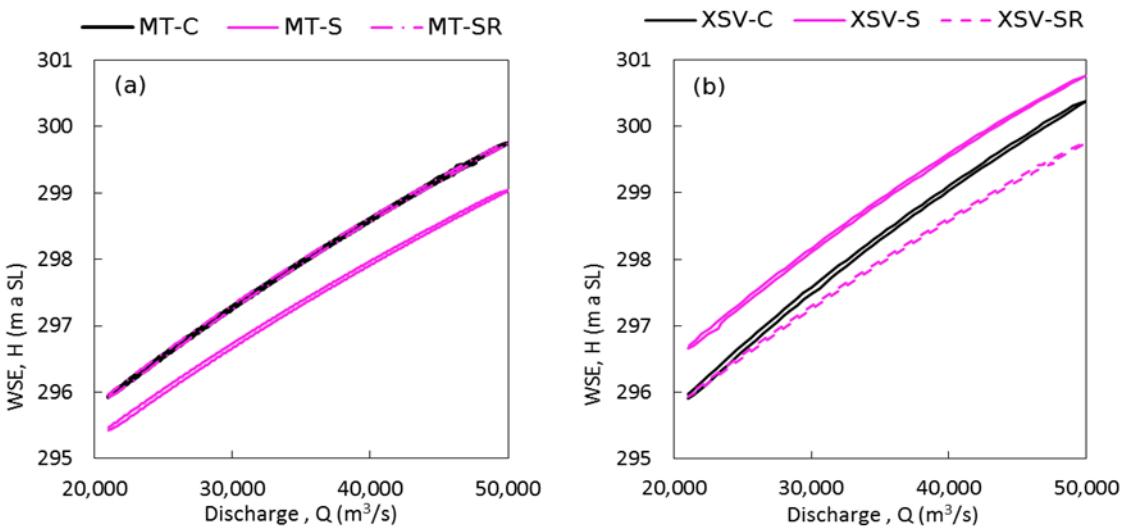

Figure 6-27. Modelled Q–H plots from unsteady model runs, extracted from upstream end of model: (a) Merging of individual channel threads; (b) Omitting cross-sectional depth variability.

The *Q–H* curves in Figure 6-27a show that when recalibrated to the low flow WSP, the model with channel threads merged produces a modelled WSE response almost identical to that resulting from the model with channel threads represented. In contrast, Figure 6-27b shows that the model with the cross-sectional depth variability removed produces a different WSE response to the model with the depth variability included. This difference in WSE response amounts to a maximum magnitude of 0.63 m

at high flow. The resulting magnitude of WSE difference is not significantly affected by the assumption that no floodplain or island inundation occurs: this was checked by repeating experiment XSV unsteady model runs with MERIT floodplain and island elevations added to the DEMs. Results are plotted in Figure 6-28, and show that inclusion of the floodplain and island terrain reduces the magnitude of WSE difference by only ~0.1 m. Inundation depths and extents during peak flow conditions resulting from the inclusion of the floodplain are shown in Appendix C.3.

The effect of the downstream boundary condition on the magnitude of WSE difference was also checked, by changing the boundary condition from a *Q–H* to a normal depth boundary. Details of this check are contained in Appendix C.4, the results showed a small increase of 0.1 m in the magnitude when a normal depth boundary was used. Allowing for both boundary condition and floodplain effects (which counter each other), the original 0.63 m maximum magnitude of WSE difference is maintained.

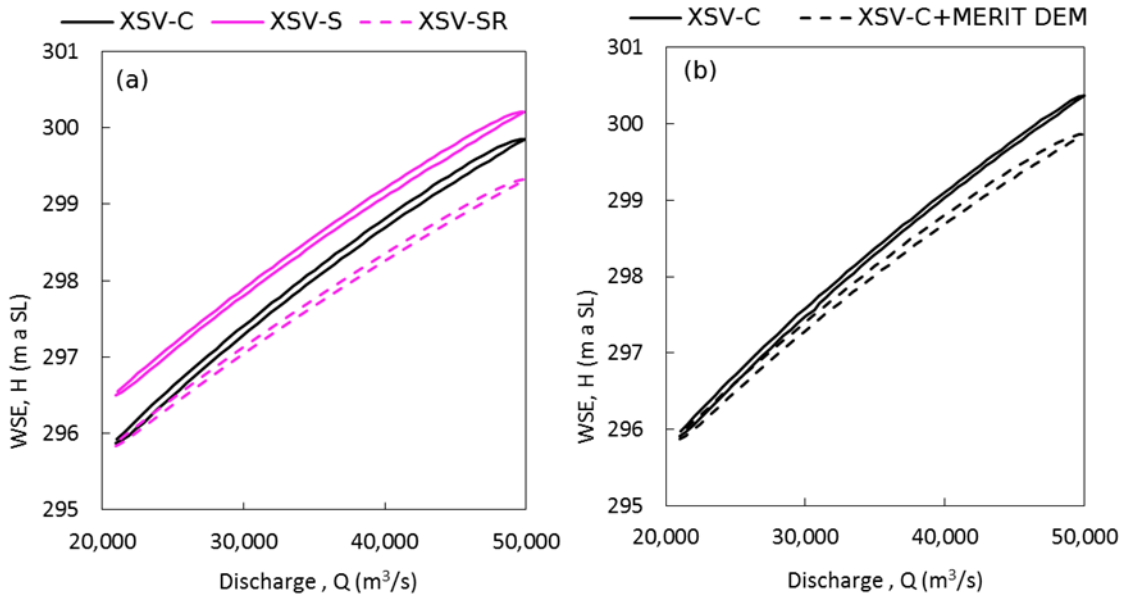

Figure 6-28. Modelled Q–H plots from unsteady model runs, extracted from upstream end of model: (a) All unsteady model runs for XSV experiment, with floodplain and island terrain represented with MERIT elevations; (b) The specific effect of adding floodplain and island terrain.

6.4.2 Refinement of Calibration Approach: Experiment XSV

Recalibration of Manning's n to Low and High Flow WSE

In the preceding analysis, recalibration of Manning's *n* to compensate for the channel geometric simplifications is carried out based on low flow WSE observations only. This may not represent the calibration approach commonly adopted for ESC models, in which *n* is calibrated to minimise RMSE according to WSE observations across a range of flows. When an allowance is made for this for experiment XSV, error in WSE is effectively apportioned equally across the low and high flow WSEs, as shown in Figure 6-29.

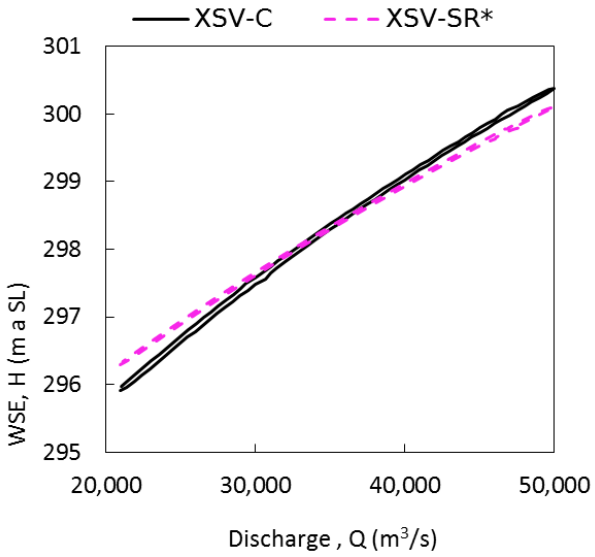

Figure 6-29. Q–H curve resulting from calibration of Manning's n to minimise RMSE to both high flow and low flow observations of WSE (denoted XSV-SR).*

Equally apportioning the WSE error across low and high flows results in a reduction in error from 0.63 m at high flow to a RMSE of 0.26 m across the flow range.

Calibration of Channel Shape

Solutions to further reduce the error arising from neglecting cross-sectional depth variability (experiment XSV) include the adoption of a compound channel shape comprising a thalweg. Another option is an in-channel Manning's *n* value that varies spatially: either vertically (with channel depth), or horizontally (with transverse location across the cross-section). However, these solutions are not compatible with the capabilities of model codes typically used to implement an ESC (Yamazaki et al., 2011; Neal et al., 2012; Schumann et al., 2013; Fleischmann et al., 2018; Bernhofen et al., 2018). A simpler and more widely applicable way of accurately reproducing the channel's

stage response would be to increase channel hydraulic efficiency at low stage, by changing the channel shape. A channel shape treatment of appropriate simplicity is presented in Neal et al. (2015), in which channel shape is defined by a the following power function:

$$W_{flow} = W_{full}\left(\frac{h_{flow}}{h_{full}}\right)^{1/s} \quad \text{Eq. 6-1}$$

The function relates flow width W_{flow} for a given depth of flow h_{flow} to the bank-full width W_{full} and bank full depth of the channel h_{full} using a shape parameter s, which can be treated as a calibration parameter alongside Manning's *n*. Any non-zero value of s will produce a unique shape; values below one will produce convex shaped banks, a value of one will produce a triangular channel, and values above one will produce concave channels that become more rectangular with increasing s values.

To establish whether the CMR's stage response can be better approximated by some simple variant of a rectangular channel shape, shape variations were explored using normal depth calculations that can be rapidly repeated to test a wide range of channel shape / Manning's *n* combinations. Channel shapes were tested on two cross-sections: one being a typical cross-section through the thalweg DEM; the other being the CMR cross-section observed at chainage 515 km. Figure 6-30 shows the derived channel shapes used for each cross-section. All simplified shapes maintain the same top width and cross-sectional area as the cross-section being approximated.

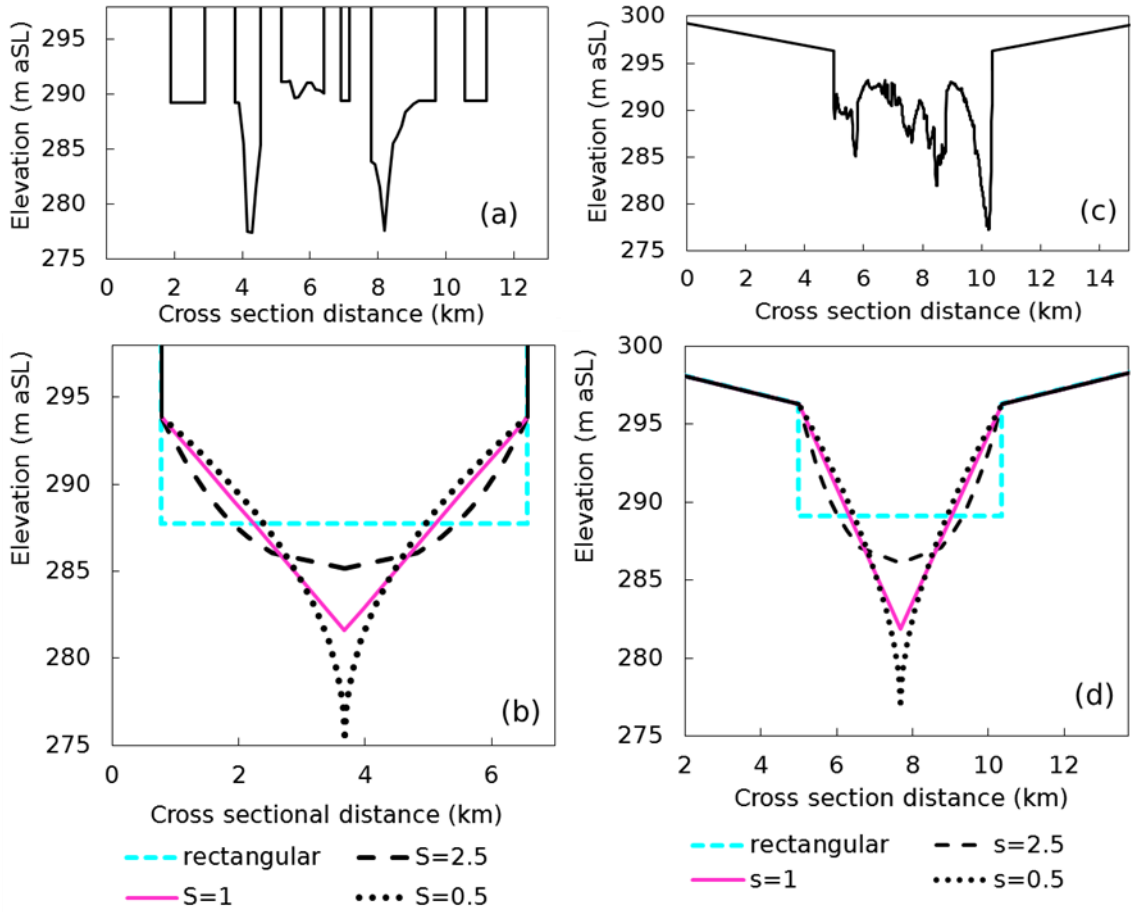

Figure 6-30. Different channel shapes used to approximate CMR bathymetry: (a) Cross-section through Thalweg DEM (section location indicated in Figure 6-21e); (b) different channel shapes used to approximate Thalweg DEM cross-section; (c) Observed cross-section from ADCP transect at chainage 515 km (section geometry is estimated above observed WSE of 294.28 m); (d) different channel shapes used to approximate ADCP. Shapes derived using power function presented in Neal et al. (2015). Top width and cross-sectional area are equal across all shapes, and are equal to the values of the cross section being approximated.

The performance of the simplified channel shapes was evaluated by comparing their resulting *Q*–*H* curves to those of the cross-section being approximated (plotted in Figure 6-31). These *Q*–*H* curves show that the channel shape derived from assigning a value of 2.5 to s (a parabolic shape) provides the best approximation to both cross-sections, and produces a particularly close approximation of the ADCP *Q*–*H* curve. The thalweg DEM is not approximated as precisely as the ADCP is, and the results indicate that a range of s values between 1 and 2.5 provide the same level of improvement over a rectangular shape. Nevertheless, the results show that the error associated with omitting CMR cross-sectional depth variability is halved if a parabolic channel shape (s

= 2.5) is used instead of a rectangle. In numerical terms, the RMSE of 0.26 m derived from Figure 6-29 reduces to 0.13 m.

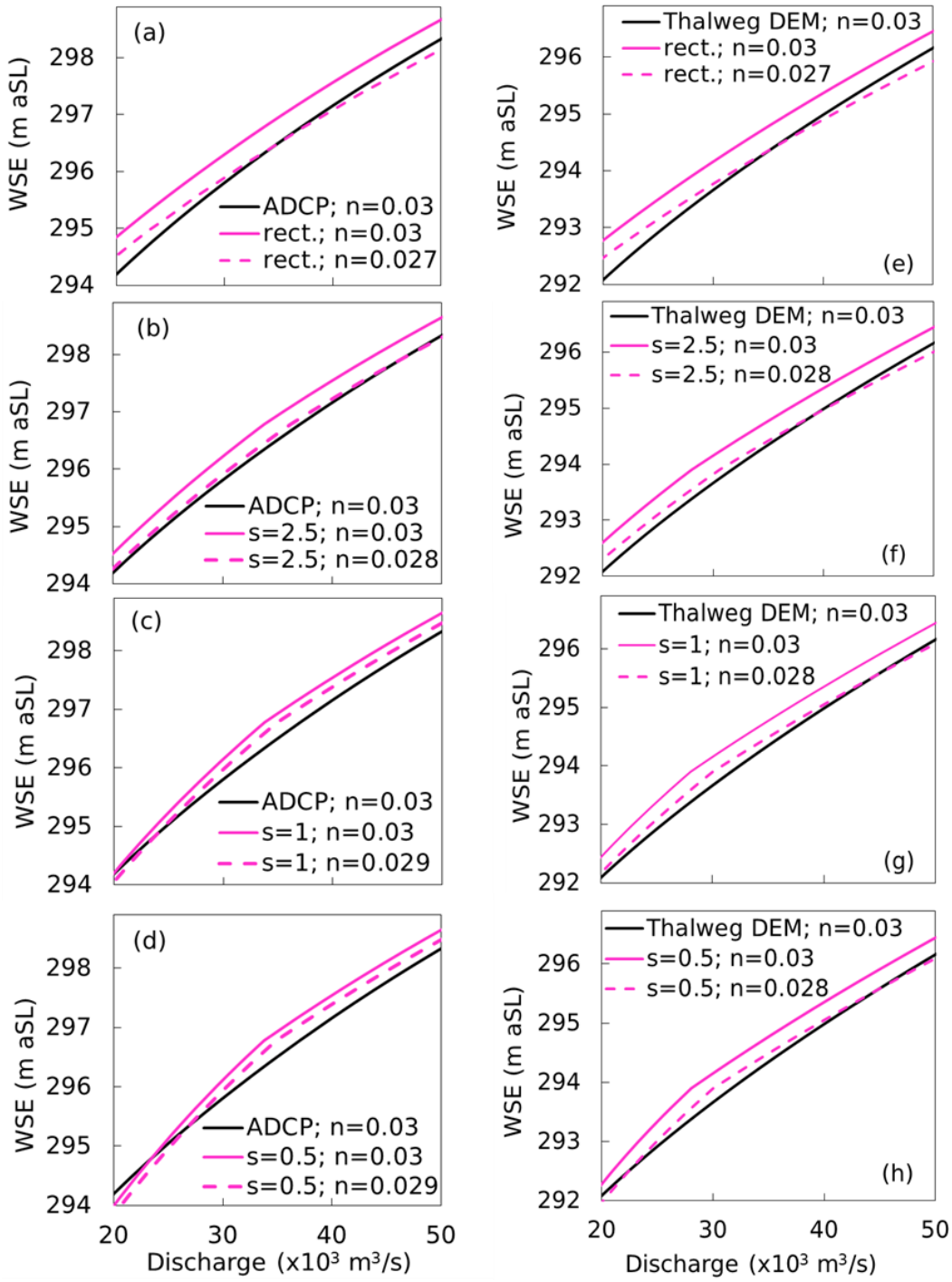

Figure 6-31. Q–H curves calculated for four channel shapes, using normal depth computations in Flood Modeller Pro (Jacobs, 2019): (a)–(d) approximations of ADCP transect at chainage 515 km; (e)–(h) approximations of thalweg DEM cross-section.

6.4.3 Modelled Flood Wave Propagation

In addition to directly affecting predictions of WSE, changes in channel hydraulic efficiency affect flood wave propagation, the timing of flood peak arrivals, and therefore the magnitude of discharge and WSE at a particular time. To quantify the effect of the channel geometry simplifications on flood wave propagation, the time taken for the flood wave peak to pass 70 km through the modelled reach was extracted from each model run (reported in Table 6-6). Travel times were converted to flood wave speeds by dividing the time by the 70 km reach length. Flood wave speeds were subsequently converted to travel times of the modelled peak through the entire 1300 km multichannel CMR, assuming the sinuosity of the 70 km study reach is representative of the multichannel CMR.

Table 6-6. Modelled flood wave peak travel times and speeds through 70 km long study reach, and corresponding travel time calculated for 1300 km long multichannel CMR.

No.	Model DEM	Channel *n* value	Travel time (hours)	Wave speed (m/s)	1300 km CMR travel time (days)
MT-C	BM	0.030	8.5	2.29	6.6
MT-SR	Single thread channel DEM	0.036	7	2.78	5.4
XSV-C	Thalweg DEM	0.038	9	2.16	7.0
XSV-SR	BM	0.030	8.5	2.29	6.6
XSV-C	Thalweg DEM + MERIT	0.04	15	1.3	11.6
XSV-SR	BM + MERIT	0.032	14	1.39	10.8

Of the channel geometric simplifications, merging of channel threads has the largest effect on modelled flood wave propagation, reducing full multichannel CMR travel time by 1.2 days. This is a result of the reduction in channel flow path length, which conveys the flood wave in a shorter period of time despite the increased Manning's *n*. From comparing XSV model runs with and without the MERIT floodplain and island terrain included, it is also clear that the inclusion of the islands and floodplain increases the flood wave travel time significantly, and this therefore needs to be allowed for when quantifying differences in flood wave travel time. Whilst the islands and floodplain could

not be included in the single thread channel model, XSV results show the inclusion of the floodplain and islands to increase flood wave time difference by a factor of 2 (i.e. from a 0.4 day difference without MERIT; to a 0.8 day difference with MERIT). Scaling up the 1.2 day time difference by 2 gives an indicative time difference of 2.4 days for the merging of channel threads when island and floodplain inundation is included.

To determine whether a 2.4 day error in flood wave travel time is significant, it can be converted to an equivalent discharge error. Available hydrograph data at Kinshasa from the SO-HYBAM website (Institut de recherche pour le développement, 2019) comprises daily time series discharge data from 1990–2018, measured using the rating curve method. Figure 6-32 shows frequency plots of recorded daily changes in discharge (ΔQ). Daily changes of greater than 1000 m^3/s occurred only four times in the time series, and were all during the high flow season when discharge exceeded 60,000 m^3/s

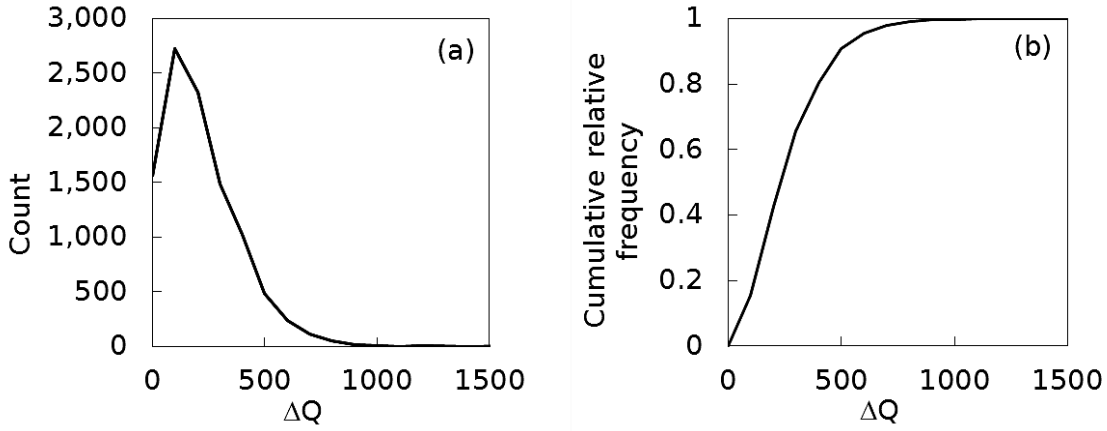

Figure 6-32. Frequency plots for daily changes in discharge (ΔQ, m^3/s) measured at Kinshasa, derived from SO-HYBAM website: https://hybam.obs-mip.fr/data/.

The time series data shows that for more than 95% of the time, daily change in discharge does not exceed 600 m^3/s. Assuming daily change in discharge to be 600 m^3/s, a travel time error of 2.4 days corresponds to a discharge error of ~1,500 m^3/s, or 3.5% of the mean discharge at Kinshasa. Given the uncertainty in any observed discharge arising from the rating curve method is estimated to be approximately 5% (Di Baldassarre and Montanari, 2009), a travel time error of 2.4 days would not contribute significantly to discharge errors in hydrodynamic models.

In terms of WSE error, the SO-HYBAM Kinshasa *Q*–*H* relationship shows that a 1,500 m^3/s flow corresponds to a maximum WSE error of 0.25 m (based on the *Q*–*H* relationship at low flow when the curve is steepest as shown in Figure 6-33). Repeating

this analysis using the mean daily change in discharge of 210 m^3/s, the corresponding WSE error over 2.4 days is only 0.1 m. The *Q–H* relationship used as a downstream boundary condition in the hydrodynamic model runs (shown in Figure 6-25) also shows a 1,500 m^3/s error to correspond to a WSE error of 0.25 m. Both *Q–H* relationships are shown in Figure 6-33.

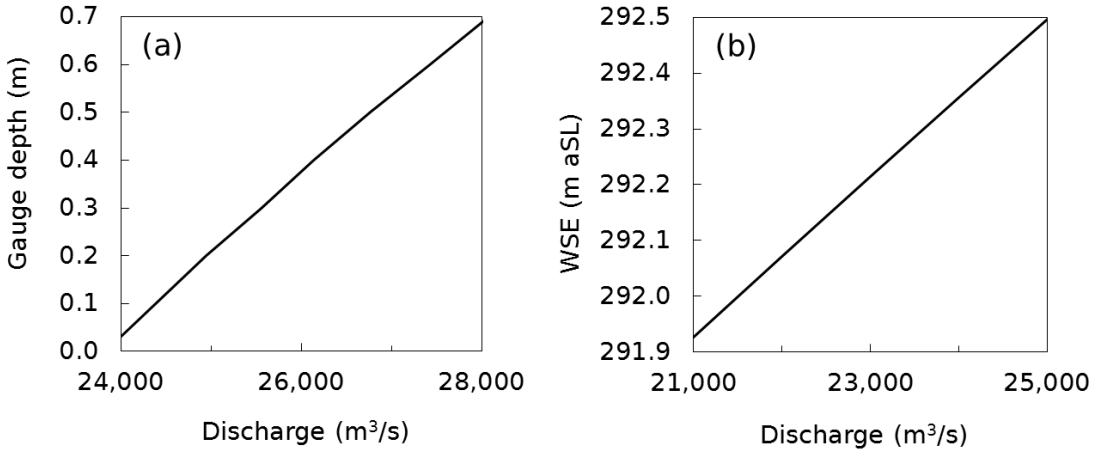

Figure 6-33. Q–H relationships at low flows: (a) SO-HYBAM gauge at Kinshasa; (b) Modelled Q–H relationship at downstream end of hydraulic model, derivation of which is described in subsection 6.3.3.

6.5 Discussion

The steady state model results show that during high flow conditions, no constriction effect emerges at the width constriction at chainage 480 km. This finding, combined with the general assessment of channel scale morphological features in subsection 6.2.2, shows that the consequences of neglecting localised longitudinal variance in multichannel CMR channel geometry are relatively small in terms of error in modelled WSE. Specifically, analysis of 5 km spaced WSE observations along the CMR show this error amounts to a RMSE of 0.15 m. Moreover, the inclusion of high resolution variability in channel width may even introduce error if it is not paired with accurate depth data of a similar spatial resolution. This is demonstrated in preliminary model test 2 in which an erroneous constriction effect results from the pairing of high resolution width information with depth data derived from a mean bed slope.

The independent effects of merging channel threads and omitting cross-sectional depth variability are both as anticipated and significant in magnitude, as shown in Figure 6-26. In terms of modelled reach average WSS, merging channel threads reduces the WSS by 15%, whilst neglecting cross-sectional variability increases the WSS by 22%. However, it is reasonable to assume that models employing an ESC will involve calibration of Manning's *n* to observed water surface information, and results of the recalibrated steady model runs plotted in Figure 6-26 show that the water surface is well approximated by doing so. The results of the unsteady model runs give insight into the more pertinent question of whether the recalibrated *n* values enable the simplified bathymetries to accurately model WSE dynamically. In the case of the single thread channel bathymetry (Figure 6-27a), the water surface through the study reach is accurately reproduced across the entire flow range. Merging of the channel threads does cause a considerable acceleration of in flood wave propagation (increase in flood wave speed of 20%). However, because the CMR flow conditions vary in time at a very slow rate (210 m^3/s per day at Kinshasa on average), this modelled flood wave propagation speed error has limited consequences for modelled WSE error: 0.1 m based on the mean daily change in discharge.

With the cross-sectional depth variability removed, the model is not able to accurately reproduce WSE across the flow range, despite the *n* value having been recalibrated. The error is 0.63 m at high flow, as a result of the model's stage response being dampened. However, when the model is calibrated to minimise the RMSE to WSEs observed during low and high flow, a better approximation results. As shown in Figure 6-29 (curve XSV-SR*), error is equally apportioned to the low and high flow WSE predictions, and translates to a RMSE of 0.26 m across the flow range. Furthermore, if

channel shape is allowed to vary by using a power function, supplementary normal depth calculations show that the RMSE of 0.26 m can be reduced again by half, i.e. to 0.13 m, when a parabolic shape is adopted. The results indicate that a parabolic shape will generally produce a better approximation of CMR bathymetry than a rectangle.

When the combined RMSE resulting from neglecting morphological features (0.15 m), channel thread sinuosity (0.1 m), and cross-sectional depth variability (0.13 m) is computed (from the square root of the sum of the squares), an overall RMSE estimate of 0.22 m is obtained. This is marginally lower than the observational errors associated with satellite altimetry: Frappart et al. (2006) estimates ENVISAT RMSE for large rivers as 0.28 m. Uncertainties in channel cross-sectional area, terrain elevation and hydrology are likely to introduce considerably larger errors in modelled WSE produced by a hydrodynamic model. Published average RMSEs between modelled and observed WSE for the validation of large river models attest to this: average RMSEs of 0.84 m, 0.95 m, and 1.21 m are reported for models of the middle Congo, Upper Niger River, and Niger River Inland Delta respectively (Neal et al., 2012; Fleischmann et al., 2018; O'Loughlin et al., 2020).

It is important to recognise here that the RMSE values estimated in this study are averages along the entire multichannel CMR. The error will vary spatially, especially at the observed WSP variations. Here, peak WSE errors are 0.3–0.6 m in magnitude and constitute appreciable components of the flood wave amplitude (3–4 m) and navigable depth thresholds (1.5–2 m). A reach-scale model situated at a WSP variation can therefore expect a significantly larger RMSE in modelled WSE. WSP variations above the smoothed WSP are particularly important for inundation modelling: they represent local WSE maxima with the highest potential for channel – floodplain connectivity and will therefore exert a significant control on inundation dynamics, assuming bank elevations do not locally rise here. The largest WSP variations are located at confluences, and their magnitude here may well exceed that observed during seasonal low flow conditions. Moreover, WSP variations at tributaries not observed during low flow conditions may emerge during higher flow conditions. Errors in modelled WSE introduced by an ESC are therefore likely to be most significant at confluences.

Based on the author's current knowledge of published literature, this is the first study to evaluate the consequences of simplifying large multi-thread channel systems to an ESC. Altenau et al. (2017a) did so to some extent for an 80 km long reach of the Tanana (a mid-size river; first order tributary of the Yukon), by simplifying a full 2D representation of individual channel threads to a 1D ESC with a uniform bed slope. The

simplification also incorporated a change from a 10 m resolution 2D model to a 500 m resolution 1D model, so the effects of the ESC are not isolated in the same way that they are in this study of the CMR. Nevertheless, it is interesting to note that the Tanana 2D model and simplified 1D ESC model produced RMSEs in main channel WSE of 0.19 m and 0.35 m respectively, implying that the simplification introduces a RMSE of 0.16 m. Whilst differences in methods preclude a direct comparison to the 0.22 m RMSE estimated in this study, the Tanana study does support the finding that simplification of multithread channels to an ESC introduces errors that are of limited consequence for hydrodynamic models used to simulate large river WSE dynamics.

6.5.1 Explicit Representation of Islands

As discussed in subsection 6.2.5, a key assumption of these findings is that representation of mid-channel island inundation can be simulated within the 2D floodplain domain of a model. Arguably, this should be true of any model that is required to simulate inundation, since island inundation constitutes a significant component of CMR fluvial inundation. To represent large numbers of mid-channel islands explicitly whilst simultaneously representing the channel in 1D would likely require development of a new method of efficiently linking 1D and 2D model domains. Currently, this is not realistically possible: models designed to model large natural river systems such as LISFLOOD-FP can only represent 1D channels as sub-grid features within a floodplain cell. Whilst some commercial models such as TUFLOW are potentially capable of representing islands within a 2D domain and channels as 1D (BMT WBM, 2016), this would involve highly time-consuming manual work such as linking the banks of each individual 2D island to multiple 1D nodes, which is not realistic for large river modelling (over hundreds or thousands of kilometres). Besides, the full Saint Venant numerical formulations used by such commercial codes are not well suited to large river modelling.

There may be circumstances where a model is not required to explicitly represent island inundation, and it is desirable to lump the islands into the channel model. Whilst the hydraulic consequences of representing mid-channel islands within an ESC have not been comprehensively assessed here, simple uniform flow calculations (documented in Figure 6-9) show that the stage response of an ESC without islands is fundamentally different to that of a channel with islands included. Therefore, it is anticipated that calibrating an ESC's friction and shape coefficient (in the manner shown in Figure 6-31) to compensate for the omission of islands would result in a poor representation of the real channel's stage response.

To investigate the incorporation of island morphology into a simple 1D channel model based on a simple channel shape more thoroughly, future research might entail a further modelling experiment, similar to the experiments documented in this research. Such an experiment would be based around a control model in which the islands are represented explicitly with MERIT elevations, and a simplified model in which the islands are removed and incorporated into an ESC with a Manning's *n* and channel shape that can be calibrated. Two complications arise here: one being due to the simplified model also removing channel thread sinuosity, thus preventing the specific effect of neglecting islands from being characterised. A second complication is the need to represent identical floodplains in each model, in order to properly assess the speed of flood wave travel (as shown in Table 6-6), which would require the simplified model's ESC to be represented within a separate 1D model domain to the 2D floodplain model. Using different model solvers for the control and simplification models would introduce an additional variable, preventing a fair comparison between models. These complications are avoidable if the aforementioned new method of efficiently linking 1D and 2D domains is developed: its use here would enable use of a 1D channel domain linked to a 2D floodplain domain for both models. In such a setup, the control model represents the islands within the 2D domain, whilst the simplified version does not. Both models would exclude channel thread sinuosity by treating the channel as a 1D ESC.

6.5.2 Potential Broader Applicability of Findings

It is hypothesised that aspects of these findings will apply to multichannel reaches of other large rivers, based on some notable assumptions. Whilst these assumptions require further investigation, their potential validity is explored below.

One assumption is that the CMR channel thread sinuosity is representative of other large multichannel rivers. Errors introduced by an ESC will increase with channel thread sinuosity, due to larger overestimation of flood wave speed. The channel threads of the world's largest anabranching rivers do not appear to show significantly greater sinuosity than the CMR, based on the appearance of anabranching channel patterns identified by other researchers (Latrubesse, 2008; Ashworth and Lewin, 2012; Nicholas et al., 2013). However, quantification of channel thread sinuosity in a range of large multichannel rivers is needed to assess this assumption fully.

Another assumption is that the characteristic rate of change in WSE with respect to time on the CMR also represents other large rivers. As this increases, the influence of flood wave speed error on modelled WSE increases. On the CMR, WSE changes at a daily rate of less than 0.1 m on average, reducing the importance of modelled flood wave

speed on WSE predictions. Other large rivers, particularly those within the 'mega river' category (mean annual discharge greater than 17,000m^3/s) proposed by Latrubesse, (2008) will show a similar rate of change in WSE, given their inherently stable seasonal flood regimes. However, the assumption is unlikely to be applicable to flashy rivers with high peak events, and for rivers below a certain size range. Further work is needed to evaluate the temporal variability in WSE for a range of rivers

A third assumption is that the upper limit of cross-sectional depth variability assessed here (shown in Figure 6-21) encompasses a range of large multichannel rivers. Whilst the availability of large multichannel river bathymetry data is limited globally, data published for reaches of the Bangladeshi Jamuna (Best and Ashworth, 1997) Argentinean Parana (Nicholas et al., 2012), and Tanana (Altenau et al., 2017a) appear to support this assumption.

Finally, it is assumed that channel scale morphological features that cause a river's WSP to deviate significantly from a smoothed profile (discussed in subsection 6.2.2) are largely absent, as is the case in the CMR. Essentially, this limits the applicability of these findings to reaches with self-adjusting alluvial channels that maintain a consistent WSP, and excludes fundamental transitions in planform such as the Chenal entrance (discussed in subsection 6.2.2). As the majority of large multichannel river reaches appear to be predominantly composed of adjustable channels (Latrubesse, 2008; Ashworth and Lewin, 2012), this limitation should not be particularly restrictive. Currently, identifying where this limitation applies is challenging: this study has relied on high resolution in-situ WSE measurements to confirm the absence of significant WSS variability. However, when data becomes available from the upcoming Surface Water and Ocean Topography (SWOT) satellite mission (discussed in subsection 2.3.6), assessment of large river WSS variability will be possible globally.

6.6 Concluding Remarks

With careful derivation, the multichannel Congo Middle Reach (CMR) can be simplified to an effective single channel (ESC) with a simple shape without introducing significant error in modelled water surface elevation (WSE). Assuming hydraulic roughness and parabolic channel shape are calibrated across the entire flow range, this study has shown the root mean square error (RMSE) in modelled WSE introduced by such a simplification can be limited to 0.22 m. This RMSE estimate has been derived by combining individual estimates of the RMSE associated with: neglecting channel scale morphological features (0.15 m); neglecting channel thread sinuosity (0.1 m); and neglecting cross-sectional variability in depth (0.13 m).

Aside from the need to accurately represent mean cross-sectional area and effective channel width, calibration of hydraulic roughness to observations of WSE across a range of flows is clearly an important part of an ESC modelling approach. Doing so will enable the hydraulic effects of the individual channel thread thalwegs and sinuosity to be effectively compensated for. Channel shape is also of importance, with a parabolic shape (shape parameter, s = 2.5) providing the best approximation of CMR bathymetry. Whilst the optimum value of s may vary between discrete reaches according to the real bathymetry, and will also be unique to a particular hydrodynamic model build, the value of 2.5 shows clear improvement over a rectangle and provides an informed first estimate that should be subject to further calibration. The spatial resolution at which channel geometry is represented is not a key consideration; there is no need to represent local variability in channel width, and even the most extreme constrictions in river width can be neglected.

An important assumption made in this evaluation of ESC applicability, is that mid-channel islands are represented within the 2D floodplain domain of a hydrodynamic model. This is largely based on the observation that seasonally inundated mid-channel islands in the CMR will constitute a significant component of fluvial inundation along this river (Comptour et al. 2020; personal observations), and this should therefore be represented explicitly. Moreover, uniform flow calculations indicate that incorporating islands into an ESC will result in poor representation of a channel's real stage response across a range of flows, even if Manning's n and channel shape parameters are optimised through calibration to WSEs across a range of flows. Currently available model codes do not appear capable of linking a 1D ESC solver to a 2D floodplain solver that includes mid-channel islands. Therefore, a new method of efficiently linking 1D and 2D model domains designed for modelling large rivers is needed.

It is speculated that these findings will hold for other large multichannel river reaches, although more work is needed to investigate this further. In particular, information on channel thread sinuosity, cross-sectional depth variability, and the characteristic rate of change in channel WSE with respect to time is needed for a range of large multichannel rivers. Moreover, the high resolution (sub-kilometre) water surface profiles (WSPs) soon to be observed globally by the SWOT satellite are needed to confirm the absence of water surface slope variability along large multichannel river reaches.

Model errors resulting from wider uncertainties in observations of WSE, mean channel cross-sectional area and width, and discharge were not evaluated in this research. Typically, these observational uncertainties will result in substantial errors themselves that when combined may be significantly greater than the 0.22 m RMSE estimated here. Therefore, it is worth noting that practical implementations of ESCs on large rivers can expect much larger errors in model predictions, as a result of observational uncertainties. Nevertheless, it is highly valuable for modellers to know that the specific errors incurred by introducing geometric simplifications to channel geometry can be minimised to the degree shown here.

CHAPTER 7
Synthesis and Conclusions

7.1 Summary

The aims of the research presented in this thesis were twofold:

1. ***To assess the water surface and in-channel hydraulic conditions along the middle reach of the Congo River, and the capacity of satellite-based observations to determine these conditions.***
2. ***To evaluate methods of channel geometric representation in hydrodynamic models of the Congo's multichannel middle reach.***

The successful completion of two major field campaigns has been of paramount importance to achieving these aims. The field data have been used throughout the research: in analysing the hydraulics of the Congo Middle Reach (CMR), modelling the bathymetry of the CMR, and modelling fluvial hydraulics and hydrodynamics. Satellite observations and derived datasets have also been used throughout the research, the work and accompanying datasets of O'Loughlin et al. (2013), Yamazaki et al. (2017), and the Hydroweb online resource (Santos da Silva et al., 2010) being key sources of data and information.

The research undertaken is documented in Chapters 4, 5, and 6. Chapter 4 sought to achieve the first aim of this thesis. The methods, results, and analysis of two field campaigns along the CMR were presented, and WSE measurements from three satellite altimeters were also analysed. The analyses provided a detailed hydraulic characterisation of the CMR, and an assessment of the spatial adequacy of satellite altimetry for capturing the water surface profile (WSP). Chapter 5 reported on the construction and validation of a multichannel bathymetry model using a novel approach that involved the estimation of bathymetry. This work was crucial for achieving the second aim of this thesis, in conjunction with Chapter 6. Chapter 6 investigated the applicability of an effective single channel approximation to the CMR, and involved a series of hydraulic modelling experiments that utilised the bathymetry model developed in Chapter 5.

7.2 Conclusions

7.2.1 Field-based Hydraulic Characterisation

The first hydraulic research field campaigns in recent decades were completed on the CMR, enabling a hydraulic characterisation of this river reach based on field data. The hydraulic characterisation predominantly covered the reach between Kinshasa and Mbandaka, as reported in Chapter 4, and was supplemented with additional analysis of the observed longitudinal water surface profile (WSP) between Mbandaka and Kisangani (subsection 6.2.2).

A key finding of the characterisation is a complete absence of any river flow constrictions, i.e. reductions in cross-sectional area that cause upstream backwater effects. Whilst planform constrictions are present along the CMR at four locations where the river width is severely constricted by erosion resistant banks, river depth is not constricted, and increases significantly at these locations in order to satisfy morphodynamic equilibrium. This is mainly evidenced by the observed absence of any substantial increase in channel velocity and water surface slope variability across these width constrictions during low flow conditions. Hydraulic modelling of flow conditions through a high resolution study reach (which includes the most extreme width constriction for the entire mainstem) confirmed the absence of any backwater effects during high flows. Backwater effects from channel constrictions have been observed along reaches of other large rivers such as the Mekong and Orinoco, and are generally formed by the localised presence of erosion resistant bedrock (Latrubesse et al., 2005). The constrictions along those rivers are a leading cause of their fluvial inundation, and strongly control regional hydrodynamics (Warne et al., 2002). Their absence along the CMR is therefore an important finding, and provides some explanation for the relatively subtle nature of fluvial inundation noted in Chapter 3. This finding also provides further support to the hypothesis that the Cuvette Centrale wetlands are mostly supplied by rainfall, rather than fluvial inundation (Alsdorf et al., 2016). The more complex question of the fluvial controls on wetland inundation dynamics remains to be addressed however.

The transition from multichannel to single channel planform at the Chenal entrance, located 270 km upstream of Kinshasa, is the site of major spatial variability in water surface slope (WSS). This feature comprises a sharp increase in downstream bed slope from 5 to 20 cm/km, which causes a drawdown effect (i.e. an increase in upstream WSS from 2 to 8 cm/km) during low flow conditions that propagates approximately 70 km upstream. Aside from this location, spatial variability in WSS is minimal along the CMR: a simple second order polynomial regression line fitted to 5 km resolution water

surface elevation (WSE) observations is generally able to describe those observations to within 0.3 m. Notable exceptions exist, where the observed water surface shows apparent backwater or drawdown effects to be present for 10-20 km, and a deviation above the regression line of up to 0.57 m occurs. However, these exceptions occupy less than 5% percent of the 1,300 km long multichannel CMR.

7.2.2 Implications for the Use of Satellite Altimetry

Conventional repeat orbit, 1D profiling satellite altimeters such as ENVISAT and Sentinel-3A (herein referred to as profiling altimeters) measure WSE along the CMR with a limited spatial interval, and as a result are unable to properly capture WSS variability such as that observed at the Chenal entrance. Pre-existing profiling altimeter data sets were found to perform poorly at estimating WSE and WSS here; an ENVISAT derived WSP deviates from field measurements by up to 2 m, which represents approximately half the annual flood wave amplitude. Moreover, when used to compute discharge, ENVISAT and Sentinel-3A produce very different discharge estimates of 30,200 m^3/s and 17,800 m^3/s respectively, as a result of large differences in WSE and WSS values produced by their different measurement locations. These findings highlight the inadequate measurement coverage of existing profiling altimeters even on highly subcritical reaches of the world's largest rivers, and the need for higher resolution WSE measurements to adequately capture WSS variability. The Surface Water and Ocean Topography (SWOT) mission, due to launch in 2022, will provide such measurements, at sub-kilometre resolution, by virtue of an interferometric SAR instrument.

Despite being unable to fully capture WSS variability along the CMR, profiling altimeters have a significant role to play in future hydrodynamic research here. This research has shown that during low flow conditions, neglecting local variations in WSS along the multichannel CMR (i.e. excluding the Chenal) amounts to a WSE error of no more than 0.3 m along 95% of the reach. Neglecting this WSS variability is unlikely to translate to significant or widespread errors in large scale hydrodynamic models, which typically predict WSE with a root mean square error (RMSE) in excess of 0.6 m even when observed bathymetry and flow data are used (e.g. Trigg et al., 2009; Bonnema et al., 2016).

7.2.3 Modelling multichannel hydraulics with spatially limited bathymetry observations

This research evaluated an approach to explicitly representing CMR multithread channel bathymetry in a hydraulic model. Specifically, a novel approach to constructing a spatially distributed 2D bathymetry model (BM) has been developed and applied to a

70 km long multichannel reach of the CMR. The approach requires little or no observed bathymetry data, and is distinct from conventional BM preparation whereby bathymetry observations are spatially interpolated. To determine bathymetry in channel areas that are outside of the spatial envelope of interpolated observations (96% of channel plan area in this case), the approach estimates the bathymetry by using Manning's equation to compute depth from values of river width, WSS, discharge, and a hydraulic roughness coefficient.

Manning's equation is used to estimate depth at regular 2 km sub-reaches along the stream-wise direction, by using the effective width of the channel belt at each sub-reach. Constant WSS, discharge, and hydraulic roughness values of 5 cm/km, 21,000 m^3/s, and 0.03 respectively, are used across all sub-reaches. Width is obtained from satellite imagery, WSS and discharge are from field observations, and hydraulic roughness is obtained from published values for large anabranching rivers. In applying Manning's equation in this manner, channel threads are assumed to have a rectangular cross-sectional shape, and to have a constant depth across the channel belt (transverse to the channel mean flow direction). A second assumption is that channel depth varies in the stream-wise direction as a function of effective channel width. This is imposed by using the effective channel belt width of each sub-reach, which results in sub-reaches with smaller effective channel widths having larger estimates of depth, and vice versa.

The BM was validated geometrically using in-situ depth observations, and hydraulically through 2D hydraulic modelling. Hydraulic validation entailed using the BM in a hydraulic model to simulate observed flow conditions, and comparing resulting in-channel velocity predictions with observed velocities. To fully evaluate the estimated bathymetry, a version of the BM with no observed data included (i.e. using estimated bathymetry only) was also hydraulically validated.

A key finding of this research is that mean channel depths and depth averaged velocities are well approximated by the estimated bathymetry where the channel is wide and multi-threaded. When bathymetry observations were removed completely from the BM, errors in velocity predictions showed negligible increase here, suggesting that the inclusion of observed bathymetry data here is of no significant benefit. Mean absolute errors (MAE) and RMSE in velocity remained less than 10% and 25% respectively. This finding implies that in the wide multi-thread reaches that characterise most of the Congo Middle Reach planform, mean channel depths and thereby general flow conditions are well approximated by the bathymetry estimation approach. Thus, the assumptions imposed by Manning's equation, and the pre-selected Manning's *n* value of 0.03, which

both underpin the bathymetry estimation approach, are valid here. The validity of these assumptions is largely attributed to the relative uniformity of flow conditions observed in the multithread channels.

In contrast, the estimated bathymetry produced large errors in channel depths and velocities where the river flows through single thread channels that are laterally constricted. At two such locations, average MAEs and RMSEs in modelled velocity were 46% and 49% respectively, on account of the estimated bathymetry being unable to predict the full extent to which the bed has been able to locally adjust through erosion in order to maintain morphodynamic equilibrium here. Interestingly, these large underestimates in depth led to an average increase in WSE through the reach of only 0.2 m, showing WSE to be relatively insensitive to bathymetry. This finding reflects the highly sub-critical nature of the flow conditions here, WSE being controlled predominantly by downstream conditions rather than local bathymetry. Inclusion of the observed bathymetry at the width constrictions reduced average MAEs and RMSEs in modelled velocity to 0% and 26% respectively here, confirming the poor performance of the estimated bathymetry, and the value of observed bathymetry data here.

The findings show that the novel approach of supplementing spatially limited bathymetry data with estimated bathymetry is appropriate for modelling multi-thread channel hydraulics in the CMR, provided that cross-sectional observations at geometric irregularities in the channel (width constrictions in this case) are included.

7.2.4 Large Scale Hydrodynamic Modelling: Applicability of Effective Single Channels

Here, the applicability of an effective single channel (ESC) approximation to the multichannel CMR was investigated, this approximation being a key component of current large river hydrodynamic modelling approaches. The work drew on research findings of previous chapters, by assuming channel parameters can be calibrated to WSE from profiling altimeters, and using the validated bathymetry model from Chapter 5. A preliminary investigation used observations of the CMR and uniform flow calculations to determine the hydraulic consequences of simplifying real multichannel bathymetry to an ESC. This was then followed by a series of hydraulic modelling experiments set up to evaluate the ESC simplification in detail.

These investigations showed that it is possible to simplify the multichannel CMR channel geometry to an ESC with a simple shape, without introducing significant error in modelled WSE. Specifically, the RMSE in modelled WSE introduced by such a simplification can be limited to ~0.22 m. This RMSE estimate was derived by combining

individual estimates of the RMSE associated with three key geometric omissions imposed by an ESC approximation, namely: neglecting channel scale morphological features (0.15 m); neglecting the sinuosity of individual channel threads (0.1 m); and neglecting cross-sectional variability in depth (0.13 m).

Aside from the need to accurately represent mean cross-sectional area and effective channel width, it is important for any model using an ESC approximation to be calibrated to observations of WSE across a range of flows. Doing so will enable the hydraulic effects of individual channel thread thalwegs and sinuosity, which are neglected in an ESC, to be effectively compensated for. Channel cross-sectional shape is also of importance, with a parabolic shape providing the best approximation of CMR bathymetry. Whilst the optimum shape may vary between discrete reaches according to the real bathymetry, and will also be unique to a particular hydrodynamic model build, a parabolic shape showed clear improvement over a rectangle and provides an informed first estimate that should be subject to further calibration. Conversely, representation of channel width variability was found to be unimportant: even the most extreme constrictions in river width can be neglected. Attempting to represent local width variability may even introduce error if it is not paired with accurate depth data of a similar spatial resolution.

It is speculated that these findings will hold for other large multichannel river reaches, although more work is needed to investigate this further. In particular, information on channel thread sinuosity, cross-sectional depth variability, and the characteristic rate of change in channel WSE with respect to time is needed for a range of large multichannel rivers. Moreover, the high resolution (sub-kilometre) WSPs soon to be acquired globally by the SWOT satellite are needed to confirm the absence of significant WSS variability along large multichannel river reaches.

An important assumption made throughout these investigations into an ESC was that mid-channel island terrain, and thereby its inundation, is represented within the 2D floodplain domain of a hydrodynamic model. This assumption was largely based on the fact that seasonally inundated mid-channel islands in the CMR will constitute a significant component of fluvial inundation along this river (Comptour et al. 2020; personal observations), and this should therefore be represented explicitly. Currently available model codes do not appear capable of linking a 1D ESC solver to a 2D floodplain solver that includes mid-channel islands. Therefore, a new method of efficiently linking 1D and 2D model domains designed for modelling large rivers is needed, to enhance the

applicability of an ESC to hydrodynamic modelling of the CMR and other multichannel river reaches.

7.3 Limitations of Research

7.3.1 Temporal Variability in Water Surface Slope

A notable limitation of this research is that temporal variability in WSS was not evaluated in detail. This was due to the lack of temporal coverage in the observed data that was obtained, which restricted the in-situ hydraulic characterisation to seasonal low flow conditions only. ENVISAT altimetry observations were analysed during seasonal low and high flow conditions, and showed no significant WSS variability. However, as has been shown in this research, ENVISAT is not capable of fully resolving WSS spatial variability. Thus, it is possible that outside of the low flow conditions observed, further spatial variability in WSS may exist, particularly at major confluences that can cause backwater effects to develop.

7.3.2 Representation of Island Morphology in Hydrodynamic Models

In researching the applicability of an ESC to the CMR, it was assumed that mid-channel island terrain, and thereby its inundation, is represented within the 2D floodplain domain of a hydrodynamic model. This assumption was largely based on the fact that seasonally inundated mid-channel islands in the CMR will constitute a significant component of fluvial inundation along this river (Comptour et al. 2020; personal observations), and this should therefore be represented explicitly. However, there may be circumstances where a model is not required to explicitly represent island inundation, and it is desirable to lump the islands into the channel model. It was not possible to thoroughly investigate such an approach in this research, and therefore no specific conclusions have been made about its applicability. Preliminary uniform flow calculations did however indicate that lumping island morphology into an ESC will result in a poor representation of a channel's real stage response across a range of flows, as hydraulic roughness was unable to effectively compensate for the omission of islands. The aforementioned new method of efficiently linking 1D and 2D model domains would enable a thorough investigation of this approach.

7.4 Discussion on Future Research Directions

Some potential directions for future research have emerged from the findings presented in this thesis, and are discussed below.

7.4.1 Water surface and Inundation Dynamics

In the coming years, there will be an unprecedented global increase in the resolution and coverage of open water observations of WSE and extent, largely from the SWOT mission. Aside from SWOT's high profile aim of monitoring discharge from space (which is discussed in the next section), major advances in understanding the dynamics of CMR fluvial inundation are likely to emerge from these observations. This will in turn facilitate much needed improvements in estimates of greenhouse gas emissions from open water in the Congo Basin, and a better understanding of the fragility of globally important wetland ecosystems and peatlands here. Observations from SWOT will also facilitate assessments of river related risks pertaining to flood hazard exposure, food security, and fluvial navigation in shallow river channels. However, SWOT observations are limited by the instrument's three year operational lifespan, and significant uncertainty over its performance when emergent vegetation obscures visibility of the water surface (Biancamaria et al., 2016). These limitations are important in the CMR, given the prevalence of inundated vegetation here, the need to analyse observations over timescales in excess of three years, and the need to understand hydrodynamic response to projected environmental changes in the Congo Basin (namely climate change, deforestation, agriculture, urbanisation, and hydraulic infrastructure). Hydrodynamic models will therefore play a key role in leveraging SWOT data for analysing hydrodynamic and related processes over long timescales, predicting inundation in wetlands where it cannot be reliably observed, and simulating hydrodynamic response to changing river flow regimes.

This research has established that a new method of efficiently linking a 1D and 2D model solvers would be of significant benefit to hydrodynamic modelling efforts on large multichannel rivers, and this should therefore be investigated. Efficient 1D-2D linking will enable the terrain of large numbers of mid-channel islands to be efficiently incorporated into a 2D model domain, and therefore eliminate significant errors that will arise from lumping island morphology into a simple channel geometry with a uniform shape and hydraulic roughness. The data and analysis presented in this thesis would enable the CMR to be used as a test bed for the development of a new method.

In lieu of an efficient 1D-2D linking method, where possible a purely 2D approach should be adopted for modelling the hydrodynamics of the CMR and other multi-thread

channel systems containing archipelagos of seasonally inundated islands. Computational resource constraints could be managed by using local inertial or diffusive wave approximations, and by using 2D sub-grid approaches (Yu and Lane, 2006b; Brunner, 2016). Whilst requisite input bathymetry data is likely to remain unavailable in many multichannel river reaches, this research has demonstrated the potential for multi-thread channel bathymetry to be estimated, which gives significant potential for future 2D multichannel hydrodynamic modelling.

Estimating Multichannel CMR bathymetry

To estimate the bathymetry along the entire multichannel CMR, the approach presented in Chapter 5 could be augmented, to make better use of observed channel cross-sections that have been obtained at over 10 locations by the CRuHM project (Tshimanga et al., 2020), and to improve bathymetry predictions at width constrictions. This research established that hydraulically significant morphological features such as bedrock control points are absent along the multichannel CMR, and showed that the CMR channel system to be highly adjustable. One implication of these findings is that hydraulic geometry theory is likely to be highly applicable (Leopold and Maddock, 1953; Dury, 2020), and could be used to efficiently estimate bathymetry from observable width. Hydraulic geometry theory states that for adjustable river channels, power law relationships exist between channel characteristics including width w, depth d, and velocity v. These relationships are usually expressed as a function of discharge, as follows:

$$w = aQ^b \qquad \text{Eq. 7-1}$$

$$d = cQ^f \qquad \text{Eq. 7-2}$$

$$v = kQ^m \qquad \text{Eq. 7-3}$$

Where $ack = 1$ and $b + f + m = 1$. Equations 7-1 and 7-2 can be combined and re-arranged (see Equations 7-4 and 7-5 respectively) to demonstrate that a power law relationship exists between depth and width for a given discharge (Neal et al., 2012):

$$Q = \left(\frac{w}{a}\right)^{1/b} = \left(\frac{d}{c}\right)^{1/f} \qquad \text{Eq. 7-4}$$

$$d = \left(\frac{c}{a^{f/b}}\right) w^{f/b} \qquad \text{Eq. 7-5}$$

The terms within brackets constitute the coefficient of the relationship, and the exponent of the relationship is a fractional term. Observations can be used to determine the coefficient and exponent of this relationship for a particular river reach. To provoke future research in this area, observed channel width and depth at 10 locations along the CMR are plotted, and power law relationships derived, as shown in Figure 7-1.

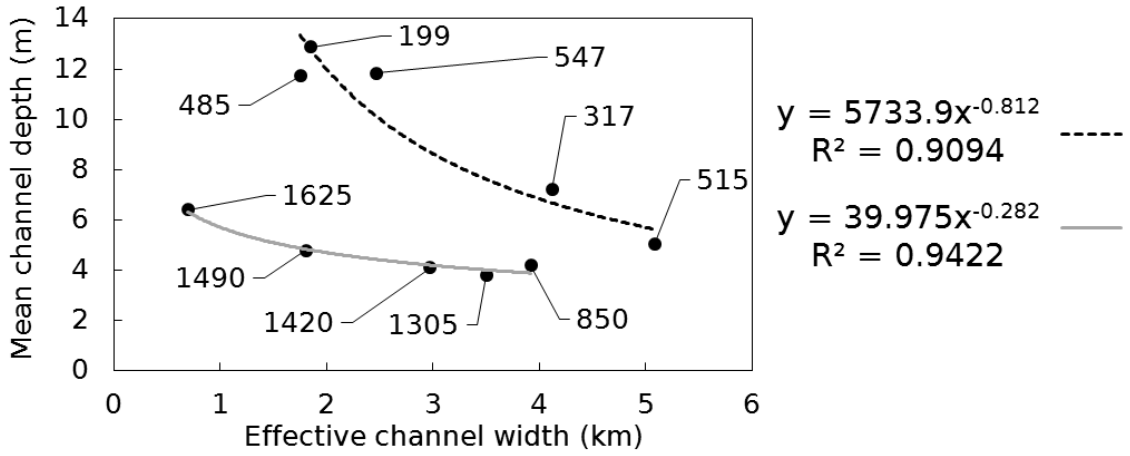

Figure 7-1. Observations of cross-sectional channel width and depth at 10 locations along the CMR, with two power law relationships fitted. Each observation is labelled with its distance from Kinshasa in kilometres, and each relationship is labelled with its equation and coefficient of determination (R^2).

Two relationships are visible in the data and are plotted as curves. The two curves cover the upper and lower halves of the CMR, from Kisangani to Mbankdaka, and Mbandaka to the Chenal entrance, and appear to fit the observations well. The apparent change in relationship near Mbandaka may reflect the large increase in discharge in this area, as the Lulonga, Ruki, and Oubangui Rivers all join the mainstem here. Clearly, more research is needed to investigate such relationships, and this should be done as part of future studies into the large scale hydrodynamics and geomorphology of the CMR.

7.4.2 Methods of Monitoring Discharge from Space

Discharge estimation from satellite remote sensing of river hydraulic variables has been widely explored in recent decades (Smith et al., 1996; Bjerklie et al., 2003; Birkinshaw et al., 2010; Durand et al., 2016). It is generally regarded as a key component of a long term sustainable solution to flow gauging on large rivers, particularly in remote regions (Calmant et al., 2009). The SWOT mission aims to make widespread satellite

gauging a reality, by estimating discharge along all river reaches more than 100 m wide. SWOT's three year operational life is only a short term solution, however. In the longer term, it is likely that discharge estimation from satellite will need to rely on less expensive conventional profiling altimeters, possibly in constellation (see CNES, 2020 for example). Due to the strong focus of the research community on developing SWOT discharge estimation algorithms, the future use of profiling altimeters for satellite gauging has received relatively little attention in recent years. Methods of gauging large rivers from profiling altimeters therefore need to be further explored, and the research presented in this thesis can serve as a platform to do so.

One possible method that could be developed and tested in the near future would entail the development of reach-scale hydraulic models that predict discharge directly from input observations of WSE from profiling altimeters. This method is analogous to a traditional rating relationship, but is capable of using WSE measurements retrieved from any location along the designated reach, rather than measurements made in a single defined spatial location. Rating curves have been used to retrieve discharge from satellite profiling altimetry before (see the efforts of Paris et al., 2016 in the Amazon Basin), but their approach relied on somewhat uncertain modelled estimates of discharge to construct rating relationships, rather the complementary use of field data and satellite data proposed here.

The designated reaches would need to be mass conserved, and show minimal variability in WSS in space and time, such that it can be assumed constant. Based on the findings of this research, the assumption of WSS invariance is likely to be largely valid on many sub-reaches of the CMR, particularly away from major confluences and the Chenal entrance. Requisite model bathymetry can be derived using the method developed in Chapter 5, and supplemented with terrain data from MERIT. The model could be calibrated using observed pairs of WSE and discharge (Q–H pairs) observed during low flow (already obtained in this research) and high flow, and validated with additional Q–H pairs. The reach would ideally need to contain a single thread channel section to allow discharge to be efficiently observed using an ADCP. Using such a model, discharge could be retrieved from a WSE measurement obtained from any profiling altimeter that passes over the reach. As an example, if the model developed in Chapter 5 was extended downstream by 80 km, and calibrated to an additional pair of WSE and discharge observations, discharge could be derived from the currently operational Sentinel-3A profiling altimeter at seven day intervals. Moreover, the hydraulic modelling experiments in Chapter 6 showed that the vast majority of CMR flows are conveyed in-channel (over 90% during seasonal high flow according to the model shown in Appendix

C3), suggesting uncertainty in discharge predictions associated with inaccurate model inundation predictions would be small.

7.4.3 Spatially Distributed In-Channel Flow Conditions

Quantification of in-channel flow conditions is necessary to study the transport of sediment and pollutants through river channels, and therefore long-term fluvial navigability and water quality. A large and growing population in the Congo Basin rely heavily on the CMR and its tributaries for transportation and potable water resources (Foster and Benitez, 2010; Partow, 2011; Dargie et al., 2019). Specifically, over 30 million people are estimated to live within 50 km of a navigable river in the Congo Basin, a region where the population growth rate is 3.2% (Schiavina et al., 2019; Trigg et al., 2020). In this context, hydrodynamic and morphodynamic modelling are key tools for assessing long term navigability and water quality, which are anticipated to be adversely affected by anthropogenic impacts (Laraque et al., 2013). Hydrodynamic and morphodynamic models are also needed to answer unresolved questions concerning the geomorphic functioning and evolution of large anabranching rivers (e.g. Nicholas, 2013). For instance, the factors that promote mid-channel island formation and stability remain unclear: discharge variability has been shown to both promote and supress multithread channels, as has the presence of vegetation (Nanson and Knighton, 1996; Eaton et al., 2010; Tal and Paola, 2010). The uniquely elongated shape of CMR mid-channel islands also remains unexplained (Ashworth and Lewin, 2012).

Accurately modelling in-channel flow conditions of large anabranching rivers is rarely done due to a paucity of data, bathymetry data in particular, to the extent that synthetic river channels are being used in such modelling in lieu of observed bathymetry data (e.g. Nicholas et al., 2013). The potential future availability of a full bathymetry dataset for the CMR would therefore present major research opportunities, and given there are indications that such data may become partially available to the scientific community (Oudart et al., 2019; R. M. Tshimanga, personal communcation, 2020), this warrants some brief discussion. The data has been obtained as part of the Projet d'Appui à la Navigabilité des voies Fluviales et Lacustres (PANAV), a 60 million euro project to improve navigation facilities in DR Congo (Deutsche Gesellschaft für Internationale Zusammenarbeit, 2019), and is believed to comprise cross-sectional observations at ~1 km intervals.

Before utilising such data in hydrodynamic and morphodynamic models, a first research step might be to evaluate and automate methods of interpolation in large multichannel rivers, which remain underdeveloped (Hilton et al., 2019). With regards to

enforcing a directional component to interpolation, which is necessary to account for both anisotropic river bathymetry and island morphology, Chapter 5 found that generation of centrelines that reflect flow direction is not possible using a conventional Voronoi tessellation method (Nyberg et al., 2015). Therefore, alternative methods of determining flow direction for interpolating multichannel river bathymetry should be investigated. One possible approach might be to adopt a method currently being developed to apply SWOT discharge estimation algorithms to multichannel rivers, which evaluates channel thread sinuosity in an automated manner (Rodriguez and Frasson, 2019). The method involves use of a network analysis to identify contiguous channels that minimise sinuosity when connected, and may provide an effective indicator of flow direction for efficiently interpolating multichannel bathymetry.

Potential over-reliance on the PANAV bathymetry data is a key concern for future management of navigation risk. Whilst river planform is somewhat stable relative to other large anabranching rivers such as the Brahmaputra (Best and Ashworth, 1997; Ashworth and Lewin, 2012), bathymetric change has long been regarded as a key challenge to navigating the CMR (e.g. Wood et al., 1986). First-hand experience of multiple unintentional vessel groundings onto shallow sand beds during the field campaigns, despite the experience possessed by the boat crew, certainly corroborates this. Predicting morphological change using a morphodynamic model is unlikely to be a realistic solution in the near future, this being a challenge even in data-rich situations such as on the Rhine River (Yossef, 2016), not least because of the difficulties in obtaining information on sediment fluxes that is necessary for quantitatively predicting morphological change (Bridge, 1993). This points to the need to periodically monitor shallow bathymetry along the navigation route, particularly at ‘hotspots’ where deposition is likely to be occurring. The question then is how to identify the locations of these hotspots in order to allocate a finite resource. Hydrodynamic modelling may be of use here, by identifying hotspots based on predictions of spatially distributed flow conditions (i.e. unit discharge) as an indicator of deposition (e.g. Nicholas et al., 2012). The research focus here would be on linking relatively simple hydrodynamic model predictions of in-channel flow conditions to occurrences of deposition on the CMR, which if demonstrated would have broader implications beyond the Congo and the specific issue of navigation risk. For example, the model may also be able to indicate erosion hotspots, notably on mid-channel islands that are used extensively for agriculture, due to their fertile soil and dependable seasonal inundation (Comptour et al., 2020).

7.5 Research Contribution to the Scientific Community

The research presented in this thesis constitutes a substantial advancement in the knowledge and understanding of the channel hydraulics of the Congo River. The research involved the acquisition and analysis of field data, complemented with satellite datasets, and extensive modelling of channel geometry, hydraulics, and hydrodynamics. The research findings have significant implications for future hydrodynamic research on the Congo River and other large rivers, and are stated below.

Congo Middle Reach hydraulic characterisation

River flow constrictions that cause backwater effects have been shown to be completely absent from the Congo Middle Reach, despite the channel width being severely constricted at four locations. Backwater effects from channel constrictions are commonly observed along continental scale rivers and where present are a leading cause of their fluvial inundation, strongly controlling regional hydrodynamics. Their absence on the Congo Middle Reach provides some explanation for the relatively subtle nature of fluvial inundation here, and provides support to the hypothesis that the Cuvette Centrale wetlands are mostly supplied by rainfall, rather than fluvial inundation.

The transition from multichannel to single channel planform at the Chenal entrance is a hydraulically significant morphological feature, exhibiting a sharp increase in downstream bed slope. This morphological feature has been shown to cause a drawdown effect during low flow conditions whereby the longitudinal water surface profile steepens significantly. Aside from this location, spatial variability in water surface slope is minimal along the Congo Middle Reach, most notably across major confluences including the Oubangui.

Spatial adequacy of current satellite altimetry datasets

Currently available satellite altimetry datasets have an insufficient density of spatial coverage to fully capture the water surface slope variability that was observed along the Congo Middle Reach at the Chenal entrance. An ENVISAT derived water surface profile deviates from field measurements by approximately half the annual flood wave amplitude here, and when used to compute discharge, ENVISAT and Sentinel-3A altimetry datasets produce very different discharge estimates. This finding highlights the inadequate measurement coverage of existing profiling altimeters even on highly subcritical reaches of the world's largest rivers, and the need for higher resolution measurements of water surface elevation, set to be provided by the SWOT mission. Despite this finding, profiling altimeters have a significant role to play in future

hydrodynamic research, ENVISAT having been shown to possess adequate spatial coverage for capturing the water surface profile along more than 1200 km of the Congo Middle Reach.

Using observed and estimated bathymetry to model multichannel hydraulics

A novel approach of supplementing spatially limited bathymetry data with estimated bathymetry was found to be a useful approach to modelling multi-thread channel hydraulics, provided that cross-sectional observations at major geometric irregularities in the channel (width constrictions in this case) are included. Specifically, mean flow depths and velocities in the wide, multithread channels were found to be well approximated. Estimation of bathymetry involved the use of Manning's equation to compute the depth of multi-threaded channels from values of river width, water surface slope, discharge, and a pre-selected hydraulic roughness coefficient.

Applicability of an effective single channel to multithread channels

It has been shown that the multi-threaded channel geometry of the Congo Middle Reach can be simplified to an effective single channel in a hydrodynamic model, without introducing significant error in modelled water surface elevation. Such a model must be calibrated to observations of water surface elevation across a range of flows, and calibration should involve optimisation of both hydraulic roughness and channel shape parameters. Doing so enables the omission of hydraulically significant channel thread morphology to be effectively compensated for. In this research, a parabolic channel was shown to be the optimum shape. Representation of channel width variability was found to be unimportant: even the most extreme constrictions in river width are negligible. Moreover, attempting to represent local width variability may actually introduce error if it is not paired with accurate depth data of a similar spatial resolution. These findings may well apply to other river reaches with anabranching channel patterns, which are commonly found on the world's largest rivers.

Appendices

Appendix A. Chapter 4 Appendices

A.1 Fieldwork Challenges and Achievements

The fieldwork expeditions carried out in 2017 and 2019 were hugely complex and challenging undertakings; largely due to the remoteness of the region, its climate, and the lack of economic and social development in the region. It required the procurement of significant volumes of equipment and resources, and numerous people to be in right place at the right time, with all necessary permissions in place and health and safety considerations fulfilled. The status of the river as an international border added further complexity, and necessitated extensive liaison with many different Congolese authorities. Despite this complexity, the fieldwork expeditions were extremely successful and large volumes of significant data were collected with no serious injuries or economic losses incurred. These data represent measurements that are new to science, and is a profound achievement for this research project. The success of the fieldwork was the result of a huge team effort involving myself and my academic supervisor, Mark Trigg; Raphael Tshimanga and his team at the Congo River Water Resources Reseach Center (CRREBaC); members of the Congo River users Hydraulics and Morphology (CRuHM) research consortium from the Universities of Bristol (UK), Rhodes (South Africa), and Dar Es Salaam (Tanzania); and staff at the DR Congo navigation authority Régie des Voies Fluviales (RVF). A brief personal experience of the fieldwork is documented below, along with Figures A-1, A-2, A-3, and A-4; to give an insight into the fieldwork and some of the challenges. A more detailed account of the fieldwork can be obtained by reading the risk assessments, fieldwork plans, and post-fieldwork reports that were prepared annually.

Each year, my pre-departure preparations involved working for two to three months on mapping and scheduling a programme of fieldwork measurements, and developing an extensive risk assessment. I also established equipment requirements and helped procure this equipment, which ranged from survey instruments and marine safety kit, to basic camping equipment that is unavailable in DR Congo. To avoid complex and inconsistent rules applied to shipped goods, myself and Mark Trigg had to transport almost all this equipment as flight luggage. On arrival in DR Congo, I spent 1 – 2 weeks in meetings with numerous authorities (in-person was mandatory), waiting for resultant permissions to be granted, testing equipment, and training CRREBaC research associates in the use of the equipment. Poor internet access and grossly inadequate

transport infrastructure (especially in Kinshasa) make logistics particularly difficult. Occasional public disturbances also hindered these preparations, in one instance I was evacuated from the University of Kinshasa because student protests turned violent. Importantly, my colleagues at CRREBaC handled these logistical challenges admirably, and always had measures in place to deal with any safety or security issues.

Fig. A-1. Some fieldwork preparations: (a) preparing some of the flight luggage; (b) conducting equipment testing and training at CRREBaC in Kinshasa; (c) A brass band plays to pass time in a typical Kinshasa traffic jam.

Typically, life on the river for me entailed a 5 am start to obtain a GNSS measurement before the boat set off at sunrise. The boat would travel for 12-18 hours a day, unless it was necessary to stop to take measurements or procure supplies. Obtaining a cross-sectional transect took 2 – 3 hours because of the huge width of the river. One multichannel transect I conducted took a whole day, as it comprised separate transects across three channel threads. Delays to fieldwork resulted from numerous set-backs. For instance, one of the two main boat engines failed on several occasions, which significantly reduced the speed of the boat. It was also necessary to repair damage to the fiberglass boat caused by a severe thunderstorm. The team all ate and slept on the boat. Meals were served twice a day and were limited by a finite store of food. Mark Trigg

and I also brought a personal supply of fresh coffee, whisky, and some tinned food from the UK. Ablution facilities comprised two shared pit latrines and buckets of river water laced with disinfectant. Experiencing some sickness was almost inevitable for both local and foreign participants. Knowledge sharing was an invaluable part of the fieldwork: I provided on-the-job training to Congolese members of the fieldwork team, and also received training. It was also common practice for team members to give presentations in the evenings.

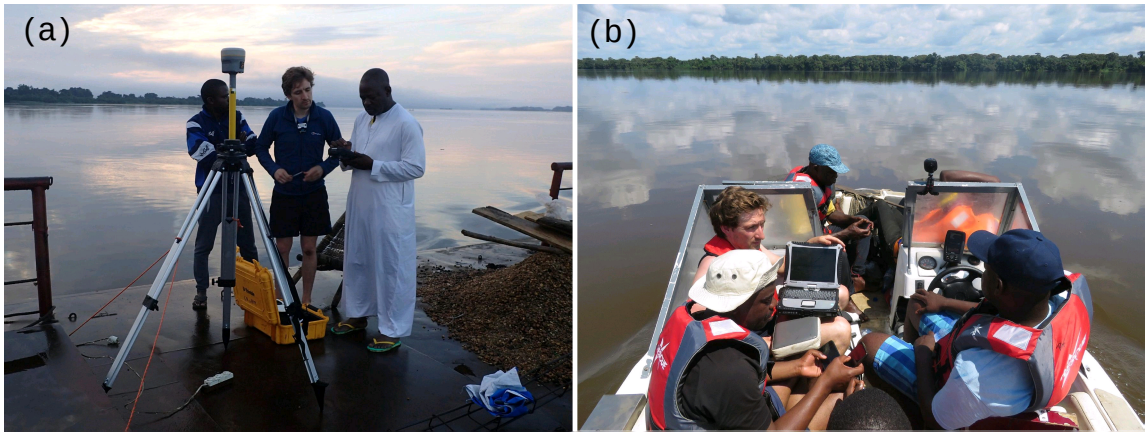

Fig. A-2. Fieldwork measurements: (a) early morning setup of GNSS; (b) Conducting an ADCP transect.

During my time spent travelling thousands of kilometres along the river, my interactions with many friendly and curious river-dwelling communities was an enlightening experience. The importance of the river to these communities was plain to see: it provides food, water, and a mode of transport for millions, and is a focal point of travel and trade. Despite its location in one the world's largest remaining wildernesses, the river itself was busy and hectic at times, particularly around ports at established population centres, with pirogues, boats and barges of all shapes, sizes and loads going about their business. Monstrous trains of barges laden with timber, charcoal and people were a sight to behold, resembling mini floating towns. Vessels comprising little more than an outboard motor and a raft of tied logs were also not an uncommon sight. Swarms of pirogues would attempt to hitch a lift upriver on our boat on a daily basis, to sell us fresh fish, vegetables, and bush-meat, as well as to make the most of the mechanical horse-power.

Fig. A-3. Communities on the river: (a) a train of barges; (b) a raft of logs; (c) pirogues hitched onto the fieldwork boat to offer fresh produce; (d) the busy port of Kwamouth.

Although the fieldwork was very arduous at times, it was also immensely rewarding and enjoyable, and I will always cherish the experiences I had. This was in no small part down to the camaraderie shared between the entire fieldwork team, including the scientific research team, the logistical team, and the boat crew. We all worked as a team towards a common goal, shared the same ups and downs, and looked after one another. In the future, it's my hope to build on these experiences and relationships, and continue these collaborative research efforts in some form.

Fig. A-4. Fieldwork team photos: (a) 2017 on Mpombie; (b) 2019 on Lomeka.

A.2 Continuous Water Surface Elevation Measurements

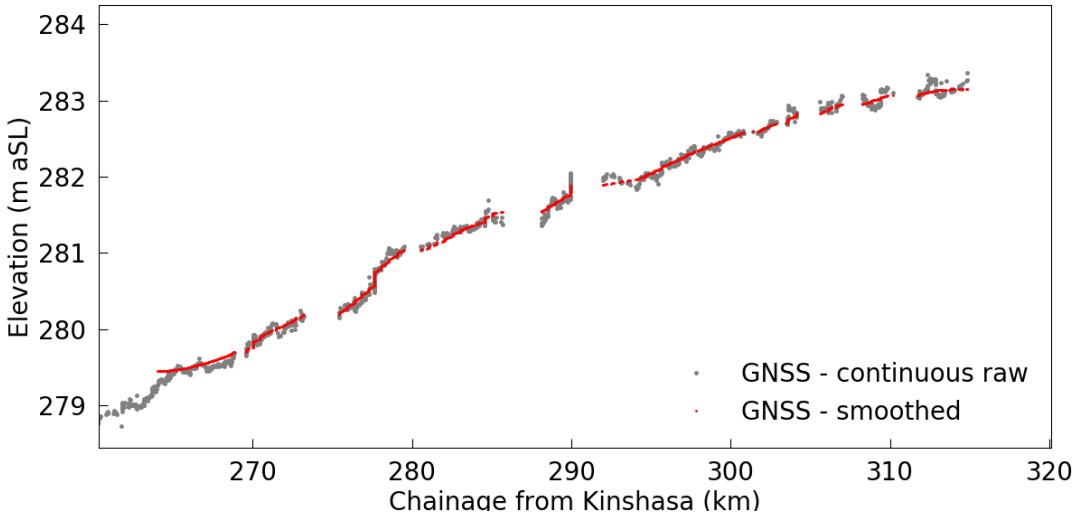

Fig. A-5. Longitudinal Plot showing 2017 continuous water surface elevation measurements. Raw data shown in grey, red shows a Gaussian filter with a window size of 75 applied to determine error due to boat movement. RMSD between measurements and the Gaussian filtered points is 6 cm. 10 km end sections upstream and downstream not included in RMSD calculation.

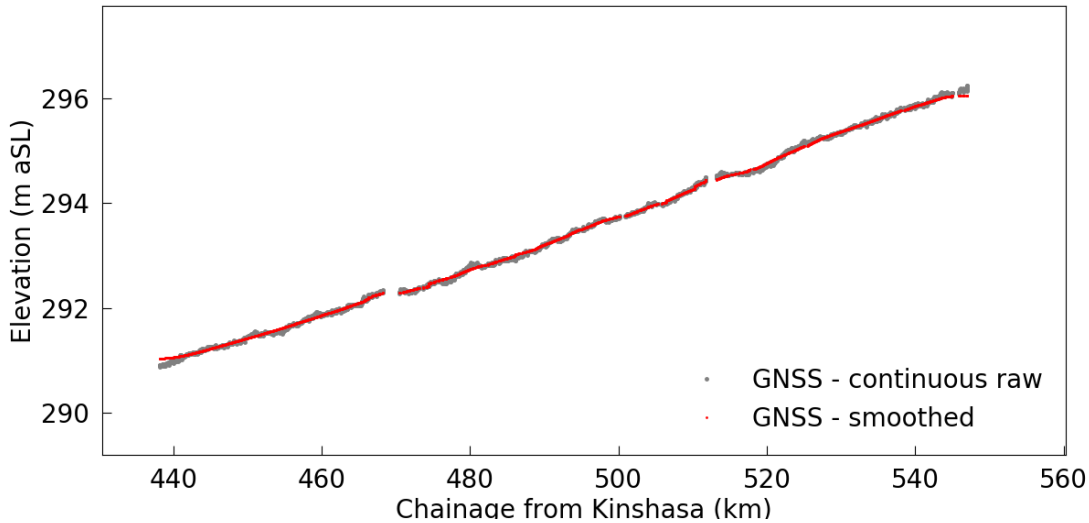

Fig. A-6. Longitudinal Plot showing 2019 continuous water surface elevation measurements between Chainage 440–550 km. Raw data shown in grey, red shows a Gaussian filter with a window size of 75 applied to determine error due to boat movement. RMSD between measurements and the Gaussian filtered points is 3 cm. 10 km end sections upstream and downstream not included in RMSD calculation.

A.3 Bathymetry Measurement Error Assessment

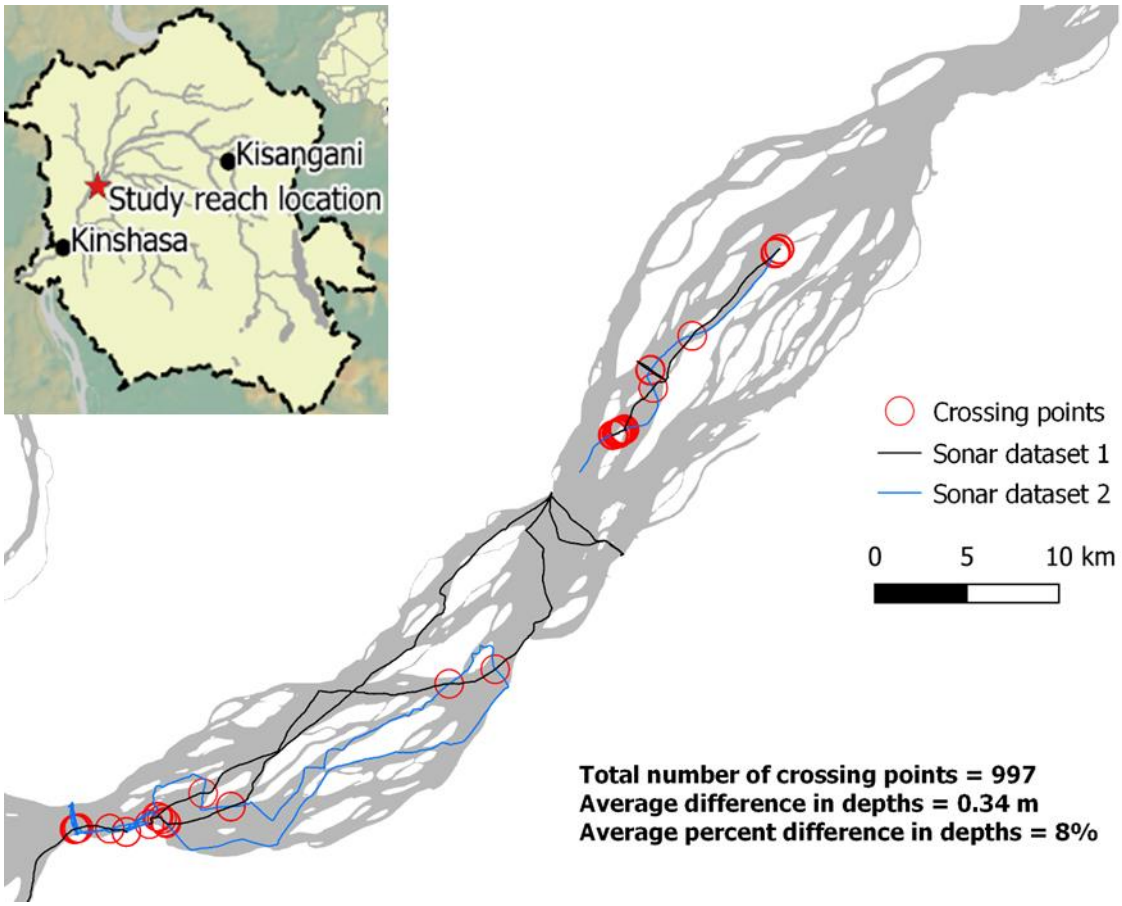

Fig. A-7. Verification of sonar data through comparison of crossing points obtained on high resolution study reach.

A.4 WSE Measurement Omitted from 2019 WSE Results

The static GNSS WSE measurement at chainage 620 km, shown in Fig. A-8, was identified as erroneous for reasons described below.

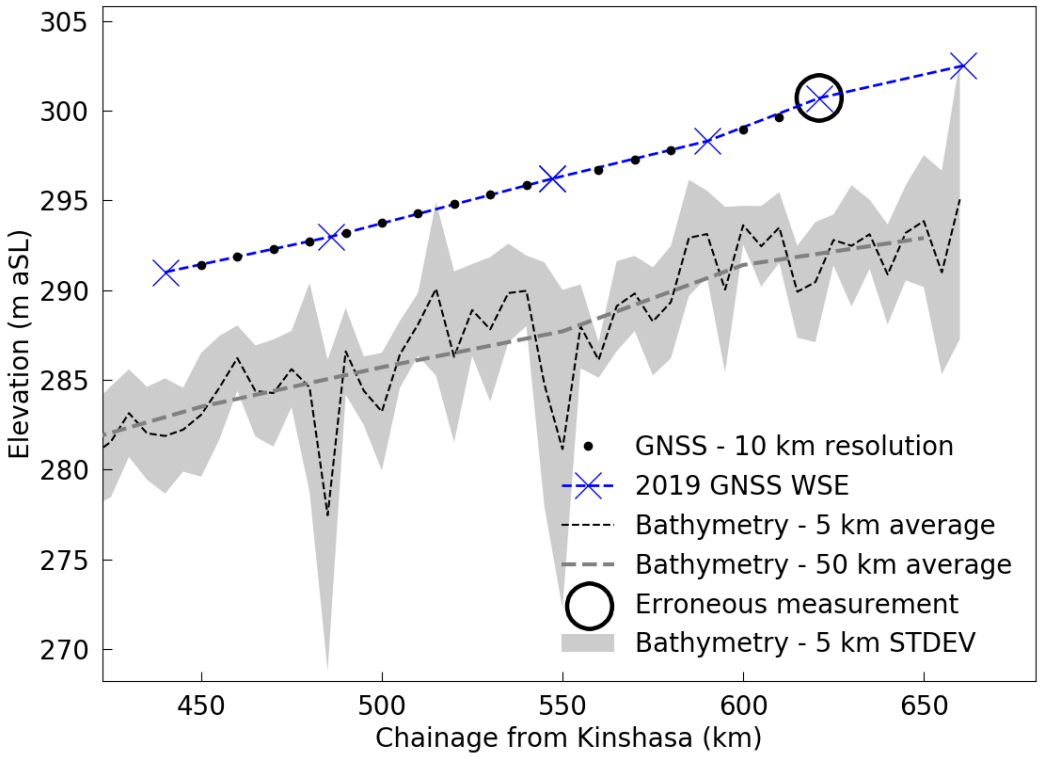

Fig. A-8. Longitudinal plot showing the static GNSS WSE measurement identified as erroneous

The raw measurements are shown in Table A-1. No outliers are apparent, the four measurements give highly consistent values.

Table A-1. Raw GNSS measurements taken at chainage 620 km

ID	X	Y	WSE
cp_1109	166771.784	-22728.592	300.711
cp_1110	166772.825	-22728.845	300.667
cp_1111	166772.909	-22728.85	300.7
cp_1112	166772.68	-22728.754	300.714
		Average	300.698
		Std Dev	0.019

The measurement shows a marked break in water surface slope: at 620–660 km, WSS is 4.5 cm/km, then, between 590 and 620 km, the WSS steepens to 7.7 cm/km. There are no obvious morphological features that might explain the slope break, such as width constrictions, confluences, or changes in bed slope. Since the slope variability is the result of measurements at one spatial location only (chainage 620 km), all other available WSE measurements were reviewed to obtain verification of the slope variability. These are shown in Fig. A-9, and consist of 2017 in-situ GNSS measurements and ENVISAT satellite altimetry from two closely spaced virtual stations (VS).

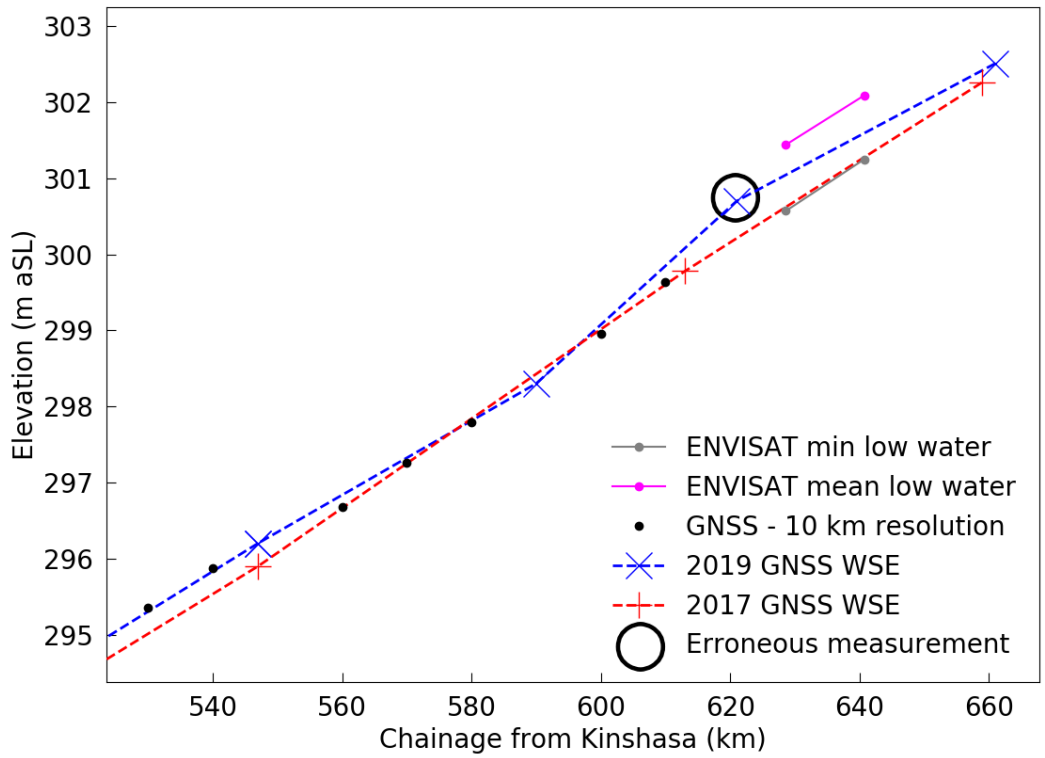

Fig. A-9. Comparison of 2019 in-situ WSEs with 2017 in-situ WSEs and ENVISAT altimetry

The WSS of 4.5 cm/km has been checked against other slope estimates along this reach (between 620 and 660 km) during low water conditions as follows:

- The mean and minimum values for low water season (July and August) of two ENVISAT virtual gauging stations, when paired to calculate WSS give: 5.9 cm/km for the mean values, and 6.2 cm/km for the minimum values.
- The 2017 static GNSS WSP gives a slope value along this reach of 5.4 cm/km.

From this review, neither the altimetry nor the 2017 in-situ GNSS WSE measurements provide any evidence of slope variability. The measurement is therefore deemed to be erroneous.

Appendix B. Chapter 5 Appendices

B.1 Example of SAGA Raster Expand and Shrink Spatial Calculation

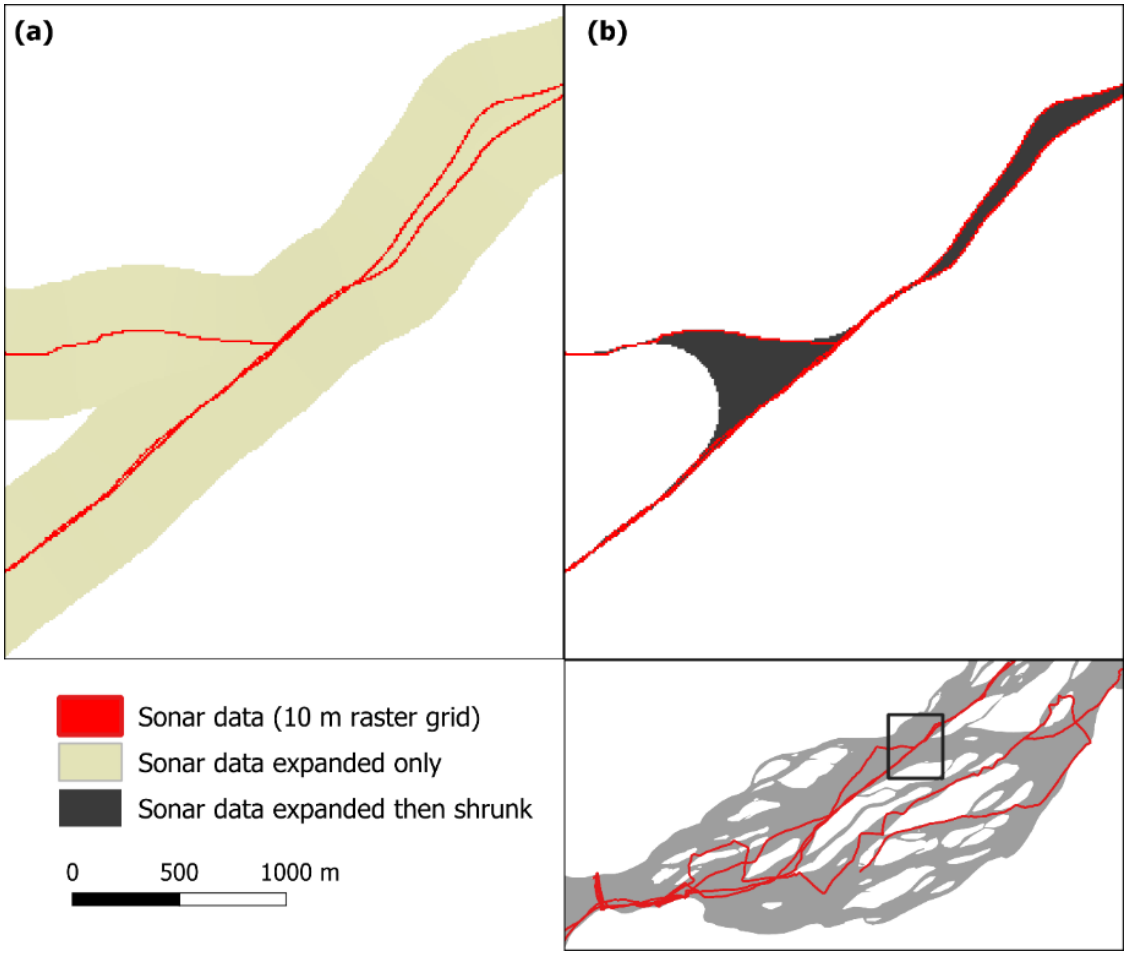

Fig. B-1: SAGA expand and shrink algorithm applied to a section of the raw sonar data: (a) Extent of raster after expansion only; (b) extent of raster grid after subsequent shrinking, holes and corners remain filled but linear edges are shrunk back to their original, providing a suitable interpolation extent.

B.2 Experimental Application of Different Interpolation Methods

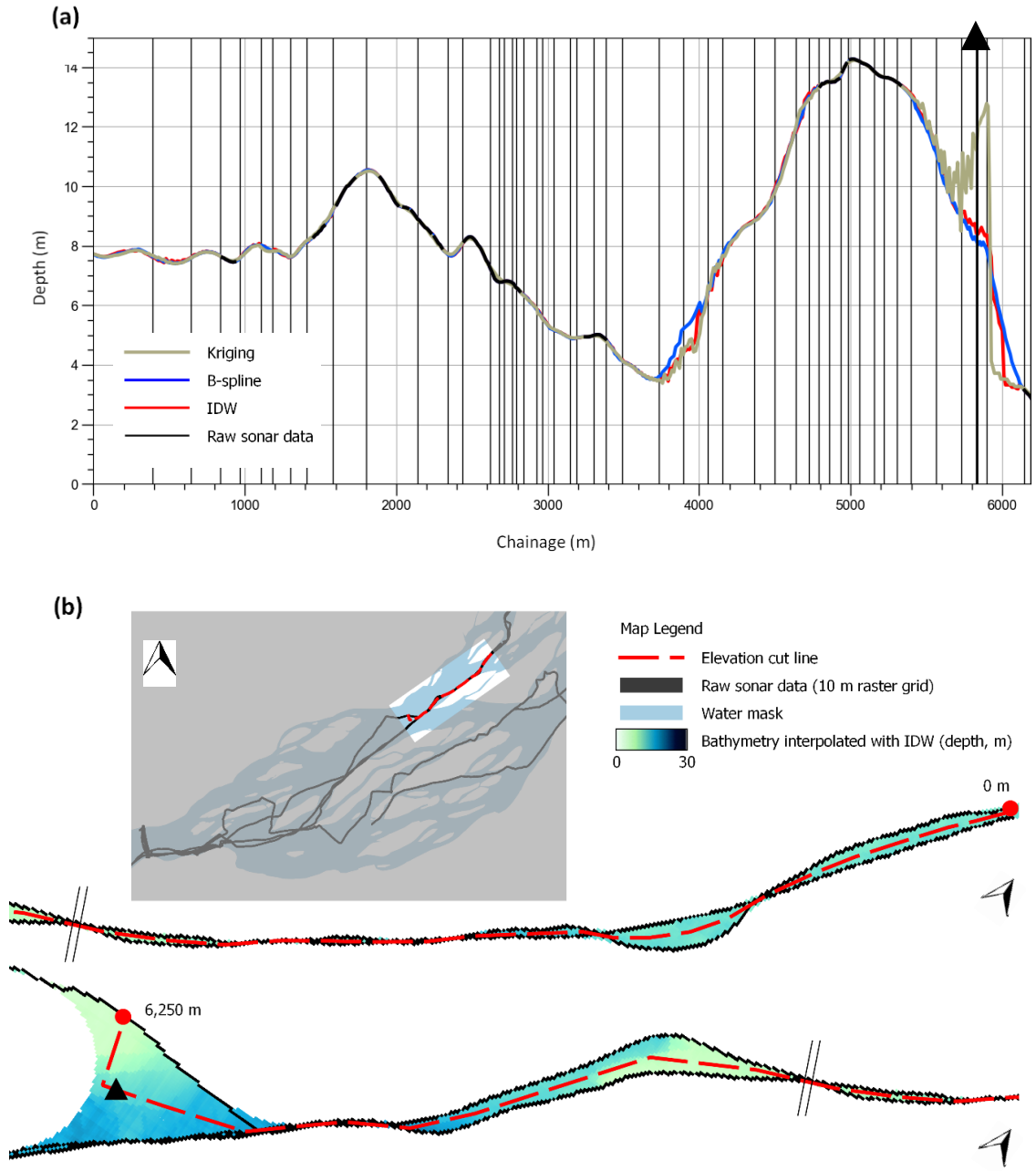

Fig. B-2: Comparison of Interpolation methods applied to a test section of sonar data: (a) plotted results of ordinary kriging, B-Spline, and inverse distance weighting (IDW), along with raw sonar data; (b) map of sonar data test section showing location of elevation cut line used to extract values plotted in (a). Black triangles mark the same location on the plot and the map.

Each method was found to produce similar results with one exception: the ordinary kriging method diverged considerably where the interpolated grid cells are furthest from the sonar, showing a large vertical drop and notable noise. Interrogation of

the raw bathymetry showed there to be no physical reason for the prediction of the vertical drop, and it may be a result of the input parameters and variogram model selected, which were set to the default values.

B.3 Example Interpolation Results of Sonar Data with and without an Interpolation Extent

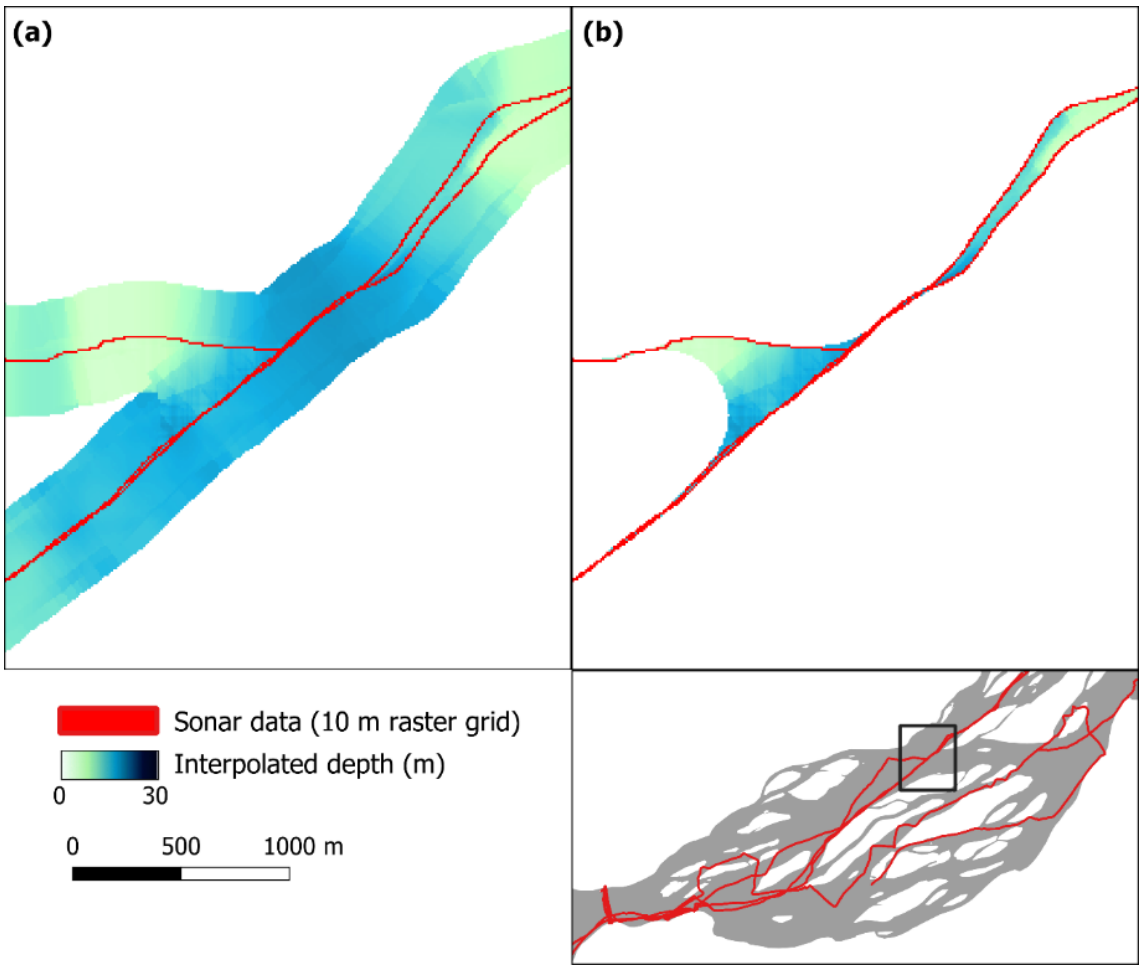

Fig. B-3: Illustration of IDW algorithm applied to a section of the raw sonar data: (a) without an interpolation extent applied (b) with interpolation extent applied.

B.4 Example estimated residual depth calculation procedure

Consider a depth estimation polygon that contains a hypothetical 1000 m wide channel with a mean channel depth of 7 m. The channel is 16 m deep across 250 m of the channel width, and is 4 m deep across the remaining 750 m of channel. Sonar data is available for the 16 m deep section, leaving the 4 m deep section to be estimated. The mean channel depth, $\overline{d}$ is calculated correctly as 7 m.

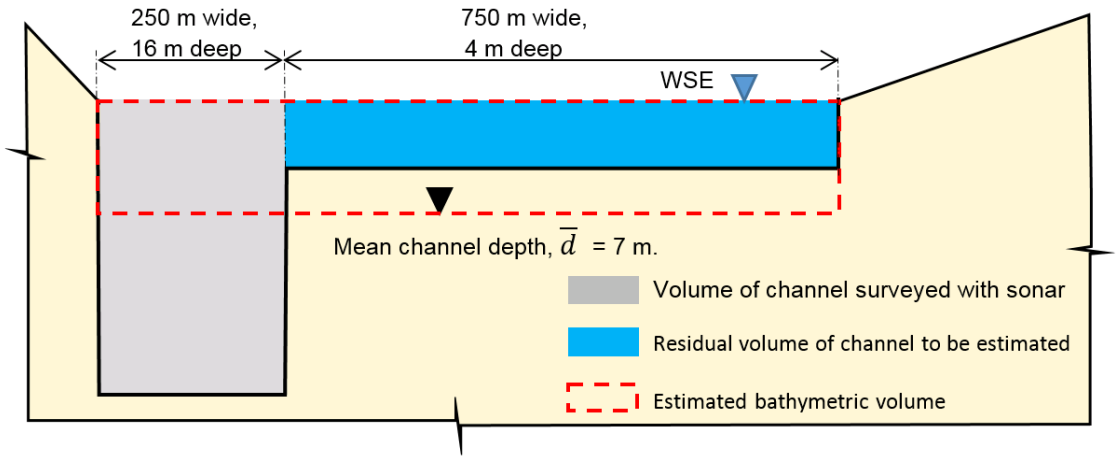

Fig. B-4: Hypothetical Channel cross section within a depth estimation polygon

If the mean depth, $\overline{d}$ is adopted directly to estimate the un-surveyed portion of bathymetry, it will give a spurious result, and in this case result in an overestimation of depth (i.e. 7 m instead of 4 m). Instead, the estimated bathymetric volume, V resulting from the calculated mean depth is conserved, and a residual volume, V_R is calculated by subtracting the sonar volume, V_S from V. An estimated residual depth, d_R can then be calculated by dividing V_R by the residual plan area, P_R. The calculation steps are presented below.

1. Mean channel depth, $\overline{d}$ is estimated using the re-arranged version of manning's formula (Chow, 1959) and the wide channel approximation (i.e. hydraulic radius is equal to flow depth):

$$\overline{d} = \left(\frac{Qn}{ws^{1/2}}\right)^{3/5} \qquad \text{Eq. 5-2}$$

2. Estimated bathymetric volume, V is calculated from the polygon length, l (2 km here), $\overline{d}$ and w:

$$V = lw\overline{d} = 2000 \times 1000 \times 7 = 14 \times 10^6\ m^3 \qquad \text{Eq. 5-3}$$

3. A residual bathymetric volume, V_R is calculated from volume of interpolated sonar, V_S and V:

$$V_R = V - V_S = 14 - 8 = 6 \times 10^6\, m^3 \quad \text{Eq. 5-4}$$

(In this example V_S is equal to $2000 \times 250 \times 16 = 8 \times 10^6\, m^3$, but is normally obtained from the interpolated sonar raster data using GIS).

4. A corresponding residual channel plan area, P_R is calculated from the plan area of interpolated sonar, P_S and the total channel plan area P:

$$P_R = P - P_S = 2 \times 10^6 - 5 \times 10^5 = 1.5 \times 10^6 \quad \text{Eq. 5-5}$$

(In this example, $P = 2000 \times 1000 = 2 \times 10^6\, m^2$; and $P_s = 2000 \times 250 = 5 \times 10^5\, m^2$, but are normally obtained from the interpolated sonar raster data and the water mask using GIS).

5. Residual depth, d_R is calculated from, V_R and P_R:

$$d_R = V_R / P_R = 6 \times 10^6 / 1.5 \times 10^6 = \mathbf{4\ m} \quad \text{Eq. 5-6}$$

B.5 Channel thread centrelines

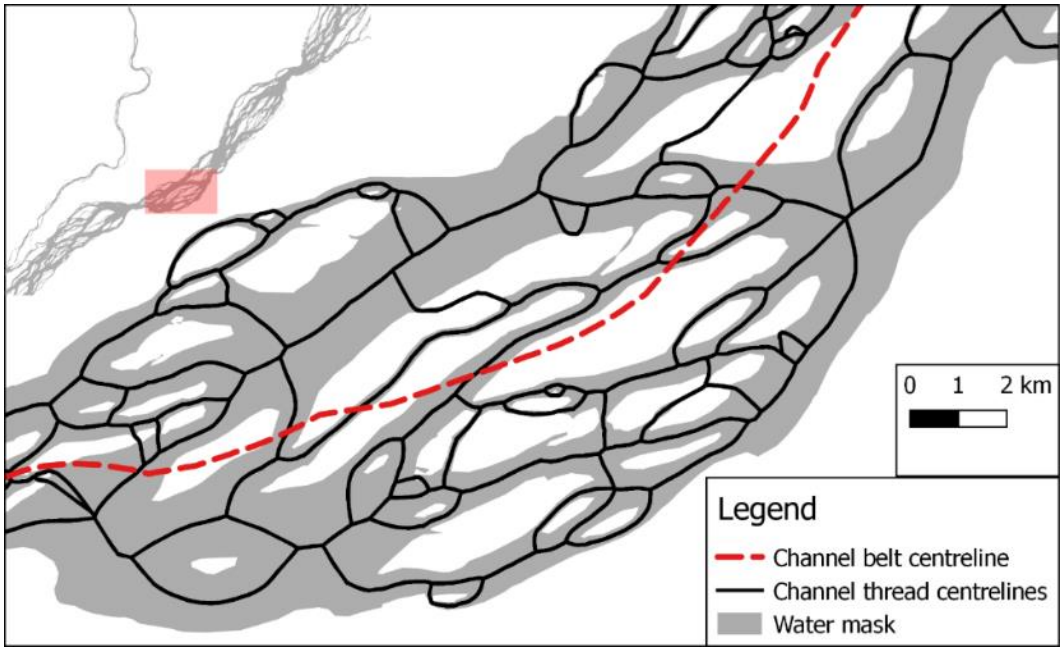

Fig. B-5: Channel thread centrelines generated from Voronoi tessellations. Many of these centrelines produce physically unrealistic flow paths.

B.6 Hydraulic Model velocity predictions with LISFLOOD-FP

Both models are expected to produce approximately the same velocity, as they have been set up with the same parameters: DEM, discharge, boundary conditions, are all the same. Both models were calibrated separately by adjusting the roughness parameter (manning's n) to match the modelled water surface elevation (WSE) to observed values. Water surface profiles for both calibrated models are plotted in Fig. B-6, showing a max local variation in WSE of 0.25 m. As LISFLOOD uses the local inertial approximation, HEC-RAS models were run using both the full SWE formulation, and a diffusive wave formulation, which verified that the use of an approximation to the SWE has negligible impact on model results (this is expected given the flow conditions; a Froude number of 0.12 was computed for the mainstem middle reach in Chapter 4).

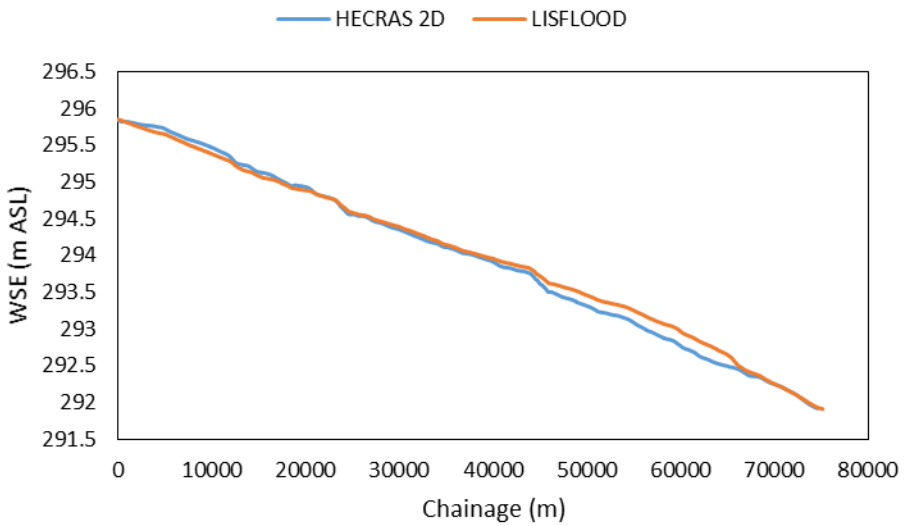

Fig. B-6: Water surface profiles of LISFLOOD-FP and HEC-RAS models

Modelled depth averaged velocities were obtained from HEC-RAS routinely using the RAS mapper utility. LISFLOOD-FP depth averaged velocities were extracted by computing the velocity magnitude from the square root of the sum of the squares of the x and y velocity components (V_x and V_y) that LISFLOOD-FP outputs in raster format. V_x and V_y values were extracted along the line of the ADCP transect by using a polygon which was sufficiently wide to sample one row of grid cells across the channel only, an example is shown in Fig. B-7.

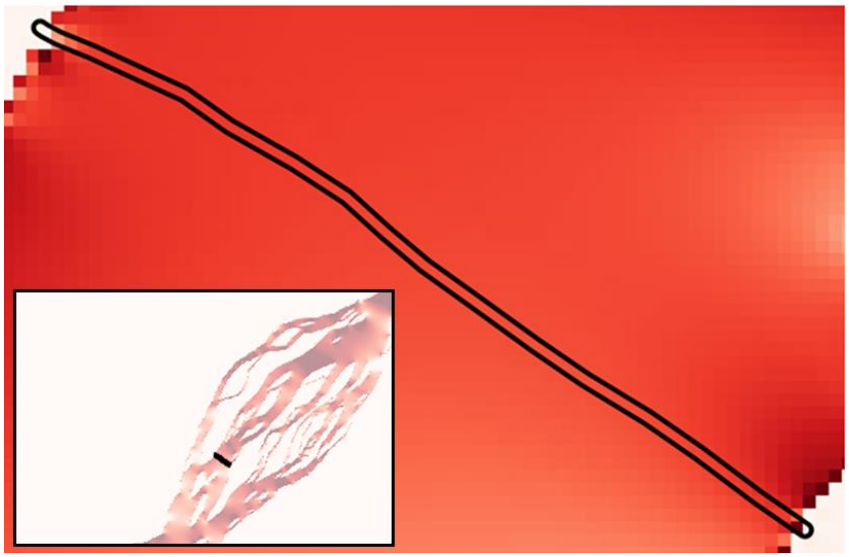

Fig. B-7: Polygon used to extract zonal statistics from velocity grid files at Transect 2

The observed and modelled depth averaged velocities across the channel at each of the four ADCP transects are plotted in Fig. B-8, and mean channel velocities are summarised in Table B-1.

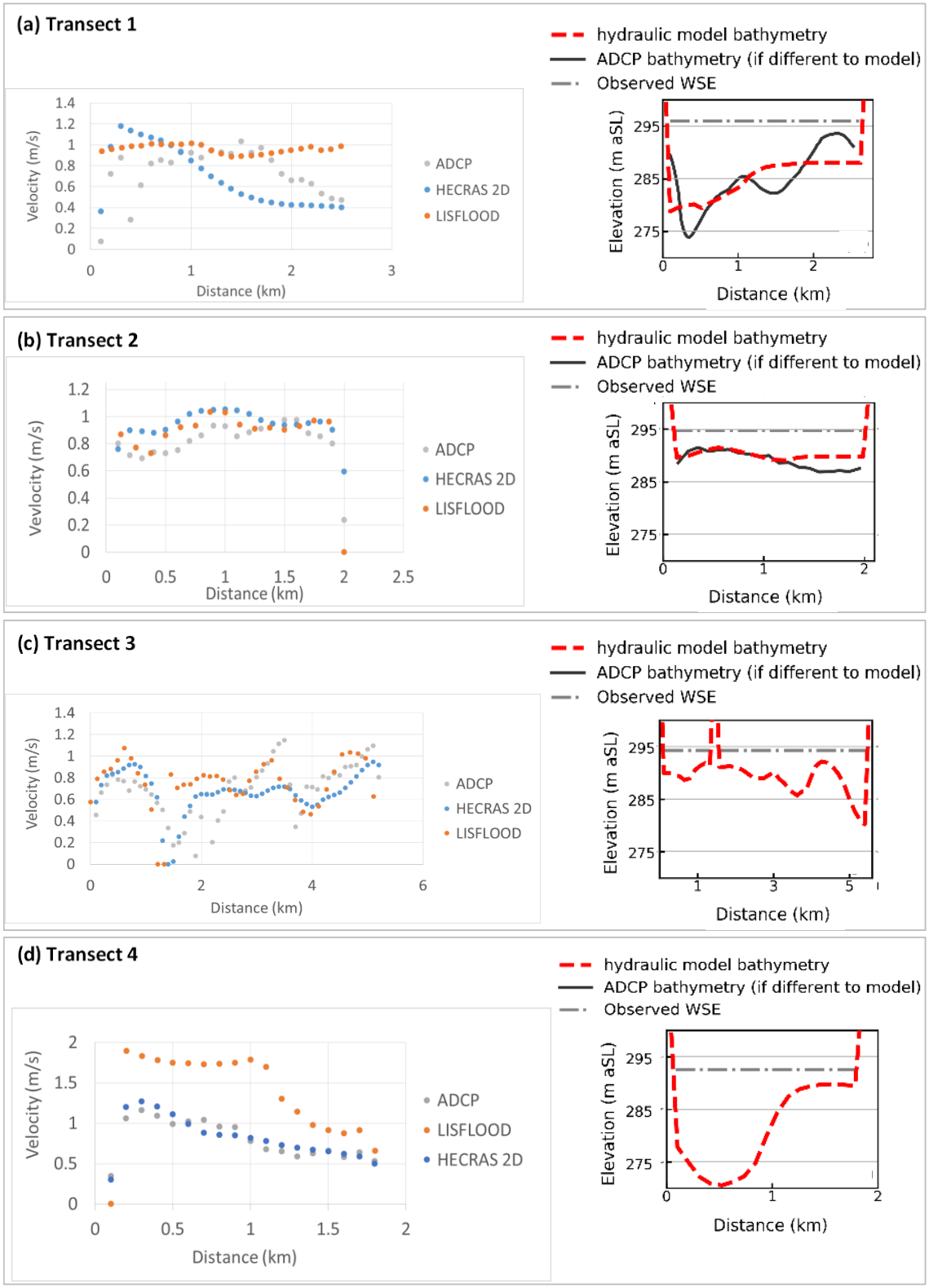

Fig. B-8: Initial LISFLOOD-FP model verification at each ADCP transect. Modelled cross sections shown on right hand side, along with ADCP cross sections if different to modelled.

Table B-1. Summary of ADCP and modelled mean channel velocities at each transect

Transect number	Mean channel velocity (m/s)		
	ADCP	HEC-RAS	LISFLOOD
1	0.77	0.74	0.96
2	0.87	0.99	0.86
3	0.82	0.83	0.75
4	0.96	0.99	1.36

From these results, the following observations are made:

- A small difference such as that observed at Transect 3 is potentially explained by differences in the model structures or numerical schemes, but the large differences at transects 1 and 4 are not.
- The close match between the ADCP and HEC-RAS depth averaged velocities at transect 4 in particular suggests that the velocities derived from the LISFLOOD-FP model are erroneous here, and may also be erroneous elsewhere, although it is less clear at other transects. In addition, the observed discharge (Q) and cross sectional area of flow (A) are known to be correctly represented here in both models. Given that mean channel velocity, $V = Q/A$, if Q is correct and A is correct, it is unclear how there can be a large error in V.
- Differences in WSE are at their maximum 0.25 m, which is less than 5% of a 6 m typical depth of flow. Therefore large velocity differences do not result from differences in WSE.
- For clarification, note that differences between the ADCP and model velocities are expected at transect 1 and 2, as the model bathymetry is different to the observed at these sections.

Based on these observations, it was decided to proceed with using HEC-RAS-2D for the BM hydraulic validation, given the reliance on depth averaged velocity predictions for assessing the performance of the BM. The explanation for the errors in the velocities derived from the LISFLOOD-FP model remain unknown. It is important to note that there are no commensurate errors in modelled WSE, which suggest that the error is specific to the velocity output grids or their subsequent post-processing to derive velocity magnitude

Appendix C. Chapter 6 Appendices

C.1 Estimate of error arising from neglecting WSP variations

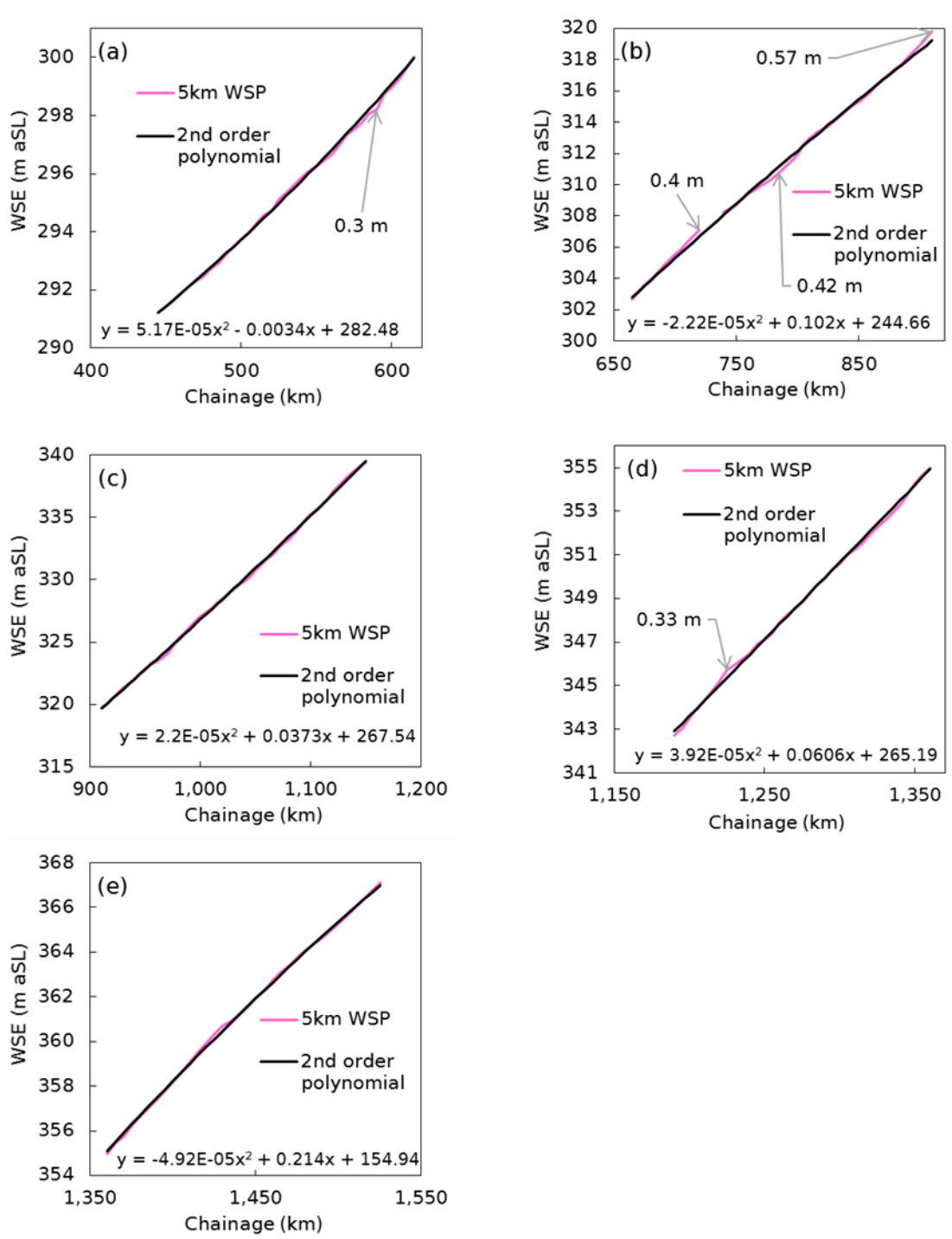

Fig. C-1. 5km resolution observed WSPs along the multichannel CMR, each ~200 km sub-reach has been resampled at ~70 km intervals and a second order polynomial regression applied to the resulting 70 km resolution points. WSP variations that deviate by ≥0.3 m from the regression are labelled with their maximum deviation.

C.2 Flood extents resulting from BM plus MERIT hydraulic model, prior to removal of irrelevant inundated areas of floodplain.

Fig. C-2 shows the modelled water extent during low flow conditions prior to removal of irrelevant inundated areas of floodplain. The DEM elevations of these inundated areas disconnected from the mainstem are below the modelled downstream fixed WSE boundary condition value that was observed and occupy the Sangha river channel and an area of its floodplain.

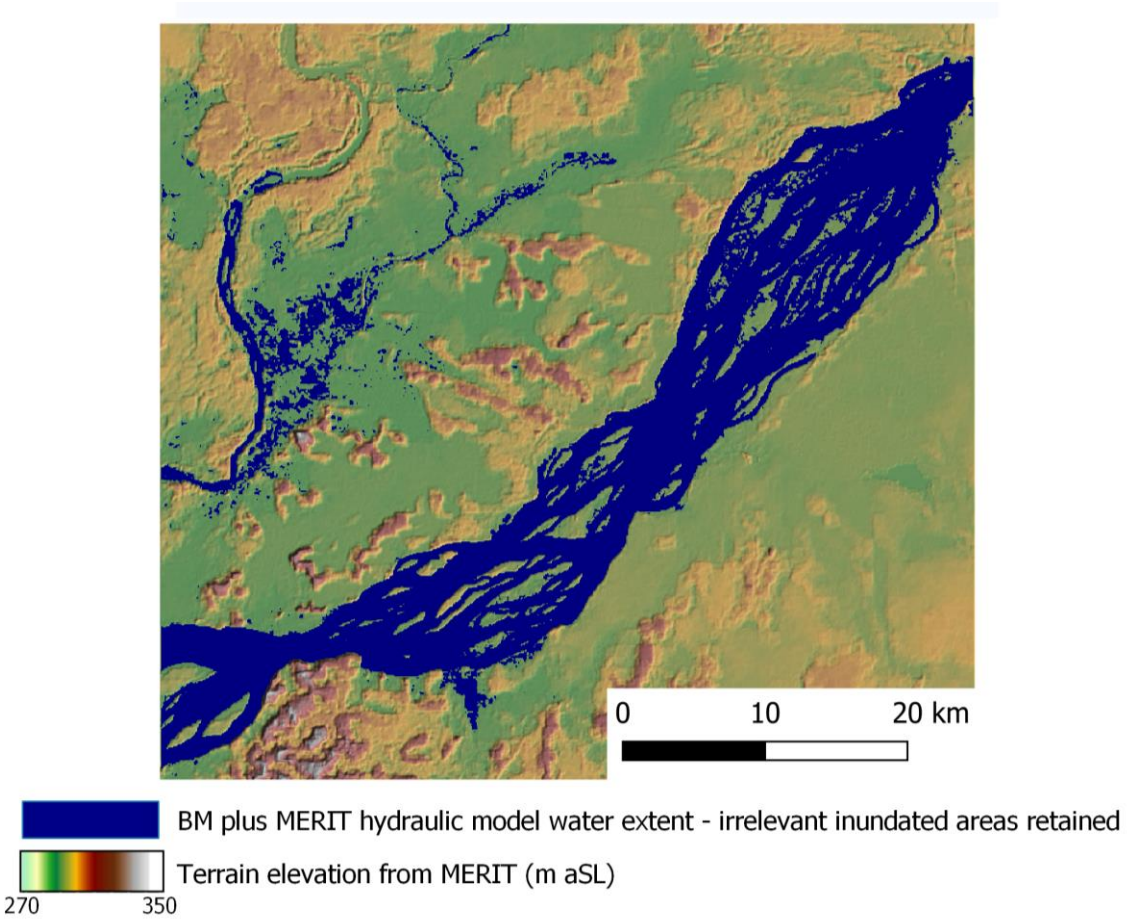

Fig. C-2. Water extents resulting from BM plus MERIT hydraulic model, prior to removal of irrelevant inundated areas of floodplain. Steady state simulation of observed low flow conditions during 2017 fieldwork.

C.3 Modelled water depths mapped for model XSV-SR

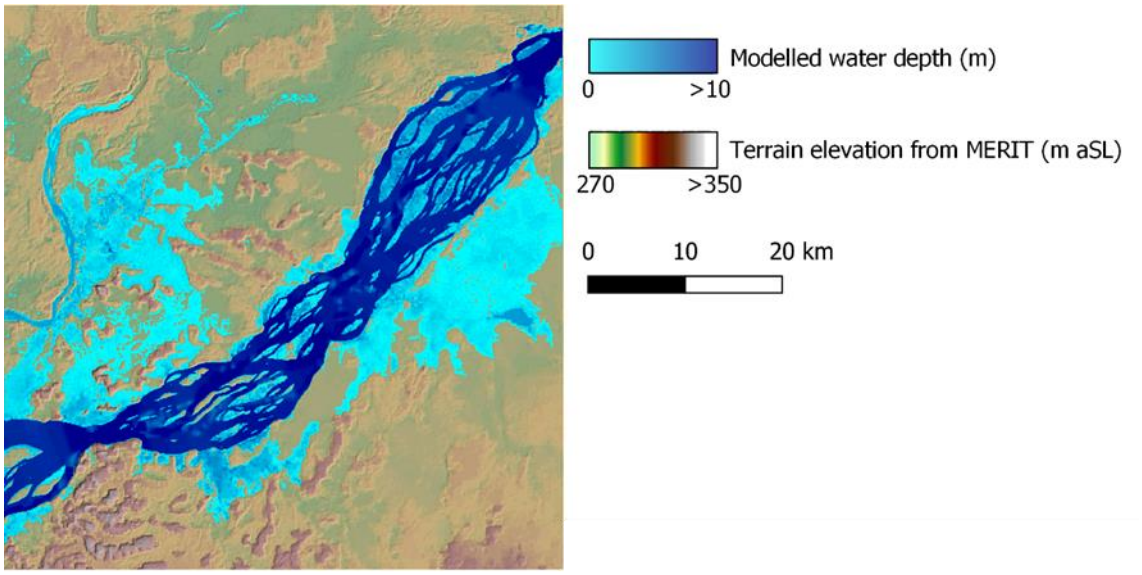

Fig. C-3. Maximum modelled water depths resulting from unsteady simulations when floodplain and island terrain represented with MERIT DEM: model XSV-SR.

C.4 Downstream boundary sensitivity check

Experiment XSV unsteady model runs were all carried out using the same downstream boundary condition: a *Q–H* boundary condition. Given the high level of downstream control (i.e. highly subcritical flow) exhibited by the CMR, such a boundary condition may act to constrain modelled WSEs to an extent that would not be seen in larger scale hydrodynamic models of the CMR. The downstream boundary is likely to be at Kinshasa; the only location at which detailed information relating discharge to WSE is available. Therefore, a more likely scenario within the multichannel CMR, and more generally for large river systems, is for modelled river reaches to be several hundred kilometres away from detailed *Q–H* information. Nearby information used to constrain / calibrate the model is likely to comprise monthly time series WSE measurements from satellite altimetry such as ENVISAT, spaced at 70 intervals along the river on average.

To confirm that a *Q–H* boundary in relatively close proximity to modelled WSEs is not effectively dampening the effects of bathymetric misrepresentation (specifically the removal of cross-sectional depth variability), additional model runs for experiment XSV were executed, with a normal depth boundary condition used. The normal depth slope of 3.7 cm/km was used for both models, the derivation of this slope value is described in subsection 6.3.3. Results are shown in Fig. C-4.

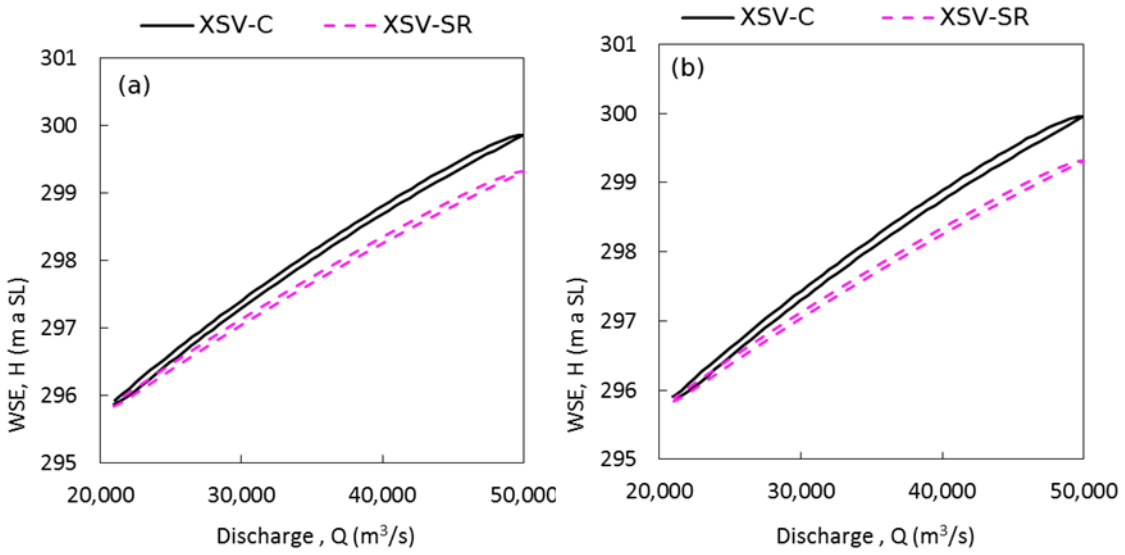

Fig. C-4: Effect of downstream boundary condition on magnitude of WSE difference between Q–H curves: (a) Q–H boundary condition used; (b) normal depth boundary condition used. MERIT DEM used to represent floodplain and island elevations in all model runs.

The results show that use of normal depth instead of a *Q*–*H* boundary increases the peak magnitude of the WSE difference by only ~0.1 m.

References

Akkermans, T., Wim, T. and Van Lipzig, N.P.M. 2013. The Regional Climate Impact of a Realistic Future Deforestation Scenario in the Congo Basin. *Journal of Climate*. **27**, pp.2714–2734.

Alho, P. and Aaltonen, J. 2008. Comparing a 1D hydraulic model with a 2D hydraulic model for the simulation of extreme glacial outburst floods. *Hydrological Processes*. **22**, pp.1537–1547.

Alin, S.R., Rasera, M.D.F.F.L., Salimon, C.I., Richey, J.E., Holtgrieve, G.W., Krusche, A. V. and Snidvongs, A. 2011. Physical controls on carbon dioxide transfer velocity and flux in low-gradient river systems and implications for regional carbon budgets. *Journal of Geophysical Research: Biogeosciences*. **116**(1).

Allan, J.D. and Castillo, M.M. 2007. *Stream Ecology: Structure and function of running waters* [Online]. Springer Netherlands. Available from: https://books.google.co.uk/books?id=4tDNEFcQh7IC.

De Almeida, G.A.M. and Bates, P. 2013. Applicability of the local inertial approximation of the shallow water equations to flood modeling. *Water Resources Research*. **49**(8), pp.4833–4844.

Aloysius, N. and Saiers, J. 2017. Simulated hydrologic response to projected changes in precipitation and temperature in the Congo River basin. , pp.4115–4130.

Alsdorf, D., Beighley, E., Laraque, A., Lee, H., Tshimanga, R., O'Loughlin, F., Mahe, G., Dinga, B., Moukandi, G. and Spencer, R.G.M. 2016. Opportunities for hydrologic research in the Congo Basin. *Reviews of Geophysics*. **54**(2), pp.378–409.

Alsdorf, D.E., Melack, J.M., Dunne, T., Mertes, L.A.K., Hess, L.L. and Smith, L.C. 2000. Interferometric radar measurements of water level changes on the Amazon flood plain. *Nature*. **404**(6774), pp.174–177.

Alsdorf, D.E., Rodriguez, E. and Lettenmaier, D.P. 2007. Measuring surface water from space. *Reviews of Geophysics*. **45**(2), pp.1–24.

Altenau, E.H., Pavelsky, T.M., Bates, P.D. and Neal, J. 2017a. The effects of spatial resolution and dimensionality on modeling regional-scale hydraulics in a multichannel river. *Water Resources Research*. **53**(2), pp.1683–1701.

Altenau, E.H., Pavelsky, T.M., Moller, D., Lion, C., Pitcher, L.H., Allen, G.H., Bates, P.D., Calmant, S., Durand, M. and Smith, L.C. 2017b. AirSWOT measurements of river water surface elevation and slope: Tanana River, AK. *Geophysical Research Letters*. **44**(1), pp.181–189.

Amsler, M.L. and Garcia, M.H. 1997. Sand-dune geometry of large rivers during floods — discussion. *Journal of Hydraulic Engineering*. **123**, pp.582–585.

Andreadis, K.M., Clark, E.A., Lettenmaier, D.P. and Alsdorf, D.E. 2007. Prospects for river discharge and depth estimation through assimilation of swath-altimetry into a raster-based hydrodynamics model. *Geophysical Research Letters*. **34**(10), pp.1–5.

Arcement, G.J. and Schneider, V.R. 1984. *Guide for Selecting Manning's Roughness Coefficients for Natural Channels and Flood Plains - Metric Version.* [Online]. Available from: https://static1.squarespace.com/static/55c211c8e4b06ea5799e6c03/t/5602fc54e4b01dadee166e55/1443036244638/GuideForSelectingManningsRoughnessCoefficients.pdf.

Ashworth, P.J. and Lewin, J. 2012. How do big rivers come to be different? *Earth-Science Reviews*. **114**(1–2), pp.84–107.

Di Baldassarre, G. and Montanari, A. 2009. Uncertainty in river discharge observations: A quantitative analysis. *Hydrology and Earth System Sciences*. **13**(6), pp.913–921.

Di Baldassarre, G., Montanari, A., Lins, H., Koutsoyiannis, D., Brandimarte, L. and Blschl, G. 2010. Flood fatalities in Africa: From diagnosis to mitigation. *Geophysical Research Letters*. **37**(22), pp.2–6.

Baran, S., Hemri, S. and El Ayari, M. 2019. Statistical Postprocessing of Water Level Forecasts Using Bayesian Model Averaging With Doubly Truncated Normal Components. *Water Resources Research*. **55**(May), pp.3997–4013.

Baronas, J.J., Stevenson, E.I., Hackney, C.R., Darby, S.E., Bickle, M.J., Hilton, R.G., Larkin, C.S., Parsons, D.R., Myo Khaing, A. and Tipper, E.T. 2020. Integrating Suspended Sediment Flux in Large Alluvial River Channels: Application of a Synoptic Rouse-Based Model to the Irrawaddy and Salween Rivers. *Journal of Geophysical Research: Earth Surface*. **125**(9), pp.1–21.

Bastviken, D., Tranvik, L.J., Downing, J.A., Crill, P.M. and Enrich-Prast, A. 2011.

Freshwater methane emissions offset the continental carbon sink. *Science*. **331**(6013), p.50.

Bates, P.D., Horritt, M.S. and Fewtrell, T.J. 2010. A simple inertial formulation of the shallow water equations for efficient two-dimensional flood inundation modelling. *Journal of Hydrology*. **387**(1–2), pp.33–45.

Bates, P.D., Neal, J., Alsdorf, D. and Schumann, G.J.P. 2014. Observing Global Surface Water Flood Dynamics. *Surveys in Geophysics*. **35**(3), pp.839–852.

Bates, P.D. and De Roo, A.P.J. 2000. A simple raster-based model for flood inundation simulation. *Journal of Hydrology*. **236**(1–2), pp.54–77.

Baugh, C.A., Bates, P.D., Schumann, G.J.P. and Trigg, M.A. 2013. SRTM vegetation removal and hydrodynamic modeling accuracy. *Water Resources Research*. **49**(9), pp.5276–5289.

Becker, M., Santos, J., Calmant, S., Robinet, V., Linguet, L. and Seyler, F. 2014. Water Level Fluctuations in the Congo Basin Derived from ENVISAT Satellite Altimetry. *Remote Sensing*. **6**, pp.9340–9358.

Bernhofen, M. V., Whyman, C., Trigg, M.A., Sleigh, P.A., Smith, A.M., Sampson, C.C., Yamazaki, D., Ward, P.J., Rudari, R., Pappenberger, F., Dottori, F., Salamon, P. and Winsemius, H.C. 2018. A first collective validation of global fluvial flood models for major floods in Nigeria and Mozambique. *Environmental Research Letters*. **13**(10).

Bertuzzo, E. and Mari, L. 2017. Hydrology, water resources and the epidemiology of water-related diseases. *Advances in Water Resources*. **108**, pp.329–331.

Best, J.L. and Ashworth, P.J. 1997. Scour in large braided rivers and the recognition of sequence stratigraphic boundaries [7]. *Nature*. **387**(6630), pp.275–277.

Betsholtz, A. and Nordlöf, B. 2017. *Potentials and limitations of 1D, 2D and coupled 1D-2D flood modelling in HEC-RAS: A case study on Höje river*.[Online] Lund University. Available from: https://lup.lub.lu.se/luur/download?func=downloadFile&recordOId=8904721&fileOId=8904723.

Biancamaria, S., Bates, P.D., Boone, A. and Mognard, N.M. 2009. Large-scale coupled hydrologic and hydraulic modelling of the Ob river in Siberia. *Journal of Hydrology*. **379**(1–2), pp.136–150.

Biancamaria, S., Lettenmaier, D.P. and Pavelsky, T.M. 2016. The SWOT Mission and Its Capabilities for Land Hydrology. *Surveys in Geophysics*. **37**(2), pp.307–337.

Bierkens, M.F.P. 2015. Global hydrology 2015: State, trends, and directions. *Water Resources Research*. **51**(7), pp.4923–4947.

Birkett, C.M., Mertes, L.A.K., Dunne, T., Costa, M.H. and Jasinski, M.J. 2002. Surface water dynamics in the Amazon Basin: Application of satellite radar altimetry. *Journal of Geophysical Research Atmospheres*. **107**(20).

Birkinshaw, S.J., Moore, P., Kilsby, C.G., O'Donnell, G.M., Hardy, A.J. and Berry, P.A.M. 2014. Daily discharge estimation at ungauged river sites using remote sensing. *Hydrological Processes*. **28**(3), pp.1043–1054.

Birkinshaw, S.J., O'Donnell, G.M., Moore, P., Kilsby, C.G., Fowler, H.J. and Berry, P.A.M. 2010. Using satellite altimetry data to augment flow estimation techniques on the Mekong River. *Hydrological Processes*. **24**(26), pp.3811–3825.

Bjerklie, D.M., Birkett, C.M., Jones, J.W., Carabajal, C., Rover, J.A., Fulton, J.W. and Garambois, P. 2018. Satellite remote sensing estimation of river discharge : Application to the Yukon River Alaska. *Journal of Hydrology*. **561**(February), pp.1000–1018.

Bjerklie, D.M., Dingman, S.L., Vorosmarty, C.J., Bolster, C.H. and Congalton, R.G. 2003. Evaluating the potential for measuring river discharge from space. *Journal of Hydrology*. **278**(1–4), pp.17–38.

BMT WBM 2016. *TUFLOW User Manual* [Online]. Available from: https://www.tuflow.com/Download/TUFLOW/Releases/2016-03/AA/Doc/TUFLOW Manual.2016-03-AA.pdf.

Bonnema, M.G., Sikder, S., Hossain, F., Durand, M., Gleason, C.J. and Bjerklie, D.M. 2016. Benchmarking wide swath altimetry-based river discharge estimation algorithms for the Ganges river system. *Water Resources Research*. **52**(4), pp.2439–2461.

Bonnerjee, S., Cann, A., Koethe, H., Lammie, D., Lieven, G., Muskatirovic, J., Ndala, B., Pauli, G. and White, I. 2009. Inland Waterborne Transport: Connecting Countries *In*: *The United Nations World Water Development Report 3: Water in a Changing World* [Online]. UNESCO. Available from: https://unesdoc.unesco.org/ark:/48223/pf0000181794.

Borges, A. V, Darchambeau, F., Teodoru, C.R., Marwick, T.R., Tamooh, F., Geeraert,

N., Omengo, F.O., Guérin, F., Lambert, T., Morana, C., Okuku, E. and Bouillon, S. 2015. Globally significant greenhouse-gas emissions from African inland waters. *Nature Geoscience*. **8**(8), pp.637–642.

Le Bouteiller, C. and Venditti, J.G. 2014. Vegetation-driven morphodynamic adjustments of a sand bed. *Geophysical Research Letters*. **41**(11), pp.3876–3883.

Bradbrook, K.F., Lane, S.N., Waller, S.G. and Bates, P.D. 2004. Two dimensional diffusion wave modelling of flood inundation using a simplified channel representation. *International Journal of River Basin Management*. **2**(3), pp.211–223.

Brakenridge, G.R. 2019. Global Active Archive of Large Flood Events. *Dartmouth Flood Observatory, University of Colorado*. [Online]. [Accessed 10 September 2019]. Available from: http://floodobservatory.colorado.edu/Archives/index.html.

Brakenridge, G.R., Nghiem, S. V., Anderson, E. and Mic, R. 2007. Orbital microwave measurement of river discharge and ice status. *Water Resources Research*. **43**(4), pp.1–16.

Bridge, J.S. 1993. The interaction between channel geometry, water flow, sediment transport and deposition in braided rivers. *Geological Society Special Publication*. **75**(75), pp.13–71.

Bristow, C.S. and Best, J.L. 1993. Braided rivers: perspectives and problems. *Braided Rivers*. **75**, pp.1–11.

Brooks, E.G.E., Allen, D.J. and Darwall, W.R.T. 2011. The status and distribution of freshwater biodiversity in Central Africa. *the IUCN red list of threatened species regional assessment*.

Brummett, R., Tanania, C., Pandi, A., Ladel, J., Munzimi, Y., Russell, A., Stiassny, M., Thieme, M., White, S. and Davies, D. 2009. Water resources, forests and ecosystem goods and services *In*: *The forests of the Congo Basin: state of the forest 2008* [Online]. Office of the European Union, Luxembourg, pp.141–158. Available from: https://hdl.handle.net/20.500.12348/1359.

Brunner, G. and Bonner, V. 1994. HEC River Analysis System (HEC-RAS). *US Army Corps of Engineers Hydrologic Engineering Center Technical Paper*. (pt 1), pp.376–380.

Brunner, G.W. 2016. HEC-RAS River Analysis System, 2D Modeling User's Manual Version 5.0. . (CPD-68A), pp.1–171.

Bultot, F. 1977. *Atlas climatique du Bassin Congolais: Atlas climatique du Bassin Zairois* [Online]. Institut National pour l'Etude Agronomique du Congo. Available from: https://books.google.co.uk/books?id=4UrnQgAACAAJ.

Bwangoy, J.R.B., Hansen, M.C., Roy, D.P., Grandi, G. De and Justice, C.O. 2010. Wetland mapping in the Congo Basin using optical and radar remotely sensed data and derived topographical indices. *Remote Sensing of Environment*. **114**(1), pp.73–86.

Caballero, I., Stumpf, R. and Meredith, A. 2019. Preliminary Assessment of Turbidity and Chlorophyll Impact on Bathymetry Derived from Sentinel-2A and Sentinel-3A Satellites in South Florida. *Remote Sensing*. **11**(6), p.645.

Calmant, S., Seyler, F. and Cretaux, J.F. 2009. Monitoring Continental Surface Waters by Satellite Altimetry. *Surveys in Geophysics*. (29), pp.247–269.

Canisius, F., Brisco, B., Murnaghan, K., Van Der Kooij, M. and Keizer, E. 2019. SAR Backscatter and InSAR Coherence for Monitoring Wetland Extent, Flood Pulse and Vegetation: A Study of the Amazon Lowland. *Remote Sensing*. **11**(6), p.720.

Carling, P., Jansen, J. and Meshkova, L. 2014. Multichannel rivers: Their definition and classification. *Earth Surface Processes and Landforms*. **39**(1), pp.26–37.

CARPE 2017. Forest Atlas of DRC: hydrographic network of the Democratic Republic of Congo. *Central Africa Regional Program for the Environment Open Data Portal*. [Online]. [Accessed 5 December 2017]. Available from: https://carpe-worldresources.opendata.arcgis.com/datasets/medd::streams?geometry=15.835%2C-1.698%2C17.57%2C-1.217.

Castellarin, A., Di Baldassarre, G., Bates, P.D. and Brath, A. 2009. Optimal cross-sectional spacing in preissmann scheme 1D hydrodynamic models. *Journal of Hydraulic Engineering*. **135**(2), pp.96–105.

Centre for Ecology and Hydrology 2019. The UK Gauging Station Network. *National River Flow Archive*. [Online]. [Accessed 14 October 2019]. Available from: https://nrfa.ceh.ac.uk/uk-gauging-station-network.

Chow, V.T. 1959. *Open Channel Hydraulics*. McGraw-Hill Book Company.

CICOS 2015. VOIES NAVIGABLES. [Accessed 18 March 2019]. Available from: http://www.cicos.int/navigation-interieure/voies-navigables/.

Cloke, H.L. and Pappenberger, F. 2009. Ensemble flood forecasting: A review. *Journal*

of Hydrology. **375**(3–4), pp.613–626.

CNES 2020a. Altimery - Future Evolutions - Constellations. *Aviso+ Satellite Altimetry Data*. [Online]. [Accessed 19 August 2020]. Available from: https://www.aviso.altimetry.fr/en/techniques/altimetry/future-evolutions/constellations.html.

CNES 2019a. Altimetry: Future Evolutions. *Aviso+ Satellite Altimetry Data*. [Online]. [Accessed 9 October 2019]. Available from: https://www.aviso.altimetry.fr/techniques/altimetry/future-evolutions.html.

CNES 2020b. SWOT: Objectives and Applications. *Aviso+ Satellite Altimetry Data*. [Online]. [Accessed 13 April 2020]. Available from: https://www.aviso.altimetry.fr/missions/future-missions/swot/objectives-applications.html.

CNES 2019b. SWOT Data products. *Aviso+ Satellite Altimetry Data*. [Online]. [Accessed 9 October 2019]. Available from: https://www.aviso.altimetry.fr/missions/future-missions/swot/data-products.html.

Coe, M.T., Costa, M.H. and Soares-Filho, B.S. 2009. The influence of historical and potential future deforestation on the stream flow of the Amazon River - Land surface processes and atmospheric feedbacks. *Journal of Hydrology*. **369**(1–2), pp.165–174.

Coe, M.T., Latrubesse, E.M., Ferreira, M.E. and Amsler, M.L. 2011. The effects of deforestation and climate variability on the streamflow of the Araguaia River, Brazil. *Biogeochemistry*. **105**(1), pp.119–131.

Comptour, M., Caillon, S. and McKey, D. 2016. Pond fishing in the Congolese cuvette: a story of fishermen, animals, and water spiritsLa pêche aux étangs dans la cuvette congolaise : une histoire de pêcheurs, d'animaux et d'esprits des eaux. *Revue d'ethnoécologie*. (10), pp.0–27.

Comptour, M., Cosiaux, A., Coomes, O.T., Bader, J.C., Malaterre, P.O., Yoka, J., Caillon, S. and McKey, D. 2020. Agricultural innovation and environmental change on the floodplains of the Congo River. *Geographical Journal*. **186**(1), pp.16–30.

Conner, J.T. and Tonina, D. 2014. Effect of cross-section interpolated bathymetry on 2D hydrodynamic model results in a large river. *Earth Surface Processes and Landforms*. **39**(4), pp.463–475.

Conrad, O., Bechtel, B., Bock, M., Dietrich, H., Fischer, E., Gerlitz, L., Wehberg, J.,

Wichmann, V. and Böhner, J. 2015. System for Automated Geoscientific Analyses (SAGA) v. 2.1.4. *Geosci. Model Dev.* **8**(7), pp.1991–2007.

Costa, M.H., Botta, A. and Cardille, J.A. 2003. Effects of large-scale changes in land cover on the discharge of the Tocantins River, Southeastern Amazonia. *Journal of Hydrology*. **283**(1–4), pp.206–217.

Creech, C.T. 2014. *Coupled Sediment Yield And Sediment Transport Model To Support Navigation Planning In Northeast Brazil*.[Online] Wayne State University. Available from: http://digitalcommons.wayne.edu/oa_dissertations Recommended.

Croneborg, L.E.M. 2013. Project Information Document (Concept Stage) - Strengthening Hydro-Meteorological and Climate Services in DRC - P144712 (English). Washington, D.C. : World Bank Group. , pp.1–9. Available from: http://documents.worldbank.org/curated/en/771081468230086348/Project-Information-Document-Concept-Stage-Strengthening-Hydro-Meteorological-and-Climate-Services-in-DRC-P144712.

Crowder, D.W. and Diplas, P. 2000. Using two-dimensional hydrodynamic models at scales of ecological importance. *Journal of Hydrology*. **230**(3–4), pp.172–191.

Daraio, J.A., Weber, L.J. and Newton, T.J. 2010. Hydrodynamic modeling of juvenile mussel dispersal in a large river: the potential effects of bed shear stress and other parameters. *Journal of the North American Benthological Society*. **29**(3), pp.838–851.

Dargie, G.C., Lawson, I.T., Rayden, T.J., Miles, L., Mitchard, E.T.A., Page, S.E., Bocko, Y.E., Ifo, S.A. and Lewis, S.L. 2019. Congo Basin peatlands: threats and conservation priorities. *Mitigation and Adaptation Strategies for Global Change*. **24**(4), pp.669–686.

Dargie, G.C., Lewis, S.L., Lawson, I.T., Mitchard, E.T.A., Page, S.E., Bocko, Y.E. and Ifo, S.A. 2017. Age, extent and carbon storage of the central Congo Basin peatland complex. *Nature*.

Deltares 2018. Navigability of Port Brazaville in Congo River. *Projects*. [Online]. [Accessed 14 February 2018]. Available from: https://www.deltares.nl/en/projects/navigability-of-port-brazaville-in-congo-river/.

Demirel, M.C., Booij, M.J. and Hoekstra, A.Y. 2013. Effect of different uncertainty sources on the skill of 10 day ensemble low flow forecasts for two hydrological models. *Water Resources Research*. **49**, pp.4035–4053.

Deshmukh, R., Mileva, A. and Wu, G.C. 2018. Renewable energy alternatives to mega hydropower: A case study of Inga 3 for Southern Africa. *Environmental Research Letters*. **13**(6).

Deutsche Gesellschaft für Internationale Zusammenarbeit 2019. Improving navigation facilities in the Democratic Republic of the Congo. *Worldwide Projects*. [Online]. [Accessed 15 May 2019]. Available from: https://www.giz.de/en/worldwide/68019.html.

Dey, S., Saksena, S. and Merwade, V. 2019. Assessing the effect of different bathymetric models on hydraulic simulation of rivers in data sparse regions. *Journal of Hydrology*. **575**(July 2018), pp.838–851.

DHI Water & Environmental 2004. MIKE 21C RIVER MORPHOLOGY: A Short Description.

Domeneghetti, A., Castellarin, A., Tarpanelli, A. and Moramarco, T. 2015. Investigating the uncertainty of satellite altimetry products for hydrodynamic modelling. *Hydrological Processes*. **29**(23), pp.4908–4918.

Douglas, J.F., Gasiorek, J.M. and Swaffield, J.A. 2001. *Fluid Mechanics* Fourth Edi. Pearson.

Driscoll, D.G., Southard, R.E., Koenig, T.A., Bender, D.A. and Holmes, R.R.J. 2014. Annual exceedance probabilities and trends for peak streamflows and annual runoff volumes for the Central United States during the 2011 floods, U.S. Geological Survey Professional Paper 1798–D. . (JANUARY).

Durand, M.T., Gleason, C.J., Garambois, P., Bjerklie, D.M., Smith, L.C., Roux, H., Rodriguez, E., Bates, P.D., Pavelsky, T.M., Monnier, J., Chen, X., Di Baldassarre, G., Fiset, J.M., Flipo, N., Frasson, R.P.M., Fulton, J.W., Goutal, N., Hossain, F., Humphries, E., Minear, J.T., Mukolwe, M.M., Neal, J., Ricci, S., Sanders, B.F., Schumann, G.J.P., Schubert, J.E. and Vilmin, L. 2016. An intercomparison of remote sensing river discharge estimation algorithms from measurements of river height, width, and slope. *Water Resources Research*. **52**(6), pp.4527–4549.

Dury, G.H. 2020. Geometry of River Systems. *Britannica*. [Online], Hydraulic Geometry. Available from: https://www.britannica.com/science/river.

Duvail, S. and Hamerlynck, O. 2007. The Rufiji River flood: Plague or blessing? *International Journal of Biometeorology*. **52**(1), pp.33–42.

Eaton, B.C., Millar, R.G. and Davidson, S. 2010. Channel patterns: Braided,

anabranching, and single-thread. *Geomorphology*. **120**(3–4), pp.353–364.

Emergency Response Coordination Centre 2019. Democratic Republic of the Congo. *DG ECHO Daily Map*. [Online]. [Accessed 20 December 2019]. Available from: https://reliefweb.int/sites/reliefweb.int/files/resources/20191216_DM_DRC_Brazzaville_Floods.pdf.

Escobar, V., Delgado Arias, Sabrina Woo, L., Neumann, T., Jasinski, M., Brown, M. and Turner, W. 2015. Ice, Cloud and land Elevation Satellite-2 2nd Applications Workshop. [Accessed 14 June 2019]. Available from: https://icesat-2.gsfc.nasa.gov/sites/default/files/general_content_files/ICESat2_2ndApplicationsWorkshop_Report_Final_05August2015_0.pdf.

Espinoza, J.C., Marengo, J.A., Ronchail, J., Carpio, J.M., Flores, L.N. and Guyot, J.L. 2014. The extreme 2014 flood in south-western Amazon basin: The role of tropical-subtropical South Atlantic SST gradient. *Environmental Research Letters*. **9**(12).

Evans, E.P., Wicks, J.M., Whitlow, C.D. and Ramsbottom, D.M. 2007. The evolution of a river modelling system. *Proceedings of the Institution of Civil Engineers: Water Management*. **160**(1), pp.3–13.

Farr, T.G., Rosen, P.A., Caro, E., Crippen, R., Duren, R., Hensley, S., Kobrick, M., Paller, M., Rodriguez, E., Roth, L., Seal, D., Shaffer, S., Shimada, J., Umland, J., Werner, M., Oskin, M., Burbank, D. and Alsdorf, D. 2007. The Shuttle Radar Topography Mission. *Reviews of Geophysics*. **45**(2), p.RG2004.

Fernandez, N., Jaimes, W. and Altamiranda, E. 2010. Neuro-fuzzy modeling for level prediction for the navigation sector on the Magdalena River (Colombia). *Journal of Hydroinformatics*. **12.1**, pp.36–50.

Fielding, C.R. 2008. Sedimentology and Stratigraphy of Large River Deposits: Recognition in the Ancient Record, and Distinction from 'Incised Valley Fills'. In Large Rivers, A. Gupta (Ed.). *In*: *Large Rivers* [Online]. John Wiley & Sons, Ltd, pp.97–113. Available from: https://onlinelibrary.wiley.com/doi/abs/10.1002/9780470723722.ch7.

Figueiredo, N.M., Blanco, C.J.C. and Moraes, H.B. 2014. Forecasting navigability conditions of the Tapajós waterway — Amazon — Brazil. *2nd International Conference on Maritime Technology and Engineering*. [Online], pp.129–137. Available from: https://www.taylorfrancis.com/books/e/9780429226663.

Filizola, N., Guyot, J.L. and Guimarães, V. 2009. Measuring the discharge of the Amazon River using Doppler technology (Manacapuru, Amazonas, Brazil). *Hydrological Processes*. **23**(22), pp.3151–3156.

Fleischmann, A., Paiva, R. and Collischonn, W. 2019. Can regional to continental river hydrodynamic models be locally relevant? A cross-scale comparison. *Journal of Hydrology X*. **3**, p.100027.

Fleischmann, A., Siqueira, V., Paris, A., Collischonn, W., Paiva, R., Pontes, P., Crétaux, J.F., Bergé-Nguyen, M., Biancamaria, S., Gosset, M., Calmant, S. and Tanimoun, B. 2018. Modelling hydrologic and hydrodynamic processes in basins with large semi-arid wetlands. *Journal of Hydrology*. **561**(August 2017), pp.943–959.

Flügel, T.J., Eckardt, F.D. and Cotterill, F.P.D. 2015. The Present Day Drainage Patterns of the Congo River System and their Neogene Evolution *In*: M. J. de Wit, F. Guillocheau and M. C. J. de Wit, eds. *Geology and resource potential of the Congo Basin* [Online]. Berlin: Springer, pp.315–337. Available from: https://link.springer.com/book/10.1007/978-3-642-29482-2.

Foster, V. and Benitez, D.A. 2010. *The Democratic Republic of Congo's Infrastructure : A Continental Perspective. World Bank, Washington, DC.* [Online]. Washington, DC 20433 USA. Available from: http://hdl.handle.net/10986/27759.

Frappart, F., Calmant, S., Cauhopé, M., Seyler, F. and Cazenave, A. 2006. Preliminary results of ENVISAT RA-2-derived water levels validation over the Amazon basin. *Remote Sensing of Environment*. **100**(2), pp.252–264.

Frappart, F., Papa, F., Malbeteau, Y., León, J.G., Ramillien, G., Prigent, C., Seoane, L., Seyler, F. and Calmant, S. 2015. Surface freshwater storage variations in the Orinoco floodplains using multi-satellite observations. *Remote Sensing*. **7**(1), pp.89–110.

Frasson, R.P. de M., Wei, R., Durand, M., Minear, J.T., Domeneghetti, A., Schumann, G.J.P., Williams, B.A., Rodriguez, E., Picamilh, C., Lion, C., Pavelsky, T. and Garambois, P.-A. 2017. Automated River Reach Definition Strategies: Applications for the Surface Water and Ocean Topography Mission. *Water Resources Research*. **53**(10), pp.8164–8186.

Friedlingstein, P., Jones, M.W., O'Sullivan, M., Andrew, R.M., Hauck, J., Peters, G.P., Peters, W., Pongratz, J., Sitch, S., Le Quéré, C., Bakker, D.C.E., Canadell, J.G.,

Ciais, P., Jackson, R.B., Anthoni, P., Barbero, L., Bastos, A., Bastrikov, V., Becker, M., Bopp, L., Buitenhuis, E., Chandra, N., Chevallier, F., Chini, L.P., Currie, K.I., Feely, R.A., Gehlen, M., Gilfillan, D., Gkritzalis, T., Goll, D.S., Gruber, N., Gutekunst, S., Harris, I., Haverd, V., Houghton, R.A., Hurtt, G., Ilyina, T., Jain, A.K., Joetzjer, E., Kaplan, J.O., Kato, E., Klein Goldewijk, K., Korsbakken, J.I., Landschützer, P., Lauvset, S.K., Lefèvre, N., Lenton, A., Lienert, S., Lombardozzi, D., Marland, G., McGuire, P.C., Melton, J.R., Metzl, N., Munro, D.R., Nabel, J.E.M.S., Nakaoka, S.-I., Neill, C., Omar, A.M., Ono, T., Peregon, A., Pierrot, D., Poulter, B., Rehder, G., Resplandy, L., Robertson, E., Rödenbeck, C., Séférian, R., Schwinger, J., Smith, N., Tans, P.P., Tian, H., Tilbrook, B., Tubiello, F.N., van der Werf, G.R., Wiltshire, A.J. and Zaehle, S. 2019. Global Carbon Budget 2019. *Earth Syst. Sci. Data*. **11**(4), pp.1783–1838.

Garambois, P., Calmant, S., Roux, H., Paris, A., Monnier, J., Finaud-guyot, P., Montazem, A. and Santos da Silva, J. 2017. Hydraulic visibility : using satellite altimetry to parameterize a hydraulic model of an ungauged reach of a braided river. *Hydrological Processes*. **31**, pp.756–767.

Garambois, P.A., Larnier, K., Monnier, J., Finaud-Guyot, P., Verley, J., Montazem, A.S. and Calmant, S. 2020. Variational estimation of effective channel and ungauged anabranching river discharge from multi-satellite water heights of different spatial sparsity. *Journal of Hydrology*. **581**(September 2019), p.124409.

Garambois, P.A. and Monnier, J. 2015. Inference of effective river properties from remotely sensed observations of water surface. *Advances in Water Resources*. **79**, pp.103–120.

Gaurav, K., Sinha, R. and Panda, P.K. 2011. The Indus flood of 2010 in Pakistan: A perspective analysis using remote sensing data. *Natural Hazards*. **59**(3), pp.1815–1826.

GDAL/OGR contributors 2020. Geospatial Data Abstraction software Library.

Gerritsen, H., Goede, E.D. d., Platzek, F.W., van Kester, J.A.T.M., Genseberger, M. and Uittenbogaard, R.E. 2008. Validation Document Delft3D-FLOW - A software system for 3D flow simulations. , p.163.

Glocker, M., Landau, H., Leandro, R. and Nitschke, M. 2012. Global precise multi-GNSS positioning with trimble centerpoint RTX. *6th ESA Workshop on Satellite Navigation Technologies: Multi-GNSS Navigation Technologies Galileo's Here, NAVITEC 2012 and European Workshop on GNSS Signals and Signal*

Processing., pp.1–8.

Goff, J.A. and Nordfjord, S. 2004. Interpolation of fluvial morphology using channel-oriented coordinate transformation: A case study from the New Jersey shelf. *Mathematical Geology*. **36**(6), pp.643–658.

GRDC 2019. The Global Runoff Data Centre, 56068 Koblenz, Germany. Available from: https://www.bafg.de/GRDC/EN/Home/homepage_node.html.

Grill, G., Lehner, B., Thieme, M., Geenen, B., Tickner, D., Antonelli, F., Babu, S., Borrelli, P., Cheng, L., Crochetiere, H., Ehalt Macedo, H., Filgueiras, R., Goichot, M., Higgins, J., Hogan, Z., Lip, B., McClain, M.E., Meng, J., Mulligan, M., Nilsson, C., Olden, J.D., Opperman, J.J., Petry, P., Reidy Liermann, C., Sáenz, L., Salinas-Rodríguez, S., Schelle, P., Schmitt, R.J.P., Snider, J., Tan, F., Tockner, K., Valdujo, P.H., van Soesbergen, A. and Zarfl, C. 2019. Mapping the world's free-flowing rivers. *Nature*. **569**(7755), pp.215–221.

Grimaldi, S., Li, Y., Pauwels, V.R.N. and Walker, J.P. 2016. Remote Sensing-Derived Water Extent and Level to Constrain Hydraulic Flood Forecasting Models: Opportunities and Challenges. *Surveys in Geophysics*. **37**(5), pp.977–1034.

Guerrero, M., Re, M., Kazimierski, L.D., Menéndez, Á.N. and Ugarelli, R. 2013. Effect of climate change on navigation channel dredging of the Parana River. *International Journal of River Basin Management*. **11**(4), pp.439–448.

Gumbricht, T., Román-Cuesta, R.M., Verchot, L.V., Herold, M., Wittmann, F., Householder, E., Herold, N. and Murdiyarso, D. 2017. Tropical and Subtropical Wetlands Distribution version 2. *Center for International Forestry Research (CIFOR), V3*. [Online]. [Accessed 27 March 2020]. Available from: https://doi.org/10.17528/CIFOR/DATA.

Hamilton, S. and Lewis, W. 1990. Basin morphology in relation to chemical and ecological characteristics of lakes on the Oricono River floodplain, Venezuela. *Archiv für Hydrobiologie*. **119**(4), pp.393–425.

Hannah, D.M., Demuth, S., van Lanen, H.A.J., Looser, U., Prudhomme, C., Rees, G., Stahl, K. and Tallaksen, L.M. 2011. Large-scale river flow archives: importance, current status and future needs. *Hydrological Processes*. **25**(7), pp.1191–1200.

Harrison, I.J., Brummett, R. and Stiassny, M.L.J. 2016. The Congo River Basin *In*: *The Wetland Book* [Online]. Dordrecht: Springer Netherlands, pp.1–18. Available from: http://link.springer.com/10.1007/978-94-007-6173-5_92-1.

Hauer, C., Leitner, P., Unfer, G., Pulg, U., Habersack, H. and Graf, W. 2018. The Role of Sediment and Sediment Dynamics in the Aquatic Environment *In*: S. Schmutz and J. Sendzimir, eds. *Riverine Ecosystem Management: Science for Governing Towards a Sustainable Future* [Online]. Cham: Springer International Publishing, pp.151–169. Available from: https://doi.org/10.1007/978-3-319-73250-3_8.

Havnø, K., Madsen, M.N. and Dørge, J. 1995. MIKE 11 – a generalized river modelling package *In*: V. P. Singh, ed. *Computer models of watershed hydrology*. Water Resources Publications, pp.733–782.

Hawker, L., Bates, P., Neal, J. and Rougier, J. 2018a. Perspectives on Digital Elevation Model (DEM) Simulation for Flood Modeling in the Absence of a High-Accuracy Open Access Global DEM. *Frontiers in Earth Science*. **6**(December), pp.1–9.

Hawker, L., Neal, J. and Bates, P. 2019. Accuracy assessment of the TanDEM-X 90 Digital Elevation Model for selected floodplain sites. *Remote Sensing of Environment*. **232**(November 2018), p.111319.

Hawker, L., Rougier, J., Neal, J., Bates, P., Archer, L. and Yamazaki, D. 2018b. Implications of Simulating Global Digital Elevation Models for Flood Inundation Studies. *Water Resources Research*. **54**(10), pp.7910–7928.

Hemri, S. and Klein, B. 2017. Analog-Based Postprocessing of Navigation-Related Hydrological Ensemble Forecasts. *Water Resources Research*. **53**(11), pp.9059–9077.

Hess, L.L., Melack, J.M., Novo, E.M.L.M., Barbosa, C.C.F. and Gastil, M. 2003. Dual-season mapping of wetland inundation and vegetation for the central Amazon basin. *Remote Sensing of Environment*. **87**(4), pp.404–428.

Hilton, J.E., Grimaldi, S., Cohen, R.C.Z., Garg, N., Li, Y., Marvanek, S., Pauwels, V.R.N. and Walker, J.P. 2019. River reconstruction using a conformal mapping method. *Environmental Modelling and Software*. **119**(May), pp.197–213.

Hoch, J.M., van Beek, R., Winsemius, H.C. and Bierkens, M.F.P. 2018. Benchmarking flexible meshes and regular grids for large-scale fluvial inundation modelling. *Advances in Water Resources*. **121**(December 2017), pp.350–360.

Huang, C., Chen, Y., Zhang, S. and Wu, J. 2018. Detecting, Extracting, and Monitoring Surface Water From Space Using Optical Sensors: A Review. *Reviews of Geophysics*. **56**(2), pp.333–360.

Hughes, D.A. 2013. A review of 40 years of hydrological science and practice in

Southern Africa using the Pitman rainfall-runoff model. *Journal of Hydrology*. **501**, pp.111–124.

Hughes, R.H. and Hughes, J.S. 1992. *A Directory of African Wetlands* [Online]. International Union for Conservation of Nature and Natural Resources, United Nations Environment Programme, and World Conservation Monitoring Centre. Available from: https://books.google.co.uk/books?hl=en&lr=&id=VLjafeXa3gMC&oi=fnd&pg=PR29&ots=j9jW_FO5ga&sig=y-sRHBmzLg4eBQPEXZ1sYU75LVI&redir_esc=y#v=onepage&q&f=false.

Hunter, N.M., Bates, P.D., Horritt, M.S. and Wilson, M.D. 2007. Simple spatially-distributed models for predicting flood inundation: A review. *Geomorphology*. **90**(3–4), pp.208–225.

Hydroweb 2019. Hydroweb Time series of water levels in the rivers and lakes around the world. [Accessed 15 February 2019]. Available from: http://hydroweb.theia-land.fr/.

Institut de recherche pour le développement 2019. SO HYBAM - The Environmental Research Observatory on the Rivers of the Amazon, Orinoco and Congo Basins. [Accessed 20 November 2017]. Available from: http://www.ore-hybam.org/.

International Federation of Red Cross 2020. *Democratic Republic of Congo and Republic of Congo: Floods* [Online]. Available from: https://reliefweb.int/sites/reliefweb.int/files/resources/IBCDCG170120.pdf.

Jackson, P., Oberg, K., Gardiner, N. and Shelton, J. 2009. Velocity Mapping in the Lower Congo River: A First Look at the Unique Bathymetry and Hydrodynamics of Bulu Reach, West Central Africa. *Symposium on River*., p.7.

Jacobs 2019. Flood Modeller. *Website of Flood Modeller*. [Online]. [Accessed 1 December 2019]. Available from: https://www.floodmodeller.com/products/.

Jamieson, S.R., Lhomme, J., Wright, G. and Gouldby, B. 2012. A highly efficient 2D flood model with sub-element topography. *Proceedings of the Institution of Civil Engineers: Water Management*. **165**(10), pp.581–595.

Jaramillo, F., Brown, I., Castellazzi, P., Espinosa, L., Guittard, A., Hong, S.H., Rivera-Monroy, V.H. and Wdowinski, S. 2018. Assessment of hydrologic connectivity in an ungauged wetland with InSAR observations. *Environmental Research Letters*. **13**(2).

Jarihani, A.A., Callow, J.N., Johansen, K. and Gouweleeuw, B. 2013. Evaluation of multiple satellite altimetry data for studying inland water bodies and river floods. *Journal of Hydrology*. **505**, pp.78–90.

Jarihani, A.A., Callow, J.N., McVicar, T.R., Van Niel, T.G. and Larsen, J.R. 2015. Satellite-derived Digital Elevation Model (DEM) selection, preparation and correction for hydrodynamic modelling in large, low-gradient and data-sparse catchments. *Journal of Hydrology*. **524**, pp.489–506.

Jiang, L., Schneider, R., Andersen, O.B. and Bauer-Gottwein, P. 2017. CryoSat-2 altimetry applications over rivers and lakes. *Water*., pp.1–20.

Johnson, B.L., Richardson, W.B. and Naimo, T.J. 1995. Past, Present, and Future Concepts in Large River Ecology. *BioScience*. **45**(3), pp.134–141.

Jowett, I.G. and Duncan, M.J. 2012. Effectiveness of 1D and 2D hydraulic models for instream habitat analysis in a braided river. *Ecological Engineering*. **48**, pp.92–100.

Jung, H.C., Hamski, J., Durand, M., Alsdorf, D., Hossain, F., Lee, H., Azad Hossain, A.K.M., Hasan, K., Khan, A.S. and Zeaul Hoque, A.K.M. 2010. Characterization of complex fluvial systems using remote sensing of spatial and temporal water level variations in the Amazon, Congo, and Brahmaputra rivers. *Earth Surface Processes and Landforms*. **35**(3), pp.294–304.

Junk, W.J., Bayley, P.B. and Sparks, R.E. 1989. The Flood Pulse Concept in River-Floodplain Systems. *International Large River Symposium. Can. Spec. Publ. Fish. Aquat. Sci.* **106**, pp.110–127.

Karney, C. 2014. Online geoid calculations using the GeoidEval utility. *GeographicLib*. [Online]. [Accessed 4 April 2019]. Available from: https://geographiclib.sourceforge.io/cgi-bin/GeoidEval.

Keddy, P.A., Fraser, L.H., Solomeshch, A.I., Junk, W.J., Campbell, D.R., Arroyo, M.T.K. and Alho, C.J.R. 2009. Wet and Wonderful: The World's Largest Wetlands Are Conservation Priorities. *BioScience*. **59**(1), pp.39–51.

Kim, D., Yu, H., Lee, H., Beighley, E., Durand, M., Alsdorf, D.E. and Hwang, E. 2019. Ensemble learning regression for estimating river discharges using satellite altimetry data : Central Congo River as a Test-bed. *Remote Sensing of Environment*. **221**(221), pp.741–755.

Komori, D., Nakamura, S., Kiguchi, M., Nishijima, A., Yamazaki, D., Suzuki, S.,

Kawasaki, A., Oki, K. and Oki, T. 2012. Characteristics of the 2011 Chao Phraya River flood in Central Thailand. *Hydrological Research Letters*. **6**(0), pp.41–46.

Laínez Samper, M.D., Merino, M.M.R., García, Á.M., Nuñez, R.P. and Tashi, T. 2011. Multisystem real time precise-point-positioning. *Coordinates*.

Lake Chad Basin Commission 2019. Interbasin Water Transfer Project (IBWTP). [Accessed 9 February 2019]. Available from: http://www.cblt.org/en/projects/interbasin-water-transfer-project.

Langhorst, T., Pavelsky, T.M., Frasson, R.P. de M., Wei, R., Domeneghetti, A., Altenau, E.H., Durand, M.T., Minear, J.T., Wegmann, K.W. and Fuller, M.R. 2019. Anticipated improvements to river surface elevation profiles from the surface water and ocean topography mission. *Frontiers in Earth Science*. **7**(May), pp.1–13.

Laporte, N.T., Goetz, S.J., Justice, C.O. and Heinicke, M. 1998. A new land cover map of central Africa derived from multi-resolution, multi-temporal AVHRR data. *International Journal of Remote Sensing*. **19**(18), pp.3537–3550.

Laraque, A. 2019. Oubangui wakes up in Congo Basin after a long sleep. *OMP News*. [Online]. [Accessed 8 December 2019]. Available from: http://www.news.obs-mip.fr/apres-un-long-sommeil-loubangui-se-reveille-dans-le-bassin-du-congo/.

Laraque, A., Castellanos, B., Steiger, J., Lòpez, J.L., Pandi, A., Rodriguez, M., Rosales, J., Adèle, G., Perez, J. and Lagane, C. 2013. A comparison of the suspended and dissolved matter dynamics of two large inter-tropical rivers draining into the Atlantic Ocean: The Congo and the Orinoco. *Hydrological Processes*. **27**(15), pp.2153–2170.

Laraque, A., Mahe, G., Orange, D. and Marieu, B. 2001. Spatiotemporal variations in hydrological regimes within Central Africa during the XXth century. *Journal of Hydrology*. **245**.

Laraque, A., N'kaya, G.D.M., Orange, D., Tshimanga, R., Tshitenge, J.M., Mahé, G., Nguimalet, C.R., Trigg, M.A., Yepez, S. and Gulemvuga, G. 2020. Recent budget of hydroclimatology and hydrosedimentology of the congo river in central Africa. *Water (Switzerland)*. **12**(9).

Latrubesse, E.M. 2008. Patterns of anabranching channels: The ultimate end-member adjustment of mega rivers. *Geomorphology*. **101**(1–2), pp.130–145.

Latrubesse, E.M., Stevaux, J.C. and Sinha, R. 2005. Tropical rivers. *Geomorphology*. **70**(3–4 SPEC. ISS.), pp.187–206.

Lee, H., Beighley, R.E., Alsdorf, D., Jung, H.C., Shum, C.K., Duan, J., Guo, J., Yamazaki, D. and Andreadis, K. 2011. Characterization of terrestrial water dynamics in the Congo Basin using GRACE and satellite radar altimetry. *Remote Sensing of Environment*. **115**(12), pp.3530–3538.

Lee, H., Yuan, T., Jung, H.C. and Beighley, E. 2015. Mapping wetland water depths over the central Congo Basin using PALSAR ScanSAR, Envisat altimetry, and MODIS VCF data. *Remote Sensing of Environment*. **159**, pp.70–79.

Lee, S., Wolberg, G. and Shin, S.Y. 1997. Scattered Data Interpolation with Multilevel B-Splines. *IEEE TRANSACTIONS ON VISUALIZATION AND COMPUTER GRAPHICS*. **3**(3), pp.228–244.

Legleiter, C.J. and Harrison, L.R. 2019. Remote Sensing of River Bathymetry: Evaluating a Range of Sensors, Platforms, and Algorithms on the Upper Sacramento River, California, USA. *Water Resources Research*. **55**(3), pp.2142–2169.

Lehner, B., Verdin, K. and Jarvis, A. 2008. New global hydrography derived from spaceborne elevation data. *Eos, Transactions, American Geophysical Union*. **89**(10), pp.93–94.

Leica Geosystems 2017. PPP service and Leica GG04/GG04 plus smart antenna. [Accessed 27 September 2019]. Available from: https://leica-geosystems.com/-/media/Files/LeicaGeosystems/Services Support/Other/License Activation Guides/Spot-Lite-Spot-Prime-Leica-Zeno-GG04.ashx?la=bg-BG&hash=6CB6A64EAC826C52A775F029775CB2C0.

Leopold, L.B. and Maddock, T.J. 1953. *The Hydraulic Geometry of Stream Channels and Some Physiographic Implications* [Online]. Washington DC, USA. Available from: https://doi.org/10.3133/pp252.

Li, S., Sun, D., Goldberg, M. and Stefanidis, A. 2013. Derivation of 30-m-resolution water maps from TERRA/MODIS and SRTM. *Remote Sensing of Environment*. **134**, pp.417–430.

Lintott, C.M. 2017. Hec-Ras 2D - An Accessible and Capable Modelling Tool *In*: *Water New Zealand's 2017 Stormwater Conference* [Online]. Water New Zealand. Available from: https://www.waternz.org.nz/Attachment?Action=Download&Attachment_id=2515.

Lopes, V.A.R., Trigg, M.A., O'Loughlin, F. and Laraque, A. 2014. Passive optical

remote sensing of Congo River bathymetry using Landsat. *AGU Fall Meeting Abstracts*. **1**(1981), p.529.

Lund, B., Snell, E., Easton, D. and de Beer, A. 2007. Aqueduct to link Central Africa with Southern Africa? A brief outline. *Civil Engineer in South Africa*. (October).

Lyzenga, D.R. 1981. Remote sensing of bottom reflectance and water attenuation parameters in shallow water using aircraft and landsat data. *International Journal of Remote Sensing*. **2**(1), pp.71–82.

Manning, R., Griffith, J.P., Pigot, T.F. and Vernon-Harcourt, L.F. 1890. *On the flow of water in open channels and pipes*.

Markus, T., Neumann, T., Martino, A., Abdalati, W., Brunt, K., Csatho, B., Farrell, S., Fricker, H., Gardner, A., Harding, D., Jasinski, M., Kwok, R., Magruder, L., Lubin, D., Luthcke, S., Morison, J., Nelson, R., Neuenschwander, A., Palm, S., Popescu, S., Shum, C.K., Schutz, B.E., Smith, B., Yang, Y. and Zwally, J. 2017. The Ice, Cloud, and land Elevation Satellite-2 (ICESat-2): Science requirements, concept, and implementation. *Remote Sensing of Environment*. **190**, pp.260–273.

Marlier, G. 1973. Limnology of the Congo and Amazon rivers *In*: B. J. Meggers, E. S. Ayensu and W. D. Duckworth, eds. *Tropical forest ecosystems in Africa and South America: A comparative review*. Washington, DC, USA: Smithsonian Institution Press, pp.223–238.

Meade, R.H., Rayol, J.M., Da Conceicao, S.C. and Natividade, J.R.G. 1991. Backwater effects in the Amazon River basin of Brazil. *Environmental Geology and Water Sciences*. **18**(2), pp.105–114.

Melack, J.M., Hess, L.L., Gastil, M., Forsberg, B.R., Hamilton, S.K., Lima, I.B.T. and Novo, E.M.L.M. 2004. Regionalization of methane emissions in the Amazon Basin with microwave remote sensing. *Global Change Biology*. **10**(5), pp.530–544.

Merwade, V., Cook, A. and Coonrod, J. 2008. GIS techniques for creating river terrain models for hydrodynamic modeling and flood inundation mapping. *Environmental Modelling and Software*. **23**(10–11), pp.1300–1311.

Merwade, V.M., Maidment, D.R. and Goff, J.A. 2006. Anisotropic considerations while interpolating river channel bathymetry. *Journal of Hydrology*. **331**(3–4), pp.731–741.

Milliman, J.D. and Meade, R.H. 1983. World-wide Delivery of River Sediment to the Oceans. *The Journal of Geology*. **91**(1), pp.1–21.

Moglen, G.E. 2015. *Fundamentals of Open Channel Flow* [Online]. CRC Press. Available from: https://books.google.co.uk/books?id=TXF3CAAAQBAJ.

Mohammadimanesh, F., Salehi, B., Mahdianpari, M., Brisco, B. and Motagh, M. 2018. Wetland Water Level Monitoring Using Interferometric Synthetic Aperture Radar (InSAR): A Review. *Canadian Journal of Remote Sensing*. **44**(4), pp.247–262.

Montazem, A.S., Garambois, P.A., Calmant, S., Finaud-Guyot, P., Monnier, J., Medeiros Moreira, D., Minear, J.T. and Biancamaria, S. 2019. Wavelet-Based River Segmentation Using Hydraulic Control-Preserving Water Surface Elevation Profile Properties. *Geophysical Research Letters*.

Moreira, D., Perosanz, F., Calmant, S., A, S., Silva, J., Ramillien, G., Rotunno, O., Monteiro, A. and Shum, C.K. 2012. Applications of GNSS data for hydrological studies in the Amazon basin. *In*: *Poster Presented at EGU General Assembly 2012* [Online]. Vienna, Austria. Available from: https://igsac-cnes.cls.fr/documents/egu12/POSTERS/Z231_Moreira.pdf.

Moreira, D.M., Calmant, S., Perosanz, F., Xavier, L., Rotunno Filho, O.C., Seyler, F. and Monteiro, A.C. 2016. Comparisons of observed and modeled elastic responses to hydrological loading in the Amazon basin. *Geophysical Research Letters*. **43**(18), pp.9604–9610.

Morlock, S.E. 1996. Evaluation of Acoustic Doppler Current Profiler Measurements of River Discharge. *U.S. Geological Survey Water-Resources Investigations Report 95–4218*., p.37.

Moussa, R. and Bocquillon, C. 1996. Criteria for the choice of flood-routing methods in natural channels. *Journal of Hydrology*. **186**(1–4), pp.1–30.

Mushi, C.A., Ndomba, P.M., Trigg, M.A., Tshimanga, R.M. and Mtalo, F. 2019. Assessment of basin-scale soil erosion within the Congo River Basin: A review. *Catena*. **178**(February), pp.64–76.

Nakmuenwai, P., Yamazaki, F. and Liu, W. 2017. Automated extraction of inundated areas from multi-temporal dual-polarization radarsat-2 images of the 2011 central Thailand flood. *Remote Sensing*. **9**(1).

Nanson, G.C. 2013. Anabranching and Anastomosing Rivers *In*: E. Wohl, ed. *Treatise on Fluvial Geomorphology* [Online]. Treatise on Geomorphology. Academic Press, pp.330–345. Available from: https://www.sciencedirect.com/referencework/9780080885223/treatise-on-

geomorphology#book-info.

Nanson, G.C. and Knighton, A.D. 1996. Anabranching rivers: Their cause, character and classification. *Earth Surf. Processes Landforms*. **21**, pp.217–239.

Ndala, B. 2009. CONGO RIVER BASIN: challenges and current initiatives *In*: *5th World Water Forum Session: The Po valley compares itself with big international basins* [Online]., pp.1–10. [Accessed 10 February 2017]. Available from: http://www.inbo-news.org/IMG/pdf/03_CICOS-PO.pdf.

Neal, J., Dunne, T., Sampson, C., Smith, A. and Bates, P. 2018. Optimisation of the two-dimensional hydraulic model LISFOOD-FP for CPU architecture. *Environmental Modelling and Software*. **107**(May), pp.148–157.

Neal, J., Odoni, N.A., Trigg, M.A., Freer, J.E., Garcia-Pintado, J., Mason, D.C., Wood, M. and Bates, P.D. 2015. Efficient incorporation of channel cross-section geometry uncertainty into regional and global scale flood inundation models. *Journal of Hydrology*. **529**, pp.169–183.

Neal, J., Schumann, G.J.P. and Bates, P. 2012. A subgrid channel model for simulating river hydraulics and floodplain inundation over large and data sparse areas. *Water Resources Research*. **48**(11), pp.1–16.

New, M., Lister, D., Hulme, M. and Makin, I. 2002. A high-resolution data set of surface climate over global land areas. *Climate Research*. **21**(1), pp.1–25.

Nicholas, A.P. 2013. Modelling the continuum of river channel patterns. *Earth Surface Processes and Landforms*. **38**(10), pp.1187–1196.

Nicholas, A.P., Ashworth, P.J., Sambrook Smith, G.H. and Sandbach, S.D. 2013. Numerical simulation of bar and island morphodynamics in anabranching megarivers. *Journal of Geophysical Research: Earth Surface*. **118**(4), pp.2019–2044.

Nicholas, A.P., Sandbach, S.D., Ashworth, P.J., Amsler, M.L., Best, J.L., Hardy, R.J., Lane, S.N., Orfeo, O., Parsons, D.R., Reesink, A.J.H., Sambrook Smith, G.H. and Szupiany, R.N. 2012. Modelling hydrodynamics in the Rio Paraná, Argentina: An evaluation and inter-comparison of reduced-complexity and physics based models applied to a large sand-bed river. *Geomorphology*. **169**–**170**, pp.192–211.

Normandin, C., Frappart, F., Diepkilé, A.T., Marieu, V., Mougin, E., Blarel, F., Lubac, B., Braquet, N. and Ba, A. 2018. Evolution of the performances of radar altimetry missions from ERS-2 to Sentinel-3A over the Inner Niger Delta. *Remote Sensing*.

10(6).

Norris, K., Asase, A., Collen, B., Gockowksi, J., Mason, J., Phalan, B. and Wade, A. 2010. Biodiversity in a forest-agriculture mosaic – The changing face of West African rainforests. *Biological Conservation*. **143**(10), pp.2341–2350.

Nyberg, B., Buckley, S.J., Howell, J.A. and Nanson, R.A. 2015. Geometric attribute and shape characterization of modern depositional elements: A quantitative GIS method for empirical analysis. *Computers and Geosciences*. **82**, pp.191–204.

O'Loughlin, F., Neal, J., Schumann, G.J.P., Beighley, E. and Bates, P.D. 2020. A LISFLOOD-FP hydraulic model of the middle reach of the Congo. *Journal of Hydrology*. **580**(October 2019), p.124203.

O'Loughlin, F., Neal, J., Yamazaki, D. and Bates, P.D. 2016a. ICESat-derived inland water surface spot heights. *Water Resources Research*. **52**(4), pp.3276–3284.

O'Loughlin, F., Paiva, R.C.D., Durand, M., Alsdorf, D.E. and Bates, P.D. 2016b. A multi-sensor approach towards a global vegetation corrected SRTM DEM product. *Remote Sensing of Environment*. **182**, pp.49–59.

O'Loughlin, F., Trigg, M.A., Schumann, G.J.P. and Bates, P.D. 2013. Hydraulic characterization of the middle reach of the Congo River. *Water Resources Research*. **49**(8), pp.5059–5070.

Oudart, T., Bertrand, O., Arnaud, J.N. and Mokango, G. 2019. Completing the Kandolo bathymetry with optimization *In*: *XXVIth Telemac & Mascaret User Club* [Online]. Toulouse, FR. Available from: http://cerfacs.fr/tuc2019-repo/TUC2019_FullPapers_PDFs/paper_Oudart_tuc2019.pdf.

Pacetti, T., Caporali, E. and Rulli, M.C. 2017. Floods and food security: A method to estimate the effect of inundation on crops availability. *Advances in Water Resources*. **110**, pp.494–504.

Page, S.E., Rieley, J.O. and Banks, C.J. 2011. Global and regional importance of the tropical peatland carbon pool. *Global Change Biology*. **17**(2), pp.798–818.

Paiva, R., Buarque, D.C., Collischonn, W., Bonnet, M.P., Frappart, F., Calmant, S. and Bulhões Mendes, C.A. 2013. Large-scale hydrologic and hydrodynamic modeling of the Amazon River basin. *Water Resources Research*. **49**(3), pp.1226–1243.

Paris, A., Paiva, R., Santos da Silva, J., Moriera, D., Calmant, S., Garambois, P., Collischonn, W., Bonnet, M.-P. and Seyler, F. 2016. Stage-discharge rating curves

based on satellite altimetry and modeled discharge in the Amazon basin. *Water Resources Research*. **52**, pp.3787–3814.

Parrish, C.E., Magruder, L.A., Neuenschwander, A.L., Forfinski-Sarkozi, N., Alonzo, M. and Jasinski, M. 2019. Validation of ICESat-2 ATLAS Bathymetry and Analysis of ATLAS's Bathymetric Mapping Performance. *Remote Sensing*. **11**(14), p.1634.

Parsons, D.R., Best, J.L., Lane, S.N., Orfeo, O., Hardy, R.J. and Kostaschuk, R. 2007. Form roughness and the absence of secondary flow in a large confluence–diffluence, Rio Paraná, Argentina. *Earth Surface Processes and Landforms*. **32**(1), pp.155–162.

Parsons, D.R., Best, J.L., Orfeo, O., Hardy, R.J., Kostaschuk, R. and Lane, S.N. 2005. Morphology and flow fields of three-dimensional dunes, Rio Paraná, Argentina: Results from simultaneous multibeam echo sounding and acoustic Doppler current profiling. *Journal of Geophysical Research*. **110**(4), pp.1–9.

Partow, H. 2011. *Water Issues in the Democratic Republic of the Congo. Challenges and Opportunities. UNEP Technical report* [Online]. Available from: http://postconflict.unep.ch/publications/UNEP_DRC_water.pdf.

Pavelsky, T.M., Durand, M.T., Andreadis, K.M., Beighley, R.E., Paiva, R.C.D., Allen, G.H. and Miller, Z.F. 2014. Assessing the potential global extent of SWOT river discharge observations. *Journal of Hydrology*. **519**(PB), pp.1516–1525.

Paz, A.R.., Collischonn, W., Tucci, C.E.. and Padovani, C.R. 2011. Large-scale modelling of channel flow and floodplain inundation dynamics and its application to the Pantanal (Brazil). *Hydrological Processes*. **25**(9), pp.1498–1516.

Pekel, J.-F., Cottam, A., Gorelick, N. and Belward, A.S. 2016. High-resolution mapping of global surface water and its long-term changes. *Nature*. **540**(7633), pp.418–422.

Philip, S., Sparrow, S., Kew, S.F., Van Der Wiel, K., Wanders, N., Singh, R., Hassan, A., Mohammed, K., Javid, H., Haustein, K., Otto, F.E.L., Hirpa, F., Rimi, R.H., Saiful Islam, A.K.M., Wallom, D.C.H. and Jan Van Oldenborgh, G. 2019. Attributing the 2017 Bangladesh floods from meteorological and hydrological perspectives. *Hydrology and Earth System Sciences*. **23**(3), pp.1409–1429.

Pinheiro, M., Amao-Oliva, J., Scheiber, R., Jaeger, M., Horn, R., Keller, M., Fischer, J. and Reigber, A. 2020. Dual-frequency airborne SAR for large scale mapping of tidal flats. *Remote Sensing*. **12**(11), pp.1–26.

Policelli, F., Slayback, D., Brakenridge, B., Nigro, J., Hubbard, A., Zaitchik, B., Carroll, M. and Jung, H. 2017. The NASA Global Flood Mapping System *In*: V. Lakshmi, ed. *Remote Sensing of Hydrological Extremes* [Online]. Cham: Springer International Publishing, pp.47–63. Available from: https://doi.org/10.1007/978-3-319-43744-6_3.

Ponce, V.M., Li, R.M. and Simons, D.B. 1978. APPLICABILITY OF KINEMATIC AND DIFFUSION-MODELS. *Proceedings of the American Society of Civil Engineers.* **104**(3), pp.353–360.

Qaddumi, H. 2008. *Practial Approaches to transboundary water benefit shairng* [Online]. London. Available from: http://www.odi.org/sites/odi.org.uk/files/odi-assets/publications-opinion-files/2576.pdf.

QGIS Development Team 2019. QGIS Geographic Information System. Available from: https://www.qgis.org/en/site/index.html.

Raymond, P.A., Hartmann, J., Lauerwald, R., Sobek, S., McDonald, C., Hoover, M., Butman, D., Striegl, R., Mayorga, E., Humborg, C., Kortelainen, P., Dürr, H., Meybeck, M., Ciais, P. and Guth, P. 2013. Global carbon dioxide emissions from inland waters. *Nature*. **503**(7476), pp.355–359.

Remo, J.W.F., Khanal, A. and Pinter, N. 2013. Assessment of chevron dikes for the enhancement of physical-aquatic habitat within the Middle Mississippi River, USA. *Journal of Hydrology*. **501**, pp.146–162.

Rexer, M. and Hirt, C. 2014. Comparison of free high resolution digital elevation data sets (ASTER GDEM2, SRTM v2.1/v4.1) and validation against accurate heights from the Australian National Gravity Database. *Australian Journal of Earth Sciences*. **61**(2), pp.213–226.

Richey, J.E., Melack, J.M., Aufdenkampe, A.K., Ballester, V.M. and Hess, L.L. 2002. Outgassing from Amazonian rivers and wetlands as a large tropical source of atmospheric CO 2. *Nature*. **416**, pp.617–620.

Richey, J.E., Mertes, L.A.K., Dunne, T., Victoria, R.L., Forsberg, B.R., Tancredi, A.C.N.S. and Oliveira, E. 1989. Sources and Routing of the Amazon River Flood Wave. *GLOBAL BIOGEOCHEMICAL CYCLES*. **3**(3), pp.191–204.

van Rijn, L.C. 1993. *Principles of Sediment Transport in Rivers, Estuaries and Coastal Seas*. Amsterdam: Aqua Publications.

Rizzoli, P., Martone, M., Gonzalez, C., Wecklich, C., Borla Tridon, D., Bräutigam, B.,

Bachmann, M., Schulze, D., Fritz, T., Huber, M., Wessel, B., Krieger, G., Zink, M. and Moreira, A. 2017. Generation and performance assessment of the global TanDEM-X digital elevation model. *ISPRS Journal of Photogrammetry and Remote Sensing*. **132**, pp.119–139.

Robert, A. 2003. *River Processes: An Introduction to Fluvial Dynamics*. Arnold.

Robert, M. 1946. *Le Congo physique*. H. Vaillant-Carmanne.

Rodriguez, E. 2016. Surface Water and Ocean Topography Mission (SWOT) Project - Science requirements Documents. *SWOT NASA/JPL Project*.

Rodriguez, E. and Frasson, R.P. de M. 2019. SWOT Discharge Estimation for Multichannel Rivers. *Unpublished Research Proposal*.

Rodríguez, E. and Frasson, R.P. de M. 2020. SWOT Discharge Estimation for Multichannel Rivers. Available from: https://swot.jpl.nasa.gov/people/161/ernesto-rodriguez/.

Rodríguez, E., Morris, C.S. and Belz, J.E. 2006. A global assessment of the SRTM performance. *Photogrammetric Engineering and Remote Sensing*. **72**(3), pp.249–260.

Rohács, J. and Simongáti, G. 2007. The role of inland waterway navigation in a sustainable transport system. *Transport*. **22**(3), pp.148–153.

Rötz, A. and Theobald, S. 2019. Model-Based Operation of Multi-Purpose River and Reservoir Systems. . **1**.

Rudorff, C.M., Melack, J.M. and Bates, P.D. 2014. Flooding dynamics on the lower Amazon floodplain: 1. Hydraulic controls on water elevation, inundation extent, and river-floodplain discharge. *Water Resources Research*. **50**(1), pp.619–634.

Runge, J. 2007. The Congo River, Central Africa *In*: A. Gupta, ed. *Large Rivers: Geomorphology and Management* [Online]. Chichester, UK: John Wiley & Sons, Ltd, pp.293–308. Available from: http://doi.wiley.com/10.1002/9780470723722.

Sampson, C.C., Smith, A.M., Bates, P.B., Neal, J., Alfieri, L. and Freer, J.E. 2015. A high-resolution global flood hazard model. *Water Resources Research*. **51**(9), pp.7358–7381.

Sampson, C.C., Smith, A.M., Bates, P.D., Neal, J. and Trigg, M.A. 2016. Perspectives on Open Access High Resolution Digital Elevation Models to Produce Global Flood Hazard Layers. *Frontiers in Earth Science*. **3**, p.85.

Samuels, P.G. 1989. Backwater lengths in rivers. *Proceedings - Institution of Civil Engineers. Part 2. Research and theory*. **87**(February), pp.571–582.

Samuels, P.G. 1990. Cross-section location in 1-D models *In*: *International Conference on River Flood Hydraulics* [Online]. Wallingford, UK, pp.339–350. Available from: https://www.researchgate.net/publication/258507253_Cross-section_location_in_1-D_models.

Sanders, B.F. 2007. Evaluation of on-line DEMs for flood inundation modeling. *Advances in Water Resources*. **30**(8), pp.1831–1843.

Santoro, M., Kirches, G., Wevers, J., Boettcher, M., Brockmann, C., Lamarche, C., Bontemps, S., Moreau, I. and Defourny, P. 2017. *Land Cover CCI Product User Guide Version 2.0* [Online]. Available from: http://maps.elie.ucl.ac.be/CCI/viewer/download/ESACCI-LC-Ph2-PUGv2_2.0.pdf.

Santos da Silva, J., Calmant, S., Seyler, F., Rotunno Filho, O.C., Cochonneau, G. and Mansur, W.J. 2010. Water levels in the Amazon basin derived from the ERS 2 and ENVISAT radar altimetry missions. *Remote Sensing of Environment*. **114**(10), pp.2160–2181.

Sanyal, J., Carbonneau, P. and Densmore, A.L. 2014. Low-cost flood inundation modelling at reach scale with sparse data in the lower Damodar river basin, India. *Hydrological Sciences Journal*. **6667**(June), p.140120033456007.

Savage, J.T.S., Bates, P., Freer, J., Neal, J. and Aronica, G. 2016. When does spatial resolution become spurious in probabilistic flood inundation predictions? *Hydrological Processes*. **30**(13), pp.2014–2032.

Sawakuchi, H.O., Bastviken, D., Sawakuchi, A.O., Krusche, A. V., Ballester, M.V.R. and Richey, J.E. 2014. Methane emissions from Amazonian Rivers and their contribution to the global methane budget. *Global Change Biology*. **20**(9), pp.2829–2840.

Schiavina, M., Freire, S. and MacManus, K. 2019. GHS-POP R2019A - GHS population grid multitemporal (1975-1990-2000-2015). *European Commission, Joint Research Centre (JRC) [Dataset]*. [Online]. Available from: https://data.jrc.ec.europa.eu/dataset/0c6b9751-a71f-4062-830b-43c9f432370f.

Schneider, R., Nygaard Godiksen, P., Villadsen, H., Madsen, H. and Bauer-Gottwein, P. 2017. Application of CryoSat-2 altimetry data for river analysis and modelling. *Hydrology and Earth System Sciences*. **21**(2), pp.751–764.

Schneider, R., Ridler, M.E., Godiksen, P.N., Madsen, H. and Bauer-Gottwein, P. 2018. A data assimilation system combining CryoSat-2 data and hydrodynamic river models. *Journal of Hydrology*. **557**, pp.197–210.

Schoemaker, J., Scholtz, A. and Enei, R. 2012. Towards low carbon transport in Europe. *Transport Research and Innovation Portal (TRIP) consortium on behalf of the European Commission's Directorate-General for Mobility and Transport (DG MOVE)*.

Schumann, G.J.P. 2014. Fight floods on a global scale. *Nature*. **507**(7491), p.169.

Schumann, G.J.P., Di Baldassarre, G., Alsdorf, D. and Bates, P.D. 2010. Near real-time flood wave approximation on large rivers from space: Application to the River Po, Italy. *Water Resources Research*. **46**(5), pp.1–8.

Schumann, G.J.P., Bates, P.D., Horritt, M.S., Matgen, P. and Pappenberger, F. 2009. Progress in intergration of remote sensing derived flood extent and stage data and hydraulic models. *Reviews of Geophysics*. **47**(2008), pp.1–20.

Schumann, G.J.P. and Moller, D.K. 2015. Microwave remote sensing of flood inundation. *Physics and Chemistry of the Earth*. **83**–**84**, pp.84–95.

Schumann, G.J.P., Neal, J., Voisin, N., Andreadis, K.M., Pappenberger, F., Phanthuwongpakdee, N., Hall, A.C. and Bates, P.D. 2013. A first large-scale flood inundation forecasting model. *Water Resources Research*. **49**(10), pp.6248–6257.

Schuurman, F., Kleinhans, M.G. and Middelkoop, H. 2016. Network response to disturbances in large sand-bed braided rivers. *Earth Surface Dynamics*. **4**, pp.25–45.

Seafloor Systems Incorporated 2017. Teledyne Odom MB1 Multibeam Echosounder Ex-Rental Sale. [Accessed 24 April 2017]. Available from: http://seafloorsystems.com/products/product/teledyne-odom-mb1-multibeam-echosounder-ex-rental-sale/category_pathway-77.

Slater, L.J., Singer, M.B. and Kirchner, J.W. 2015. Hydrologic versus geomorphic drivers of trends in flood hazard. *Geophysical Research Letters*. **42**(2), pp.370–376.

Smith, A., Bates, P.D., Wing, O., Sampson, C., Quinn, N. and Neal, J. 2019. New estimates of flood exposure in developing countries using high-resolution population data. *Nature Communications*. **10**(1), pp.1–7.

Smith, L.C. 1997. Satellite remote sensing of river inundation area, stage, and discharge: a review. *Hydrological Processes*. **11**(10), pp.1427–1439.

Smith, L.C., Isacks, B.L., Bloom, A.L. and Murray, A.B. 1996. Estimation of discharge from three braided rivers using synthetic aperture radar satellite imagery: Potential application to ungaged basins. *Water Resources Research*. **32**(7), pp.2021–2034.

Smith, M.W., Macklin, M.G. and Thomas, C.J. 2013. Hydrological and geomorphological controls of malaria transmission. *Earth-Science Reviews*. **116**(1), pp.109–127.

Société nationale d'électricité 2014. The Grand Inga Project *In*: *The Japan-Africa Business Forum 2014* [Online]. Tokyo. Available from: https://afdb-org.jp/wp-content/themes/meteo/pdf/67. DRC_Minister NEMOYATO_Mr. Ibalanky.pdf.

Spencer, R.G.M., Hernes, P.J., Dinga, B., Wabakanghanzi, J.N., Drake, T.W. and Six, J. 2016. Origins, seasonality, and fluxes of organic matter in the Congo River. *Global Biogeochemical Cycles*. **30**(7), pp.1105–1121.

Stanley, H.M. 1885. *The Congo and the founding of its free state: A story of work and exploration*. New York: Harper and Brothers.

Tadono, T., Ishida, H., Oda, F., Naito, S., Minakawa, K. and Iwamoto, H. 2014. Precise Global DEM Generation by ALOS PRISM. *ISPRS Annals of Photogrammetry, Remote Sensing and Spatial Information Sciences*. **II-4**(May), pp.71–76.

Tal, M. and Paola, C. 2010. Effects of vegetation on channel morphodynamics: Results and insights from laboratory experiments. *Earth Surface Processes and Landforms*. **35**(9), pp.1014–1028.

Tavares da Costa, R., Mazzoli, P. and Bagli, S. 2019. Limitations posed by free DEMs in watershed studies: The case of river Tanaro in Italy. *Frontiers in Earth Science*. **7**(June).

Tockner, K., Bunn, S.E., Gordon, C., Naiman, R.J., Quinn, G.P. and Stanford, J.A. 2008. Flood plains: Critically threatened ecosystems *In*: *Aquatic Ecosystems: Trends and Global Prospects*., pp.45–62.

Tomczak, M. 1998. Spatial Interpolation and its Uncertainty Using Automated Anisotropic Inverse Distance Weighting (IDW) - Cross-Validation/Jackknife Approach. . **2**(2), pp.18–30.

Trefon, T. 2016. *Congo's Environmental Paradox: Potential and Predation in a Land of*

Plenty [Online]. Zed Books. Available from: https://books.google.co.uk/books?id=8HNjDgAAQBAJ.

Trigg, M.A., Bates, P.D., Wilson, M.D., Schumann, G.J.P. and Baugh, C. 2012. Floodplain channel morphology and networks of the middle Amazon River. *Water Resources Research*. **48**(10).

Trigg, M.A., Birch, C.E., Neal, J., Bates, P.D., Smith, A., Sampson, C.C., Yamazaki, D., Hirabayashi, Y., Pappenberger, F., Dutra, E., Ward, P.J., Winsemius, H.C., Salamon, P., Dottori, F., Rudari, R., Kappes, M.S., Simpson, A.L., Hadzilacos, G. and Fewtrell, T.J. 2016. The credibility challenge for global fluvial flood risk analysis. *Environmental Research Letters*. **11**(9), p.094014.

Trigg, M.A., Michaelides, K., Neal, J. and Bates, P.D. 2013. Surface water connectivity dynamics of a large scale extreme flood. *Journal of Hydrology*. **505**, pp.138–149.

Trigg, M.A., Tshimanga, R.M., Ndomba, P., Mtalo, F.A., Hughes, D.A., Mushi, C.A., Bola, G.B., Kabuya, P.M., Carr, A.B., Bernhofen, M., Neal, J., Baya, J.T., Ngandu, F.K. and Bates, P. 2020. Putting river users at the heart of hydraulics and morphology research in the Congo Basin *In*: D. E. Alsdorf, ed. *Congo Basin Hydrology, Climate, and Biogeochemistry: A Foundation for the Future*. AGU Books. Manuscript submitted for Publication.

Trigg, M.A., Wilson, M.D., Bates, P.D., Horritt, M.S., Alsdorf, D.E., Forsberg, B.R. and Vega, M.C. 2009. Amazon flood wave hydraulics. *Journal of Hydrology*. **374**(1–2), pp.92–105.

Trimble 2019. Trimble RTX Frequently Asked Questions. [Accessed 24 September 2019]. Available from: https://positioningservices.trimble.com/services/rtx/centerpoint-rtx/.

Tsai, C.W. 2003. Dynamic Wave Models to Unsteady Flow Routing. *Journal of Hydraulic Engineering*. **129**(8), pp.613–628.

Tshimanga, R.M. and Hughes, D.A. 2014. Basin-scale performance of a semidistributed rainfall-runoff model for hydrological predictions and water resources assessment of large rivers: The Congo River. *Water Resources Research*. **50**(2), pp.1174–1188.

Tshimanga, R.M. and Hughes, D.A. 2012. Climate change and impacts on the hydrology of the Congo Basin: The case of the northern sub-basins of the Oubangui and Sangha Rivers. *Physics and Chemistry of the Earth*. **50**–**52**, pp.72–

83.

Tshimanga, R.M., Trigg, M.A., Neal, J.C., Ndomba, P., Hughes, D.A., Carr, A.B., Kabuya, P.M., Bola, G.B., Mushi, C.A., Beya, J.T., Ngandu, F.K., Mokango, G.M., Mtalo, F. and Bates, P. 2020. New measurements of Congo River water dynamics and sediment transport *In*: D. E. Alsdorf, ed. *Congo Basin Hydrology, Climate, and Biogeochemistry: A Foundation for the Future*. Wiley-Blackwell, AGU Books. Manuscript submitted for Publication.

Tshimanga, R.M., Tshitenge, J.M., Kabuya, P., Alsdorf, D., Mahe, G., Kibukusa, G. and Lukanda, V. 2016. A Regional Perspective of Flood Forecasting and Disaster Management Systems for the Congo River Basin *In*: *Flood Forecasting: A Global Perspective*., pp.87–124.

Tuozzolo, S., Langhorst, T., de Moraes Frasson, R.P., Pavelsky, T., Durand, M. and Schobelock, J.J. 2019. The impact of reach averaging Manning's equation for an in-situ dataset of water surface elevation, width, and slope. *Journal of Hydrology*. **578**(April), p.123866.

Twilley, R.R., Bentley, S.J., Chen, Q., Edmonds, D.A., Hagen, S.C., Lam, N.S.N., Willson, C.S., Xu, K., Braud, D.W., Hampton Peele, R. and McCall, A. 2016. Co-evolution of wetland landscapes, flooding, and human settlement in the Mississippi River Delta Plain. *Sustainability Science*. **11**(4), pp.711–731.

Uddin, K., Matin, M.A. and Meyer, F.J. 2019. Operational flood mapping using multi-temporal Sentinel-1 SAR images: A case study from Bangladesh. *Remote Sensing*. **11**(13).

United Nations 2019. DR Congo President and UN chief meet at a 'historic moment' for democracy in the country. *UN News*. [Online]. [Accessed 26 February 2020]. Available from: https://news.un.org/en/story/2019/09/1045402.

UNOSAT 2019. *SATELLITE-DETECTED FLOOD WATERS, AS OF 29 NOVEMBER 2019, OVER LOUKOLÉLA, CUVETTE DEPARTMENT, REPUBLIC OF CONGO* [Online]. Available from: https://unitar.org/maps/map/2996.

Urban, T.J., Schutz, B.E. and Neuenschwander, A.L. 2008. A Survey of ICESat Coastal Altimetry Applications : Continental Coast , Open Ocean Island , and Inland River. . **19**(1), pp.1–19.

Vested, H.J., Tjerry, S., Christensen, B.B. and Dubinski, I.M. 2014. Numerical simulation of estuarine and river morphology *In*: *Small scale morphological*

evolution of coastal, estuarine and river systems [Online]. Available from: https://www.dhigroup.com/upload/publications/mike21/Vested_2014.pdf?_ga=2.113934595.548954691.1581333379-671665957.1581333379.

Vieira, J.H.D. 1983. Conditions governing the use of approximations for the Saint-Vénant equations for shallow surface water flow. *Journal of Hydrology*. **60**(1–4), pp.43–58.

Voisin, N., Wood, A.W. and Lettenmaier, D.P. 2008. Evaluation of precipitation products for global hydrological prediction. *Journal of Hydrometeorology*. **9**(3), pp.388–407.

Vander Vorste, R., McElmurray, P., Bell, S., Eliason, K.M. and Brown, B.L. 2017. Does stream size really explain biodiversity patterns in lotic systems? A call for mechanistic explanations. *Diversity*. **9**(3), pp.1–21.

Warne, A.G., Meade, R.H., White, W.A., Guevara, E.H., Gibeaut, J., Smyth, R.C., Aslan, A. and Tremblay, T. 2002. Regional controls on geomorphology, hydrology, and ecosystem integrity in the Orinoco Delta, Venezuela. *Geomorphology*. **44**(3–4), pp.273–307.

Wasser, L. and Goulden, T. 2017. Going On The Grid - An Intro to Gridding & Spatial Interpolation. *National Ecological Observatory Network Tutorials*. [Online]. [Accessed 14 May 2018]. Available from: https://www.neonscience.org/spatial-interpolation-basics.

Wilson, M.D., Bates, P., Alsdorf, D., Forsberg, B., Horritt, M., Melack, J., Frappart, F. and Famiglietti, J. 2007. Modeling large-scale inundation of Amazonian seasonally flooded wetlands. *Geophysical Research Letters*. **34**(15), pp.4–9.

Winemiller, K.O., McIntyre, P.B., Castello, L., Fluet-Chouinard, E., Giarrizzo, T., Nam, S., Baird, I.G., Darwall, W., Lujan, N.K., Harrison, I., Stiassny, M.L.J., Silvano, R.A.M., Fitzgerald, D.B., Pelicice, F.M., Agostinho, A.A., Gomes, L.C., Albert, J.S., Baran, E., Petrere, M., Zarfl, C., Mulligan, M., Sullivan, J.P., Arantes, C.C., Sousa, L.M., Koning, A.A., Hoeinghaus, D.J., Sabaj, M., Lundberg, J.G., Armbruster, J., Thieme, M.L., Petry, P., Zuanon, J., Vilara, G.T., Snoeks, J., Ou, C., Rainboth, W., Pavanelli, C.S., Akama, A., van Soesbergen, A. and Saenz, L. 2016. Balancing hydropower and biodiversity in the Amazon, Congo, and Mekong. *Science*. **351**(6269), pp.128–129.

Wohl, E. 2007. Hydrology and Discharge *In*: A. Gupta, ed. *Large Rivers:*

Geomorphology and Management. Wiley, pp.29–41.

Wood, M., RKO Pictures and British Broadcasting Corporation 1986. River Journeys: The Congo. Available from: https://www.youtube.com/watch?v=TazS5BzAd-8.

World Bank 2014. Transformational Hydropower Development Project Paves the Way for 9 Million People in the Democratic Republic of Congo to Gain Access to Electricity. *FEATURE STORY*. [Online]. [Accessed 28 September 2019]. Available from: https://www.worldbank.org/en/news/feature/2014/03/20/transformational-hydropower-development-project-paves-the-way-for-9-million-people-in-the-democratic-republic-of-congo-to-gain-access-to-electricity.

World Bank Group 2014. Inga-3 Basse Chute and Mid-size Hydropower Development Technical Assistance Project. *Inga-3 Basse Chute and Mid-size Hydropower Development Technical Assistance Project*.

Wu, C.Y., Mossa, J., Mao, L. and Almulla, M. 2019. Comparison of different spatial interpolation methods for historical hydrographic data of the lowermost Mississippi River. *Annals of GIS*. **25**(2), pp.133–151.

Yamazaki, D., Ikeshima, D., Tawatari, R., Yamaguchi, T., O'Loughlin, F., Neal, J., Sampson, C.C., Kanae, S. and Bates, P.D. 2017. A high-accuracy map of global terrain elevations. *Geophysical Research Letters*. **44**(11), pp.5844–5853.

Yamazaki, D., Kanae, S., Kim, H. and Oki, T. 2011. A physically based description of floodplain inundation dynamics in a global river routing model. *Water Resources Research*. **47**(4).

Yan, K., Di Baldassarre, G., Solomatine, D.P. and Schumann, G.J.P. 2015. A review of low-cost space-borne data for flood modelling: topography, flood extent and water level. *Hydrological Processes*. **29**(15), pp.3368–3387.

Yoon, Y., Durand, M., Merry, C.J., Clark, E.A., Andreadis, K.M. and Alsdorf, D.E. 2012. Estimating river bathymetry from data assimilation of synthetic SWOT measurements. *Journal of Hydrology*. **464**–**465**, pp.363–375.

Yossef, M.F.M. 2016. Morphological model of the River Rhine branches in The Netherlands *In*: *Deltares Webinar* [Online]. [Accessed 14 October 2019]. Available from: https://www.deltares.nl/app/uploads/2016/10/Delft3D-DVR-Webinar-20161012.pdf.

Yu, D. and Lane, S.N. 2006a. Urban fluvial flood modelling using a two-dimensional diffusion-wave treatment, part 1: Mesh resolution effects. *Hydrological Processes*.

20(7), pp.1541–1565.

Yu, D. and Lane, S.N. 2006b. Urban fluvial flood modelling using a two-dimensional diffusion-wave treatment, part 2: Development of a sub-grid-scale treatment. *Hydrological Processes*. **20**(7), pp.1567–1583.

Yuan, T., Lee, H., Jung, H.C., Aierken, A., Beighley, E., Alsdorf, D.E., Tshimanga, R.M. and Kim, D. 2017. Absolute water storages in the Congo River floodplains from integration of InSAR and satellite radar altimetry. *Remote Sensing of Environment*. **201**(September), pp.57–72.

Zwally, H.., Schutz, R., Bentley, C., Bufton, J., Herring, T., Minster, J., Spinhirne, J. and Thomas, R. 2012. GLAS/ICESat L2 Antarctic and Greenland Ice Sheet Altimetry Data, Version 33, [GLA14].